NON-INVASIVE MEASUREMENTS OF TISSUE HEMODYNAMICS WITH HYBRID DIFFUSE OPTICAL METHODS

Turgut Durduran

A Dissertation

in

Physics and Astronomy

Presented to the Faculties of the University of Pennsylvania in Partial

Fulfillment of the Requirements for the Degree of Doctor of Philosophy

2004

Arjun G Yodh

Supervisor of Dissertation

Randall D Kamien

Graduate Group Chairperson

Dedication

This work is dedicated to

“Nene”

and

My parents

Acknowledgements

I begun working in Arjun Yodh's lab around the end of 1995 as an undergraduate. Since then, my scientific thinking has developed under the leadership of Arjun. His critical approach to complex problems and his keen eye to notice key strengths and weaknesses in our results have proven themselves to be of great value in doing my research. Both as an undergraduate and as a graduate student, I have worked on a large variety of projects and I am confident that now I can sit down with a new collaborator and jump start a project. I owe this to Arjun's enthusiasm and quick thinking in expanding the horizons of biomedical optics, always pushing the limits. I am looking forward to my time in his group as a post-doctoral fellow.

A key to our success in this field was the help of our collaborators. I won't be able to list all our collaborators over these years but I am indebted to them nevertheless.

I single out Joel Greenberg from Department of Neurology with whom I have spent countless hours discussing our measurements. He has always been eager to listen to weaknesses, strengths and complications of our methods and critically approach our ability to obtain physiologically relevant data. Both him and researchers in his lab have helped me push our field forward in imaging cerebral hemodynamics. Without his help, most of the studies described in this work would not have been possible. Over the years, I have worked with Daisuke Furuya, Tomokazu Shimazu and Mark Burnett in Joel's lab. Together we have enjoyed the research we did, and our time outside the lab. Through Joel, I have also got the chance to collaborate with other keen researchers, of which, John Detre has been a valuable advisor in translating our technology to measurements in the human brain.

Another collaborator, Britton Chance (B.C), a world famous scientist and countless number of people from his laboratory have also helped me greatly in this research. B.C's amazing insight into

understanding physiological problems have always proven itself to be of great value in relating my results to the underlying physiology. From his laboratory, I have enjoyed collaborating with Vasilis Ntziachristos, Xavier Intes, Yu Chen, Shoko Nioka and Gwen Lech. I owe a lot to Vasilis and Xavier for their help while I was learning image reconstruction and Shoko Nioka and Gwen Lech for their enthusiasm in pushing the muscle hemodynamics project forward.

Another advantage of being Arjun's group was the opportunity to be mentored by great scientists of this field. In my undergraduate years, I had the opportunity to work with David Boas and Xingde Li. David taught me intricate details of photon migration in tissues and Xingde introduced me to experimental tools. With their help I had a strong background when I begun my graduate studies under close supervision of Joseph Culver. Joe has helped me in everything I worked on from theoretical issues to experimental ones. His patient and calm approach to science, combined with his ability to summarize complicate problems in a way a beginning Ph.D student can understand was of great value. He was like a second advisor to me. Cecil Cheung and Leonid Zubkov have also mentored me on early years of my work. I owe most of my knowledge in diffuse correlation to Cecil and my knowledge about laboratory "tricks" to Leonid. Leonid also provided the much needed touch of humor to our group.

Over the years, I have also had the opportunity to work with many graduate students, postdoctoral fellows and undergraduates. Regine Choe (Regina) has been a supporting colleague and a close friend all through my graduate work. Regina and I have spent many many days in the laboratory working together on problems as well as countless number of trips to "odd" restaurants all over the country. Many of this work would not have been produced without her help. I am looking forward to continue working with her as a postdoc. She is one of the most loyal friends a person can have. Guoqiang Yu has joined our group toward the end of my graduate work. His ambitious

approach to science and strong background in electronics helped me to push forward hybrid optical technologies. I enjoyed working with him. Alper Corlu, Ulas Sunar, Joe Giammarco, Monica Holboke, Kijoon Lee and Chao Zhou are other members of Arjun's lab that have helped me over the years. We turned our offices into "kahvehane" with Alper and Ulas on many occasions.

I thank the staff in Department of Physics and Astronomy for their help in putting the paperwork in order. Various members of the business office have played a significant role – may be unknown to them – in getting projects done in time by timely placing tens of complex purchase orders I have placed. Glen Fechner has been of great help in arranging countless number of meetings with our collaborators.

Without my family and their guidance I would not have made it to where I am today. My mother, Sefika, has taught me self-discipline and confidence which are critical in doing good science. My father, Alpay, raised me as an inquiring person with an analytical mind. He introduced me to doing experiments with hobby electronics and household goods, to proving theorems from basic principles and most importantly to using computers to solve problems. Their confidence in my abilities and constant encouragement helped me proceed through hardships of life without falling down. My grandmother, "Nene", has always been with me from childhood and she raised me while my parents were busy at work. She has waited all these years defying her old age to see my graduation.

Finally, Eylem was always with me, helping me go through my life. She has supported me with her love and encouragement. Without her, I would not have enjoyed my life outside the lab. Without her, endless hours of research would have drained me physically and emotionally. I am looking forward to sharing my whole life with her.

Abstract

Non-Invasive Measurements of Tissue Hemodynamics with Hybrid Diffuse Optical Methods

Turgut Durduran

Arjun G Yodh

Diffuse optical techniques were used to measure hemodynamics of tissues non-invasively. Spectroscopy and tomography of the brain, muscle and implanted tumors were carried out in animal models and humans. Two qualitatively different methods, diffuse optical tomography and diffuse correlation tomography, were hybridized permitting simultaneous measurement of total hemoglobin concentration, blood oxygen saturation and blood flow. This combination of information was processed further to derive estimates of oxygen metabolism (e.g $CMRO_2$) in tissue. The diffuse correlation measurements of blood flow were demonstrated in human tissues, for the first time, demonstrating continous, non-invasive imaging of oxygen metabolism in large tissue volumes several centimeters below the tissue surface.

The bulk of these investigations focussed on cerebral hemodynamics. Extensive validation of this methodology was carried out in *in vivo* rat brain models. Three dimensional images of deep tissue hemodynamics in middle cerebral artery occlusion and cortical spreading depression (CSD) were obtained. CSD hemodynamics were found to depend strongly on partial pressure of carbon dioxide. The technique was then adapted for measurement of human brain. All optical spectroscopic measurements of $CMRO_2$ during functional activation were obtained through *intact* human skull non-invasively. Finally, a high spatio-temporal resolution measurement of cerebral

blood flow due to somatosensory cortex activation following electrical forepaw stimulation in rats was carried out with laser speckle flowmetry. New analysis methods were introduced for laser speckle flowmetry.

In other organs, deep tissue hemodynamics were measured on human calf muscle during exercise and cuff-ischemia and were shown to have some clinical utility for peripheral vascular disease. In mice tumor models, the measured hemodynamics were shown to be predictive of photodynamic therapy efficacy, again suggesting promise of clinical utility.

In total, the research has pioneered the development of diffuse optical measurements of blood flow, oxygenation and oxygen metabolism in a large range of research and clinical applications.

Contents

Dedication **iv**

Acknowledgements **v**

Abstract **viii**

List of Tables **xvii**

List of Figures **xxi**

1 Introduction **1**

2 Theory **9**

2.1 Diffuse Optical Tomography and Spectroscopy 9

2.1.1 Introduction 9

2.1.2 Photon Diffusion in Tissues 10

2.1.3 Spectroscopy in the Semi-Infinite Approximation 13

2.1.4 Diffuse Optical Tomography in the Frequency Domain 15

2.1.5 Regularized Singular Value Decomposition (SVD) Approach to DOT . . . 19

2.1.6 Two Layer Model in k-Space 21

2.1.7 Multi-Spectral Spectroscopy and Tomography 24
2.1.7.1 Spectroscopy using *a priori* Spectral Information 25
2.1.7.2 Image Reconstruction using *a priori* Spectral Information 26
2.1.8 Differential Pathlength Formulation of Photon Migration 28
2.2 Diffuse Correlation Spectroscopy and Tomography 32
2.2.1 Introduction 32
2.2.2 Correlation Diffusion 32
2.2.3 Correlation Spectroscopy in the Semi-Infinite Approximation 35
2.2.4 Two Layer Approximation for Diffuse Correlation Tomography 36
2.2.5 Tomography with Diffuse Correlation 40
2.3 Metabolic Rate of Oxygen Extraction (MRO_2/$CMRO_2$) 43
2.4 APPENDIX: Segmented Tomography using *a priori* Spectral Information 48

3 Hybrid Instrumentation **55**
3.1 Introduction 55
3.2 Common Instrument Characteristics and Modules 58
3.2.1 Instrument Characteristics 59
3.2.2 Common Modules 62
3.3 Generation I: Hybrid Instrumentation/Non-Contact Probe 67
3.4 Generation II: Hybrid, Portable, Small-Tissue Imager 68
3.5 Generation III: Frequency Domain Multiplexing System 71
3.5.1 Instrument design 73
3.5.1.1 Frequency division multiplexing method 73
3.5.1.2 Instrumentation 73

3.5.1.3 Instrument performance characteristics 76
3.5.2 Outline of a higher temporal and spatial imaging system 77
3.6 Generation IV: Portable, Deep-Tissue Spectroscopy 78
3.7 Few Words on Instrumentation 79
3.8 APPENDIX: *In vivo* measurements of somatosensory cortex activation by forepaw stimulation on rat brains using Generation III system 80

4 Cerebral Hemodynamics **85**
4.1 Introduction 85
4.2 Diffuse Optical Measurements of Cerebral Hemodynamics of Rats 86
4.2.1 Validation of Hybrid Measurements During Hypercapnia, Hypoxia and Cardiac Arrest 87
4.2.2 Transient Focal Ischemia Induced By Middle Cerebral Artery Occlusion . 91
4.2.2.1 Introduction 91
4.2.2.2 Animal Preparation 92
4.2.2.3 Results 92
4.2.3 Cerebral Hemodynamics during Cortical Spreading Depression at different cerebral PCO_2 97
4.2.3.1 Introduction 97
4.2.3.2 Materials and Methods 99
4.2.3.3 Instrument and Probe 99
4.2.3.4 Animal Preparation 99
4.2.3.5 Results and Discussion 101
Imaging of the Hemodynamics During CSD 101

Effect of Brain PCO_2 On CSD Hemodynamics 106
4.2.3.6 Conclusions 109
4.3 Spatio-Temporal Quantification of Cerebral Blood Flow During Functional Activation in Rat Somatosensory Cortex Using Laser Speckle Flowmetry 111
4.3.1 Introduction 111
4.3.2 Materials and Methods 112
4.3.2.1 Surgical Preparation and Stimulus Presentation 112
4.3.2.2 Laser Speckle Flowmetry Instrument 113
4.3.2.3 Data Analysis 114
Theory of Laser Speckle Flowmetry 114
Correlation Coefficient Imaging 116
Temporal and Spatial Response 117
Statistical Analysis 118
4.3.3 Results 118
4.3.4 Discussion 124
4.3.5 Conclusion 128
4.4 Hybrid Measurements of Hemodynamics of Human Brain 128
4.4.1 Introduction 128
4.4.2 Materials and Methods 131
4.4.2.1 Instrumentation 131
4.4.2.2 Protocol 132
4.4.2.3 Data Analysis 133
4.4.3 Results 133

4.4.3.1 Partial Volume Effects . . . 133
4.4.3.2 Partial Volume Corrected Results . . . 135
4.4.4 Conclusion . . . 138
4.5 Future of Hybrid, Diffuse Optical, Cerebral Hemodynamic Measurements . . . 138
4.6 APPENDIX: Principal Components Analysis of Speckle Flowmetry . . . 146
4.7 APPENDIX: Hemodynamics of Hyperventilation Measured on Human Brain . . . 154

5 Hemodynamics of Other Physiological Conditions 159

5.1 Outline . . . 159
5.2 Muscle oxygenation and flow during cuff occlusion of arm and leg flexor muscles and during plantar flexion exercise . . . 160
5.2.1 Introduction . . . 160
5.2.1.1 Clinical Relevance . . . 160
5.2.1.2 Need for Optical Techniques . . . 162
5.2.1.3 Translation of Small-Tissue Instrumentation to Human Muscles . 163
5.2.2 Experimental Protocol . . . 164
5.2.2.1 Cuff Occlusion . . . 164
Cuff Occlusion of Arm flexors . . . 166
Cuff Occlusion of Leg flexors . . . 168
5.2.2.2 Plantar Flexion Exercise . . . 168
5.2.2.3 Volunteer Population . . . 169
5.2.3 Data Analysis . . . 169
5.2.3.1 Oxygenation and Flow . . . 169
5.2.3.2 Tissue metabolic rate of oxygen consumption . . . 170

5.2.3.3 Investigation of Response from Different Layers 171
5.2.3.4 Data Presentation and Response Characterization 172
5.2.4 Results and Discussion 172
5.2.4.1 Do both DCT and DOT Probe Deep Muscle Tissue? 172
5.2.4.2 Characterization of the Hemodynamic Response 175
Cuff Occlusion 175
Plantar Flexion Exercise 177
$TMRO_2$ during Exercise 181
5.2.4.3 Diseased Tissue Response 182
5.2.4.4 Myoglobin or Hemoglobin? 183
5.2.5 Conclusions 184
5.3 Monitoring of Tissue Hemodynamic Response to Photodynamic Therapy for the Prediction of Treatment Efficacy 185
5.3.1 Introduction 185
5.3.2 Materials and Methods 189
5.3.2.1 Tumor Model and PDT Dose 189
5.3.2.2 Non-contact DCT System 189
5.3.2.3 Broadband absorption spectrometer 190
5.3.2.4 Power Doppler Ultrasound 191
5.3.2.5 Statistical Analysis 192
5.3.3 Results 194
5.3.3.1 Comparison of Power Doppler Ultrasound and DCT Flow 194

5.3.3.2 Effect of PDT treatment on Relative Blood Flow, Oxygenation and Oxygen Consumption 196
5.3.3.3 Prediction of long-term Tumor Response to Treatment 200
5.3.3.4 Prediction of PDT efficacy from Flow Dynamics *During* Treatment 202
5.3.4 Conclusion 203

6 Summary **205**

Glossary **209**

Bibliography **212**

List of Tables

3.1 Instrument performance characteristics of prototype system 77

3.2 Temporal, spectral and spatial resolutions of Generation III system 78

4.1 Hypercapnia: Comparison with Literature 88

4.2 Ischemia: Comparison with Literature 93

4.3 Tabulation of peak-CBF 121

4.4 Tabulation of activation area 122

5.1 Characterization of the hemodynamic response to cuff-occlusion 177

5.2 Characterization of the hemodynamic response to plantar flexion exercise 179

5.3 PDT Response: DCT vs Doppler Ultrasound 196

5.4 PDT Response: StO_2 and $rTMRO_2$ 199

List of Figures

1.1 Spectra of tissue chromophores 2

2.1 Illustration of Frequency Domain Measurements 12

2.2 Illustration of Semi-Infinite Approximation 13

2.3 Schematic of a 2-layered diffuse medium 22

2.4 Multi-Spectral image reconstruction 29

2.5 Schematic of a 2-compartment medium 31

2.6 Illustration of Diffuse Correlation Tomography 33

2.7 Autocorrelation functions vs distance and D_B 37

2.8 Comparison of Brownian Motion and Random Flow Models for DCT 38

2.9 Calculated autocorrelation functions in two layer media 39

2.10 Human skull model filled with Intralipid solution. 40

2.11 Correlation functions from the skull phantom 41

2.12 “n” parameterizing the autorcorrelation curves. 42

2.13 Condition number vs “n” 44

2.14 Compartmentalized model of the vasculature 45

2.15 Optical properties of the simulated heterogeneity 49

2.16 Ellipsoidal heterogeneity mimicing a tumor 50
2.17 Comparing Multi-Spectral and traditional spectroscopy I 51
2.18 Bulk properties of healthy breast 52
2.19 Comparing multi-spectral and traditional spectroscopy II 53
2.20 Comparing multi-spectral and traditional spectroscopy III 54
3.1 Basic DOT Detection Module 63
3.2 Basic DCT Detection Module 67
3.3 Non-contact Hybrid system 69
3.4 D_B vs Methly Cellulose Concentration 70
3.5 Schematic of Frequency Domain Multiplexing 74
3.6 Linearity of FDM Prototype 76
3.7 DOT of Forepaw Stimulation, Set-Up 81
3.8 DOT of Forepaw Stimulation, Images 82
3.9 DOT of Forepaw Stimulation, Time Series 84
3.10 DOT of Forepaw Stimulation, 4-8 Second Stimuli 84
4.1 Global Cerebral Hemodynamics 89
4.2 Laser Doppler compared to DCS during hypocapnia 90
4.3 Illustration of MCAO induced ischemic stroke 91
4.4 Images of hemodynamics during ischemic stroke 95
4.5 Temporal hemodynamics during ischemic stroke 96
4.6 CSD illustration and Source-detector layout 100
4.7 3D Imaging Geometry for CSD 103
4.8 3D imaging of $rCBF$ under CSD 104

4.9 3D imaging of $rCBF$ under CSD: ROI 105

4.10 Oxygen Metabolism during CSD 107

4.11 $rCBF$ for CSD under different ventilation states 108

4.12 Parametrization of CSD Hemodynamics 109

4.13 Effect of cerebral PCO_2 on $rCBF$ 110

4.14 Effect of cerebral PCO_2 on $rCMRO_2$ 110

4.15 Sketch and white-light image of speckle setup 115

4.16 Illustration of correlation coefficient imaging 117

4.17 Time series images of forepaw stimulation 119

4.18 Correlation coefficient image 120

4.19 CBF vs current and duration 121

4.20 Activation area 123

4.21 CBF in concentric rings 124

4.22 Probe for finger tapping studies 131

4.23 Sketch of Photon Paths in Brain 134

4.24 Finger tapping results from one individual 136

4.25 $CMRO_2$ change in finger tapping 137

4.26 Eigenvalues vs eigenvalue index plotted as a “scree” plot 149

4.27 Eigenimages showing principal components of AFC 150

4.28 Temporal components from PCA 152

4.29 Correlation of the stimulus presentation with temporal components 153

4.30 Placement of probes for hyperventilation studies 157

4.31 Hemodynamic response in human brain due to hyperventilation. 157

5.1 Schematic of the probe used for muscle measurements 165
5.2 Muscle Study Protocol 167
5.3 Probing different layers in human muscles 174
5.4 Muscle Parameters 176
5.5 Hemodynamic responses during plantar flexion exercise 178
5.6 Fast Flow Changes During Exercise 180
5.7 Sketch of PDT Experiment 190
5.8 Sketch of Broadband Spectrometer 192
5.9 Doppler Ultrasound flow vs DCT Flow 195
5.10 Flow Response During and After PDT Treatment 197
5.11 Bar Graph showing Hemodynamic Response to PDT 198
5.12 PDT Efficacy Predictors 201

Chapter 1

Introduction

Light is an obvious tool with which to probe tissues. As early as 1930s [96], light was used to "see" tumors and the basic ideas from those measurements still survive to today. The propagation of light through tissues is complicated by certain properties of the tissue, namely their scattering and absorption. In late 1970s, Jobsis [202] realized that there exists a "window" in the near-infrared spectrum wherein photons could travel deep into tissue because of the reduced absorption of water (see Figure 1.1). Models for light propagation in the late 1980s formalized the field and paved the way for a large variety of applications ranging from imaging of breast tumors to functional imaging of brain [404]. Technological developments such as the wide availability of laser diodes, fast optical switches and fast computers further assisted this growth. Thus light is still the tissue probe, photon migration in tissues is now well understood to be a diffusive process. "Diffuse optical tomography" (DOT), "near infrared spectroscopy" (NIRS) and "photon migration" (PM) are some of the terms used to identify the field [1].

The diffuse optical technique, which aims to probe tissues as deep as several centimeters below

[1] In this manuscript, DOT is used to refer to both spectroscopic and tomographic applications of diffuse optics

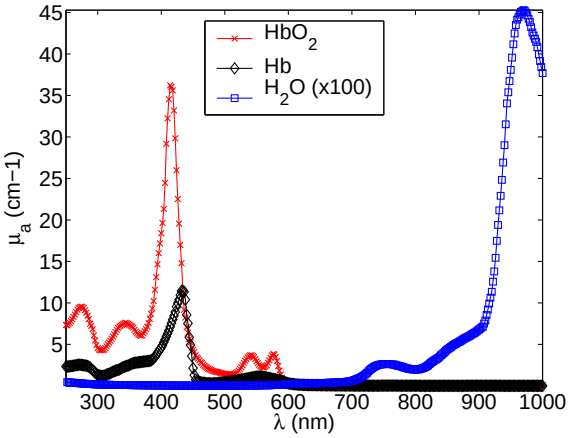

(a)

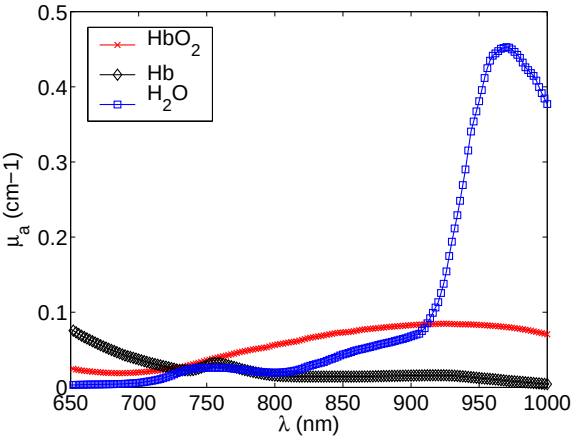

(b)

Figure 1.1: (a) Absorption spectra of main tissue chromophores over a large wavelength range, (b) the "physiological window" in the near-infrared where the water and hemoglobin absorption is relatively low. In this part of the spectrum, the light can penetrate several centimeters into the tissue due to this low absorption. Furthermore, there are clear features in the spectra which enables estimation of the chromophores by measuring absorption at several wavelengths.

the tissue surface, has enabled direct measurement of oxy- and deoxy-hemoglobin (HbO_2,Hbr), water, lipid, and scattering as well as some less common variants of hemoglobin and other tissue chromophores [403]. These species represent the main endogenous contrast available for DOT. It was also possible to measure the distribution and lifetime of exogenous dyes which improve contrast in tissues such as the tumors [177, 271]. Research has shown promise for increased specificity for breast tumors and in measurement of critical dynamic parameters in brain. For an excellent tutorial on the subject, see Yodh and Boas [404].

There are three main experimental paradigms employed for diffuse optical measurements: (1) Time domain (TRS) methods use the temporal broadening of a short pulse of light by tissue. TRS provides the highest information content per source-detector pair, but at the expense of increased complexity and price of instrumentation [29, 194, 273, 285, 324]. (2) Frequency domain (FD) methods use light sinusoidally modulated at a single (generally 100-1000 MHz) frequency and then injected into the tissue. The reduction in amplitude and the phase shift of the transmitted light are then measured [67, 255, 278, 399]. Some instruments sweep through frequencies to increase the amount of information, a scheme that essentially makes the information content equivalent to the TRS methods [365]. Even though FD techniques provide less information than TRS per source-detector pair, it has proven to be adequate for separating absorption and scattering information. (3) Continuous wave (CW) methods wherein a steady amplitude light beam is injected into the medium, and the reduction in transmitted amplitude is measured. CW techniques provide the least information content per source-detector pair and there have been doubts about its ability to separate scattering effects from absorption [13]. However, with developments in algorithms [86, 191], it is now possible to achieve that separatio. Recently, we have presented a methodology which with the correct choice of wavelengths and by use of a spectral algorithm has shown that the uniqueness

problem can be avoided [86]. Hence, CW methods are becoming increasingly popular due to their simplicity, low-cost, size and speed [89, 200, 339].

There have been significant applications in the field, including optical mammography [65, 89, 117, 256, 271, 274, 299, 335], brain functional spectroscopy and imaging [38, 91, 188, 298, 404], exercise medicine [26, 27, 32, 68, 87, 97, 196, 237, 249, 282, 303, 319, 354, 391], monitoring of photodynamic therapy [107] and more. A key limitation of diffuse optical methods, however, is its relatively low resolution (several millimeters). Even though this factor has been discouraging in some applications such as the optical mammography, the fact that key physiological parameters are accessible to the method has led to development of multi-modality and hybrid methods [76, 274]. These approaches have overcome many obstacles in imaging and have increased information content of the method. A complete summary of the field is beyond the scope of this work and interested readers may refer to recent reviews of the field [12, 38, 179, 180, 271, 375, 404, 404] for more information.

Additional information can be obtained from the diffusing photons particularly regarding the dynamics of the scatterers, e.g red blood cells. This information is obtained by monitoring the speckle fluctuations of the scattered light. Fluctuations in time and space reveal the dynamics of the probed tissue and have been the topic of study in a variety of fields [30, 31, 39, 44, 46, 47, 52, 54, 79, 94, 95, 148, 170, 234, 241, 294, 302, 348, 357, 360, 370]. The most common approach measures the electric field temporal autocorrelation function or its Fourier Transform. The optical field correlation function is explicitly related to the motions of scatterers within the samples studied; the most significant signal is from blood flow. Most physiological work, thus far, however, was carried out within a single-scattering approximation and/or with additional corrections [183, 209, 276, 311, 336, 348–350, 356, 357, 388]. Essentially all Laser Doppler commercial instruments as well as

more recent CCD-based speckle devices (which have not been commercialized) utilize pairs of very closely separated optodes (e.g $\sim$0.25 mm), limiting the information content to the superficial tissue (few hundreds of microns). The single scattering approximation simplifies the experimental analysis, but also limits the reliability and amount of information that can be extracted from real tissue samples.

Our laboratory pioneered the extension of dynamic light scattering to deep tissues i.e. the development of diffuse correlation spectroscopy (DCS) for tissues. We derived a diffusion equation that describes the transport of the electric field temporal autocorrelation function through turbid media [39, 41, 44]. The so-called correlation diffusion equation unified earlier models [46, 241, 294, 347] of the spectral broadening experienced by highly scattered light in materials such as colloids, emulsions, foams, and tissue. The generalization of the photon diffusion equation was very exciting because it provided a precise mathematical description about how motional fluctuations are impressed upon the temporal correlations of diffuse light fields propagating in tissue. The equation included the effects of tissue absorption, scattering, and cellular motions. Importantly, it provided a natural framework for consideration of heterogeneous turbid media. As a result of these accomplishments we have developed theory and instrumentation to optically probe blood flow in thick tissues. We have used techniques developed for DOT in this new context, obtaining tomographic images of blood flow in phantoms and in tissues and thereby establishing the basis of diffuse correlation tomography (DCT) [39, 91] [2].

In the recent years, we have hybridized the two methods in portable instruments [76, 91]. This hybrid approach combining diffuse optical tomographical methods with diffuse correlation tomography forms the core of this thesis. By combining DOT with diffuse correlation tomography to

[2]DCT is used throughout this manuscript to refer to both spectroscopic and tomographical applications of diffuse correlation.

measure blood oxygen saturation (Y_t), total hemoglobin concentration (THC) and blood flow speed (BF). These three quantities measured together are valuable parameters for estimation of important physiological parameters such as the metabolic rate of oxygen (MRO_2).

In this thesis, I outline applications of hybrid optical techniques in an extended sample set of tissues from small (mouse tumors, rat brains) to large (human brain and muscle) tissues. Chapter 2 describes the basic theory of DOT and DCT. Common solutions to diffusion equations are shown, and algorithms for implementing these solutions to derive ("reconstruct") physiological parameters are shown. In this chapter, two new techniques are also introduced. One utilizes *a priori* spectral information for DOT to reduce inter-parameter cross-talk and increase signal-to-noise in reconstructed images. This spectral approach is later applied to reconstruct three dimensional images of hemodynamics in the rat brain. The other technique optimizes DCT data for image reconstruction. Chapter 3 describes different generations of the hybrid instrument that we used to acquire the data presented in this thesis. Different instrument generations improved upon the spatial and temporal resolution and adapted to different sensitivity requirements. A novel method wherein we frequency encode wavelengths improving the acquisition speed significantly is described in detail, characterized in the laboratory and tested *in vivo* in imaging forepaw stimulation on rat brain.

Chapter 4, Section 4.2 describes validation and application of the hybrid technique to measure rat brain hemodynamics during various physiological perturbations. Validation is carried out by correlating the measured response to global changes measured with other physiological data, modalities and with the literature. The first images of cerebral metabolic rate of oxygen ($CMRO_2$) through intact skull with optical methods were obtained in rats during transient focal ischemia (Chapter 4, Section 4.2.2). The response to cortical spreading depression under altered ventilation states was also investigated revealing new physiological information. The first three dimensional,

all-optical images of cerebral metabolism are also presented (Chapter 4, Section 4.2.3). Finally, we describe application of another relevant technique in rat brain studies; Laser speckle flowmetry (LSF), was used to characterize the somatosensory cortex response to electrical forepaw stimulation (Chapter 4, Section 4.3). A new instrument was constructed and new analysis techniques used to obtain new, fundamental physiological information. Chapter 4, Section 4.4 adapts these techniques for measurements of cerebral blood flow, blood oxygenation and $CMRO_2$ through intact skull on humans. It is applied to motor cortex stimulus by controlled finger tapping, providing the first all optical measurement of cerebral blood flow (CBF) and $CMRO_2$ in intact human brain during functional activation. An extensive discussion about potential applications and comparison to other modalities follows.

Chapter 5, Section 5.2 describes characterization of muscle hemodynamics in the exercising and cuffed muscles in humans and a possible clinical application to peripheral vascular disease. The hybrid technique provides robust signals, penetrating through the upper layers of the tissue and into the muscles. Chapter 5, Section 5.3 describes hybrid measurements on implanted tumors on mice undergoing photodynamic therapy. New parameters based on hemodynamic measures are introduced which enabled preliminary predictions of tumor response to therapy and therapy efficacy. This has significant potential clinical applications.

These studies pave the way for a great deal of applications with increased physiological information. The key contribution is the addition of diffuse correlation techniques for measurement of blood flow. A strong emphasis is given to the measurement of cerebral blood flow, since as stated in a recent review, "*[t]he optimal method for measuring cerebral blood flow (CBF) has yet to be discovered.*" [413]. This is true for measurements of hemodynamic parameters in general and in other organs discussed in this work. I believe, this field has a bright future and many exciting

methods remain to be developed.

Chapter 2

Theory

In this Chapter, I outline the basic theory of static and dynamic models of photon diffusion and explain algorithms used for data analysis for following Chapters. Several new contributions to (mostly) the algorithmic problem are also presented; (1) multi-spectral spectroscopy and tomography using wavelength dependent *a priori* information, (2) optimization of the data-sets for diffuse correlation spectroscopy , (3) a two-layer model for diffuse correlation and (4) a validation of a two-layer model. The selection of the material described is based on their use in the experimental analysis.

2.1 Diffuse Optical Tomography and Spectroscopy

2.1.1 Introduction

Diffuse optical tomography and spectroscopy aims to investigate tissue physiology millimeters to centimeters below the tissue surface by working in a wavelength range ($\sim$ 650-950nm) where the tissue absorption is relatively low [38, 403, 404]. The cost of this aim is that traditional optical

spectroscopies and microscopy methods are no longer applicable. In this wavelength regime the effects of tissue absorption and internal motion must be separated from the effects of tissue scattering. The most critical advance in the field has been the recognition and widespread acceptance that light transport over long distances in tissues is well approximated as a diffusive process [66, 403]. Using this physical model it is possible to quantitatively separate tissue scattering from tissue absorption, and to accurately incorporate the influence of boundaries, such as the air-tissue interface, into the transport theory [285, 286]. Waves of diffuse light energy density [160, 403] or their time-domain analogs [29, 100, 194, 285] propagate deeply in tissues (i.e. $\sim$10 cm) and displaying the expected wave-like phenomena (e.g refraction, interference) [42, 135, 279, 280, 325, 334, 366].

2.1.2 Photon Diffusion in Tissues

For the purposes of this manuscript, we have used the solutions to this "diffusion equation" where the measurable, near-infrared photon fluence rate, $\Phi(\mathbf{r}, \mathbf{t})$ (photons/[cm^2·s]) obeys the following diffusion equation [66, 149, 167, 192, 203]:

$$\nabla \cdot (D \nabla \Phi(\mathbf{r}, t)) - v\mu_a \Phi(\mathbf{r}, t) + vS(\mathbf{r}, t) = \frac{\partial \Phi(\mathbf{r}, t)}{\partial t} \; . \tag{2.1}$$

Here $\Phi(\mathbf{r}, t)$ is proportional to the photon number density ($U(\mathbf{r}, t)$ (photons/cm^3)), v is the speed of light in medium (cm/s), μ_a (cm^{-1}) is the absorption coefficient, μ_s'(cm^{-1}) is the reduced scattering coefficient and D= $\frac{v}{3\mu_s'}$ is the photon diffusion coefficient [1]. $S(\mathbf{r}, \mathbf{t})$ is an isotropic source term which gives the number of photons emitted at position $\mathbf{r}$ and time t per unit volume per unit time. The right-hand side of Equation (2.1) represents the rate of change of photons within a sample

[1] There is an ongoing debate about the definition of the diffusion coefficient which should be noted here [9, 25, 61, 116, 122, 124, 150]

volume element. This rate equals the number of photons scattered into the volume element per unit time from its surroundings, *minus* the number of photons absorbed per unit time within the volume element, *plus* the number of photons emitted per unit time from any sources in the volume element.

Previously, in Chapter 1, I mentioned three experimental techniques are employed in DOT wherein three types of sources are used. Since, we employ such frequency domain methods in our experiments, I will concentrate on the diffusion equation in the frequency domain where we measure the amplitude and phase of the AC component of the transmitted diffuse light waves or diffuse photon density waves (DPDWs). In this case, the source term is written as

$$S(\mathbf{r},t) = (S_{DC} + S_o e^{-i\omega t})\delta(\mathbf{r}) \,, \tag{2.2}$$

where S_{DC} and S_o are DC and AC components of the source strength representing the number of photons emitted per second. ω is the source modulation frequency which is generally tens of megahertz (e.g. 70 MHz in our experiments). The total photon fluence now has DC and AC components. The detection circuitry employed (see Chapter 3) is generally sensitive only to the AC component. Therefore, rewriting $\Phi(\mathbf{r},t)$ as $\Phi(\mathbf{r})e^{-i\omega t}$, i.e with a photon fluence which oscillates at ω, in equation 2.1 we obtain

$$\nabla \cdot (D(\mathbf{r})\nabla\Phi(\mathbf{r})) + (i\omega - v\mu_a(\mathbf{r}))\,\Phi(\mathbf{r}) = -vS_o e^{iS_\phi}\delta(\mathbf{r}) \,. \tag{2.3}$$

Here I have replaced the optical properties (D and μ_a) with their heterogeneous versions. S_o and S_ϕ are the source amplitude and phase.

Frequency domain measurements are illustrated in Figure 2.1. Amplitude modulated (70 MHz)

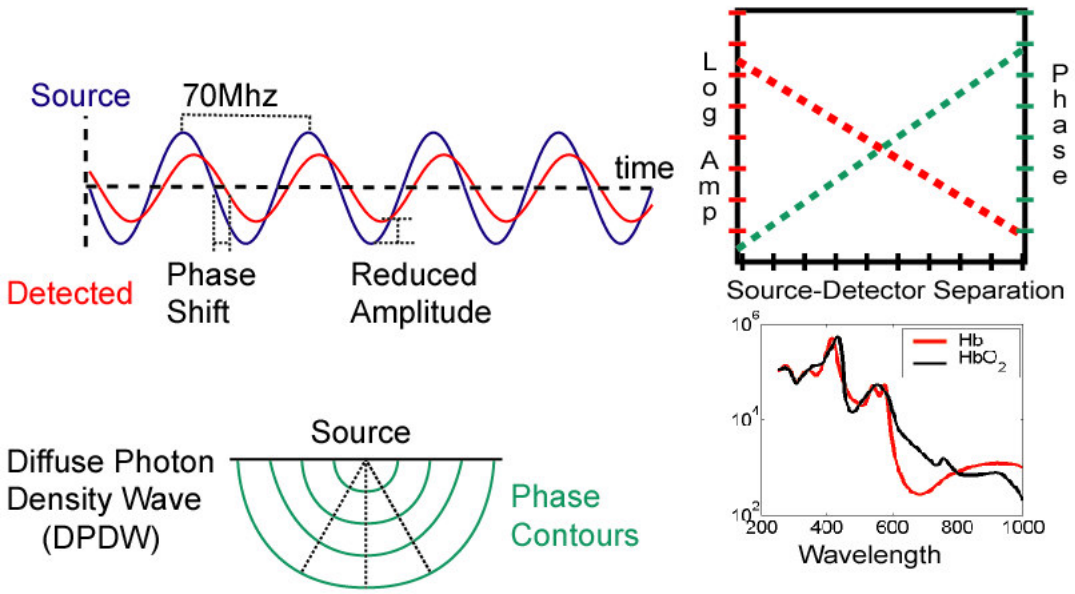

Figure 2.1: Schematic showing measurements in the frequency domain. Amplitude modulated (70 MHz) sources at multiple wavelengths (either frequency encoded and shone simultaneously or in series) illuminate the tissue. The reduction in amplitude and the phase shifts of diffuse photon density waves are detected at multiple source-detector separations. Optical properties are reconstructed using these measurements and using the spectra of hemoglobins. Physiological information is then extracted.

sources at multiple wavelengths (either frequency encoded and shone simultaneously or in series) illuminate the tissue. Diffuse photon density waves obey usual wave propagation rules, for example, equal phase contours are shown. The reduction in amplitude and the phase shifts of diffuse photon density waves are detected at multiple source-detector separations. Optical properties are reconstructed using these measurements, e.g by plotting the logarithm of the detected amplitude vs source detector separation and fitting the slope. Finally, using the spectra of hemoglobins, physiological information is extracted.

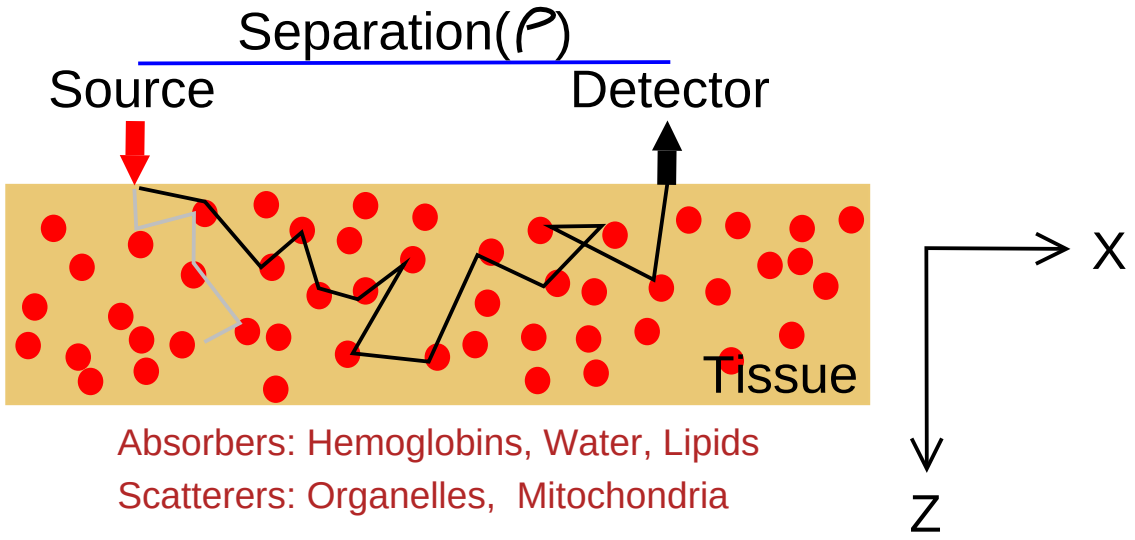

Figure 2.2: Illustration of semi-infinite approximation for diffuse optical measurements. The photons are injected at the source position and detected some distance away. Both emission and detection take place through optical fibers placed flush with the surface which forms the main boundary. The tissue is assumed to extend to "infinity" away from the boundary.

2.1.3 Spectroscopy in the Semi-Infinite Approximation

The simplest and most commonly used physical model for tissue spectroscopy treats the sample as a semi-infinite, homogeneous medium. In this case the sources and detectors are placed on the "air side" of the tissue surface. The source is modeled as an isotropic, point source. Emission and detection take place through optical fibers placed flush with the surface (see Figure 2.2). Diffusion theory for semi-infinite media predicts the reflectivity $R(\mathbf{r})$ as a function of distance $(\mathbf{r})$ which is the source-detector separation along the sample surface. $R(\mathbf{r})$ is derived from photon flux and fluence rate at the boundary [176, 285]. The reflectivity is often approximated as the z-component of the flux which, in turn, is proportional to $\Phi(\mathbf{r})$. The tissue optical properties at a fixed wavelength are derived by fitting to $\Phi(\mathbf{r})$. A thorough description of the semi-infinite approximation for tissue

spectroscopy was given by Li [226]. Here, I re-write the basic solution that was obtained:

$$\Phi(\mathbf{r}) = \frac{vS_o e^{S_\phi}}{4\pi D}\left(\frac{e^{ikr_1}}{r_1} - \frac{e^{ikr_2}}{r_2}\right) \tag{2.4}$$

where

$$\mathbf{r} = r_1 = \sqrt{\rho^2 + (z - z_o)^2} \tag{2.5}$$

$$r_2 = \sqrt{\rho^2 + (z + z_o + 2z_b)^2}\,. \tag{2.6}$$

This equation was derived using the so-called "extrapolated zero" boundary condition where the fluence is set to be equal to zero at a distance $z_b = \frac{2}{3\mu_s'}\frac{1+R_{eff}}{1-R_{eff}}$ above the turbid medium. ρ is the distances parallel to the tissue boundary in cartesian coordinates and z is the distance perpendicular to the boundary, into the turbid medium. $z_o = \frac{1}{\mu_s'}$ is equal to the random walk step. The sources are assumed to be isotropic, point-like if moved by z_o into the medium. The first term on the right hand side is the infinite medium solution and the second term comes from an image source with negative amplitude reflected about the "extrapolated zero" boundary. R_{eff} is the effective reflection coefficient to account for the index mismatch between tissue and air, given approximately as

$$R_{eff} = -1.440n^{-2} + 0.710n^{-1} + 0.668 + 0.00636n \tag{2.7}$$

where $n = n_{in}/n_{out}$, the ratio of the index of refraction of "inside" and "outside" media. k can be considered as a complex wave-number for DPDWs and $k^2 = (-v\mu_a + i\omega)/D$.

Many schemes have been developed to search for the optimal parameters based on Equation 2.4, and their relative success depends on measurement signal-to-noise ratio, and the accuracy

of the physical model. When everything works, one obtains a best estimate of the absorption factor and scattering factor at one or more optical wavelengths. The absorption coefficient is then decomposed into contributions from different tissue chromophores, i.e.

$$\mu_a(\lambda) = \sum_i \varepsilon_i(\lambda)\ c_i. \tag{2.8}$$

Here the sum is over the different tissue chromophores. $\varepsilon_i(\lambda)$ is the extinction coefficient as a function of wavelength (λ) for the i^{th} chromophore. c_i is the concentration of the i^{th} chromophore. The c_i are unknowns to be reconstructed from the wavelength-dependent absorption factors. Three unknowns require measurements at a minimum of three optical wavelengths (generally more, since tissue scattering is also an unknown). Oxy- and deoxy-hemoglobin concentrations (e.g. c_{HbO_2}, c_{Hb} respectively) along with water concentration are the most significant tissue absorbers in the NIR (see Figure 1.1). They can be combined to obtain blood volume (which is another name for total hemoglobin concentration $(THC = c_{Hb} + c_{HbO2})$ and blood oxygen saturation (i.e. Y_t =[c_{HbO_2} / ($c_{Hb} + c_{HbO_2}$)] x 100), which in turn provide useful physiological information. This the basis of what is known as "Near Infrared Spectroscopy" (NIRS) where THC, Y_t, c_{HbO_2}, c_{Hb} are measured either statically or dynamically and either as "bulk properties" [117] or point by point in a 2D/3D map. Although it is possible to measure water, lipid and other chromophore concentrations, throughout this manuscript I will stress the utility of blood oxygen saturation and total hemoglobin concentration.

2.1.4 Diffuse Optical Tomography in the Frequency Domain

Tissues are quite heterogeneous and there is often useful information about subject well-being that can be derived from the knowledge of the heterogeneities. Therefore, it is natural to attempt to

make images using DPDWs (i.e. diffuse optical tomography, DOT). Our experience with imaging with DPDWs was briefly discussed in Chapter 1. For the purposes of a theoretical introduction to DOT, I will now briefly outline different methodologies that were employed.

Optical characterization of the heterogeneous tissues has been attempted since 1929 [96] in an area named *diaphanography* and it has gained considerable interest in 1980s [24, 63, 154, 246, 301, 337, 338, 380, 385]. This approach has proven itself to be inadequate for clinical use since the acquired data was not suitable for 3D image reconstruction in presence of absorbtion and scattering. However, the diffusion equation provides a workable framework for tomographic reconstruction and many different approaches have been developed over years [10, 12, 14, 16] including back-projection [80, 378], diffraction tomography in k-space and variants [75, 227, 247, 327], transport based [60, 310, 329, 398], basic perturbation [15, 18, 281, 328], series expansion [197–199, 287, 288, 297, 400], gradient-based [17], elliptic systems [169, 213], truncated Newton [315–317] and Bayesian [126] methods. Furthermore, a variety of new formalisms and analyses were carried out to improve understanding of image fidelity such as analytic inversion formulas [242–245], differencing [290] and differential methods [272] and image segmentation based on secondary modalities [210, 225, 274, 275, 331, 417]. Perturbation approaches based on Born or Rytov approximations [204] can use analytic forms or iterative techniques based on numerical solutions. The numerical solutions are relatively slow and computationally intensive, but in principle realistic boundaries present no significant limitations for these methods.

The starting point of DOT is the *time-independent* form of the diffusion equation (Equation2.3). The problem to be solved is the estimation of the variation of the absorption coefficient and the

diffusion coefficient with respect to position based on a finite set of measurements. These measurements are generally taken on the tissue surface as mentioned above, and a perturbation approach is taken to tackle the image reconstruction problem. We write $D(\mathbf{r}) = D_o + \Delta D(\mathbf{r})$, and $\mu_a(\mathbf{r}) = \mu_{ao} + \Delta\mu_a(\mathbf{r})$; here D_o and μ_{ao} are constant (for applications described here), "background" optical properties. The next step in the perturbation approach is to relate the fluence measured in presence of heterogeneities to some "background" fluence. This "background" fluence can be simulated, measured before a heterogeneity was introduced or obtained from the baseline measurements before the system was perturbed. There are two common approaches to this problem, called the "Born-type" and "Rytov-type" schemes. Here, I concentrate on the "Rytov-type" approach which was used throughout this manuscript. For an excellent discussion on imaging with DPDWs see O'Leary [278].

In the "Rytov approximation", the photon density is written in terms of fluence as

$$U(\mathbf{r}) = e^{\Phi_o(\mathbf{r})+\Phi_{sc}(\mathbf{r})} \tag{2.9}$$

$$U(\mathbf{r})_o = e^{\Phi_o(\mathbf{r})} \tag{2.10}$$

where one can view $\Phi_o(\mathbf{r})$ as the incident wave and $\Phi_{sc}(\mathbf{r})$ as the wave produced by the scattering of this incident wave off of the absorptive and diffusive heterogeneities. Next, $D(\mathbf{r})$, $\mu_a(\mathbf{r})$, $\Phi_o(\mathbf{r})$ and $\Phi_{sc}(\mathbf{r})$ are substituted into equation 2.3 and, after some algebra, we obtain

$$\begin{aligned}\Phi_{sc}(\mathbf{r_d}-\mathbf{r_s}) &= -\frac{1}{\Phi_o(\mathbf{r_d}-\mathbf{r_s})}\int \Phi_o(\mathbf{r}-\mathbf{r_s})G(\mathbf{r}-\mathbf{r_d})\left(\frac{v\Delta\mu_a(\mathbf{r})}{D_o}\right)d\mathbf{r} \\ &+ \frac{1}{\Phi_o(\mathbf{r_d}-\mathbf{r_s})}\int \nabla\Phi_o(\mathbf{r}-\mathbf{r_s})\cdot\nabla G(\mathbf{r}-\mathbf{r_d})\left(\frac{\Delta D(\mathbf{r})}{D_o}\right)d\mathbf{r}\,. \end{aligned} \tag{2.11}$$

Here $\mathbf{r}_s$ is the source position, $\mathbf{r}_d$ is the detector position and $\mathbf{r}$ is a position within the sample.

The integration is over the entire sample volume. $G(\mathbf{r},\mathbf{r}')$ is the Green's function associated with Equation 2.3. The problem of deriving $\Delta\mu_a(\mathbf{r})$ and $\Delta D(\mathbf{r})$ from Φ_{sc} is intrinsically nonlinear, because Φ and G are both nonlinear functions of $\Delta\mu_a(\mathbf{r})$ and $\Delta D(\mathbf{r})$.

The most broadly useful image reconstruction schemes involve dividing the tissue into a number of (N_v) volume elements ("voxels" of volume h^3) and converting the integrals to summations over these voxels. Equation 2.11 then becomes a matrix equation

$$b = \mathbf{W}x \tag{2.12}$$

where b is a vector of measured $\Phi(\mathbf{r_d} - \mathbf{r_s})$ (size N_sN_d x 1), x is a vector of unknown optical properties, $[\Delta\mu_a(\mathbf{r})|\Delta D(\mathbf{r})]$ (size $2N_v$ x 1) and $\mathbf{W}$ is the so-called "weight matrix" (size N_sN_d x $2N_v$). N_v, N_s, N_d are number of voxels, sources and detectors respectively. The weight matrix is an augmented matrix consisting of absorption and scattering pieces similar to the terms on the right hand side of Equation 2.11, i.e.

$$\mathbf{W} = \left[\mathbf{W}^{\mu_a}|\mathbf{W}^{\mu_s'}\right] \tag{2.13}$$

$$\mathbf{W}_{\mathbf{ij}}^{\mu_a} = -\frac{1}{\Phi_o(\mathbf{r_d} - \mathbf{r_s})}\Phi_o(\mathbf{r} - \mathbf{r_s})G(\mathbf{r} - \mathbf{r_d})\left(\frac{vh}{D_o}\right) \tag{2.14}$$

$$\mathbf{W}_{\mathbf{ij}}^{\mathbf{D}} = \frac{1}{\Phi_o(\mathbf{r_d} - \mathbf{r_s})}\nabla\Phi_o(\mathbf{r} - \mathbf{r_s}) \cdot \nabla G(\mathbf{r} - \mathbf{r_d})\left(\frac{h}{D_o}\right) \tag{2.15}$$

for i^{th} source-detector pair and j^{th} voxel. Since the weight matrix is, in general, not a square matrix, the inversion is formulated as

$$x = \left(\mathbf{W^T} \cdot \mathbf{W}\right)^{-1} \cdot \mathbf{W^T} \cdot b \tag{2.16}$$

where T stands for the matrix transpose. The image reconstruction problem can now be stated as the problem of inverting $\mathbf{W^T} \cdot \mathbf{W}$ to obtain x. Following other fields [204] non-linear, iterative and linear direct or iterative inversion algorithms have been employed in DOT.

The non-linear, iterative approaches follow similar algorithms: 1) the optical properties (μ_a and D) are initialized, 2) the forward problem is solved, 3) a chi-squared (χ^2) is calculated and convergence is checked, 4) the inverse problem is setup, 5) the inverse problem is solved, 6) the optical properties are updated and a return to step 1 occurs. The forward problem is defined as calculating the diffuse photon density, $\Phi_C(\mathbf{r}, \mathbf{r_s})$, for each source position $\mathbf{r}_s$ and is typically found using Finite Elements or Finite Difference methods and Equation 2.3. A chi-squared (χ^2) is defined to quantify the difference between the measured ($\Phi_M(\mathbf{r}, \mathbf{r_s})$) and the calculated diffuse photon density. By comparing χ^2 to some defined error, ε, a convergence criterion is defined and checked. We then need a way of updating the optical properties from their previous values and many approaches were adopted [10, 12, 14, 16].

Throughout this manuscript, I concentrate on imaging only the absorption coefficient but the algorithms used can be extended to imaging of scattering.

2.1.5 Regularized Singular Value Decomposition (SVD) Approach to DOT

In general, a linear algorithm inverts the weight matrix and multiplies the measurement vector, b on the left by $\mathbf{W^{-1}}$. The iterative versions use iterative matrix inversion techniques such as ART and SIRT. The direct inversion technique uses a decomposition of the weight matrix to invert in a single-shot. Singular value decomposition (SVD) is a most commonly employed method for direct inversion and is used in this work.

Unfortunately, DPDWs inherently lead to an ill-posed image reconstruction problem. The

ill-posedness leads to a variety of complications including inter-parameter cross-talk and non-uniqueness [10, 13, 16, 152, 278]. There are many approaches to handling these type of problems. Here, I use "regularization" where one tries to invert a modified version of the weight matrix which is better behaved than the original. The Moore-Penrose generalized inverse with depth-dependent Tikhonov regularization [10, 16, 297] can be written as

$$x_{est} = \left(\mathbf{W^T} \cdot \mathbf{W} + \lambda_r(z)\mathbf{I}\right)^{-1} \cdot \mathbf{W^T} \cdot \ b \tag{2.17}$$

where subscript $_{est}$ was used to denote "estimated" properties and $\mathbf{I}$ is the identity matrix (N_v x N_v). The regularization parameter is λ_r, $\lambda_r(z) = \lambda_o + \lambda_e e^{-z}$, where λ_o and λ_e tune the constant and depth (z measured from source-detector plane) dependent parts. Higher regularization leads to a more "smooth" reconstruction with lowered artifacts at the expense of resolution and contrast. The choice of the regularization parameters is tricky and we have adopted the so-called "L-curve" method for choosing λ_r [92, 152, 173, 174].

Another point is worthy of note in connection with image reconstruction; many of our measurements are differential. For example, diffuse optical data are typically obtained before and after some perturbation. In this case the experimental measurements use the exact same geometry within a short time of one another, thereby minimizing positional and movement errors and instrumental drift. Furthermore the use of differential measurements minimize systematic errors associated with the effect of surface absorbers such as hair or skin. Under these circumstances the differential signal $\Delta\Phi$, can be related to the differential changes in optical properties, and can be reconstructed using essentially the same formalism described above.

2.1.6 Two Layer Model in k-Space

In order to investigate the signals from layered media, I have employed the angular-spectrum representation of the DPDWs (k-space) [118, 227, 228, 247, 248, 308]. This representation is ideal for the representation of cylindirically symmetric geometries because of the nature of the two-dimensional fourier transforms employed. Here, I follow the formalism of Ripoll *et al* [307, 309] and Li *et al* [228] and present the solutions of equation 2.3 for a two layer medium in k-space.

If the source (at the origin, $(0, 0, 0)$) is taken to be a point emitter on the planar input surface (source plane, $(x_s, y_s, 0)$), the expansion of the Green's function in the k-space is written in the following form:

$$G_0(\mathbf{r_d}, \mathbf{r}) = \int\int dpdq\hat{G}_0(p, q, z_d, z)e^{-i(p(x_d-x)+q(y_d-y))} , \tag{2.18}$$

where the z-axis is defined in the direction normal to the plane surfaces, and (p, q) are the 2D spatial (k-space) frequencies conjugate to the x- and y-coordinates. The angular spectrum (Weyl expansion) representation of the Green's function is [21, 284]

$$\hat{G}_0(p, q, z_d, z) = \frac{i}{2m}e^{im|z_d-z|} , \tag{2.19}$$

where $m = \sqrt{k_0^2 - (p^2 + q^2)}$ is the complex propagator wavenumber and the imaginary part of m is positive, $\Im(m) > 0$. Hat ($\hat{}$) indicates quantities in k-space and subscript $_d$ indicates coordinates in detection plane. The normal, total flux in the k-space is then given as

$$\hat{J}_n(p, q, z_d) = -D\frac{\partial\hat{G}_0(p, q, z_d, z)}{\partial z} = -iDm\hat{G}_0(p, q, z_d, z) , \tag{2.20}$$

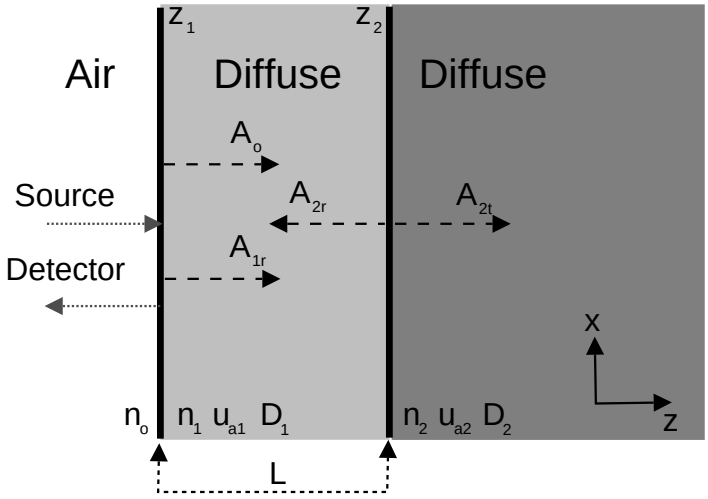

Figure 2.3: Schematic of a 2-layered diffuse medium. The media are characterized by their indices of refraction (n_0, n_1, n_2), absorption coefficients ($\mu_{a1},\ mu_{a2}$), scattering coefficients (μ'_{s1}, μ'_{s2}) and the thickness of the top medium ($L = z_2 - z_1$). Sources and detectors are at the source plane ($x_s, y_s, 0$).

which corresponds to the Fick's law in the k-space.

Figure 2.3 demonstrates the modeled two-layer geometry. Now, I denote the incident, reflected and transmitted amplitudes as:

$$A_0 : \quad \text{Incident amplitude} \tag{2.21}$$

$$A_{1r} : \quad \text{Reflected amplitude from air/diffuse boundary} \tag{2.22}$$

$$A_{2r} : \quad \text{Reflected amplitude from diffuse/diffuse boundary} \tag{2.23}$$

$$A_{2t} : \quad \text{Transmitted amplitude through diffuse/diffuse boundary} \tag{2.24}$$

with $L = |z_2 - z_1|$ as the thickness of the top layer (medium 1). Subscripts, 1 and 2 denote the

first and second media respectively. The photon fluences in the media are then written as;

$$\Phi_1 = A_0 e^{im_1 z} + A_{1r} e^{im_1(z_1 - z)} + A_{2r} e^{im_1(z_2 - z)} \tag{2.25}$$

$$\Phi_2 = A_{2t} e^{im_2(z_2 - z)} \, . \tag{2.26}$$

If the boundary conditions at two interfaces (air/diffuse, diffuse/diffuse) are defined, these equations can be solved for the unknown amplitudes (or the "reflection coefficients" and "transmission coefficients"). Using partial current [8, 226, 307] boundary condition, I write the boundary conditions as;

$$\alpha \Phi_1 + \frac{\partial \Phi_1}{\partial z} = 0 \quad \text{at z} = \text{z}_1 \tag{2.27}$$

$$\alpha = \frac{1 - R_{eff}}{1 + R_{eff}} \frac{v}{D_1} \tag{2.28}$$

$$D_1 \frac{\partial \Phi_1}{\partial z} = D_2 \frac{\partial \Phi_2}{\partial z} \quad \text{at z} = \text{z}_2 \, . \tag{2.29}$$

The diffuse/diffuse boundary condition is given by the conservation of the total flux density (see Equation 2.20). The photon fluence anywhere in this two-layer system can be obtained by solving the resultant equations simultaneously. This formalism can easily be transformed into the diffuse photon correlation by adopting the relevant properties and wavenumbers. For a more complete treatment see Ripoll [307] and for an alternate two-layer solution for DCT see Boas [37]. The angular spectrum approach is often chosen over the alternate approaches for its simplicity and computation speed of the solutions since fast Fourier transforms and Hankel transforms can be employed.

2.1.7 Multi-Spectral Spectroscopy and Tomography

The previous formalisms relied on individually "inverting" or fitting the solutions to the diffusion equation (Equation 2.3) at *each* wavelength employed, and then combining the thus obtained absorption coefficients according to Equation 2.8 to obtain Y_t and THC. However, in the presence of experimental noise, errors in tissue modelling and "amplitude-phase cross-talk" (in case of frequency domain measurements) contaminate the measurements. Therefore, inter-parameter cross-talk wherein variations in one parameter (e.g μ_a) are mistakenly observed as variations in another parameter (e.g μ_s') is induced. This problem is related to the well-known "non-uniqueness" problem that DPDWs suffer from in the continous wave ($\omega = 0$ domain) [13]. It is, therefore, natural to try to obtain better estimates of the physiological parameters by employing constraints [119]. The work described here employed one such constraint extensively. Namely, I have used *a priori* information about the wavelength dependence of the parameters. In this section, I formulate this algorithm and present few examples demonstrating its utility and superiority over the conventional method. Recently, we have also shown how this type of approach can be used to select the "correct" wavelengths for CW domain imaging and thus overcome the non-uniqueness problem [86].

I begin by re-writing equation 2.8, i.e.

$$\mu_a(\lambda) = \sum_i \varepsilon_i(\lambda)\ c_i. \tag{2.30}$$

The reduced scattering coefficient can also be written in its wavelength dependent form as

$$\mu_s'(\lambda) = a x^b \lambda^{-b}\ . \tag{2.31}$$

Equation 2.31 was obtained from a simplified Mie-scattering approximation [268,270] and has

been shown to be applicable to tissues, such as the breast tissue [65, 88, 117]. Here a, b are free parameters. a is proportional to the density of the scattering centers and b depends on their size. $x = 2\pi r n_m$ where n_m is the index of refraction of the medium and r is the homogeneous sphere radius for a "typical scatterer". For the tissues with a distribution of different size scatterers, we define a "Mie-equivalent radius" ($r = r_e$) as an "average" scatterer size [268], and use a simplified version of equation 2.31, which has been shown to be a reasonably good approximation over the wavelength range we employ and wherein the x dependence is lumped into the coefficient A, then

$$\mu_s'(\lambda) = A\lambda^{-b} \,. \tag{2.32}$$

With this formulation, the scattering properties are described by paremeters A and b. b has been shown to be of some utility for optical spectroscopy and imaging of the breast [65] where it is referred to as the "scatter power". Its reported values range from 0.23 to 2.

2.1.7.1 Spectroscopy using *a priori* Spectral Information

Equations 2.8 and 2.32 can be used to recast equation 2.4 with c_i's, a and b as the free-parameters. In these calculations, I minimize $\chi^2 = \sum_{s,d} |\Phi_m(\mathbf{r_s}, \mathbf{r_d}) - \Phi_c(\mathbf{r_s}, \mathbf{r_d})|^2$ where Φ_m is the measured fluence and Φ_c is the calculated fluence. The sum is over the source-detector pairs and all wavelengths. We use the Nelder-Mead simplex (direct search) method implemented in MATLAB function "fminsearch" to fit for the unknowns by minimizing χ^2. We then calculate blood oxygen saturation and blood volume from the relevant hemoglobin concentrations. For most applications, we have assumed average values for a and/or b, unless otherwise noted. For a successfull implementation of this algorithm in the context of the bulk optical properties of healthy breast, see Durduran *et al* [117].

The differential spectroscopy problem can also be formulated in a similar manner where one would fit for Δc_i and Δa (formulation of Δb is more tricky) directly. In that case, the χ^2 is re-written as $\chi^2 = \sum |\frac{\Phi_m}{\Phi_{m0}} - \frac{\Phi_c}{\Phi_{c0}}|^2$. This differential formulation of the spectroscopic problem is prefered for the analysis of time-series data because it avoids many issues about probe and instrument calibration. However, it may be error prone due to the selection/estimation of the baseline optical properties (used to calculate Φ_{c0}). To overcome this problem, different variations of χ^2 have been tested and it was found that under different experimental conditions and using different experiments, variations should be used. For example, for some applications, I have found that the amplitude and phase measurements should be weighed differently when calculating the χ^2, e.g $\chi^2 = \chi^2_{amp} + \chi^2_{phase} = K_1 \sum |\frac{Amp_m}{Amp_{m0}} - \frac{Amp_c}{Amp_{c0}}| + K_2 \sum [(Phase_m - Phase_{m0}) - (Phase_c - Phase_{c0})]$ where K_1 and K_2 are weight factors. See Appendix 2.4 and following Chapters for validations and use of this method in simulated and *in vivo* data.

2.1.7.2 Image Reconstruction using *a priori* Spectral Information

The next step is to re-formulate the image reconstruction problem (Equations 2.10, 2.11, 2.12 and 2.15) in terms of Δc_i, Δa and Δb. This can be achieved by re-writing $\mathbf{W}$ in Equation 2.15 by taking the appropriate partial derivatives as

$$W_{ij}^{C_k} = \sum_g \frac{G(r_{di}, r_j, \lambda_g) U_0(r_j, r_{si}, \lambda_g) \epsilon_k(\lambda_g) h^3}{U_0(r_{di}, r_{si}, \lambda_g)} \tag{2.33}$$

$$W_{ij}^{a} = \sum_g \frac{\nabla G(r_{di}, r_j, \lambda_g) \cdot \nabla U_0(r_j, r_{si}, \lambda_g) (\lambda_g^{b_0}) h^3}{-3 U_0(r_{di}, r_{si}, \lambda_g) a_0^2} \tag{2.34}$$

$$W_{ij}^{b} = \sum_g \frac{\nabla G(r_{di}, r_j, \lambda_g) \cdot \nabla U_0(r_j, r_{si}, \lambda_g) \ln(\lambda_g) (\lambda_g^{b_0}) h^3}{-3 U_0(r_{di}, r_{si}, \lambda_g) a_0} \tag{2.35}$$

where the sum over g is over all the measurement wavelengths, C_k are the kth chromophore, h^3 is the voxel volume, subscripts i refer to the i^{th} source-detector pair and j to the j^{th} voxel. These equations formulate the inversion problem completely. A formalism can also readily be developed to regularize the weight matrix. The results from spectroscopy and segmented-tomography suggest this formulation should reduce the inter-parameter cross-talk in image reconstruction.

It is also informative to consider the number of unknowns and measurements in both cases. For the "traditional" imaging *each* inversion has $2\ N_v$ unknowns and $N_s N_d$ measurements. There are at least N_λ (number of wavelengths) independent inversions to carry out. Finally, resulting in $2\ N_\lambda\ N_v$ unknowns. The factor two comes from reconstructing $\Delta\mu_a$ and $\Delta\mu_s'$. For "multi-spectral" or "wavelength dependent" imaging, there is *only one* inversion with $(2+N_C)N_v$ unknowns where N_C is the number of chromophores and the additional two unknowns are a and b. When $(2+N_C) < 2\ N_\lambda$, the "wavelength" dependent method has *fewer* unknowns. For example, if only oxy- and deoxy-hemoglobins (ΔHbr and ΔHbO_2), water and lipids are reconstructed, then $(2+N_C)=6$. In this case, if $N_\lambda > 3$, then there is a clear advantage to use the "wavelength dependent" algorithm. The advantage of the "multi-spectral" method can further be seen by considering that there are $N_\lambda N_s N_d$ measurements employed in both cases. This means that the number of measurements per unknown is greatly increased by use of the "multi-spectral" method.

To illustrate this point, I use an extreme example which is the parallel plate optical mammography system used in our laboratory [77,89], where for a median breast thickness of 6.5 cm, a 16 x 16 x 6.5 = 1664 cm^3 tissue volume is imaged. This volume is divided into $N_v = 50000$ nodes in the finite-element calculations. There are 48 source fibers, 570 x 400 detectors and six wavelengths. In "traditional imaging", we would reconstruct 600,000 unknowns in six independent inversions. The number of measurements per unknown in this system is 110, and is independent of wavelength.

On the other hand, the "multi-spectral" approach reduces the number of unknowns greatly, to N_v x (# of chromophores + 2) = 300,000. This gives 220 measurements/unknown and scales linearly with the number of wavelengths.

To demonstrate this algorithm, I have simulated two identical spherical objects with radius ~ 0.3 cm. Its properties were defined by $Y_t = 35\%$ and $THC = 50\mu M$. The background properties were $Y_t = 75\%$ and $THC = 35\mu M$ with $50 : 50$ ratio of water to lipids. Random 1% noise was added to the amplitude and random 0.1^o noise was added to the phase. Three wavelengths, 690, 785, 830 nm , were simulated. This geometry is illustrated in Figure 2.4(a). The resulting images are shown in Figure 2.4(b), the concentrations are recovered fairly accurately for both objects. This method is used for image reconstruction for our experiments in rat brain (see Section 4.2)

2.1.8 Differential Pathlength Formulation of Photon Migration

In order to estimate changes in hemoglobin concentrations in a rapid and simple manner, another method was used, which I refer to as the "differential pathlength method" or "DPF method" [110, 373]. In this formulation, the standard Beer-Lambert law is modified to account for the lengthening of the mean photon pathlength due to scattering. A "differential pathlength factor" (DPF) is introduced, which is the ratio of the mean photon pathlength to the physical separation of the sources and detectors in a given.

$$DPF = \frac{\partial A}{\partial \mu_a} r^{-1} \,, \tag{2.36}$$

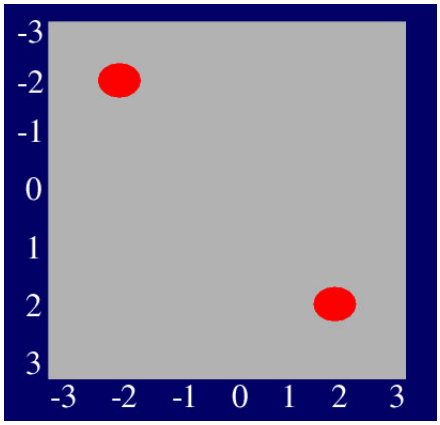

(a)

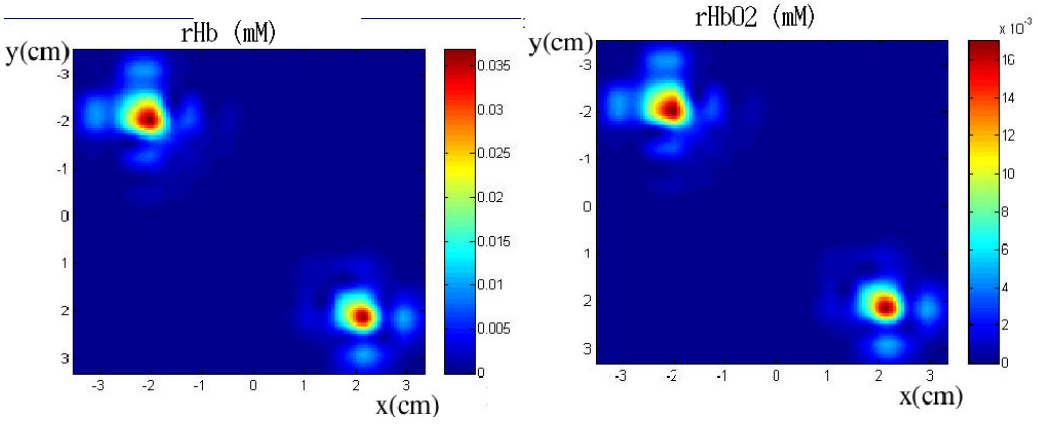

(b)

Figure 2.4: (a) Illustration of the simulated data, (b) Wavelength dependent image reconstruction of rHb and $rHbO_2$

where A is the logarithm of the ratio of the signal intensity corresponding to a change in μ_a (I) to the baseline intensity (I_0) as follows;

$$A(\lambda) = \log \frac{I}{I_0} \Delta\mu_a(\lambda) DPF(\lambda) r \ . \tag{2.37}$$

Here r is the source detector separation, A, $\Delta\mu_a$ and DPF are all wavelength dependent and subscript $_0$ denotes a baseline measurement. In a similar manner to spectroscopy using diffusion approximation, changes in hemoglobin concentrations can be calculated by solving for $\Delta\mu_a(\lambda)$ at several wavelengths. For example, for two wavelengths they are given by

$$\Delta Hb = \frac{\epsilon_{HbO_2}(\lambda_2)\frac{A(\lambda_1)}{DPF(\lambda_1)} - \epsilon_{HbO_2}(\lambda_1)\frac{A(\lambda_2)}{DPF(\lambda_2)}}{(\epsilon_{Hb}(\lambda_1)\epsilon_{HbO_2}(\lambda_2) - \epsilon_{Hb}(\lambda_2)\epsilon_{HbO_2}(\lambda_1))r} \tag{2.38}$$

$$\Delta HbO_2 = \frac{\epsilon_{Hb}(\lambda_1)\frac{A(\lambda_2)}{DPF(\lambda_2)} - \epsilon_{Hb}(\lambda_2)\frac{A(\lambda_1)}{DPF(\lambda_1)}}{(\epsilon_{Hb}(\lambda_1)\epsilon_{HbO_2}(\lambda_2) - \epsilon_{Hb}(\lambda_2)\epsilon_{HbO_2}(\lambda_1))r} \ . \tag{2.39}$$

Both intensities (I,$I+0$) are measured, A is calculated and using values from the literature for the extinction coefficients and DPF values, the changes in hemoglobin concentrations are calculated.

It is straightforward to apply this formulation to the data in real-time and with careful choice of the variable parameters, useful qualitative as well as quantitative information can be obtained. This method was chosen for some studies of the brain and muscle since only a single source-detector pair was available and it provided a more robust method than analytically fitting diffusion models. Furthermore, it is *the most common* method used in near-infrared spectroscopy of brain. A great deal of literature exists on the weaknesses and strengths of this formulation [40, 277, 346, 351] and experimental tabulations of the differential pathlength factor are available for several organs [110]. This formulation can be derived from diffusion approximation by use of Green's function solutions

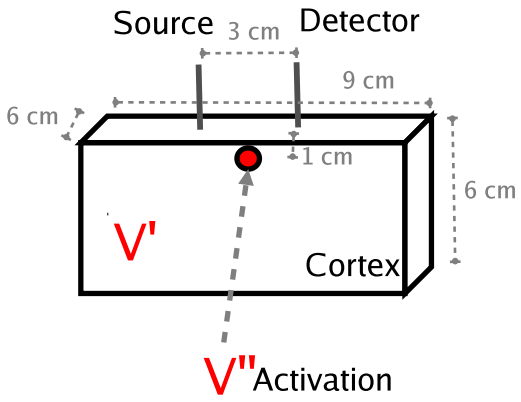

Figure 2.5: Schematic of a 2-compartment diffuse medium as an illustration of the partial pathlength factor.

[11].

However, this formulation ignores the heterogeneity of the tissues. If we assume a compartmentalized or layered tissue, DPF can be replaced by a "partial pathlength factor" (PPF), redefining A as

$$A(\lambda) = r \sum_{i=1}^{N} \Delta\mu_{ai}(\lambda) PPF_i(\lambda) \tag{2.40}$$

where $_i$ denotes the i^{th} compartment. PPF is a measure of the mean pathlength of the photons that travelled through the i^{th} compartment normalized by the source-detector separation. Following Strangman *et al* [351], it is straightforward to show that without accounting for PPF, the changes in μ_a would be underestimated for focal activity such as functional activation in the brain or activity in a lower layer as in the case of exercising muscle. For example, Figure 2.5 shows a simplification of diffuse optical measurements of local activation in the brain where V' and V'' are different "compartments". I have used this information in the following Chapters and relevant approaches that I took to account for this understimation is explained there.

2.2 Diffuse Correlation Spectroscopy and Tomography

2.2.1 Introduction

So far, I have concentrated on "static" properties of the tissues, however, even more information is impressed upon these diffusing optical fields if we consider the dynamics of the particles, i.e red blood cells in tissue. The so-called "dynamic" methods essencially monitor the speckle fluctuations of the scattered light, which in turn are sensitive to the motions of scatterers such as red blood cells.

2.2.2 Correlation Diffusion

Speckle fluctuations of the scattered light are sensitive to the motions of scatterers such as red blood cells. In most flow experiments the quantity of interest is the electric field temporal autocorrelation function G_1(**r**,τ) $= \langle$**E**(**r**,t) **E*(r**, t + τ)$\rangle$ or its Fourier Transform. Here the angle brackets $\langle \quad \rangle$ denote ensemble averages or averages over time for most systems of practical interest. τ is called the correlation time. The field correlation function is explicitly related to the motions of scatterers within the samples we study. Figure 2.6 illustrates a DCT measurement configuration in a turbid medium in the semi-infinite geometry.

The study of these motions in deep tissues is made possible by the fact that the electric field temporal autocorrelation function for light traveling in highly scattering media also obeys a diffusion equation [39, 41, 44]. In steady-state (i.e. CW light sources, $\omega = 0$), and in homogeneous media this *correlation diffusion equation* is quite simple:

$$\left(D\nabla^2 - v\mu_a - \alpha k_o^2 \mu_s' \left\langle \Delta \mathbf{r}^2 (\tau) \right\rangle / 3\right) G_1 (\mathbf{r}, \tau) = -vS (\mathbf{r}) . \tag{2.41}$$

Here $k_o$is the wavevector of the photons in the medium. $\langle \Delta \mathbf{r}^2(\tau) \rangle$ is the mean-square displacement

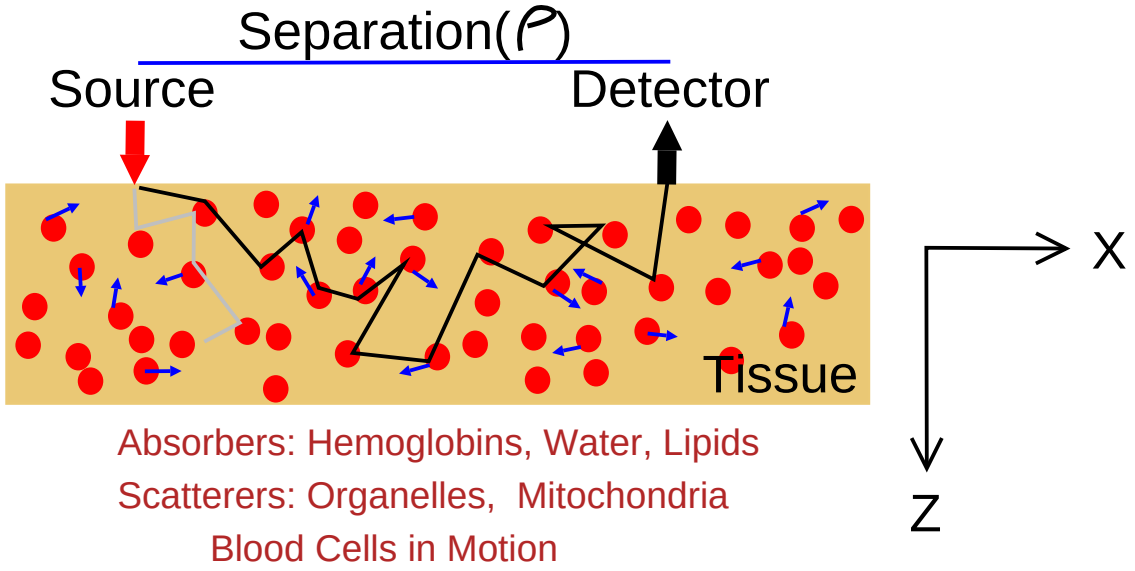

(a)

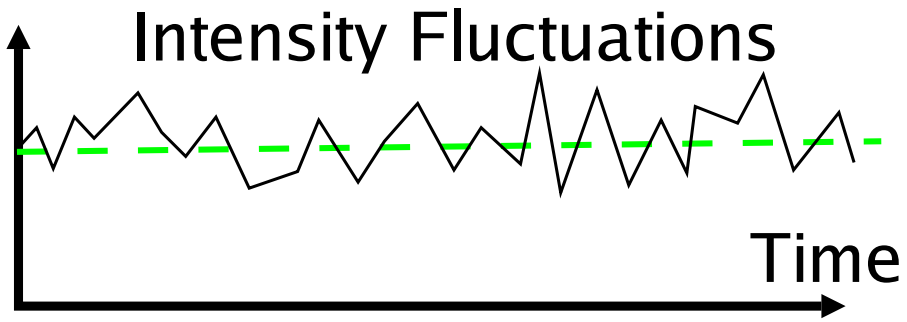

(b)

Figure 2.6: (a) Schematic of a of diffuse correlation tomography in a turbid medium. Sources and detectors are placed on the "air-side" of the tissue. The photons undergo scattering, absorption and experience Doppler shifts when they scatter from moving particles. The motion of the scatterers leads to fluctuations in intensity which are detected by a photon counting detector. (b) The temporal autocorrelation functions of the intensity are then calculated using an autocorrelator.

in time τ of the scattering particles (e.g. blood cells); this is the quantity we measure and attribute to blood flow or changes thereof. S(**r**) is the source light distribution, and α represents the fraction of photon scattering events in the tissue resulting from moving cells or particles. The correlation diffusion equation can have different forms depending on the nature of the particle motion, and on the variations of these motions with position in the sample. The mean-square displacement $\langle \Delta \mathbf{r}^2(\tau) \rangle$ = 6D$_B\tau$, for organelles or cells undergoing Brownian motion with "particle" diffusion coefficient D$_B$. For the important case of random flow which can arise in the tissue vasculature, $\langle \Delta \mathbf{r}^2(\tau) \rangle = \langle \mathrm{V}^2 \rangle \tau^2$where $\langle \mathrm{V}^2 \rangle$ is the second moment of the cell speed distribution. In the latter case the correlation function will decay exponentially as τ.

It is instructive to rewrite Equation 2.41 in the following format for a point source located at (x_s, y_s, z_s) as before;

$$(\nabla^2 - K^2(\tau)) G_r(\mathbf{r}, \tau) = -\frac{v S_0}{D} \delta^3(\mathbf{r} - \mathbf{r_s}) \, , \tag{2.42}$$

where $K^2(\tau) = v(\mu_a + \frac{1}{3}\alpha\mu_s' k_0^2 < \Delta r^2(\tau) >)/D$. Notice that for $\tau \rightarrow 0$, $\langle \Delta \mathbf{r}^2(\tau) \rangle \rightarrow 0$, Equations 2.41 and 2.42 reduce to the steady-state diffusion equation for diffuse photon fluence rate (i.e. Equation 2.3 with ω = 0). Formally, the equations for transport of diffuse photon correlation and diffuse photon fluence rate are the same. Thus the same sorts of general analyses applied in the case of photon fluence rate will be valid for photon correlation. Multi-distance measurements of G_1(**r**,τ) on the tissue surface provide dynamical information about the motions within the sample in exactly the same way that multi-distance measurements of diffusive waves on the tissue surface provide information about scattering and absorption properties. The layout of the sources and detectors is similar to the diffusive wave schemes, but the correlation measurements are more complex. One needs a special piece of equipment called an autocorrelator for the measurements. The autocorrelator takes the detector output and uses the photon arrival times to compute G_1(**r**,τ),

or (more precisely) its light *intensity* analog. The photon correlation technique has an advantage over its Fourier counterpart (i.e. LDF) in the low signal limit, because the photon correlation instruments are essentially single photon counting devices. This advantage is important for us, because it enables the experimenter to probe more deeply into the tissue samples. Blood flow is derived from the temporal decay of the diffuse light intensity temporal autocorrelation function. Typically this autocorrelation function can be fit with an exponential decay. Its decay rate, Γ (sec^{-1}), depends on the parameter α (proportional to the tissue blood volume fraction), and on the motion of blood cells. Relative changes in Γ (sec^{-1}) correspond to relative changes in blood flow. For more details on instrumentation see Chapter 3.

2.2.3 Correlation Spectroscopy in the Semi-Infinite Approximation

The solutions for DCT in a semi-infinite geometry would resemble those in Equation 2.4 as follows

$$G_1(\mathbf{r},\tau) = \frac{3\mu_s'}{4\pi}\left(\frac{e^{-K(\tau)\mathbf{r}}}{\mathbf{r}} - \frac{e^{-K(\tau)\mathbf{r_2}}}{\mathbf{r_2}}\right) , \tag{2.43}$$

where $\mathbf{r}$ and $\mathbf{r_2}$ are defined in equation 2.6. Experimentally, we measure the intensity autocorrelation function, $g_2(\mathbf{r},\tau) =< I(t)I(t+\tau) > / < I >^2$ which is related to $g_1(\mathbf{r},\tau) = G_1(\mathbf{r},\tau)/ < E(t)E^*(t) >$ by the Siegert relation;

$$g_2(\mathbf{r},\tau) = 1 + \beta|g_1(\mathbf{r},\tau)|^2 , \tag{2.44}$$

where β is a parameter that depends on the source coherence, detection optics, ambient light and other external factors. Figure 2.7 shows sets of autocorrelation functions for different source-detector separations and D_B. The curves decay faster with increasing D_B, i.e. increased flow, and

increased source-detector separation. The slope and/or the decay rate provides information about the optical properties and the motion of the scatterers.

By comparing the extensive set of data from many different tissues and phantoms under different conditions, we have determined empirically that the "Brownian motion" model fits the data more accurately than the "random flow" model (see Figure 2.8) Therefore, all the data presented in this manuscript reports either D_B or ΔD_B. We stress once more that the formulation of the diffuse correlation tomography is *identical* to the continous wave (CW) formulation of DOT.

2.2.4 Two Layer Approximation for Diffuse Correlation Tomography

The application of diffuse correlation spectroscopies for quantification of blood flow has not been reported through human skull. This is partly a result of the fact that fewer people are familiar with the technical advances of DCT, but is also due to the new challenges in applying DCT to humans. Most significantly, the DCT measurements must have adequate signal-to-noise at the large source-detector separations necessary to probe through a skull whose thickness varies between $\sim$0.4cm and $\sim$1cm.

As a first step toward application of DCT in human brain I have conducted two preliminary studies: (1) have modified two layer analytical solution for light diffusion (see Section 2.1.6) so that it can be used to predict correlation diffusion in layered media [309] , and have theoretically investigated the temporal autocorrelation functions as a function of layer thickness and source-detector separation, (2) have carried out a DCT experiment using a human skull filled with Intralipid solution. In both investigations a thick ($\sim$0.6 cm) highly scattering static medium was placed over a dynamic highly scattering medium. This confirmed that the temporal correlation functions were indeed measurable, and that a two-layer model was useful to extract the flow of the

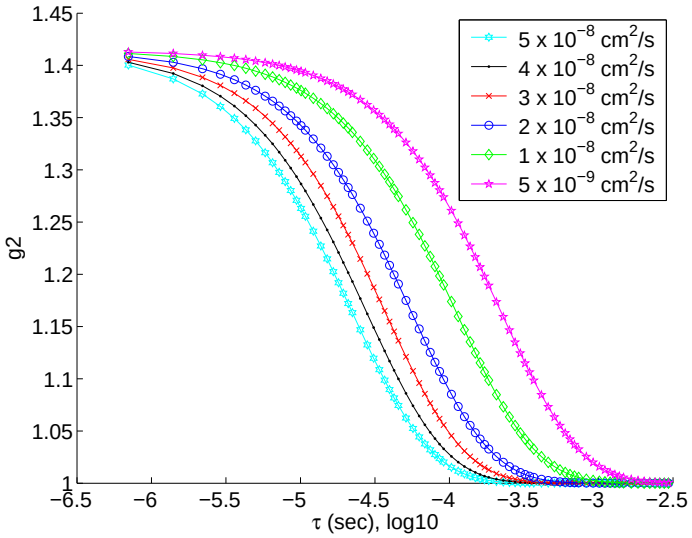

(a)

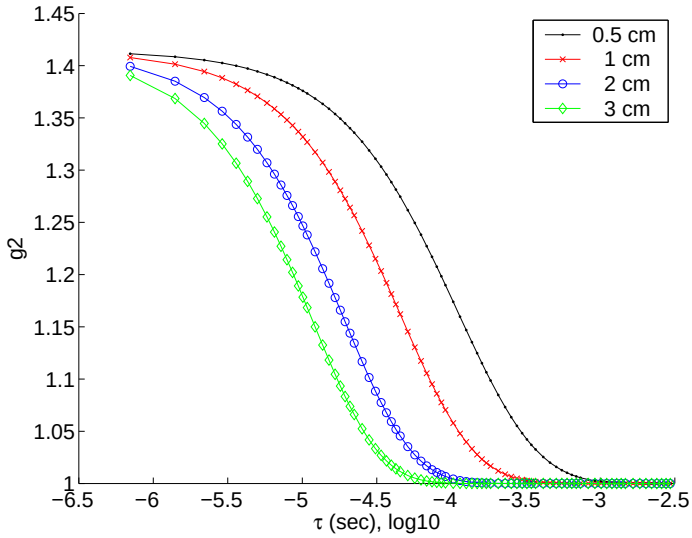

(b)

Figure 2.7: Assuming $\mu_s' = 10$ cm^{-1}, $\mu_a = 0.1$ cm^{-1}, (a) Autocorrelation functions for $r = 0.5$ cm for different D_B, (b) Autocorrelation functions for $D_B = 1$ x 10^{-8} cm^2/s for different r

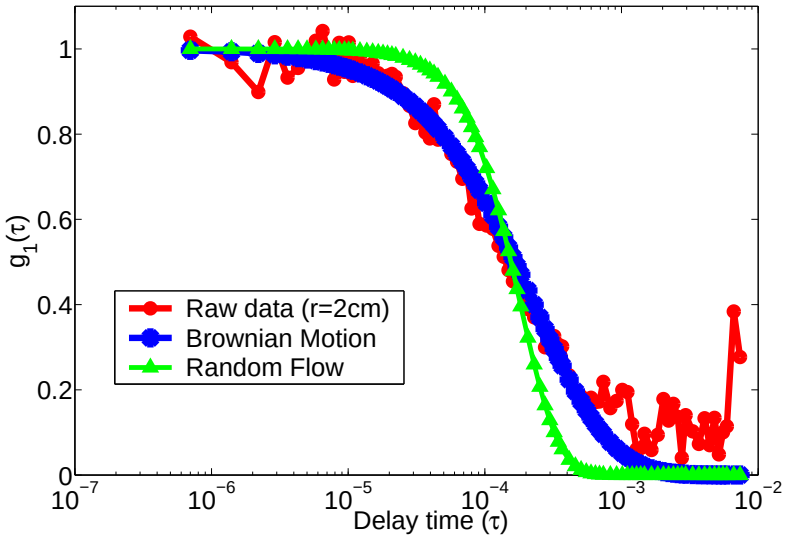

Figure 2.8: Three autocorrelation functions showing the measured data from muscle tissue, fitted data with Brownian motion and random flow models. Brownian motion model fits the data significantly better than the random flow model

dynamic medium.

A k-space solution to the diffusion equation was used to model two layer turbid medium as described in details in Section 2.1.6. The medium was homogeneous with $\mu_s' = 10\text{cm}^{-1}$ and $\mu_a = 0.05\text{cm}^{-1}$. The thickness of the static layer was 0.5 cm. The dynamic medium was taken to be governed by Brownian motion with Brownian diffusion coefficient $D_B = 1\text{x}10^{-8}\text{cm}^2/\text{s}$; in practice the correlation functions would be expected to decay even faster for blood flow in the brain (upto $4\text{x}10^{-8}$). The resultant decay curves are shown in Figure 2.9 for three source-detector separations (1 cm, 2 cm and 3 cm), with and without the static layer. The main effect of the layer is to reduce the decay time as expected. Importantly however, even for media with the static layer, the shape of the curve reveals information about the lower dynamic region. This is a significant finding since it indicates that diffuse correlation methods will be able to probe flow through thick static layers whose optical properties resemble those of the human brain.

Later, a human skull was filled with Intralipid solution ($\mu_s' = 10\text{cm}^{-1}$, $\mu_a = 0.05\text{cm}^{-1}$,

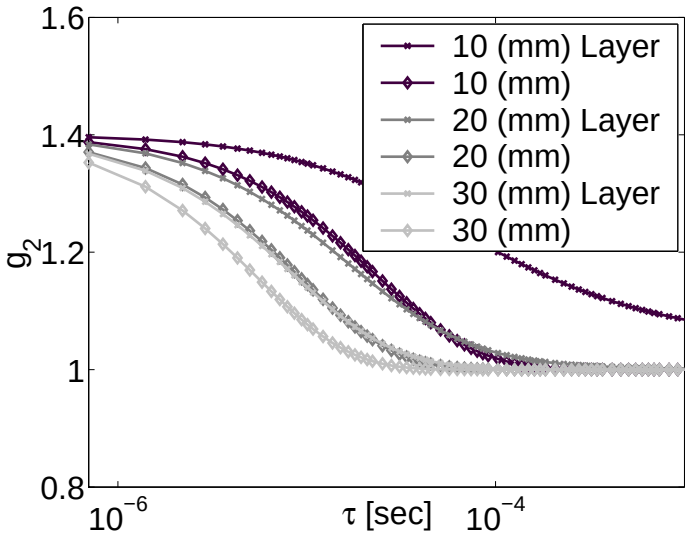

Figure 2.9: Calculated diffuse, temporal autocorrelation functions as a function of source-detector separations, with and without the static over-layer.

$D_B = 1.4\text{x}10^{-8}\text{cm}^2/s$), and we used our contact probe to measure flow with source detector separations of 1, 1.5, 2, 2.5, 3, 4, 4.5, 5 cm. Figure 2.10 shows a photo of the measurement geometry and apparatus. The skull was held inverted so that the Intralipid solution did not leak out. At 3 cm source-detector separation $\sim$27 seconds of data gave high signal-to-noise ratio (laser power was 40mW). The same data can be post-processed to filter noise, in which case the measurement range extended to 4.5 cm. Therefore, 256 correlation curves (each curve takes 106 msec to obtain) were averaged to derive an adequate signal-to-noise ratio at these source-detector separations. Obviously, this is an unacceptably long data acquisition time, but, in the future, this problem can be tackled by bundling four detector fibers together at each location to obtain the same number of curves in $\sim$7 sec. I have empirically determined that source detector separations $>$ 2 cm were sufficient to measure functional activation in the human brain (see Chapter 4.4) with only $\sim$ 3 seconds of averaging with a *single* detector fiber. Hence measurement of motor cortex activation is possible. Bundling four fibers together reduced the acquisition time to $\sim$ 2 seconds. Similarly,

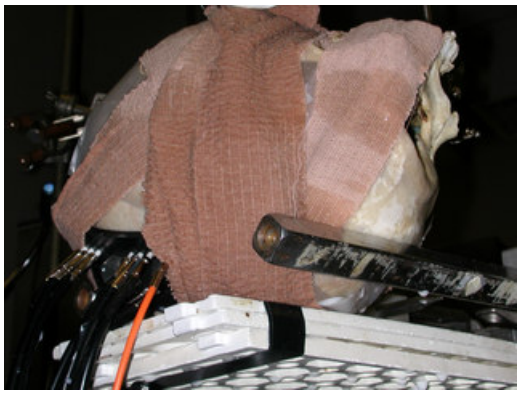

Figure 2.10: Human skull model filled with Intralipid solution. The lighter fiber is the source fiber and the 8 black fibers are the detector fibers. The skull is held inverted, filled with Intralipid. The probe is secured tightly to the skull with elastic bandage.

with measurements on human calf muscle, we have shown it is possible to separate the response of skin/fat layers and deep muscle (see Chapter 5.2).

In Figure 2.11 the correlation functions are shown, again for separations between 1 cm and 3 cm. Fitting the data with the two-layer model, gives a best fit for thickness =0.53 cm and for $D_B = 1.2\text{x}10^{-8}\text{cm}^2/s$, close to the expected value considering that skull curvature and refractive index mismatches were ignored. In carrying out these fits we found that the recovered Intralipid particle diffusion constant was relatively insensitive to the assumed optical properties of the skull ($\mu_a = 0.1\text{cm}^{-1}$ and $\mu_s' = 8\text{cm}^{-1}$ at 800 nm).

2.2.5 Tomography with Diffuse Correlation

Image reconstruction with auto-correlation functions, i.e diffuse correlation tomography (DCT), follows a similar formalism as DOT. However, the instrumentation involved, the signals, the noise and the type of data acquired are *different*. Therefore, I will briefly outline a linearized image reconstruction method for DCT based on DOT (see Section 2.1). Then I describe how to optimize the selection of the data set. Finally a spatially dependent regularization scheme is implemented.

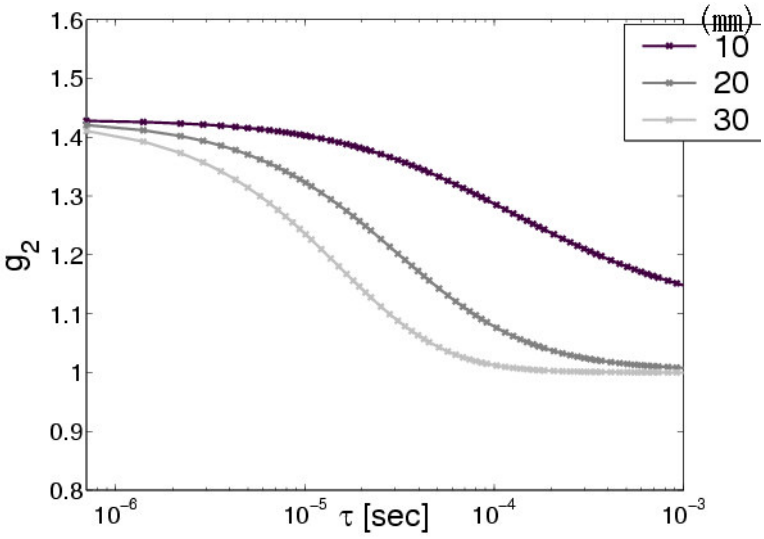

Figure 2.11: Correlation functions taken at different source-detector separations. Probe is on the human skull filled with Intralipid. The skull thickness was measured to be about 0.6 cm

This formalism is used extensively to image blood flow in rat brain in Chapter 4.2.

I begin by making an assumption, relying on the fact that changes in blood flow are $\sim 3-20$ times larger than changes in oxy- and deoxy-hemoglobin concentrations for the models studied, that $\Delta\mu_a(\mathbf{r}) = 0$ and $\Delta\mu_s'(\mathbf{r}) = 0$. The changes in flow are considered (as before) to be perturbations from a constant, homogeneous "background" as $D_B(\mathbf{r}) = D_B^0 + \Delta D_B(\mathbf{r})$. In Rytov approximation, this leads to a result equivalent to Equation 2.15, i.e.

$$\mathbf{W_{ij}^{D_B}} = -\frac{1}{G_{10}(\mathbf{r_d}-\mathbf{r_s},\tau)} G_{10}(\mathbf{r}-\mathbf{r_s},\tau) G(\mathbf{r}-\mathbf{r_d},\tau) \left(\frac{2vh\mu_s'\tau}{D_0}\right) \tag{2.45}$$

for i^{th} source-detector pair and j^{th} voxel. G_{10} is the autocorrelation function for the background and G is the corresponding Green's function. Two observations are notable: (1) formally this weight matrix is identical to $\mathbf{W_a^\mu}$, (2) a particular τ should be chosen for reconstruction. The choice of τ effects the properties of the weight matrix and therefore, the resultant image. It is not practical and not readily apparent that it is advantageous to employ multiple delay times should be

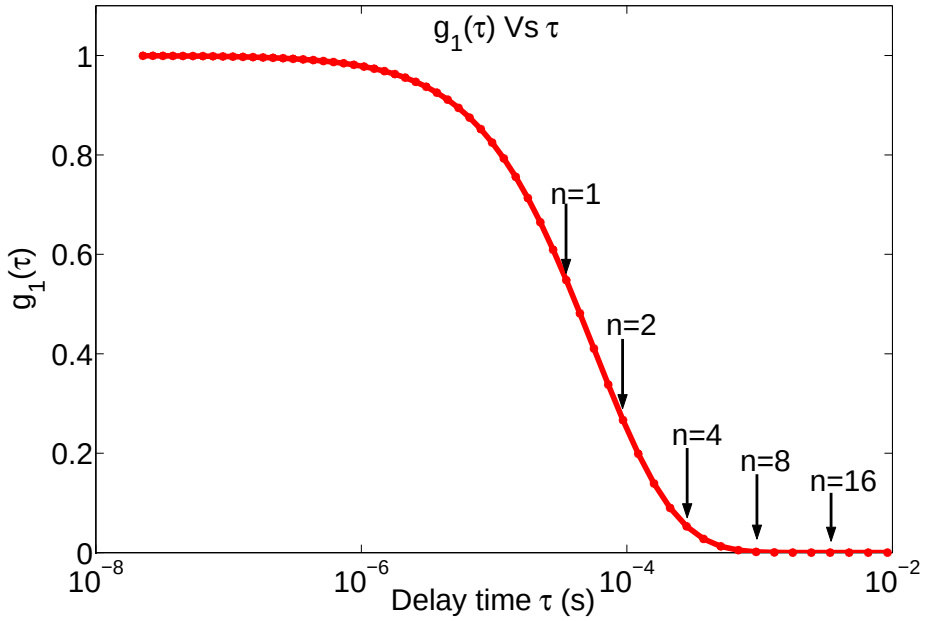

Figure 2.12: Choice of "n" to parameterize the autocorrelation curves.

employed in the reconstruction. Previously [91] we have have chosen τ such that G_1 has decayed to e^{-1} of its initial value, and we were able to obtain dynamic images of CBF during focal ischemia. Instead, we now, look at the condition number of the weight matrix which is the ratio of the largest singular value to the smallest singular value and can be used to "tune" the noise amplification in the reconstruction [416]. The variation of the condition number is investigated by parametrizing the curve by a parameter n which defines a value of τ (τ_c) for which the correlation function decays to e^{-n} of its original value (see Figure 2.12). n is related to the other variables in this problem, i.e.

$$(K(\tau_c) - K(0)) \cdot |r_s - r_d| = n \tag{2.46}$$

which gives τ_c:

$$\tau_c = \frac{1}{\mu_s' k_0^2 D_B} \left(\frac{n^2}{|r_s - r_d|^2} + \frac{2n\sqrt{3\mu_a\mu_s'}}{|r_s - r_d|} \right) . \tag{2.47}$$

Figure 2.13 shows the variation of the condition number vs "n" for a semi-infinite imaging

geometry. This reveals that the condition number is independent of n for $n < 0.5$ and decays rapidly for larger n. Suprisingly (at least to us), the minimum condition number is around $n = 100$ which is a point where the curve decays to an unreasonably low value. At high n the curve is dominated by noise. Therefore, we pick n (generally $n = 1 - 8$) such that the curve is still many standard deviations higher than the noise level. Different τ_c is picked for different source-detector pairs, but n is kept constant.

After the selection of the data set (τ_c), a depth dependent regularization is applied as described in Section 2.1.

2.3 Metabolic Rate of Oxygen Extraction (MRO_2/$CMRO_2$)

One aim of the hybrid optical methods in this thesis is to derive estimates of the variations in metabolic rate of oxygen extraction in tissues. In the realm of cerebral hemodynamics, cerebral metabolic rate of oxygen ($CMRO_2$) is one of the most sought after quantities and is the subject of extended research for decades. Similar quantities are becoming prominent in other paradigms such as the exercising muscle as it is understood that blood flow and/or blood oxygenation are not sufficient as stand-alone measures to adequately characterize the tissue status.

In this section, I describe a basic model for synthesizing our measurements to calculate dynamics of relative $CMRO_2$. An extended discussion of metabolic measures for other tissues is beyond the scope of this thesis, however, the basics described here were shown to be generally applicable to muscle and tumor metabolism and are used in the experiments. This description is compiled from a set of recent papers on $CMRO_2$ which cover the modern understanding of $CMRO_2$ models for synthesis of hemodynamic data [58,59,145,155,190,253,254,368,415]. The differences between these models is not relevant for our measurements because of the timescales

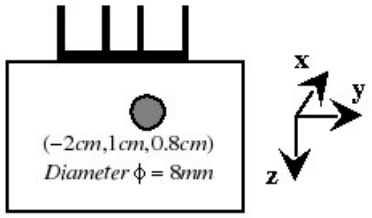

(a)

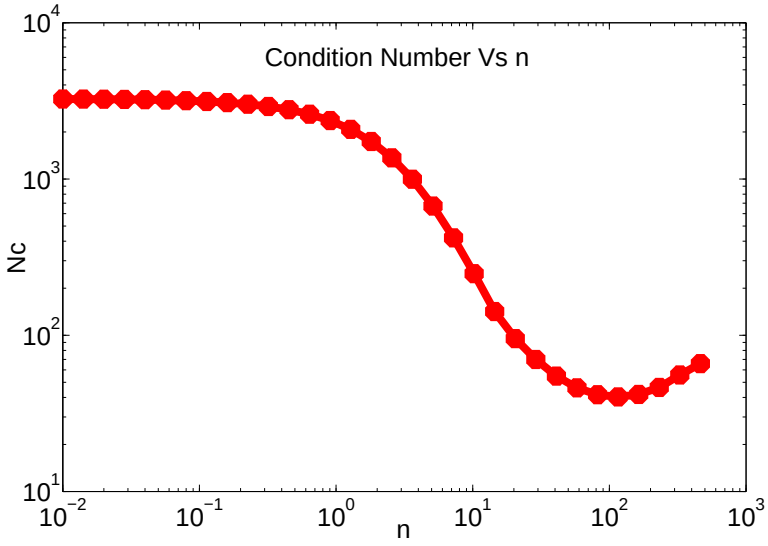

(b)

Figure 2.13: (a) Imaging geometry with a spherical inclusion, (b) Variation of the condition number of **W** vs "n". for small "n" it is independent of "n" whereas the minimum is at a fairly large "n" ($n \approx 100$).

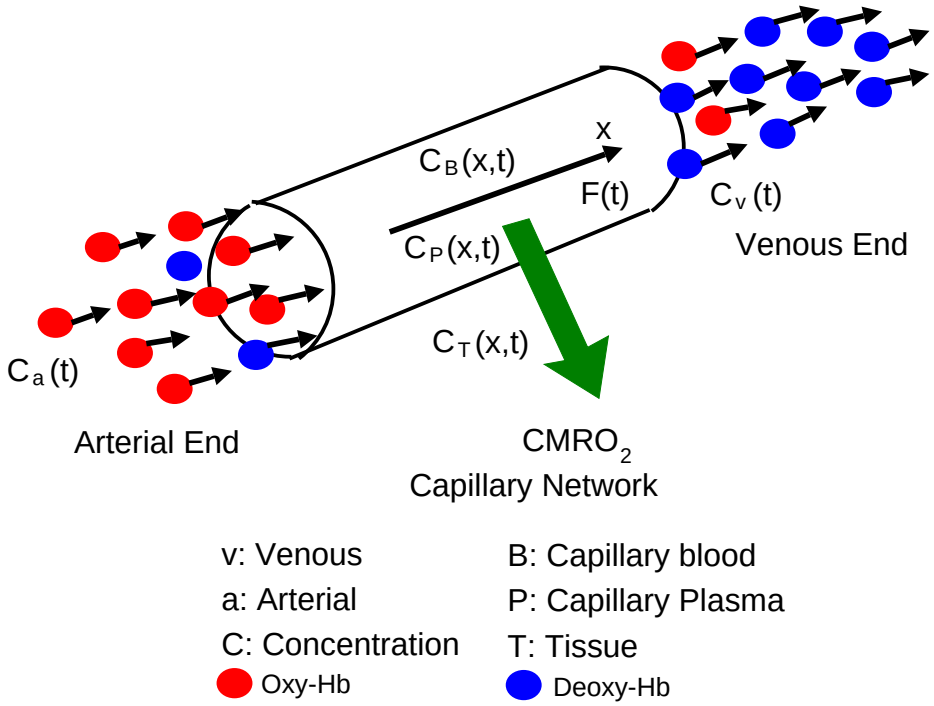

Figure 2.14: Compartmentalized model of the vasculature; oxygenated blood flows in from the arterial end through the capillaries and out from the venuous end.

and paradigms employed.

Following Valabregue *et al* [368], a compartmentalized model of the vasculature is assumed as shown in Figure 2.14. Oxygenated blood enters the capillary from the arterial end, and flows through the capillary with a given flow rate ($F(t)$ or $CBF(t)$). In the capillaries, oxygenation is reduced by passive diffusion through the blood-brain barrier which depends on the concentration gradient between capillary and tissue compartments. Finally, mostly deoxygenated blood flows out the venous end.

The oxygenation changes of the capillaries is due to blood flow supply and passive diffusion through the blood-brain barrier into the tissues. Tissue oxygen concentration (taken to be zero by earlier models [58, 155, 190]) depends on intake from capillaries and consumption by the cells ($CMRO_2$). Non-zero tissue oxygen concentration allows for the backflux from the tissue. In

addition to this model, one could consider the variations in oxygen concentration in blood and plasma and relate that to the gradients accross the blood-brain barrier.

Given these relationships and set of approximations about the blood distribution in capillaries a coupled set of equations can be derived from mass conservation and Fick's law. In steady state, we get

$$\frac{dC(x)}{dx} = -\frac{K}{CBF}\left(C_P(x) - C_T\right) \tag{2.48}$$

$$CMRO_2 = K(< C_P > - C_T) \tag{2.49}$$

where x is distance along the capillary, $C(x)$ is the blood oxygen concentration in capillary, K is a constant related to surface area and permeability of the capillaries, $C_P(x)$ is the oxygen concentration in plasma, C_T is the tissue oxygen concentration, CBF is blood flow and $< C_P >$ is the mean of $C_P(x)$. Cerebral metabolic rate of oxygen ($CMRO_2$) is given in mL.min^{-1}.(100 g)$^{-1}$ or 1/0.0224 μmol.min^{-1}.(100 g)$^{-1}$. The cerebral blood flow (CBF) is given in mL.min^{-1}.(100 g)$^{-1}$. All the oxygen concentrations are given in mmol.L^{-1}. Constant K is 3000 mL.min^{-1}.(100 g)$^{-1}$. The position along the capillary is denoted by a coordinate (x) normalized to the capillary length which is unitless. It is interesting to note that these equations allow for uncoupling of CBF and $CMRO_2$ below a certain range.

For stationary state, which is assumed by the studies in this work, Equation 2.48 can be integrated along the capillary and by substituting into Equation 2.49 we get

$$CMRO_2 = CBF(C_a - C_v) = (OEF)(CBF)(C_a) \tag{2.50}$$

where OEF is the oxygen extraction fraction , $OEF = (C_a - C_v)/C_a$, C_a and C_v are oxygen

concentrations in the arterial and venous ends. $CMRO_2$ in the stationary state is related to the oxygen extraction fraction and blood flow. Diffuse optical tomography, however, does not measure arterial or venous oxygenation, rather it is sensitive to the oxygen saturation of the complex medium, which is an average of different vessels such as capillaries, arteries and veins. Therefore, in order to estimate $CMRO_2$ based on knowledge of CBF, we must assume a steady-state balance between C_a and hemoglobin concentration which gives

$$OEF = \frac{(C_a - C_v)}{C_a} \approx \frac{(Y_{ta} - Y_{tv})}{Y_{ta}} \ . \tag{2.51}$$

The measured blood oxygen saturation (Y_t) can be written as

$$Y_t = k_1 Y_{ta} + k_2 Y_{tc} + k_3 Y_{tv} \tag{2.52}$$

where $k_{1...3}$ are the weights of arterial, capillary and venous saturations to total hemoglobin concentration respectively. Subscripts a, c, v correspond to arterial, capillary and venous compartments. Another simplification is to write the capillary saturation as a weighted average of arterial and venous saturations, i.e. $Y_{tc} = k_4 Y_{ta} + k_5 Y_{tv}$ with $k_4 + k_5 = 1$. With this approximation Equation 2.52 becomes

$$Y_t = (1 - \gamma) Y_{ta} + \gamma Y_{tv} \tag{2.53}$$

where $\gamma = k_3 + k_2 k_5$ is the percentage of blood volume in the venous compartment of the vascular system. So finally Equation 2.51 becomes

$$OEF = \frac{(Y_{ta} - Y_t)}{\gamma Y_{ta}} \ . \tag{2.54}$$

Y_{ta} can be estimated from blood gases or from the literature and is generally constant. γ is unknown but if we assume that it is unchanged, $rOEF$ and, therefore, $rCMRO_2$ can be calculated from the measured oxygen saturation (Y_t) and relative blood flow ($rCBF$).

Whenever oxy- and deoxy-hemoglobin concentrations are measured instead of oxygen saturation, another formulation can be derived by using $Y_t = HbO_2/THC$ and $1 - Y_t = Hb/THC$ as

$$rCMRO_2 = \left(Y_{ta} + \frac{\Delta Hbr}{Hbr_o}\right)\left(Y_{ta} + \frac{\Delta HbT}{HbT_o}\right)^{-1} rCBF \tag{2.55}$$

where $_o$ corresponds to baseline values. For an extendend analysis of modelling assumptions and limitations relevant to our measurements, see Culver *et al* [91].

2.4 APPENDIX: Segmented Tomography using *a priori* Spectral Information

Another problem where the utilization of the *a priori* spectral information is expected to be useful is the segmented tomography problem where a secondary modality (such as ultrasound, MRI or x-ray in case of optical mammography) provides an approximate position and shape/size of a heterogeneity whose optical properties are to be measured. I have investigated this problem using numerical simulations. The simulated data was generated using a finite-difference method which was also used as the forward model for the inversion. The inversion was non-linear in the sense that at each iteration the Green's functions were updated. It is considered to be segmented tomographic because even though the whole volume is modelled with a heterogeneity, the properties of only the pre-determined heterogeneity volume are allowed to vary and, even then, as a whole unit.

I have considered cases of single-heterogeneities for (1) the measurement of "bulk properties"

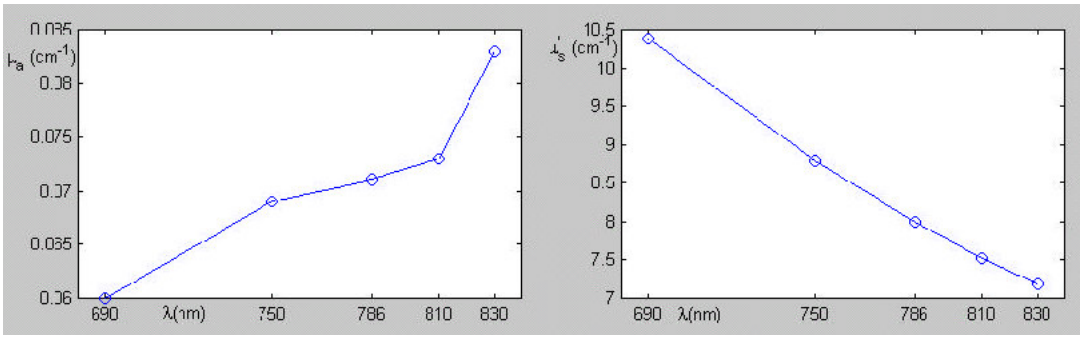

Figure 2.15: Optical properties of the simulated heterogeneity corresponding to a THC=35μM, $Y_t = 75\%$

of healthy breast considering its shape information, (2) characterization of a spherical "tumor". Amplitude and phase noise, a so-called "off-set" noise (see Chapter 3) which causes a amplitude-phase cross-talk, errors in boundary conditions and incorrect estimation of the heterogeneity geometry were considered as sources of error to compare the "traditional" and "wavelength dependent" methods. Five wavelengths , 690, 750, 786, 810 and 830 nm, were used. The optical properties of the heterogeneities are illustrated in Figure 2.15.

First case considered mimics characterization of a tumor which is an ellipsoidal heterogeneity in a parallel plate transmission geometry as illustrated in Figure 2.16. Single source (x) with a grid of 90 detectors with random noise added (5% amplitude, 2^o phase) is simulated. The tumor volume is estimated to be a sphere rather than an ellipsoid in the inversion which mimics an error due to estimating a volume from 2D images such as ultrasound. Figure 2.17(a) shows the obtained properties with both methods. Inter-parameter cross-talk is clearly apparent using the "old" method. Even though the wavelength dependent method is *unable* to recover the correct properties, we are able to recover their *wavelength dependence* accurately. Therefore, it is possible to recover the THC (39% vs 25% error) and Y_t (20% vs 2%) more accurately using the latter method as shown in Figure 2.17(b).

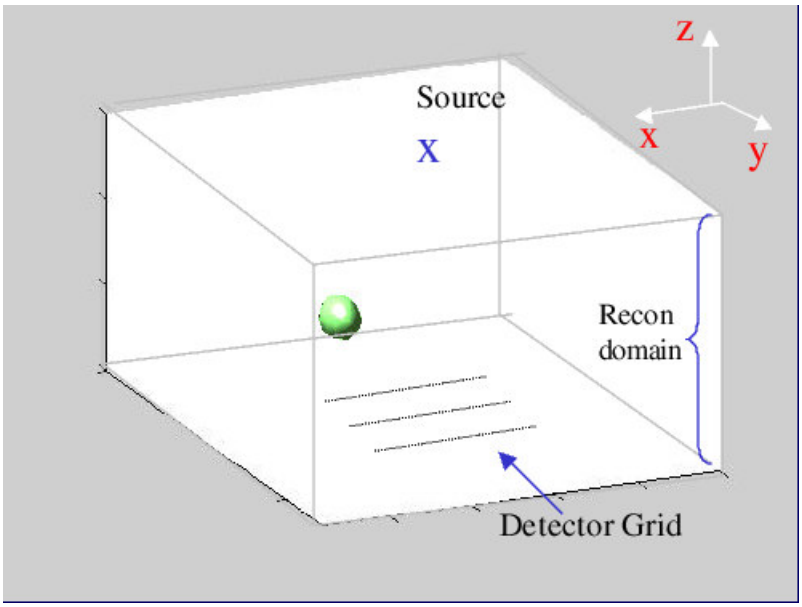

Figure 2.16: Ellipsoidal heterogeneity mimicing a tumor in parallel plate transmission geometry. Single source (x) with a grid of 90 detectors with random noise added (5% amplitude, 2^o phase).

The second case considered mimics a problem that is applicable for optical mammography when estimating the "background" fluence. The geometry is illustrated in Figure 2.18 where a whole breast including a chest-wall is considered as a heterogeneity in a parallel plate geometry (red-volume). 90 detectors are arranged in a grid and a single source (x) with five wavelengths is used. Optical properties are same as before. 1% random noise is added to the amplitude, 1^o random noise is added to the phase, 1% of maximum amplitude is taken as off-set noise and the geometry is underestimated by 20% in volume. This time we consider the effect of fixing b.

Figure 2.19(a) shows the obtained properties with both methods. Inter-parameter cross-talk is clearly apparent using the "old" method. This time, when b is kept free, even the new method is not doing well. However, if b is fixed (either correctly or by $\sim 10\%$ error), a significant improvement is visible. Even though the wavelength dependent method is still *unable* to recover the correct properties, we are able to recover their *wavelength dependence* accurately. It is not possible to achieve a signficant improvement for the recovery of THC (7.5% vs 7% vs 8.5% error). However,

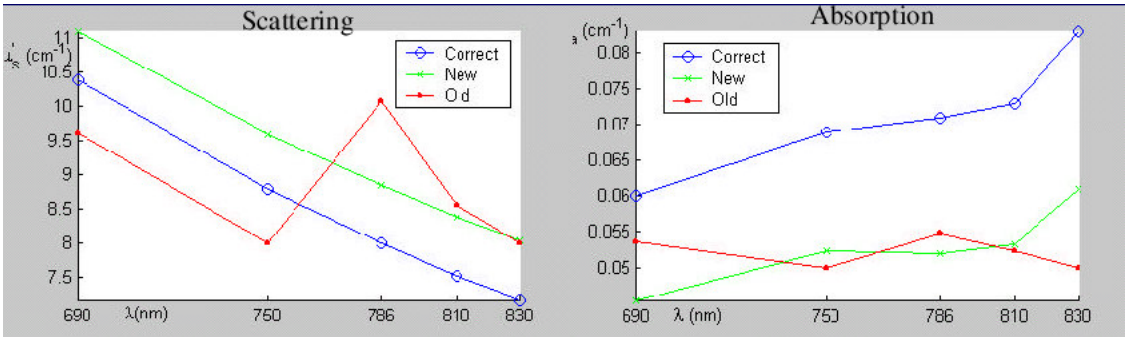

(a)

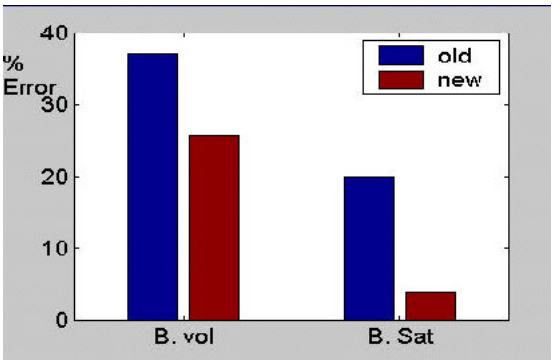

(b)

Figure 2.17: (a) “Measured” optical properties from both methods, (b) comparison of two methods for the recovery of the physiological parameters

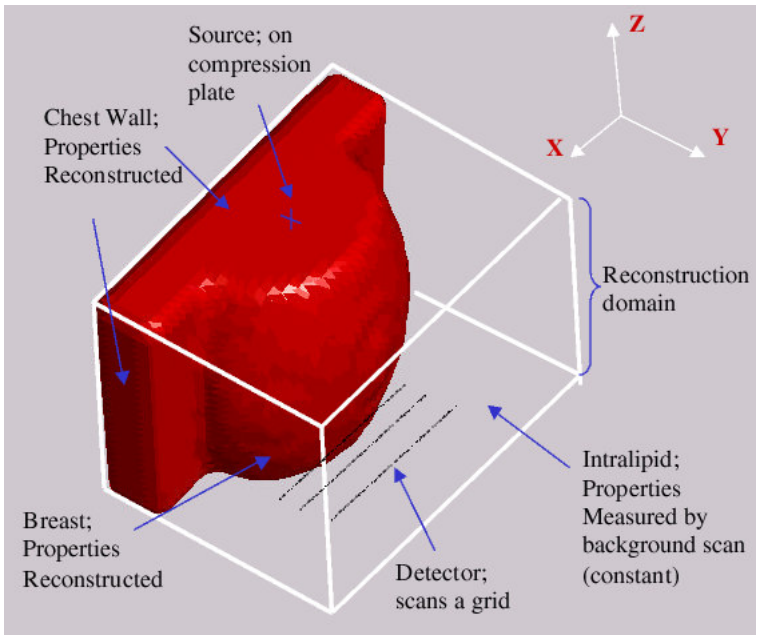

Figure 2.18: A whole breast including a chest-walll as a heterogeneity in a parallel plate geometry (red-volume). 90 detectors are arranged in a grid and a single source (x) with five wavelengths is used.

Y_t is recovered significantly better when b is free (8% vs 5% error) and even better when it is fixed, only 1.5% error as shown in Figure 2.19(b).

Finally, a more extreme case was considered with 10% random error in amplitude, 2^o error in phase, 10% underestimation of geometry by volume, 10% error in boundary conditions and 1% of maximum amplitude is taken as off-set noise.

Figure 2.20(a) shows the obtained properties with both methods. Inter-parameter cross-talk is clearly apparent using the "old" method with a significant improvement visible with the new method. Even though the wavelength dependent method is again *unable* to recover the correct properties, we are able to recover their *wavelength dependence* accurately. As seen in Figure 2.20(b), the "old" method does poorly with 18% error in THC and 17% error in Y_t, whereas with the wavelength dependent method the errors are reduced to 11% and 2% for THC and Y_t respectively.

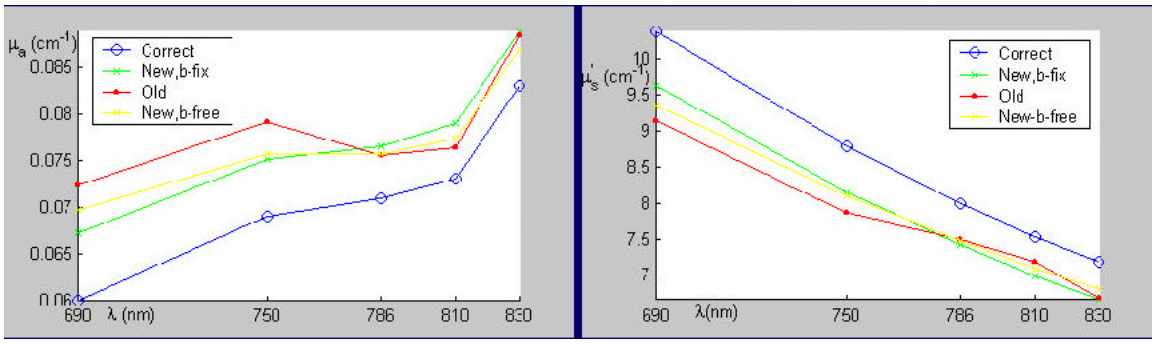

(a)

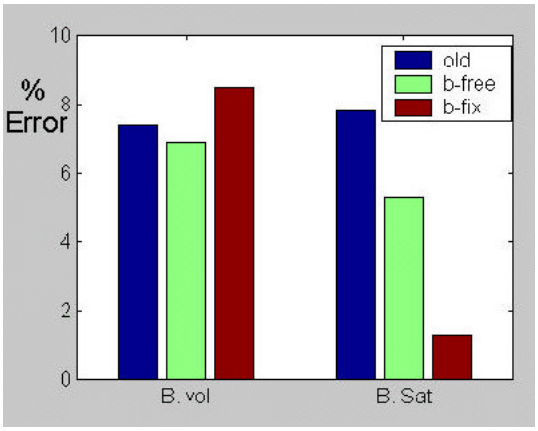

(b)

Figure 2.19: (a) “Measured” optical properties from both methods, (b) comparison of two methods for the recovery of the physiological parameters

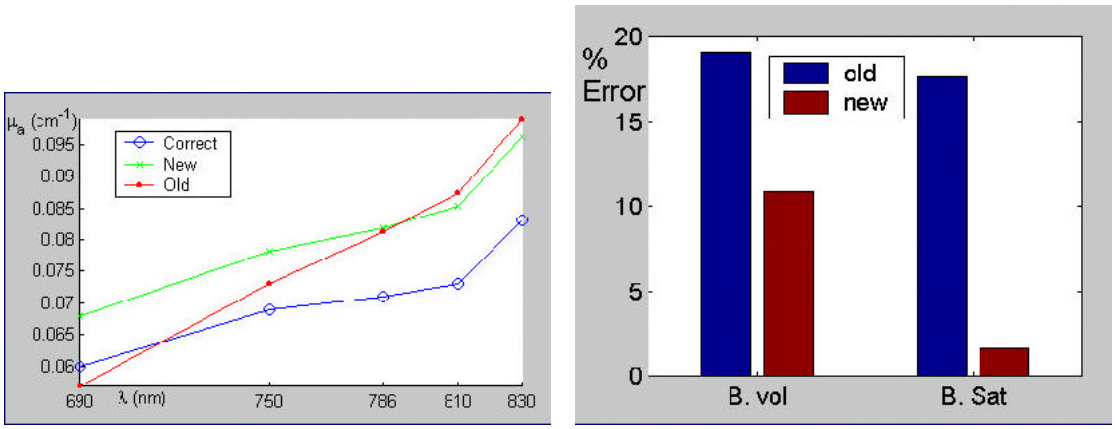

(a) (b)

Figure 2.20: (a) “Measured” optical properties from both methods, (b) comparison of two methods for the recovery of the physiological parameters

Chapter 3

Hybrid Instrumentation

3.1 Introduction

The hybrid instrumentation scheme that was used for the measurements described in this manuscript was first introduced by Cheung *et al* [76]. A frequency domain (70 MHz) diffuse optical tomography instrument with 12 source positions, 3 wavelengths (690nm, 786nm, 830nm) and four detector channels working in parallel were hybridized with a diffuse correlation tomography instrument with similar characteristics, but with a continuous wave, long coherence length laser source working at 800nm. Source positions and wavelengths were multiplexed by a series of optical switches. A frame rate of 2.5 minutes per frame was obtained in these initial experiments. The measurements were validated by extended hypercapnia on rat brains and relative cerebral metabolic rate of oxygen extraction ($CMRO_2$) was estimated. It was shown that the results were in good agreement with the blood gas measurements of $PaCO_2$. A second validation study including hypoxia, hypercapnia and cardiac arrest was later carried on, again, showing good agreement with the literature and other measurable parameters [90]. The measured CBF changes were also compared with simultaneous

laser Doppler measurements on the contra-lateral site during extended hypercapnia/hypocapnia, again showing good agreement between the two. We have demonstrated the first DOT and DCT images of ischemic stroke in rats due to middle cerebral artery occlusion (MCAO) [91]. The development of the ischemic hemodynamic response was monitored continuously in a large field of view ($\approx 10\text{mm}^2$) and the ischemic penumbra was imaged. The simultaneous measurement of blood oxygen saturation and relative cerebral blood flow allowed continuous imaging of CMRO_2. These measurements quantitatively demonstrated the need for multi-parameter imaging since the monitoring of only one parameter would not have allowed the distinction between hypercapnia, hypoxia and ischemia be made. Finally, the response of implanted mouse tumors to tumor necrosis factor (TNF) treatment was measured and compared to measurements with a Doppler ultrasound [258]. This instrument is referred to as "Generation I". I will describe some of these results in the following sections.

These earlier results have answered important design, physiological and technical questions regarding diffuse correlation tomography: (1) It is possible to design DCT systems with similar characteristics to previously employed DOT instruments. Therefore, development of similar measurement schemes are possible. (2) The reported blood flow changes, specially in the brain, agree very well with physiological expectations. (3) DCT is capable of penetrating through *intact skull* in animal models. This latter point distinguishes DCT from previously available optical methods for monitoring of CBF, such as laser Doppler flowmetry and laser speckle imaging.

These results have enabled the development of faster, more robust systems for the measurement of a large variety of physiological systems described in this thesis. Newer generations of instrumentation were developed in three, somewhat distinct directions, which I will now describe in brief details. The designs were chosen to address different physiological problems;

1. A portable, relatively fast (several seconds per frame), large field of view instrument was necessary for more advanced imaging of cerebral hemodynamics (e.g cortical spreading depression) in rat brains and monitoring of photodynamic therapy of RIF tumors. This was the first upgrade of the Generation I instrument. We have achieved this by optimizing the signal-to-noise, upgrading to faster optical switches and using a faster correlator board. This instrument was used extensively for the work described here, and is referred to as the "Generation II" device.

2. A highly parallelized, high spectroscopic content, large field of view, fast imaging instrument for imaging of rapid cerebral hemodynamics in rats and other small animal models was desirable. A full frame for such an instrument should be obtained in less than a second to image fast hemodynamics. It has to be able to distinguish oxy- and deoxy- hemoglobin as well as water concentrations accurately – hence the need for high spectroscopic content. It has to cover the whole brain (> 10 mm^2) and perform regional imaging. A modular design is necessary to combine fast tomographic abilities with even faster (up to 50 Hz) spectroscopic measurements. We were able to address these problems by combining frequency domain multiplexing (FDM) of the wavelengths with time domain multiplexing (TDM) of the source and detector positions for DOT. This instrument is now built and characterized and is referred to as the "Generation III" device. I will describe the DOT part of this instrument in great detail since it is a unique design and is descriptive of the earlier designs.

3. The sensitivity of the above instruments was optimized for small tissue volumes . However, in order to transfer these technologies to human tissues, we need to probe into deeper tissue layers. Therefore, it is necessary to use larger source-detector separations, which bears a

significant cost, in the achievable signal-to-noise. After doing a feasibility study in human muscles and brain, where for the first time, we have used the hybrid instrumentation to measure oxygen metabolism, a new instrument design was apparent. This instrument should be able to do basic spectroscopy with the ability to distinguish layered response while being adequately fast to monitor hemodynamics. A prototype was recently built where large diameter (3 mm) APDs and low noise equivalent power (NEP) PMTs were used with larger detection area fibers ($3 \sim 6$ mm) . DCT instrument was more challenging since the detection required single-mode fibers (diameter $\sim 7\mu$m at 800nm) and fast photon counting detectors. This was overcome by longer averaging times and parallelizing several detector channels. The signal-to-noise increase roughly as $\sqrt{N}$, where N is the number of correlation curves measured. This instrument was completed very recently and obtained very promising results in the human muscles and brain. It is currently capable of basic spectroscopy and is referred to as the "Generation IV" device.

In this Chapter, I first describe how to characterize the instruments and the common modules. Then, the design issues for each Generation is briefly outlined. Generation I instrument is used as the basis for the validation of the new DCT method. A basic phantom experiment is described as the validation and extensive *in vivo* validations are presented in the following Chapters.

3.2 Common Instrument Characteristics and Modules

All the instruments employed, had to be modular in design since we aimed to use them under a large variety of experimental conditions. Nuclear Instrumentation Bins (NIM BINs) were found to be ideal for this purpose. They provided reliable wiring for power supplies, robust mounts

and designs and most importantly, decent shielding against electro-magnetic fields. This latter point was particularly crucial for radio frequency (RF) circuitry used in the DOT instrumentation where RF leakage would have otherwise contaminated the signals. Therefore, the instruments were housed in a series of NIM BINs (Mech-Tronics, IL), and powered by stable, low noise DC power supplies (Astrodyne, MA). The pin-layout of the power supplies into each NIM BIN was also mostly kept constant.

Prior to designing and testing an instrument a set of goals which would define the minimum specifications had to be developed. We have roughly kept a common denominator for different generations of instrumentation while varying others such as the temporal, spatial and spectral information content. In order to assess whether a given instrument design met these goals, a set of tests were also needed.

3.2.1 Instrument Characteristics

1. *Stability:* All laser sources should have a long term ($>$ 3 hours) stability of less than 1% variation in signal amplitude. Furthermore, for the DCT , the probability of "mode-hopping" should be very low for many hours of operation. The optical switches and electronic attenuators must be repeatable with respect to light delivery levels and signal attenuation for similar durations of operation in order to achieve these levels of stability. This was assessed by operating the lasers, switches and attenuators for hours in a cyclic manner shining on a static phantom and measuring the transmitted DC and/or AC signals with photodetectors.

2. *Electronic and Optical Linearity:* These parameters were again defined empirically for the DCT instrumentation by repeated measurements. The fast, photon counting, avalanche photo diodes (APDs) employed are linear up to count rates of $\approx$ 10 MHz. However, it was

found that the correlation curves were distorted for count rates larger than $\approx$ 3.5 MHz. This provides about 30 dB of dynamic range in power. This range can be extended by the addition of optical attenuators which were used whenever necessary.

On the other hand, DOT instruments are characterized very thoroughly for electronic and optical linearity. Electronic linearity is defined to be the input RF signal range for which the output from the demodulators (explained in details below) is linear. This was tested by disconnecting the APDs and connecting a 70 MHz signal that is phase locked to the reference signal through a series of variable, electronic attenuators (Weinschel, MA). By varying the attenuation of the input signal, the output signal can be tested for linearity. The output signal is plotted vs input signal, both in units of dBm. The usable range was defined to be range where the deviation from the "linear line" (slope=1) is less than 1%. A single detection circuit was found to be linear in amplitude over a range $>$ 80 dB. The linearity in phase is harder to test, however, these attenuators are phase compensated and once a small calibration factor is applied at each step, it should stay constant. The linear range can be further constrained by specifying the standard deviation of the phase to be less than 1^o. This shortens the linear range by $< 10dB$.

Optical linearity is defined in a similar manner, this time the APDs are connected and are in contact with a thin diffusing medium. The input laser source is adjusted such that the read-out is well above the saturation level. A variable optical attenuator, either a manual one (Oz-Optics, Canada) or a series of electronic ones (Oz-Optics, Canada), are attached at the end of the source fiber before the medium. The output from the attenuator is split into two by an optical splitter (Oz-Optics, Canada) and one end is connected to a power meter. The manual optical attenuator is a better choice since it effects the phase minimally, however, it

is cumbersome to use and is very slow. The electronic attenuators on the other hand require calibration for the phase but can be controlled by a computer and a whole curve is obtained in a few minutes. The linear range is defined in the same way as above by plotting the output voltage (dBmV) vs input power (dBmW). Finally, once the center of the curve is roughly known, the detection fiber is fed into an optical power meter to calibrate the measurement of the input power to the detectors.

3. *Noise-Equivalent Power (NEP) / "Off-set Noise":* For the DCT instrumentation, the noise level was defined by the combination of APD and correlator board parameters. For our measurements, a signal of $\sim$ 10 KHz (photons per second) with $\sim$ 1 second averaging was empirically determined to be adequately above the noise level (signal-to-noise ratio $\gg 1$). Better signal-to-noise levels were achieved by averaging more curves (S/N improves as $\approx \sqrt{N}$) either by increased collection time or by bundling several fibers together. This is not equivalent to the definition of NEP but was nevertheless used.

   NEP for DOT instrumentation was defined by the "offset" and "offset noise" which are in this type of radio frequency circuitry derived from the voltage read-out when no sources were turned on. The offset noise ($\sim$5 μV) was minimized by careful shielding of all the components. An offset of < 1 mV was measured at the beginning of each frame and subtracted from the signal. The noise equivalent power (NEP) was determined by converting the offset noise level to units of power using the measured linearity curve.

4. *Interchannel Cross-Talk:* Interchannel cross-talk is not an issue for the DCT instrumentation as long as the detection fibers are isolated from each other and external lighting. This is achieved by a thick, black tubing around each single-mode fiber. It is, however, a major

design issue for the DOT since RF signals are employed. Each major part should be adequately shielded from external RF signals as well as against leakage out from the module. NIM BINs, coupled with a series of filters and chokes were employed to achieve good levels of isolation. This was tested by looking at the largest change in signal in other channels when the signal in one channel is varied through a large range. We were able to achieve < -40dBmW cross-talk even for the worst case scenario (the frequency encoded system).

5. *Phantoms:* The use of phantoms for testing various aspects of instruments and algorithms is commonplace in diffuse optics as in other modalities. We have tested each instrument and algorithm by liquid (Intralipid + ink + methyl cellulose) and solid (silicone + carbon black + TiO_2) phantoms. The optical and flow properties were varied and the ability to recover both the absolute and relative changes were tested. The details of these methods are described elsewhere [76, 89].

3.2.2 Common Modules

1. *Basic DOT Detection Module:*

   In-phase/Quadrature (I/Q) homodyne technique [399] was used for the detection of the amplitude and phase of the diffuse photon density waves. The basic detection module was mostly kept common for all the generations. The exceptions were the variation of a single detector channel in the Generation III instrument where a frequency encoding method was used. I will now describe a single detection module which is illustrated in Figure 3.1.

   I/Q technique was chosen because of its simplicity and low-cost. Many years of experience in our laboratory under different experimental conditions made this choice ideal for the development of this instrumentation. A 70 MHz, local oscillator (Wilmanco, CA) is

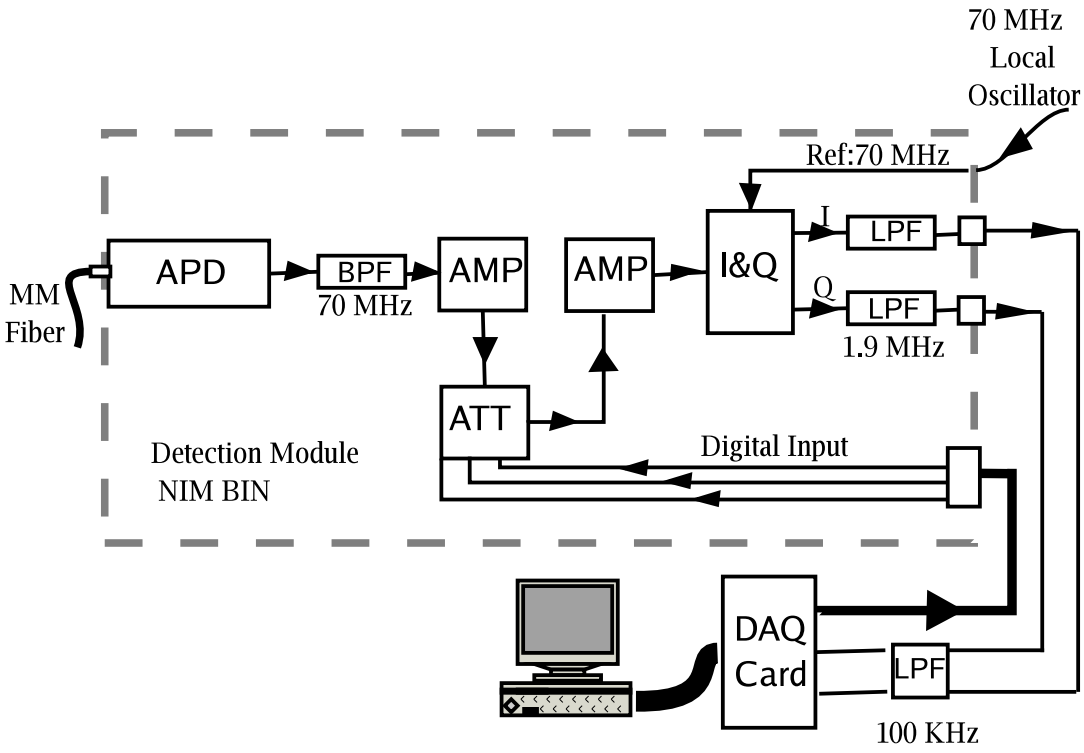

Figure 3.1: Basic DOT detection module.

used to drive the lasers and provide the reference signal to the I/Q demodulator (MIQY-70D; Mini-Circuits, NY). The signal is collected by a fast APD (C5331-03; Hammamatsu, NJ), band-pass filtered (70 MHz center frequency, SBP-70, Mini-Circuits, NY), amplified (ZFL-1000HLN, Mini-Circuits, NY), passed through a variable, electronic attenuator (ZFAT-51020, Minicircuits, NY), amplified again (ZFL-500HLN, Mini-Circuits, NY) and fed to the I/Q demodulator. The demodulator has a 0^o and a 90^o power splitter connected to a double balanced mixer. Thus, the phase-shifted and unshifted signals from the reference ($\sin(\omega t)$) and detector output ($A\sin(\omega t + \phi)$ are mixed and fed to two outputs as

$$\begin{aligned} I(t) &= 2A\ sin(\omega t + \phi)sin(\omega t) + I_o && (3.1)\\ &= Acos(\phi) - Acos(2\omega t + \phi) + I_o && (3.2)\\ Q(t) &= 2A\ sin(\omega t + \phi)cos(\omega t) + Q_o && (3.3)\\ &= Asin(\phi) + Acos(2\omega t + \phi) + Q_o && (3.4) \end{aligned}$$

where ω is the modulation frequency, A and ϕ are the output amplitude and phase, I_o and Q_o are the so-called "off-sets". These signals are then fed to a series of low pass filters (SLP-1.9, Mini-Circuits, NY) eliminating the parts oscillating at 70 MHz (see equation 3.4). Finally, they are digitized by two channels of a 16-channel 16-bit data acquisition board (PCI-6032E, National Instruments, TX). The off-sets are subtracted, amplitude ($\sqrt{I_c^2 + Q_c^2}$) and phase ($tan^{-1}\frac{Q_c}{I_c}$) are calculated. I_c and Q_c correspond to the off-set corrected signals. The whole unit, except the A/D board is housed in a 1 inch wide NIM BIN. High-quality, metallic, coaxial cables with gold SMA connectors are used to connect different components. The accurate measurement of the off-set with the sources blocked and keeping a low noise

in the off-set signal is crucial for the working of an I/Q system.

2. *Basic DOT Source Module*

   The source module consists a laser diode that is coupled to a F.C connectorized fiber and a driver circuit which takes the output of the local oscillator as input. There are two main requirements for the lasers: (1) the above-mentioned long term stability, (2) high modulation depth. The modulation depth is defined as the ratio of the amplitude of the AC part to the DC amplitude. The higher this ratio is, the more detectable signal is delivered to the tissues. Many factors effect this ratio and if not tuned to its optimal value, effects the stability of the system. There are many varieties of laser diodes and therefore each laser diode should be fine-tuned carefully. When using the single frequency system, it is possible to house several laser diodes and drives in a single NIM BIN to save space and weight. Otherwise, it is better to isolate each diode.

3. *DCT Detection Module*

   DCT detection module is fairly simple as shown in Figure 3.2. It is important to use high quality single-mode fibers that work in the right wavelength (800 nm) which are isolated from light leaks by thick, black tubing. The detector is a fast, photon counting APD (SPCM-AQR-14, Perkin-Elmer, Canada) with low dark current. The APD is factory-packaged with an amplifier-discriminator unit and outputs a standard TTL signal corresponding to the number of photons counted. This signal is fed into a custom build, fast, multi-Tau correlator board (Correlator.com, Bridgewater, NJ). These boards are software configured and are available in multi-channels (here 4 and 9 channels used). One curve is obtained every 106 ms. It is possible to read-out each individual curve or a longer average which is effectively

an average of many curves. The signal-to-noise ratio increases with the square root of the number of curves averaged. The multi-Tau technique [54] uses a quasi-logarithmic spacing of the temporal bins allowing collection of a large range of delay times with a limited (255) number of channels which is essentially equivalent to using 255 independent correlators with increasing delay times (doubled at each octave). They rely on the assumption that as long as the delay time is much longer than the sampling time, there is no need to sample the signal over time scales that are orders of magnitude less than the delay time. This can be characterized by the ratio of the delay time (τ) and the integration time over which the signal is averaged. This reduces the number of calculations to be made and is specially effective for long delay times. Correct choice of the bin spacing is important to avoid triangular averaging related errors and is defined by the correlator hardware. The above scheme , doubling the integration time at each octave (every eight bins) is common in hardware correlators. Finally, the output from all correlators is combined to obtain the desired autocorrelation function. This method improves the signal-to-noise while keeping a large dynamic range (in delay times) and therefore, the efficiency. Even though, there are recent attempts at making software correlators, the smallest delay times that are accurately measurable are still not optimal for the fast decaying autocorrelation curves in our measurements [235, 236].

4. *Other Modules*

   Many other modules are necessary depending on the complexity of the instrument. Several NIM BINs host the fast optical switches for wavelength and position switching. These switches are controlled by dedicated digital input-output (DIO, 777387-01, National Instrument, CA) boards. The connector boards are also hosted in dedicated NIM BINs. Other modules include low-pass filters, local oscillators and attenuators.

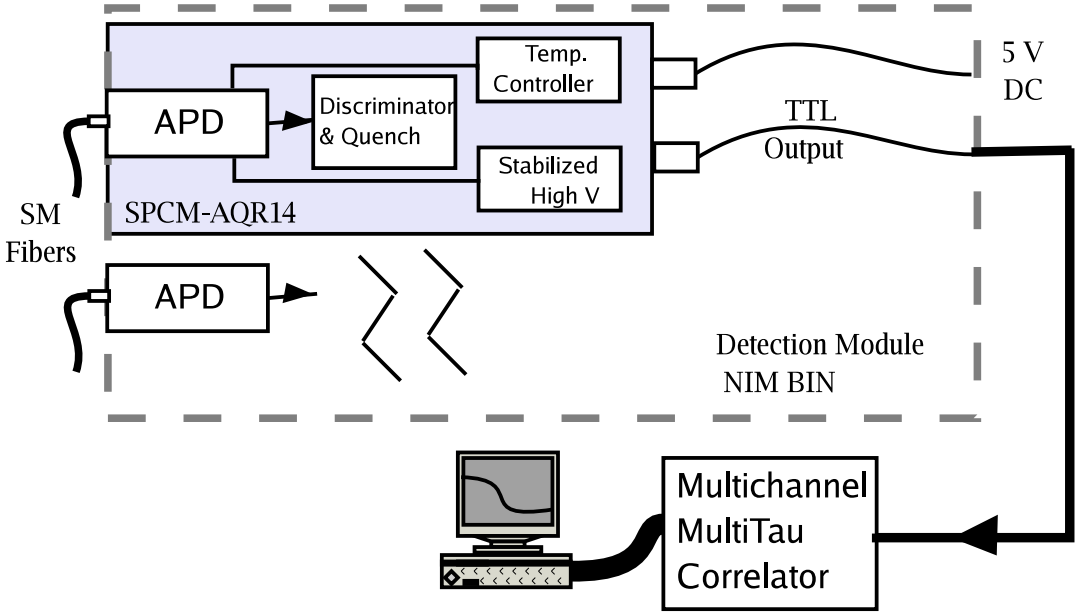

Figure 3.2: Basic DCT detection module.

3.3 Generation I: Hybrid Instrumentation/Non-Contact Probe

This system was first introduced by Cheung *et al* [76]. A frequency domain (70 MHz) diffuse optical tomography instrument with 12 source positions, 3 wavelengths (690nm, 786nm, 830nm) and four detector channels working in parallel were hybridized with a diffuse correlation tomography instrument with similar characteristics but with a continuous wave, long coherence length laser source working at 800nm. Source positions and wavelengths were multiplexed by a series of optical switches. A frame rate of 2.5 minutes per frame was obtained. Each DOT amplitude and phase were the result of averaging of one second, whereas autocorrelation functions were averaged for six seconds. A novel non-contact light-delivery/detection probe was developed and used in studies on rat brains and mouse tumors [76, 90, 91, 258]. The custom built probe with a grid-like pattern of source/detector fibers was mounted on the film-plane of a 35 mm camera body. The camera body acted as a light sealed, robust box to hold the lens system and the probe. DCT ($\approx 7\mu$ m) and DOT (1 mm) detection fibers were packed closely. The depth-of-focus of the camera lens

reduces the motional artifacts along the optical axis of the lens. Furthermore, in most probe designs cross-polarizers where used to eliminate surface reflections from the tissue. The non-contact probe is desirable when contact pressure must be eliminated or when sterile conditions are crucial. The source fibers were shared by the optical switches. The position switches used (Dicon, CA) took > 500 ms to change channels and settle. A schematic of the hybrid system and the non-contact camera probe is shown in Figure 3.3.

The DOT system was characterized and tested using the methods described above. It has conformed to the expected linear range, signal-to-noise and stability conditions. This DCT system was the first clinical, multi-channel, portable system that was employed extensively. The ability to characterize changes in flow or rather changes in the brownian motion of suspended particles was demonstrated in a liquid phantom by varying the concentration of methly cellulose concentration in an Intralipid-ink solution. Methly cellulose is a water-soluble polymer that increases the viscosity of the solution exponentially. This expected increase was measured by the DCT instrument (see Figure 3.4) [76]. The technique, in general, has been validated extensively on phantoms and simulations by Boas *et al* [37, 44]. Further, validations in *in vivo* measurements are described in following Chapters.

3.4 Generation II: Hybrid, Portable, Small-Tissue Imager

A portable, relatively fast (several seconds per frame), large field of view instrument was necessary for more advanced imaging of cerebral hemodynamics (e.g cortical spreading depression) in rat brains and monitoring of photodynamic therapy of RIF tumors. This was the first upgrade of the Generation I instrument. We have achieved this by optimizing the signal-to-noise, upgrading to faster optical switches and using a faster correlator board.

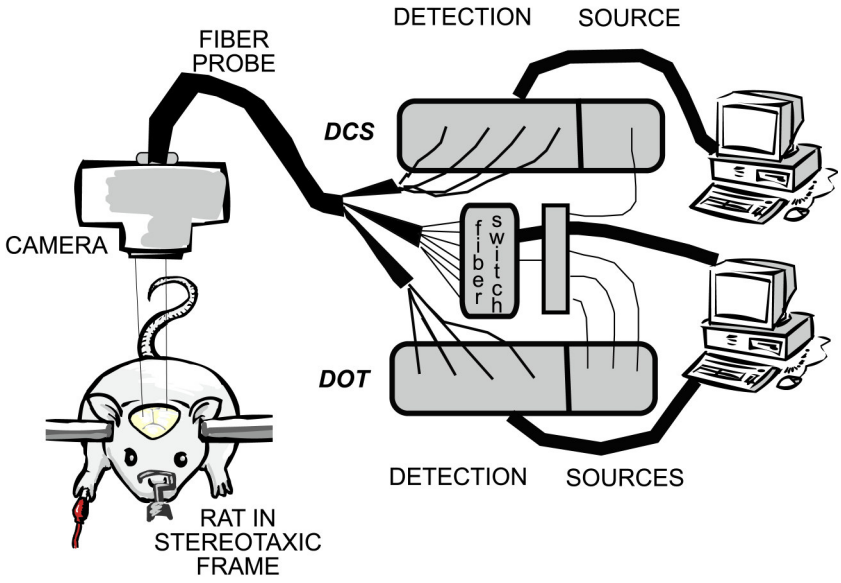

(a)

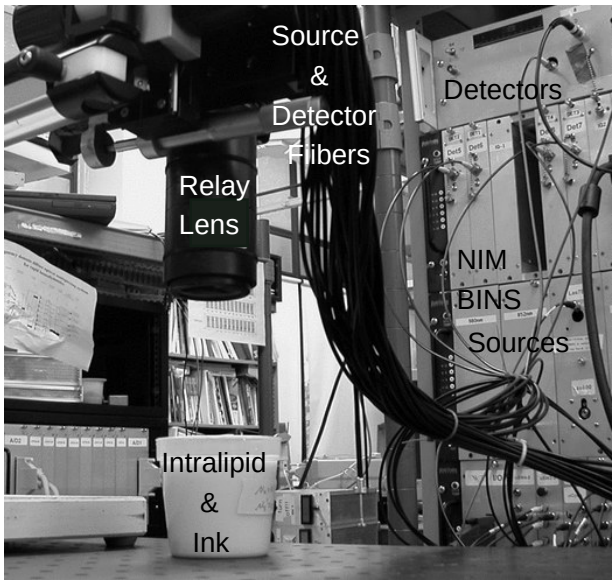

(b)

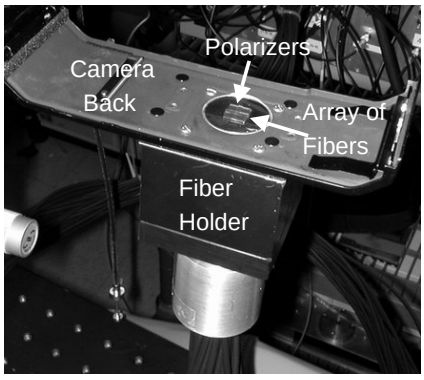

(c)

Figure 3.3: (a) A schematic of the hybrid system with the non-contact camera probe. A typical experiment on the rat-brain is shown with the rat on a stereotaxic frame. (b) A photo of the system showing the non-contact probe during measurement of an intralipid phantom with instrumentation NIM BINs in the background. (c) A close-up of the camera-back showing the fiber holder, the source and detector fiber array and the cross-polarizers.

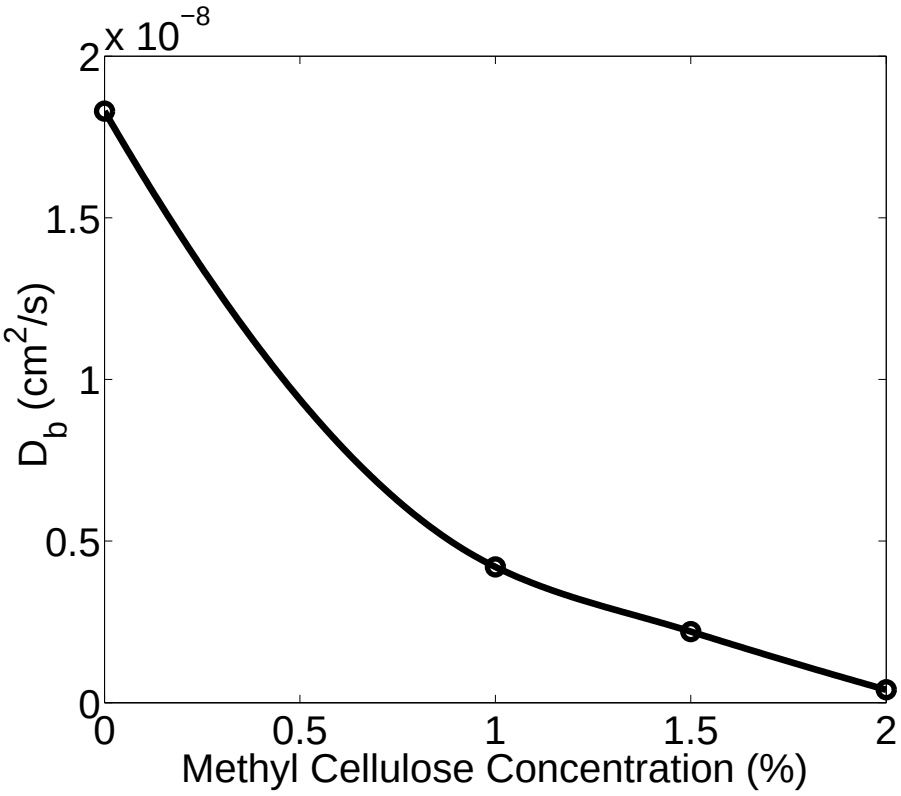

Figure 3.4: Decrease in D_B vs Methly Cellulose concentration follows the expected exponential curve. Data courtesy of Cheung [76].

The optical switches used for positional switching were upgraded to a series of faster 1x4 switches (switching time < 15 ms (Dicon, CA). The number of available positions was increased to 15. The averaging time was reduced to 20 ms for DOT and to 520 ms (rat brain, PDT) for DCT. A 9-channel correlator board that is controlled through the USB port was used along with five new APDs. Finally, three wavelengths (690 nm, 785 nm, 830 nm) and four detectors were available for DOT and one wavelength (800 nm) and nine detectors were available for DCT. Other characteristics such as the linearity and stability were kept constant. This instrument was used for rat brain studies reported in Chapter 4.2 and mouse tumor studies reported in Chapter 5.3.

3.5 Generation III: Frequency Domain Multiplexing System

This instrument was developed in two stages. First, a two channel prototype was built, characterized and tested in animal studies. Later, an 8 channel, 5 wavelength system was built. I will describe this system in more details than the others since the frequency encoding technique that was employed is unique to our system. The DCT part is same as Generation II. The advantages of this system are yet to be exploited in more extensive studies. This section is developed along the lines of our recent publication [407].

Previous generations of instrumentation used time-division multiplexing (TDM) which can be used to encode each source, detector, or wavelength, and thus perform many measurements nearly simultaneously to increase the data acquisition rate. Franceschini *et al* reported a fast imaging system in the frequency domain with eight source positions, two detectors and two wavelengths using 16 laser diodes [143]. Sixteen laser diodes (two wavelengths) were electronically time-division multiplexed (TDM) at a rate of 100 Hz (10 ms on-time per diode) yielding a frame acquisition

time of 160 ms (6.25 Hz). Wolf *et al* have recently reported a fast instrument working in the frequency domain with four source positions, four detectors and one wavelength utilizing the TDM method to change the source positions [392]. The sample rate for one frame was 96 Hz in this case.

In order to reduce the image acquisition time even further, several groups have employed frequency-division multiplexing (FDM) instead of the TDM to access source positions and/or wavelengths in their CW systems [216, 326, 339]. Siegel *et al* used the FDM technique to derive one CW image with eight source positions, eight detectors and two wavelengths in 0.5 second (2 Hz) [339]. Schmitz *et al* developed a similar CW instrument that provides one image with 25 source positions, 32 detectors and 1-4 wavelengths in 0.37 second (2.7 Hz) [326].

Prior to our instrument, Yang *et al* described the only frequency domain, FDM instrument which is a dual wavelength homodyne system that employs the FDM method to determine the optical properties of tissue [399]. They tested this system using Intralipid and ink, and they evaluated the accuracy of the instrument *in vitro* for determining hemoglobin saturation at a rate of one data point per minute with a single source-detector separation. The spatial, spectral and temporal resolutions of their system were inadequate for *in vivo* DOT. Nevertheless they demonstrated that the FDM technique could reduce the measuring time for frequency-domain devices significantly, at the cost of moderate increased expense and complexity.

With this instrument, we introduce a combination of TDM and FDM to acquire rapid images in the frequency domain. The FDM coding of spectral wavelength has no temporal skew; errors typically caused by channel-to-channel delay in the case of the TDM are reduced and the acquisition time is significantly shortened. We then combine this method with TDM to optimize instrument size and cost through sharing of detection electronics, electronic switches, and fast optical switches. Here I describe an extensive characterization of a prototype instrument which operated with three

wavelengths, six source positions and two detectors, achieving a full frame rate of 2.5 Hz with adequate signal-to-noise ratio during *in vivo* measurements of rat brain stimulation.

3.5.1 Instrument design

3.5.1.1 Frequency division multiplexing method

A schematic of our frequency domain multiplexing system is shown in Figure 3.5. The FDM method simultaneously codes for three laser diodes operating at 690 nm, 786 nm and 830 nm respectively. Each wavelength operates continuously, but at slightly different modulation frequencies ω_1, ω_2, and ω_3 around 70 MHz with modulation frequency differences of $\sim$30 kHz. The modulated light sources are combined and introduced into the turbid medium by optical fibers. The reflected/transmitted light from the turbid medium contains three signals and is detected by an avalanche photodiode (APD). Three in-phase and in-quadrature (I&Q) demodulators working at center frequencies ω_1, ω_2, and ω_3, are used to decode the superimposed signals in parallel. Two low-pass filters with an 80 Hz cutoff frequency were used to obtain the dc components, in-phase $I_{i-dc} = A_i \cos(\theta_i)$ and in-quadrature $Q_{i-dc} = A_i \sin(\theta_i)$, from the outputs of the demodulators. Here $i = 1-3$ represent particular wavelengths, θ_i is the phase shift, and A_i is the AC amplitude of the measured DPDW. The amplitudes and phases of the DPDW can then be determined as before.

3.5.1.2 Instrumentation

Figure 3.5 shows a diagram of the instrument. The instrument represents a compromise between temporal and spatial resolution. Based on these considerations as well as circuit simplicity, cost and instrument size we combined the FDM and TDM methods.

With the FDM method, three low noise RF signal oscillators (70 Hz, 13 dB; Wilmanco) drive

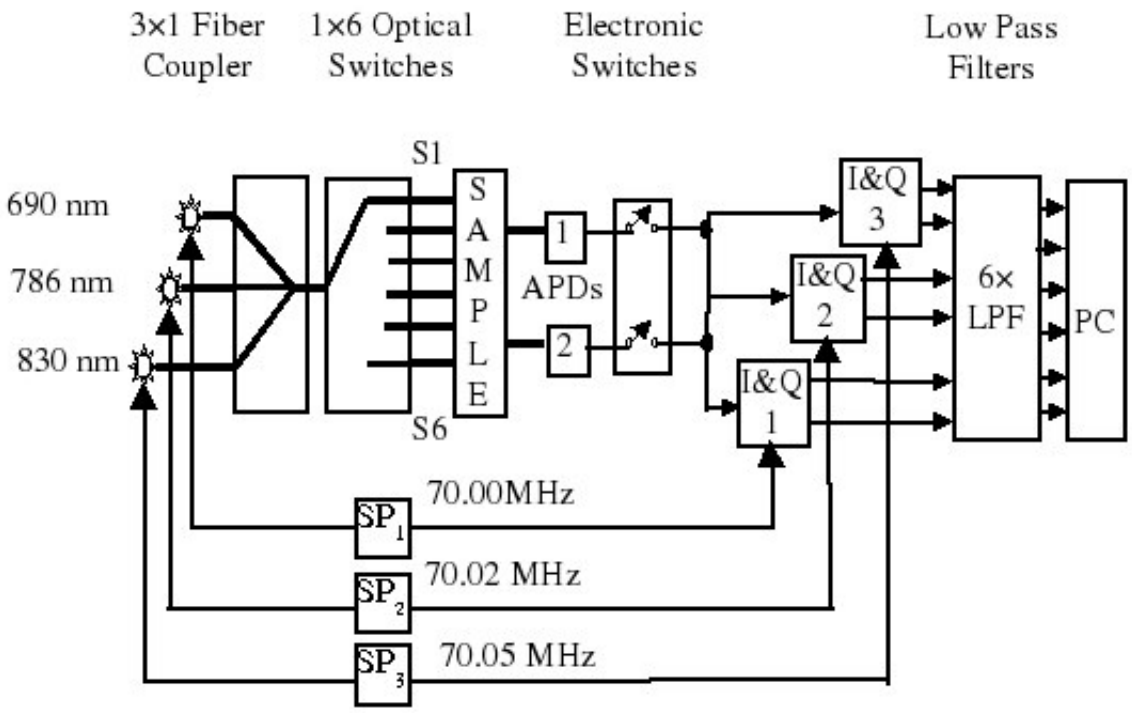

Figure 3.5: A frequency domain multiplexing system with 3 wavelengths (690 nm, 785 nm and 830 nm), 6 source positions (S1, S2, ... and S6) and 2 detectors (D1 and D2). Three oscillators (ω_1, ω_2 and ω_3) drive 3 laser diodes and provide the reference signals to 3 demodulators (I&Q 1, I&Q 2 and I&Q 3).

three laser diodes, 690 nm (HL6738MG, 30 mW; Hitachi), 786 nm (DL7140-201, 70 mW; Sanyo) and 830nm (HL8325G, 40 mW; Hitachi) at slightly different modulation frequencies (70.00 MHz, 70.03 MHz, 70.05 MHz). The modulated light is combined and switched into six source positions by an optical fiber coupler (C_TM-DL-01-0410-85-FC/FC; FOCI Fiber Optic Communications) and several fast optical switches (1×4 Prism switch, switch time $<$ 10 ms; Dicon Fiberoptics) (TDM method). The signal from each of the two APD's (C5331-03; Hammamatsu) is alternately switched to IQ demodulators using electronic switches (8000 serials/DIP Reed Relay, switch time $<$ 0.5 ms; Coto Technology) to reduce detection hardware costs and instrument dimensions. Each channel consists of three narrow-band I&Q demodulators (MIQY-70D; Minicircuits) to decode the three modulated signals. A pair of low-pass filters with a cutoff frequency of 80 Hz are connected with the output of each I&Q demodulator to filter out all high-frequency signals. The six channel signals (one detector channel $\times$ three decoders $\times$ two) are then digitized by a 16-channel 16-bit data acquisition board (PCI-6032E; National Instrument). One frame (three wavelengths, six source positions and two detectors) with signal averaging times of 20 ms can be obtained in less than 0.4 second with this new instrument. The data acquisition time per source-detector per wavelength of this instrument is a factor of 50 times shorter than that of our previous device [76]. The hardware was modularized according to function; for example, the lasers, detectors, switches, I&Q, and low pass filters, were kept in different nuclear instrumentation boxes (NIM BIN). NIM BIN modules adequately isolated radio frequency signals, keeping the instrument noise low. This design also provides flexibility for enlarging the number of source-detector pairs in the system by increasing the APDs and optical switches.

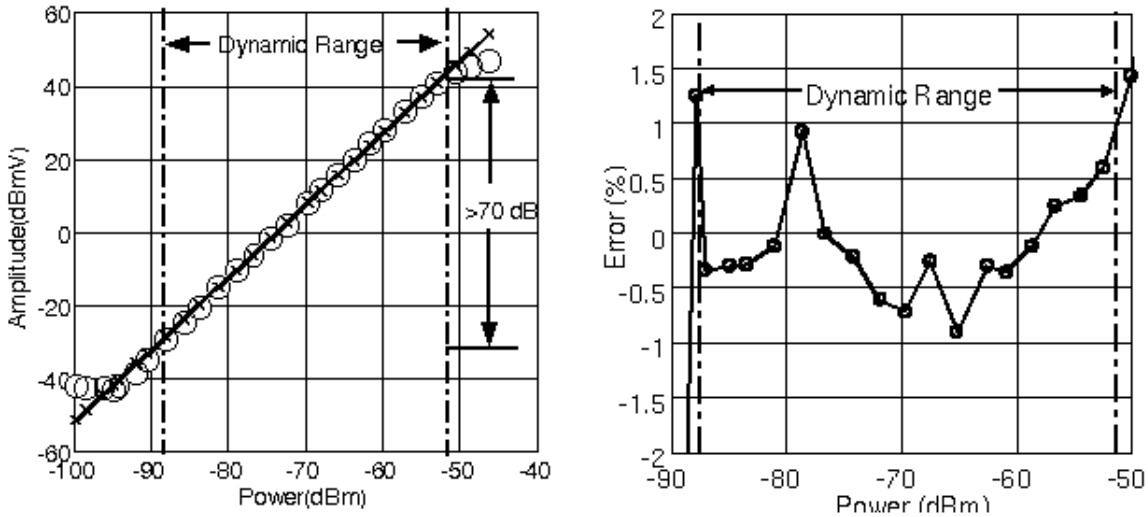

Figure 3.6: (Left) The dynamic range test result (measured amplitude vs power through medium) for the 785 nm wavelength (only amplitude is shown); noise level: $<$ -85 dBm, saturation level: -15 dBm, Dynamic range: $>$ 70 dB (amplitude in vertical axis). (Right) Percent deviation of amplitude from a least-squares-fit line (is less than 1%).

3.5.1.3 Instrument performance characteristics

The systems were characterized according to the recipe described in Section 3.2. The experimental evaluation of the prototype system performance is shown in Table 3.1. Figure 3.6 shows one measurement of the dynamic range (amplitude only, at 786 nm). The voltage range (amplitude in vertical axis) defines the dynamic range ($>$ 70 dB). Our noise equivalent power (NEP = 2 pW) is reasonable compared with the specified NEP of the APDs. A dynamic range of $>$ 70 dB is similar to other instruments [76] and is adequate for imaging the rat brain with our source detector arrangement ($<$ 50 dB, refer to Figure 3). The interchannel cross-talk of $<$ -40 dBmV is much less than the expected signal variations.

The prototype system was tested on an *in vivo* setting where the oxygenation and blood volume response to electrical stimulation was imaged and measured under two different conditions (see Appendix 3.8 for details).

Parameter	Value
Noise Equivalent Power	2 pW (rms)
Dynamic Range	$>$70 dB
Cross-Talk	$>$ -40 dBmV
Stability	$\pm 1\%$ in amplitude, $< 1^o$ in phase
Temporal Response	80 Hz

Table 3.1: Performance characteristics of the prototype system

3.5.2 Outline of a higher temporal and spatial imaging system

The modular instrument design makes possible the enlargement of our current system. Having successfully built and evaluated the instrument discussed above, we are now developing imaging systems with higher temporal and spatial resolution. This system combines FDM and TDM into one instrument with 5 wavelengths, 16 source positions and 8 detectors operating in the frequency domain. With the FDM method, five wavelengths (675 nm, 786 nm, 830 nm, 860 nm and 980 nm) are modulated at five different frequencies while with the TDM method, the modulated light is switched into 16 source positions by optical switches. Four detector channels are multiplexed to eight fiber coupled APDs using eight electronic switches (TDM) to cut down detection hardware costs and instrument dimensions. Each detection channel consists of five narrow-band I&Q demodulators to decode the five modulated signals. The total 40 channel signals (4 detector channels $\times$ 5 decoders $\times$ 2) are collected by a 64-channel 16-bit data acquisition board. One frame (5 wavelengths, 16 source positions and 8 detectors) with signal averaging times of the order 20 ms can be obtained in less than 1 second (1 Hz). This novel design provides great flexibility to balance the temporal resolution and spatial resolution as source-detector pairs can be easily selected by software without changing any hardware. Table 2 3.2 lists different possible temporal and spatial resolutions achieved by the Generation III system. The highest data acquisition rate depends on the measurement time for each source-detector pair and on the temporal response of the system

Number of λ	Number of Sources	Number of Detectors	Acquisition Rate (Hz)
5	1	4	50.0
5	1	8	25.0
5	9	4	2.5
5	16	8	1.0
5	45	24	0.16

Table 3.2: Temporal, spectral and spatial resolutions of Generation III system

(80 Hz). In order to reduce the noise level and increase the dynamic range of the current instrument, we use 20 ms (dwell time) to average the detected signal for each source-detector pair; thus, the highest data acquisition rate of our instrument is 50 Hz. The design is very modular allowing addition and removal of sources, detectors and wavelengths by simply swapping different NIM BINs.

We evaluated the performance of the Generation III system using the same method as described for the protoype and we achieved similar results shown in table 1: the NEP $<$ 10 pW, dynamic range $>$ 70 dBmV, interchannel cross-talk $<$ -40 dBmV. The instrument is further optimized and animal studies are underway for *in vivo* verification of the system efficacy.

3.6 Generation IV: Portable, Deep-Tissue Spectroscopy

A natural extension of our studies was to begin transferring the hybrid techniques to measurements on humans which was a new challenge because of the large tissue volumes to be probed. The DOT part of the problem is well known and we had significant expertise in that. In order to probe large volumes, it is necessary to use larger source-detector separations which is a significant cost in the achievable signal-to-noise. After doing a feasibility study in human muscles and brain, where for the first time, we have used the hybrid instrumentation to measure oxygen metabolism, a new instrument design was apparent. This new instrument should be able to do basic spectroscopy with

the ability to distinguish layered response while being adequately fast to monitor hemodynamics. The distinction of layered response is critical for tissues (muscles and human brain) we are interested in measuring, because there are thick ($\sim 0.5 - 1$ cm) overlayers.

These problems were solved by (1) adapting more sensitive detectors, (2) averaging more signals, (3) modelling the layered structure by phantoms and simulations, and finally, (4) by employing a large range of source detector separations. We have identified that the smallest separation should be around 0.5 cm while the largest should extend upto 6 cm (if possible). This last requirement necessitates either a larger dynamic range (both optically and electronically) or a mixture of different sensitivity detectors arranged on a carefully designed probe. A prototype was recently built using a mixture of detectors where large diameter (3 mm) APDs and low noise equivalent power (NEP) PMTs were used with larger detection area fibers ($3 \sim 6$ mm). DCT instrument was more challanging since the detection required single-mode fibers (diameter $\approx 7\mu m$ at 800nm) and fast photon counting detectors. This was overcomed by longer averaging time and parallelizing several detector channels. The signal-to-noise increases roughly as $\sqrt{N}$, where N is the number of correlation curves measured. This instrument was completed very recently and very promising results in the human muscles and brain were obtained. It is currently capable of basic spectroscopy and is refered to as the "Generation IV".

3.7 Few Words on Instrumentation

I have outlined the design and applications of four different generations of hybrid instrumentation. This work has taken the hybrid instrumentation a long way towards clinical applications. However, there are still challanges and opportunities for improvement.

DOT instrumentation has been developed in many flavours to which I have alluded in the Introduction (Chapter 1). Newer designs have been continously introduced improving signal-to-noise, temporal and spatial resolution and spectroscopic content. It is feasible to use ideas described in this work to hybridize those instruments with DCT. It is also feasible to combine DCT with other optical methods such as optical intrinsic imaging [146, 162–165] and laser speckle flowmetry [45,52,53,112,113] to take advantage of high resolution mapping of the surface hemodynamics and combine it with deep tissue capabilities of the diffuse optical methods.

DCT instrumentation is relatively new and therefore, it has not yet been exploited to its fully potential. Improvements in signal-to-noise ratio and spatio-temporal resolution are conceivable. Some ideas can be borrowed from the extensive literature of correlation spectroscopy and from literature of dynamic light scattering experiments in soft-condensed matter physics. It is now, important to review developments in other similar areas to compare and contrast to the opportunities offered by diffuse correlation spectroscopy. New technological advances in laser source and detector design also offer promise to develop more compact instrumentation.

3.8 APPENDIX: *In vivo* measurements of somatosensory cortex activation by forepaw stimulation on rat brains using Generation III system

In order to verify the system efficacy *in vivo*, we used the Generation III instrument to measure blood oxygen changes in the rat somatosensory cortex during periodic electrical forepaw stimulation.

Adult rats (300-350 g) were anesthetized with halothane (1 % to 1.5 %) in a mixture of 70 %

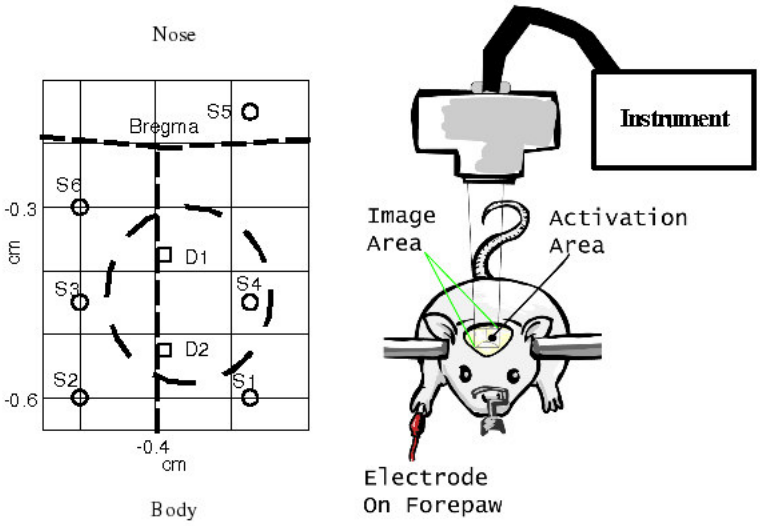

Figure 3.7: Scheme for measuring the oxy- and deoxy-hemoglobin concentrations in rat somatosensory cortex during periodic electrical forepaw stimulation. The left part of the figure shows the optical probe map with 6 source positions (S1, S2, .. and S6) and 2 detectors (D1 and D2).

nitrous oxide and 30 $\%$ oxygen. An arterial catheter was inserted to monitor the blood pressure and heart rate and a catheter was inserted into the femoral vein for drug delivery. The body temperature was maintained at 37^o C using a temperature controlled heating pad. After a tracheostomy, the animal was placed on a mechanical ventilator and the head was secured in a stereotaxic frame to reduce motion artifacts. The scalp was reflected to avoid the fur induced distortion onto the near-infrared signals. Following the surgical procedures, halothane was withdrawn and anesthesia was maintained with α-chloralose (60 mg/kg), followed by supplemental dose of 30 mg/kg every hour. A periodic electrical stimulation signal (5 Hz, 2.0 mA) was applied to the median nerve between the forepaw to produce a localized neuronal activation of the brain.

The source (circle) and detector (square) optical fibers assembled on a non-contact probe were arranged in a two-dimensional planar pattern as shown in Figure 3.7

Initially, measurements were taken at 2.5 Hz (frame acquisition rate) using six source positions and two detectors. A series of images were obtained to locate the response area stimulated by

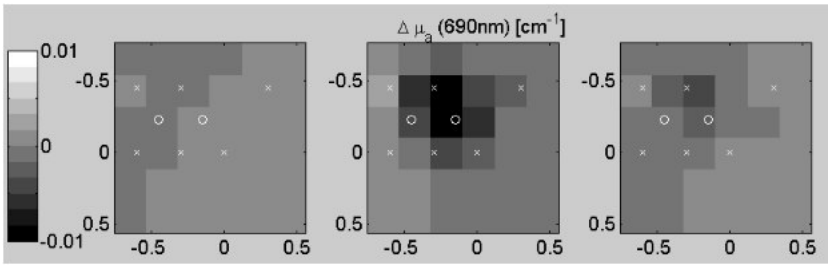

Figure 3.8: 2D images of absorption perturbation at 690nm, reconstructed at 2mm deep (from the top of the skull). Decrease in absorbtion at 690nm (due to decrease in deoxy-hemoglobin concentration) is apparent in the middle image shown at peak of stimulation. Left and right images correspond to baseline and recovery periods.

forepaw stimulation. Figure 3.8 shows three images of absorption coefficient changes at 690 nm before (-4 s), during (5 s at peak response) and after (25 s) forepaw stimulation (8 s stimulus duration with an intra-stimulus time of 30 s). The images show that the response area is at the area around the source position 4 (S4) and the two detectors (D1 and D2). When the source-detector pair was identified with a strong differential signal, further measurements were taken at 20 Hz using that source position and two detectors (i.e. S4, D1 and D2, $\sim$3 mm apart). Measurements at three wavelengths (690 nm, 786 nm and 830 nm) were used to extract hemoglobin concentrations and blood oxygen saturation.

Figure 3.9 shows the relative concentration changes of the HbO_2, Hbr and [HbT], induced by a series of stimulations. The stimulus duration was 8 s with an intra-stimulus time of 30 s. The stimulus frequency was 5 Hz at 2 mA. Data was collected at 20 Hz with one source and two detectors (S4, D1 and D2). The corresponding change of StO_2 is also shown. During the stimulation, the total hemoglobin concentration increased 5 μM - 7 μM from baseline, while the StO2 increased 9 % - 11 % relative to baseline. The average half-width half-maximum (HWHM) of the peaks was 4.5 seconds. The short duration, small amplitude response signal induced by

forepaw stimulation required the measurement system's high sampling rate, low noise and long-term stability. The results shown in Figure 3.9 demonstrate that our instrument was able to achieve good signal-to-noise ratio (SNR $>$ 10) and dynamic sampling (20 Hz).

We also measured the relative change of StO2 during periodic forepaw stimulation of either 8 seconds or 4 seconds. Figure 3.10 shows changes of StO_2 induced by two different stimulus durations (8 s or 4 s). Data was collected at 20 Hz with one source and two detectors (S4, D1 and D2). The average delay to response (DR), defined as the latency from stimulus onset to initial response, was 2 seconds for both of the two stimulation series. Note that longer stimulation (8 s) causes an activation response consisting of an initial peak followed by a plateau whereas the 4 seconds stimulation led to a peak response only. Increasing the duration of stimulation to 60 seconds produces a more prolonged response with a distinctive initial peak, followed by a plateau which slowly decreases toward the baseline level during the second half of the stimulation period (not shown). These temporal characteristics demonstrate the temporal resolution of our device and are consistent with studies using laser Doppler [103], O_2 microelectrodes [2] and laser speckle flowmetry (see Chapter 4.3). DOT has potential for 3D imaging which is a major advantage.

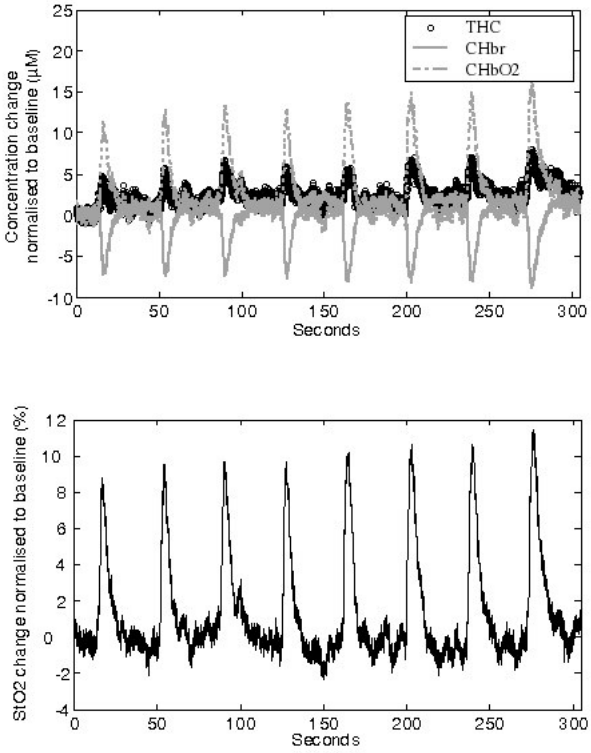

Figure 3.9: (Top) Concentration changes (relative to baseline) of HbO2, Hbr and THC for the serial stimulation. (Bottom) The change (relative to baseline) of tissue blood oxygen saturation (StO_2). The stimulus duration was 8 s with an intra-stimulus time of 30 s; stimulus frequency was 5 Hz at 2 mA. The sampling rate was 20 Hz using one source and two detectors (S4, D1 and D2). StO2 is given in percentage and concentrations are given in micromole.

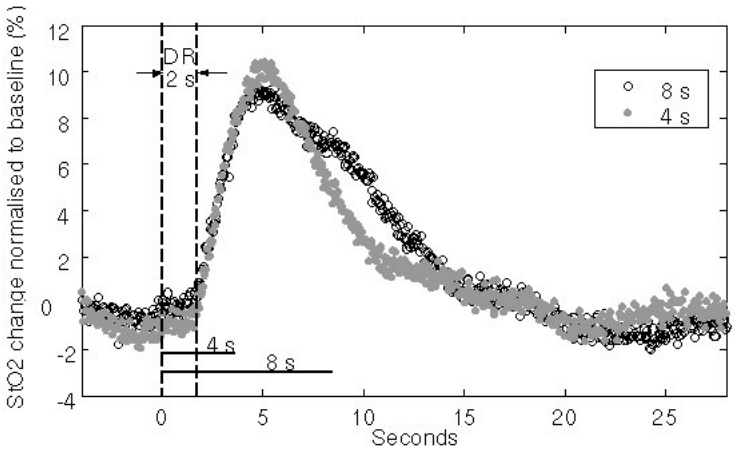

Figure 3.10: StO2 changes for 8 s (open circles) or 4 s (solid dot) of forepaw stimulation with 30 s or 34 s inter-stimulus interval. Stimulus frequency was 5 Hz at 2mA. The sampling rate was 20 Hz using one source and two detectors (S4, D1 and D2).

Chapter 4

Cerebral Hemodynamics

4.1 Introduction

The coupling between functional stimulation and regional changes in cerebral blood flow (CBF), often referred to as activation flow coupling (AFC), has been known for over a century, but is still poorly understood [232, 376]. Since most neuroimaging methods rely on AFC as an indicator of neuronal activity, a detailed characterization of AFC under normal conditions improves our understanding of normal as well as pathological brain physiology. Thus far numerous methods have been employed to measure blood flow changes in brain during functional activation, including positron emission tomography (PET) [141], single photon emission computed tomography (SPECT) [374], magnetic resonance imaging (MRI) [211, 219] , autoradiography [323] and laser Doppler flowmetry [4, 267], but there is still a need for relatively simple and inexpensive techniques with high spatial and temporal resolution. Changes in oxygenation are also a by product of AFC and relevant optical methodologies were reviewed in Chapter 1.

This Chapter focuses on optical measurements of cerebral hemodynamics in a developmental order (i.e. in order of degree of difficulty) from validation in animal models to translation of the technology to humans. The hybrid optical method was first used in rats for measuring global changes during hypercapnia and hypoxia, middle cerebral artery occlusion (MCAO) induced local ischemia, and cortical spreading depression under different ventilation states. A new instrument for Laser speckle flowmetry was also build and new analysis techniques were introduced characterizing the spatio-temporal response to forepaw stimulation in rats with high spatial resolution. Finally, an all-optical method was used to measure blood flow and blood oxygenation simultaneously in human brain through *intact skull* detecting a robust hemodynamic response to sensorimotor cortex activation by finger-tapping.

4.2 Diffuse Optical Measurements of Cerebral Hemodynamics of Rats

Rats have been employed as a model for the study of normal and diseased physiology for decades. Cerebral hemodynamics of the rat brain during functional activation and abnormal conditions is of special interest and provides valuable information for the understanding of cerebral physiology. To this end, we have conducted a series of experiments where we first validated the accuracy of the hybrid optical for measurements *through intact rat skull*, and then proceeded to investigate interesting physiological phenomena. We were able, *for the first time*, to obtain 3D, dynamic images of $CMRO_2$ by all optical methods through the intact skull. The basic set-up for these experiments is shown in Figure 3.3.

The hybrid optical method used, as previously mentioned, had several advantages over other

available methodologies: the measurements (1) were performed through the intact skull enabling long term studies without much discomfort to the animal, (2) have provided some amount of depth specificity several millimeters into the brain tissue, (3) have enabled low resolution imaging of hemoglobin concentrations, blood oxygen saturation, total hemoglobin concentration, blood flow and cerebral metabolic rate of oxygen extraction.

This section first describes previously published studies [76, 90] that validate the accuracy of our oxygenation and flow measurements during basic global alterations such as hypercapnia, hypoxia and cardiac arrest. Then imaging capabilities are demonstrated via dynamic images of several parameters including $CMRO_2$ during transient, focal ischemia. Finally, the effect of altering the cerebral pCO_2 on cortical spreading depression (CSD) is studied dynamically. It is shown that pCO_2 levels and previous episodes of CSD cause significant changes in brain metabolism during and after CSD. These findings can be significant in understanding and treating clinical cases where CSD-like phenomena play an important role such as in migraine headaches and ischemia. The last subsection describes the development of a Laser speckle flowmetry instrument for characterization of the spatio-temporal cerebral blood flow response to somatosensory cortex activation by forepaw stimulation.

4.2.1 Validation of Hybrid Measurements During Hypercapnia, Hypoxia and Cardiac Arrest

These results were published in two papers by Cheung *et al.* [76] and Culver *et al.* [90]. Global alterations of the cerebral oxygenation and flow were chosen as models as a result of their simplicity and robustness. In addition to those studies where blood gases were used to correlate the results, I have carried out a comparative study where a laser Doppler (LDF) probe was placed on

	rCBF (%)	rTHC (%)	ΔY_t (%)	rCBF/mmHg (%/mmHg)
Optical	77	17	16	2.1
Literature	74-130	12-40	n/a	2.0-3.5

Table 4.1: Comparison of hemodynamics measured by optical methods during hypercapnia and the data available from the literature. The comparison is done between relative changes and correspond to a 37 mmHg increase in $PaCO_2$ during hypercapnia.

the contralateral side of the brain to the hybrid probe during hypocapnia (reduced pCO_2). The Generation I instrument, with the novel non-contact, light-delivery/detection probe, was used as previously described in Section 3.3 and shown in Figure 3.3. The data was taken at a frame rate of 2.5 minutes per frame, where a frame consisted of twelve source positions, three lasers at three wavelengths for DOT and one long-coherence CW laser for DCT shared sequentially. Four DOT and four DCT detectors worked in parallel.

The first *in vivo* validation was carried on rat brains during extended hypercapnia. The relative cerebral metabolic rate of oxygen extraction ($CMRO_2$) was estimated [76]. It was shown that the results were in good agreement with the blood gas measurements of $PaCO_2$. Figure 4.1(a) shows changes in the cerebral blood flow (CBF), the total hemoglobin concentration (THC) and the tissue blood oxygen saturation (Y_t) during and after 8% CO_2 was introduced to the breathing mixture. As shown in Table 4.1, the $PaCO_2$ increased from 38 mmHg to 75 mmHg resulting in an average increase of 77% in CBF, 17% increase of THC and 16% increase of Y_t. The CBF increase corresponded to 2.1% per mmHg which is in the range of other measurements ($2.0 - 3.5\%$ per mmHg) of CBF increase due to hypercapnia [130, 131, 136]. THC measurements also fell within the range of other measurements ($12 - 40\%$) with microvascular techniques [23, 168, 377]. In another group of rats, a study including hypoxia, hypercapnia and cardiac arrest was carried on, again, showing good agreement with the literature and other measurable parameters [90]. Figure 4.1(b) shows changes in three quantities during hypercapnia, hypoxia and cardiac arrest. It is

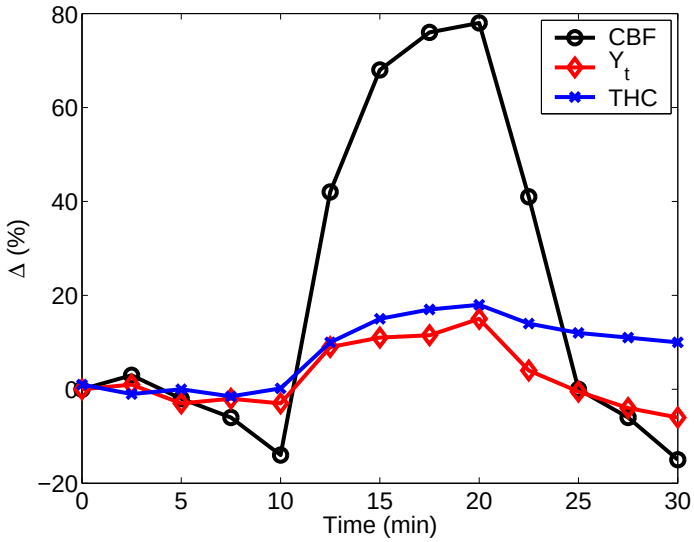

(a)

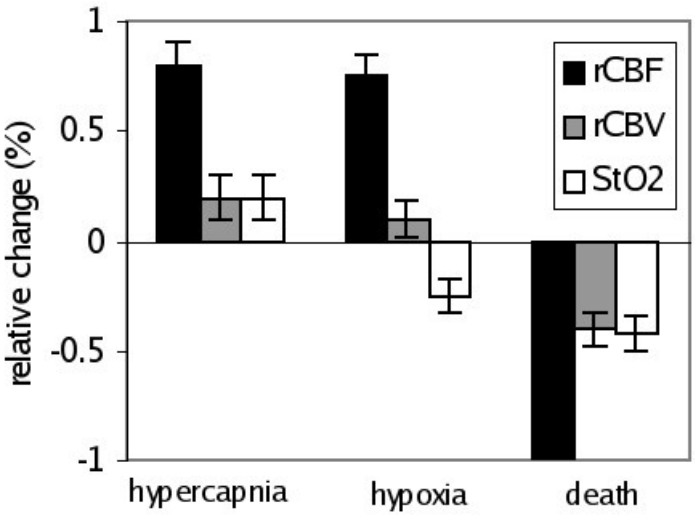

(b)

Figure 4.1: (a) Time course of changes in CBF, THC and Y_t during extended hypercapnia, (b) Relative changes during hypercapnia, hypoxia and death.

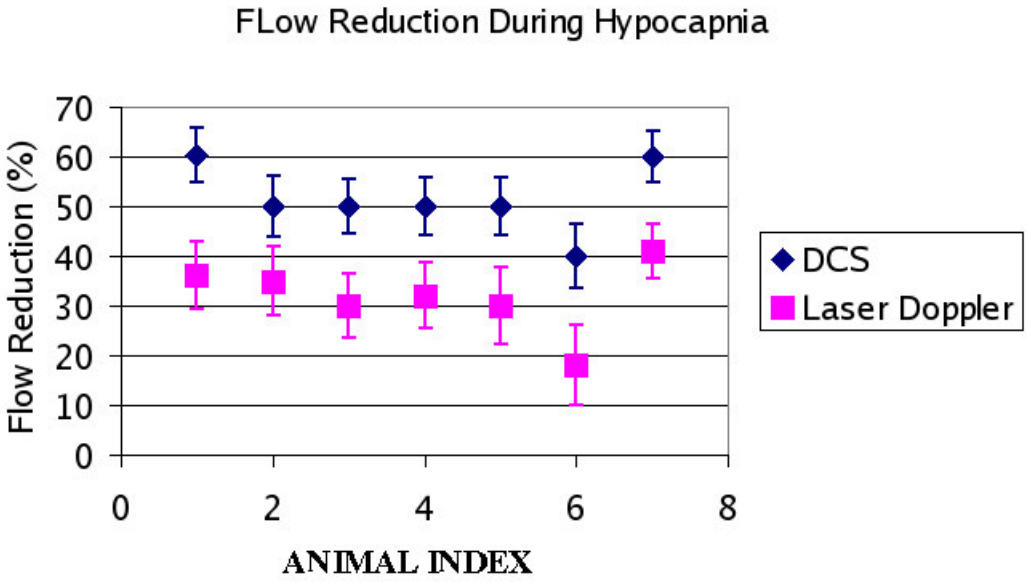

Figure 4.2: CBF changes observed by a single Laser Doppler (squares) probe compared to changes measured by DCS (diamonds) in seven animals. DCS found changes that are $10 \sim 15\%$ higher than LD.

interesting to note here that it is *not* possible to fully characterize these three manipulations using only a single parameter. It is useful to measure them simultaneously.

Furthermore, in yet, another set of animals, a standard laser Doppler (LDF) probe was placed on the contralateral hemisphere of the brain during extended hypercapnia and hypocapnia. The LDF technique has an information content similar to the correlation method. Since it is a frequency domain analog of the correlation technique. However, the commonly employed LDF methodologies are sensitive to surface tissues only because of the small source-detector separations employed, and their analysis is based on single-scattering models. Therefore, as expected, we did not observe absolute quantitative agreement between DCS and LDF except in the simplest of models. As seen in Figure 4.2, DCS found changes $10 \sim 15\%$ greater than those measured by LD during hypocapnia in seven animals, while both followed a very similar time course. These small absolute differences are tolerable and further studies may improve our understanding of them.

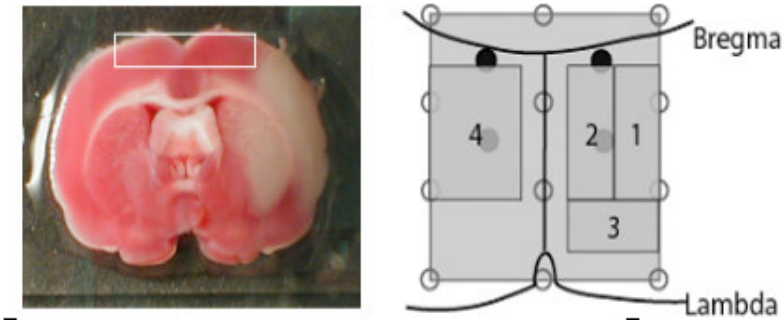

Figure 4.3: (Left) a brain section illustrating the imaging volume (rectangle) and the core infarct zone (light). The imaged tissue volume is right adjacent to core and covers the penumbra extending to the contralateral side. (Right) A schematic showing the bregma, the selected regions of interest and the source-detector lay-out.

4.2.2 Transient Focal Ischemia Induced By Middle Cerebral Artery Occlusion

4.2.2.1 Introduction

First DOT and DCS images were demonstrated on an ischemic stroke model in rats due to middle cerebral artery occlusion (MCAO). Here I briefly outline our results following Culver *et al* [91]. The development of the ischemic hemodynamic response was monitored continuously in a large field of view ($\approx 10\text{mm}^2$) and the ischemic penumbra was imaged. The simultaneous measurement of blood oxygen saturation and relative cerebral blood flow allowed continuous imaging of CMRO_2. Stroke physiology provides a widely studied heterogeneous hemodynamic and metabolic imaging model in rat brain. To date there have been few quantitative spatial-temporal studies of stroke pathophysiology based on diffuse optical signatures. The measurements were again obtained *through the skull*, and spanned brain tissue within the infarct volume, adjacent to the infarct volume, and just outside the infarct volume (penumbra). In addition an equivalent brain tissue volume on the contralateral side was probed, see Figure 4.3.

4.2.2.2 Animal Preparation

Adult male Sprague-Dawley rats weighing 300-325 g were fasted overnight with free access to water. They were anesthetized with a $1 - 1.5\%$ halothane, 70% nitrous oxide, 30% oxygen mixture. Catheters were placed into a femoral artery for monitoring of arterial blood pressure. Body temperature was maintained at $37 \pm 0.5^{\circ}$ C by a controlled heat pad. The animals were tracheotomized, mechanically ventilated, and the head was fixed on a stereotaxic frame. The scalp was reflected to avoid additional complications due to the fur. A custom stereotaxic stage was used which allowed the animal to be turned around for easy access for the MCAO occlusion. Blood gases were obtained at regular intervals.

Intraluminal suture occlusion was used to block the middle cerebral artery and induce focal ischemia [217, 231]. A nylon filament was inserted through the external carotid through the common carotid artery into the internal carotid artery until resistance was noted. The nylon filament was custom made with enlarged tip. Before the final advancement of the filament, inducing the ischemia, the rat was placed on the stereotaxic frame and twenty minutes of baseline was obtained. The acquisition was not stopped and the filament was further advanced and left in place for sixty minutes. Following sixty minutes of occlusion the filament was pulled back and allowed to reperfuse. After reperfusion data was acquired, the animals were sutured and returned to cages. Twenty four hours later, they were killed and the brains were removed and stained with 2,3,5 triphenyltetazolium chloride (TTC) following Takahashi *et al* [353].

4.2.2.3 Results

Histological analyzes confirmed focal ischemic damage on all rats, for example, Figure 4.3 shows a TTC stain of the infarct region. The white rectangle illustrates the volume reconstructed by diffuse

	rCBF (%)	ΔY_t (%)	rCMRO$_2$ (%)
Optical	42±4	11±4	59±4
Literature	20-30	7	70

Table 4.2: Comparison of hemodynamics measured by optical methods during ischemia and the data available from the literature. The comparison is done between relative changes.

optical methods. As expected, a volume adjacent to the ischemic core (penumbra) was imaged and an equivalent volume on the contralateral (undamaged) side was also covered. After images from all animals were averaged over the group, three time points, baseline (-16.8 to -11.2 minutes), occlusion ($+5.6$ to $+56$ minutes), and reperfusion ($+75.6$ to 92.4 minutes), are shown in Figure 4.4. The reconstruction volume shown, consists of a slice of tissue extending from 1.5mm anterior of bregma to 7.5mm posterior of bregma, from 4.5mm on either side of midline, and from a depth of 1.0mm to 2.5mm below the top of the skull (i.e. the upper $\sim$ 1.5mm of brain tissue). Time curves of THC ($[HbT]$), Y_t (StO_2), rCBF and rCMRO$_2$ (top to bottom) during MCAO induced ischemic stroke are shown from selected regions of interest are shown in Figure 4.5. The ischemic region is clearly visible as indicated by reduced CBF, Y_t and metabolism which recovers to baseline after reperfusion.

In the first region of interest (ROI-1) shown in Figure 4.3, the relative flow decreased to $42\pm4\%$ of baseline which, following reperfusion, rapidly increased close to the pre-ischemic levels. In peri-infarct regions, the flow decreased to 63% and 83% of baseline. Reperfusion was observed in all regions. The control hemisphere (contralateral side) did not show a significant change in blood flow throughout the experiment ($102 \pm 10\%$ of baseline). Oxygen saturation changes followed a similar trend with a largest change of $59 \pm 2\%$ in ROI-1. $rOEF$ in ROI-1 showed the largest change of 1.39 ± 0.06 as opposed to smaller ~ 1.29 change in ROI-2 and ROI-3. A small change was observed in the contralateral side of 0.89 ± 0.12. $rCMRO_2$ changes follow a similar pattern

with $rCBF$ in ROI-1 as 0.59 ± 0.07, in ROI-2 as 0.8 ± 0.1, in ROI-3 as 1.1 ± 0.11 and in ROI-4 as 0.87 ± 0.12. $rCMRO_2$ recovered to baseline following reperfusion. A summary of the comparison with the literature is shown in Table 4.2.

Again, the numbers obtained with the diffuse optical methods compare favorably with more established measurements of the same animal models using different experimental techniques. For example, the baseline measurements of tissue oxygen saturation (StO_2 or Y_t) were in very good agreement with the cryomicrospectrophotometric measurements of Weiss *et al* [386] and changes were comparable to the other cryomicrospectrophotometric measurements (i.e. $11 \pm 4\%$ compared to 7% [264]), as well as to PET measurements of relative oxygen extraction fraction-rOEF [181, 182]. Our measurements of relative cerebral blood flow, a decrease to $\sim 40\%$ of pre-ischemic levels, is somewhat less than the reduction to $20 - 30\%$ of pre-ischemic levels which is generally accepted as the standard response for this animal model [1,353]; however since we did not sample the core of the ischemic region completely, it is likely that our experiments measured a response that effectively average the ischemic region with penumbral regions. Similarly, our "calculations" of relative cerebral metabolic rate of oxygen consumption are in the same range as the cryomicrospectrophotometric measurements (~ 0.72 [264]) and similar PET studies in cat brain (which gave ~ 0.70 [181, 182]). Various approximations that effect these results are discussed in detail elsewhere [91].

With this investigation, the power of dual diffuse optical modalities is evident. In the long run it may be possible to assess tissue damage (and response to therapy) more effectively by following metabolic changes rather than oxygenation or flow by themselves.

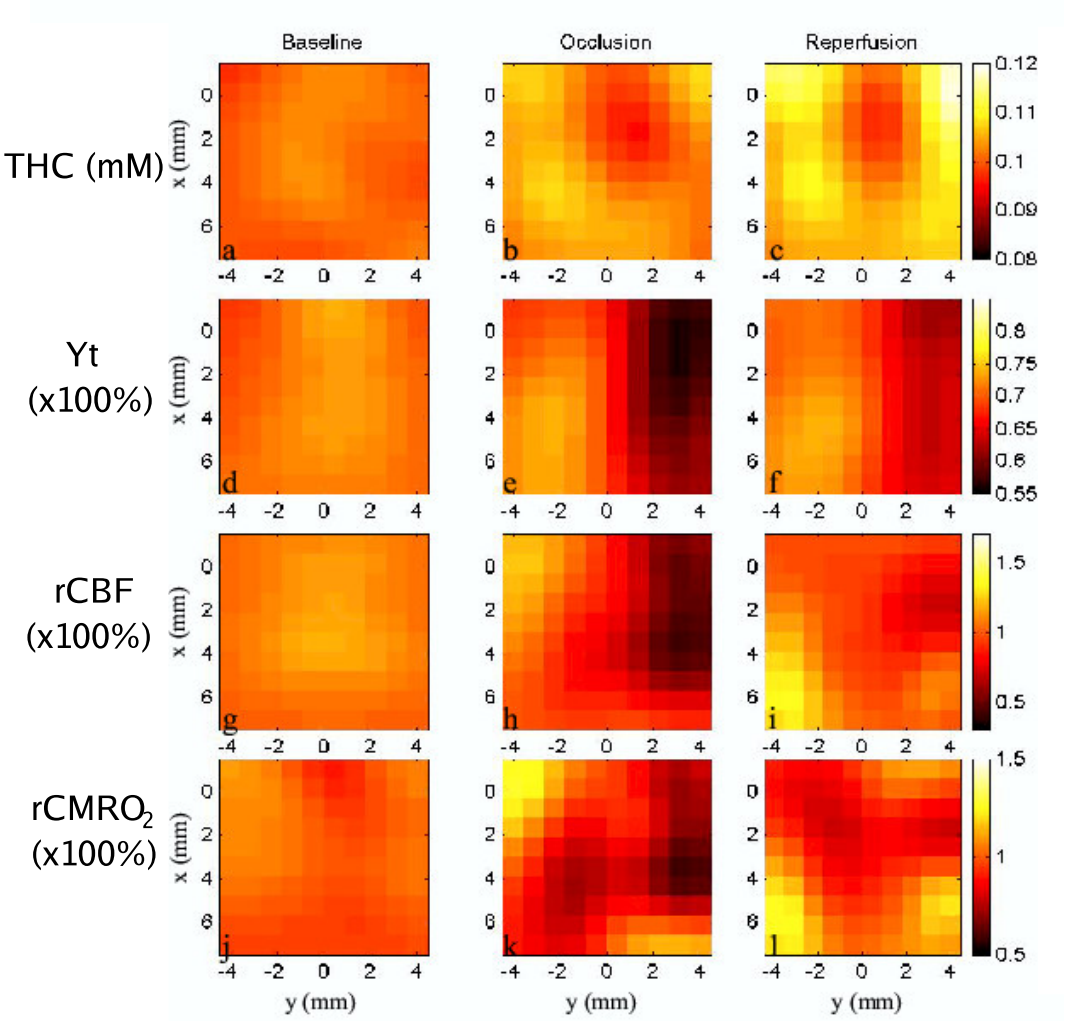

Figure 4.4: Images of THC, Y_t, rCBF and rCMRO$_2$ (top to bottom) during MCAO induced ischemic stroke are shown during baseline, occlusion and reperfusion (left to right). The ischemic region is clearly visible as indicated by reduced CBF, Y_t and metabolism.

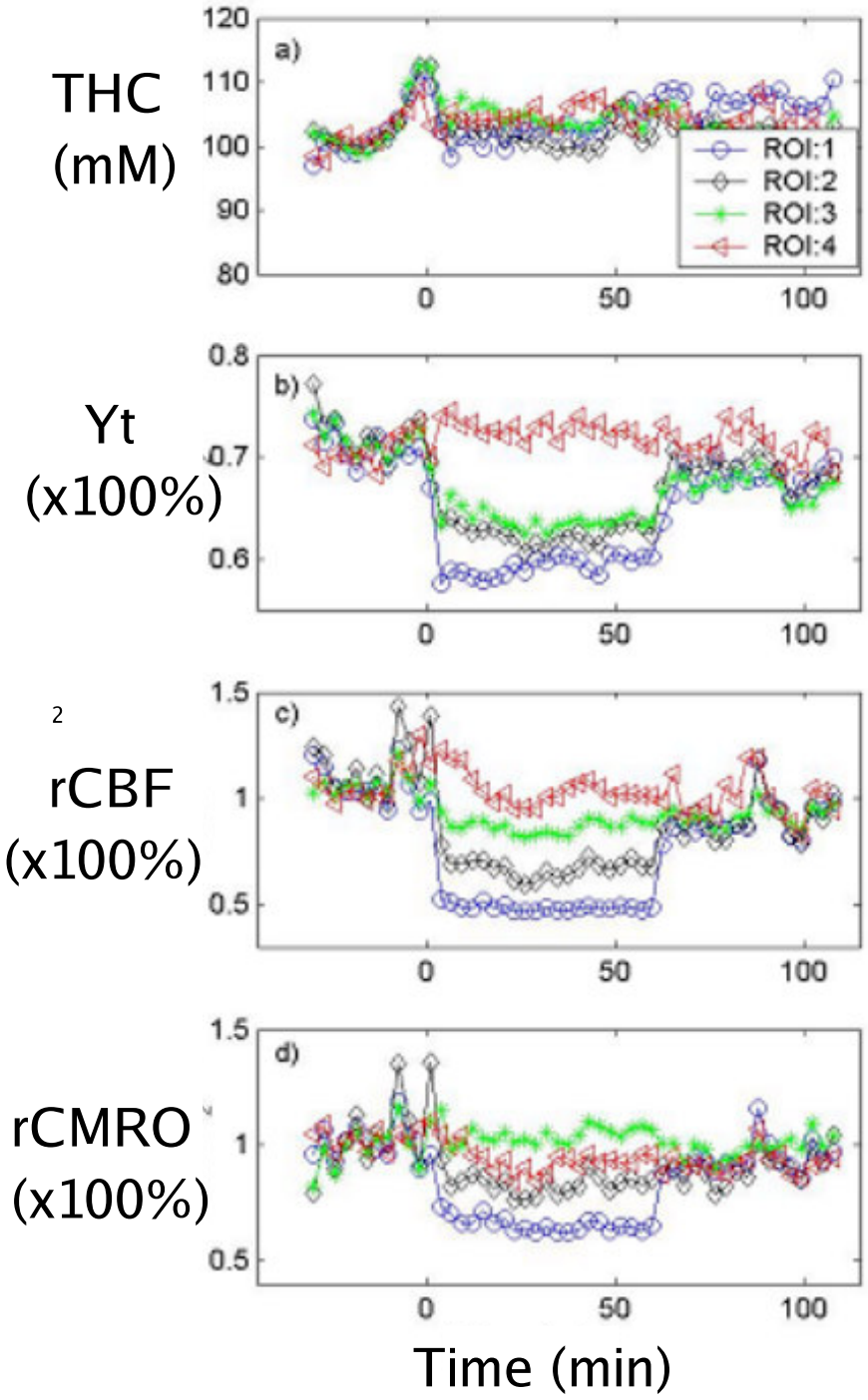

Figure 4.5: Time curves of THC, Y_t, rCBF and rCMRO$_2$ (top to bottom) during MCAO induced ischemic stroke are shown during baseline, occlusion and reperfusion from selected regions of interest. The ischemic region is clearly visible as indicated by reduced CBF, Y_t and metabolism. The recovery after reperfusion is also measured.

4.2.3 Cerebral Hemodynamics during Cortical Spreading Depression at different cerebral PCO_2

4.2.3.1 Introduction

Cortical spreading depression (CSD) was first related to migraine in 1944 by Leao [223] and has since gained considerable attention. It is a wave of excitations and depolarizations of neuronal cells that spreads radially at 2-6 mm/min over the cerebral cortex (Figure 4.6(a)) [1] It leads to temporary loss of specific cell function and is associated with migraine headaches and auras, peri-infarct depolarizations during cerebral ischemia which lead to increased damage and transient impairment of function. Furthermore, it has also been identified as a neuro-protector against ischemic damage and epileptic attacks – although the mechanisms are unknown. CSD was only recently observed in humans [251] and first MRI images of CSD during migraine were also obtained [171]. For an excellent review of the physiology of CSD see a recent review by Gorji [159]. Most of the physiological discussion I present is based on this paper. For a recent review of mechanisms of CSD see Somjen [344].

During CSD the neuronal ion pumps are activated, leading to increased metabolic activity and therefore a rise in oxygen demand. The recovery of CSD depends on energy metabolism and the status of cerebral auto-regulation. Normal tissue responds to this increase in demand by increasing cerebral blood flow. However, different oxygenation states of the tissue such as stroke, alter this metabolic-flow coupling. Mayevsky *et al* [345] studied the effect of brain oxygenation (hypoxia, partial ischemia) during CSD in rat brain using a multi-parametric probe. They found that during hypoxia, electrical and ionic responses were similar to that seen in normoxia, but the wave duration

[1] Here I concentrate on cortical spreading depression as opposed to spreading depression in general

was significantly longer and the recovery was slower. Similar results were seen during partial ischemia. They concluded that the metabolic and hemodynamic responses could be reversed (at least initially) during hypoxia. Measurements of cerebral blood flow and oxygen consumption during CSD indicate an increase in oxygen consumption was matched by a comparable increase in local blood flow so that substrate delivery was not limiting [250, 252]. This indicates that a parametrical approach to investigating the hemodynamic changes during CSD may reveal significant physiological information, i.e the speed with which CSD spreads, the duration of each depression wave, its amplitude, and the delay between each wave, measured through their hemodynamic signatures.

CSD causes very large changes in cerebral blood flow and relatively smaller changes in total hemoglobin concentration and blood saturation. We have induced CSD with KCl during different ventilation (hypocapnia, hypercapnia, normocapnia) states where the tissue partial pressure of carbon dioxide (PCO_2) is varied. This method was chosen since alterations of CO_2 cause changes in blood flow and other physiological parameters without changing $CMRO_2$. Using a model, along with the simultaneous measurements of total hemoglobin concentration (THC), tissue averaged blood oxygen saturation (Y_t) and cerebral blood flow (CBF), we estimate changes in cerebral metabolic rate of oxygen ($CMRO_2$) due to CSD during these different states (see Section 2.3). Both time course curves and three dimensional images are used for the analysis. These images are, to the best of our knowledge [2], the first three dimensional images of rCBF (and $CMRO_2$) using all optical methods. Finally, the observed hemodynamic response is parametrized as above and its correlation with PCO_2 status is investigated revealing strong effects on CSD peak-frequency and peak-amplitude but not on duration.

[2]Note that in our previous work we have segmented the brain into layers for analysis [91] and 3D imaging of oxygenation during forepaw activation was achieved by Culver *et al* [93]

4.2.3.2 Materials and Methods

4.2.3.3 Instrument and Probe

Near infrared spectroscopy was previously used to monitor CSD related changes [214, 393–395]. Our measurements with DCT and the hybrid instrument were the first of its kind. The Generation II instrument (see Section 3.4) was used; DOT with 15 source and 4 detector positions, and, DCT with 3 source and 8 detector positions (see Figure 4.6(b)). The fibers were arranged on the back of the non-contact probe and projected to the skull surface via a lens system. This non-contact probe (described in Section 3.3) enabled manipulations to the animal without movement of the probe, hence avoiding experimental artifacts. A full frame was acquired every ≈6.5 seconds. This arrangement optimizes the temporal resolution while providing enough source-detector pairs to enable dynamic, 3D imaging of the hemodynamics allowing us to investigate the spatial behavior of the CSD wave.

4.2.3.4 Animal Preparation

Adult male Sprague-Dawley rats weighing 300-325 g were fasted overnight with free access to water. They were anesthetized with a $1-1.5\%$ halothane, 70% nitrous oxide, 30% oxygen mixture. Catheters were placed into a femoral artery for monitoring of arterial blood pressure. Body temperature was maintained at $37 \pm 0.5^{\circ}$ C by a controlled heating pad. Blood gases were obtained frequently and the respirator was adjusted in order to keep the blood gases within the normal physiological range. The animals were tracheotomized, mechanically ventilated, and the head was fixed on a custom stereotaxic, frame. The scalp was reflected to avoid additional complications due to the fur. A 2-mm burr-hole was made over the frontal cortex of the right hemisphere leaving the

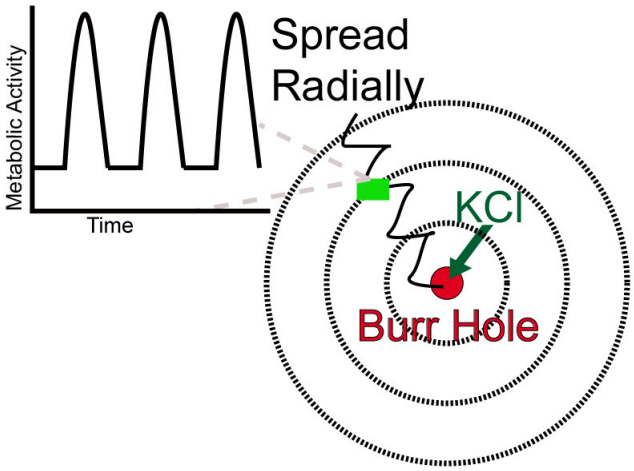

(a)

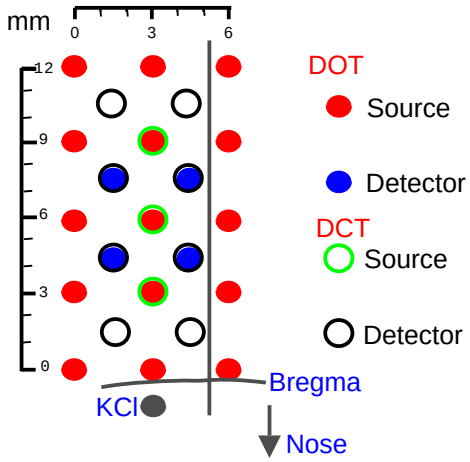

(b)

Figure 4.6: (a) CSD waves originate at the KCl placement location and spread out radially, (b) Sketch of the source-detector layout as projected on to the rat brain via the non-contact probe. Details are indicated in the Figure legend.

dura intact. CSD was evoked by placing a 1-mm^2 filter paper soaked in 2 mol/L potassium chloride (KCl) onto the dura for the duration of the desired induction of CSD-waves ($\sim$ 30 minutes). The paper was changed rapidly every 15 minutes. The set-up is illustrated in Figure 4.6. After measuring 5-10 CSD waves the KCL was removed and the brain was washed with saline. Some animals were made hypercarbic by placing them on 8-10$\%$ CO_2, or hypocarbic by increasing the rate of respiration. In those animals, CSD was induced seven minutes after the change in PCO_2.

A wide range of PCO_2 was observed and could roughly be classified into three main categories; normoxic ($[N]$), hypercapnic ($[H]$) and hypocapnic ($[h]$). Each category was measured on four different animals. Furthermore, in an additional set of four (n=4) rats, CSD was produced under normoxic conditions and hypercapnia was produced after three CSD waves were observed ($[\hat{H}]$). For each animal, at least two sets of CSD was induced producing different combinations. After the study, it became apparent that the second series of CSD was affected by the nature of the first series. The analysis of this effect is beyond this stage of the study so I do not present data from the second wave. We used the second series to qualitatively investigate the effect of PCO_2 on the hemodynamics by using the additional data.

4.2.3.5 Results and Discussion

Imaging of the Hemodynamics During CSD

Three dimensional (3D) images of relative cerebral blood flow, blood oxygen saturation and total hemoglobin concentration were reconstructed using methods described in Chapter 2. Specifically, blood flow images were obtained using the optimized data set and multi-spectral reconstruction was used for direct reconstruction of oxy- and deoxy-hemoglobin concentrations from which oxygen saturation and total hemoglobin images were derived. The flow data set was optimized by

considering the condition number of the weight matrix and by selecting the value of the correlation function at each source-detector pair based on this optimization criteria. Multi-spectral reconstruction uses all the data from different wavelengths simultaneously to directly reconstruct the chromophore concentrations. This has reduced inter-parameter cross-talk and improved the fidelity of the images as discussed previously.

The reconstructed volume extended $\pm$ 3mm in lateral direction (x), $\pm$ 6mm along midline (y) and 4mm deep from the middle of the skull (z) with $\sim$ 0.1 mm^3 voxel volume. A spatial dependent regularization was employed and the parameters were chosen with an L-curve analysis. Images of contrast-to-noise (CNR) which are obtained by dividing each image by an image of the standard deviation of the baseline were built [93]. These were then used to identify the regions of highest contrast for selection of regions of interest (ROIs). CNR increases contrast in the image and reduces artifacts due to source-detector coupling coefficients. These ROIs were applied to original images and time traces were obtained.

A series of example images corresponding to layers illustrated in Figure 4.7 of rCBF are shown in Figure 4.8. The burr-hole is located at the top, slightly to the left of the midline (roughly at x=0). Each panel is reconstructed by averaging over 0.5 mm ($\sim$ 2 reconstructed slices) in depth direction (z) at top of the skull, 0.9$\pm$0.25mm, 1.9$\pm$0.25mm and 2.9$\pm$0.25mm from top to bottom respectively. Images (from left to right) are shown every 20 seconds from immediately before KCl was applied until the end of the first CSD peak as shown in the time trace from a middle ROI in Figure 4.9(a). The panel titles indicate the corresponding time point in this figure. Along the surface of the cortex ($\sim$ 1 mm deep), a strong increase in blood flow appears from the top and proceeds to the bottom. After the peak, there is a sustained decrease in blood flow which covers the most of the image area. The sustained decrease was observed previously [159] and

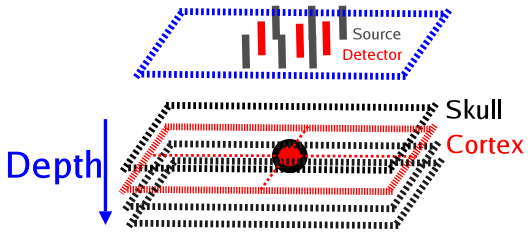

Figure 4.7: 3D Imaging Geometry for CSD showing the reconstructed layers. Elevated blood flow region is indicated by the filled circle.

is compatible with the inhibition of the neuronal activity. Lauritzen studied [221] this effect in detail under different PCO_2 conditions and concluded this hypoperfusion is due to a vasconstrictor stimulus which is stronger than the pH related effects of brain CO_2. It is important to point out here that no significant activity is visible in the top panel, which corresponds mostly to the skull and in the bottom panel which penetrates below the cortex (although, the lessened sensitivity of the optical method accounts for some of this). On the bottom part of the cortex, a CSD-wave is visible but of much lower intensity. Figure 4.9(b) shows the dependence of maximal rCBF on depth using the same middle ROI as before. The maximal change occurs around 1mm deep from the surface of the skull which corresponds to the surface of the cortex. The peak spreads $\pm$ 0.5mm around the surface as expected from the broadening due to the diffuse nature of photons. There is no significant change at the surface and in deeper regions. Clearly, 3D information was revealed by this method. Similar observations are made in images of changes in hemoglobin concentrations and $CMRO_2$.

Figure 4.10(a) shows oxy- and deoxy-hemoglobin changes during CSD in normoxic conditions. Same region of interest was used as in Figure 4.9. Oxy-hemoglobin increased more than de-oxyhemoglobin decreased, leading to an overall increase in total hemoglobin concentration suggesting hyperemia [395]. These changes were much smaller than changes in CBF.

Figure 4.10 shows the obtained changes in $CMRO_2$ from the same ROI. There are strong

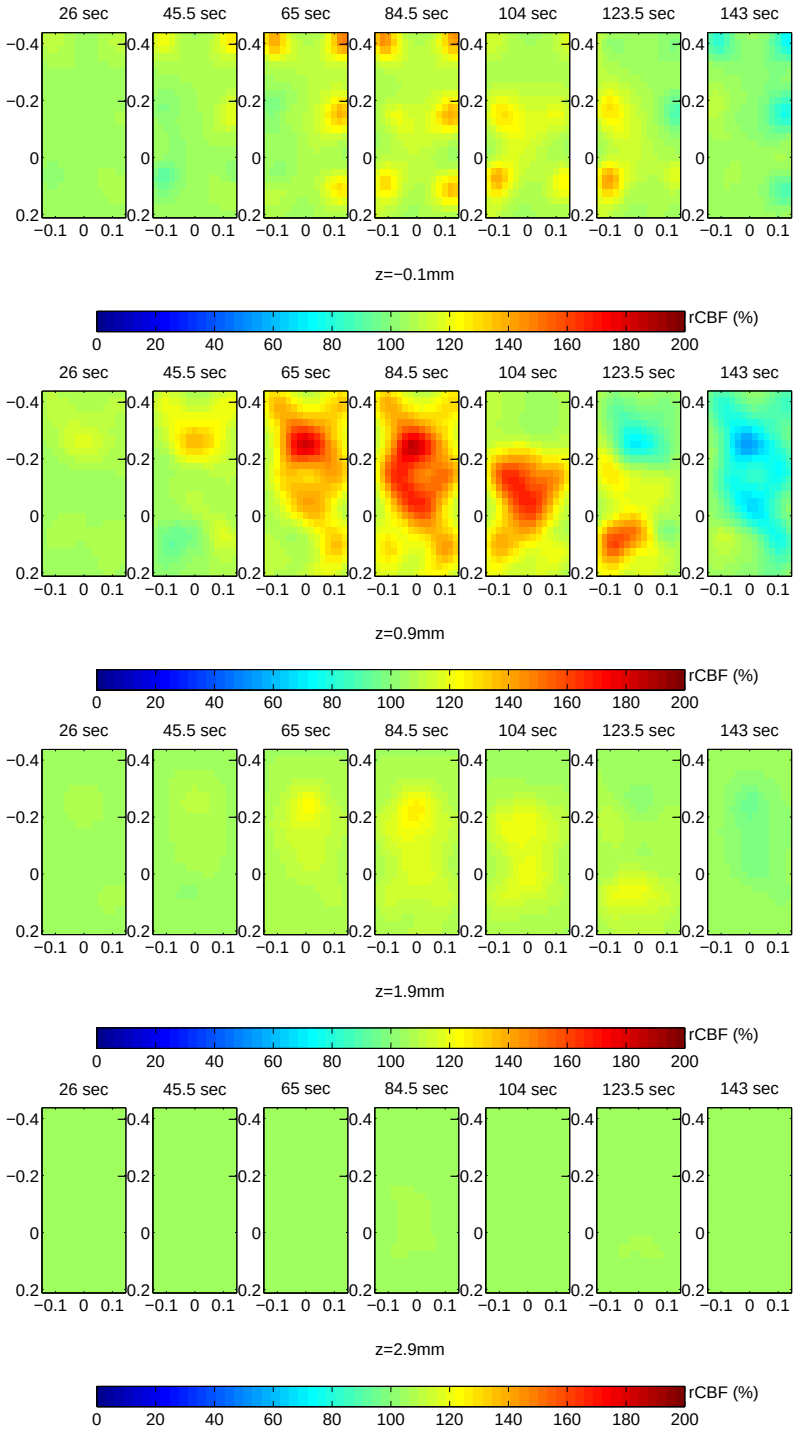

Figure 4.8: Images at selected time points at different depths; from top to bottom, surface of the skull,, 0.9±0.25 mm, 1.9±0.25 mm and 2.9±0.25 mm deep into the brain.

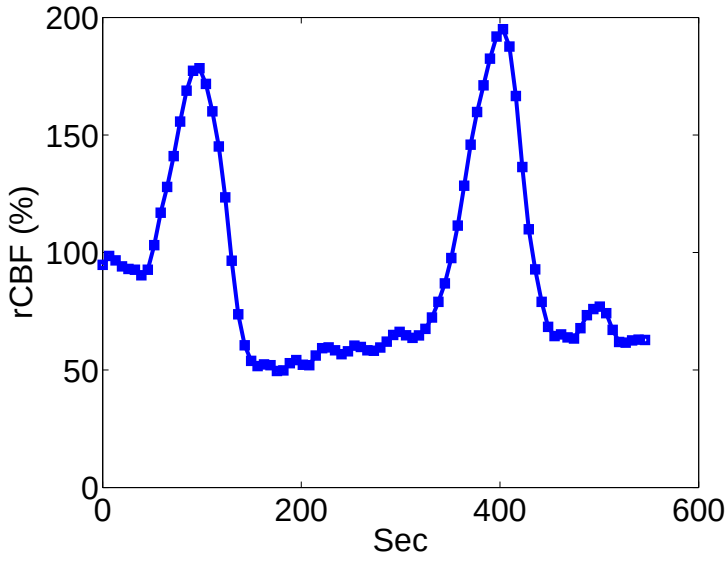

(a)

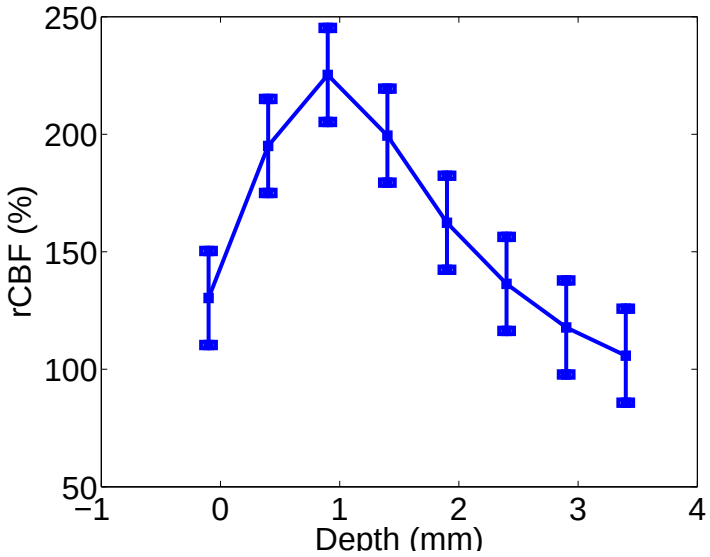

(b)

Figure 4.9: (a) $rCBF$ temporal profile from a central region of interest. (b) Dependence of maximal $rCBF$ on depth, from same region of interest.

changes in oxygen metabolism as expected which are potentially de-coupled from changes in CBF (compare Figure 4.9(a) and Figure 4.10(b)). The observed changes are in quantitative agreement with multi-parametric, point measurements of others [250, 252]. The uncoupling was previously studied in the context of the glucose consumption and an impairment of the coupling was observed following CSD [222].

Effect of Brain PCO_2 On CSD Hemodynamics

Figure 4.11 shows the time traces under three different ventilation states. We use the normoxic state (Figure 4.11(a)) as a reference. As seen in Figure 4.11(b) hypercapnia led to a sustained increase in blood flow consistent with results described in Section 4.2.1. Once CSD was induced, peaks that appear different than normoxic state are visible on top of an elevated flow baseline. However, unexpectedly, hypercapnia (increased PCO_2) led to two distinct behaviors. Figure 4.11(c) shows the variant behavior which was visible in roughly 50% of the series. In this variant behavior, once KCl was applied the flow dropped down from its elevated state to near the baseline and CSD peaks are visible over this new baseline. This is an interesting hemodynamic response which is currently being studied further. In the hypocapnic state, the behavior was simple, the blood flow was reduced due to the onset of hypocapnia and yet more different hemodynamic responses are visible in this lowered baseline (see Figure 4.11(d)). Note, for this qualitative analysis we used secondary (even tertiary) CSD series which are qualitatively in agreement with the primary series.

In order to quantify these observations, we have parametrized the observed hemodynamic response and described it by three parameters (1) peak-duration based on the full-width at half maximum, (2) peak-amplitude as the maximal change, (3) peak-frequency as the inverse of the mean time between peaks. At least three peaks are identified for each CSD series prior to the removal of

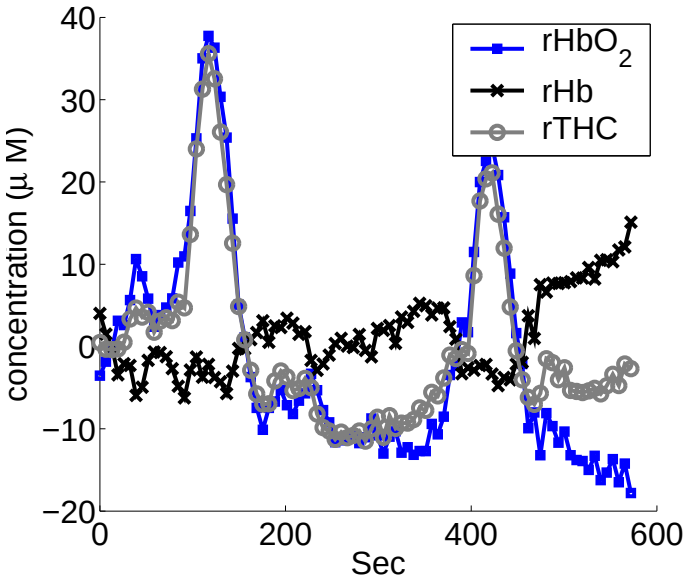

(a)

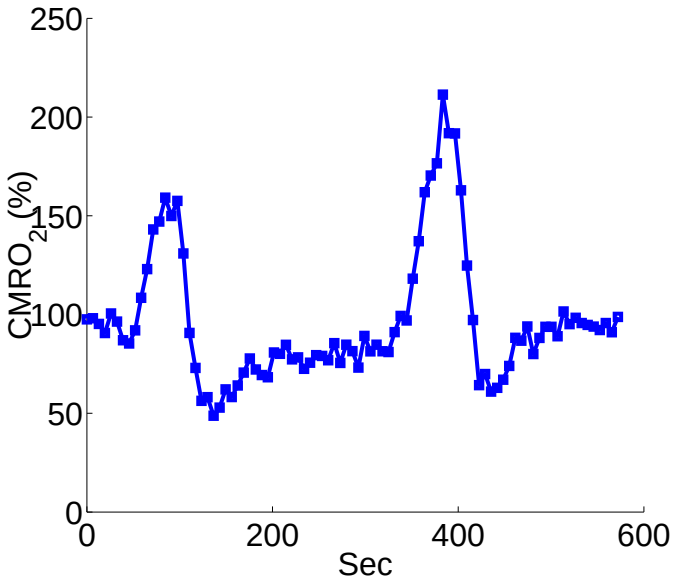

(b)

Figure 4.10: (a) Changes in oxy- and deoxy-hemoglobins and total hemoglobin concentration, (b) changes in $CMRO_2$. Both curves obtained using the same ROI as in Figure 4.9

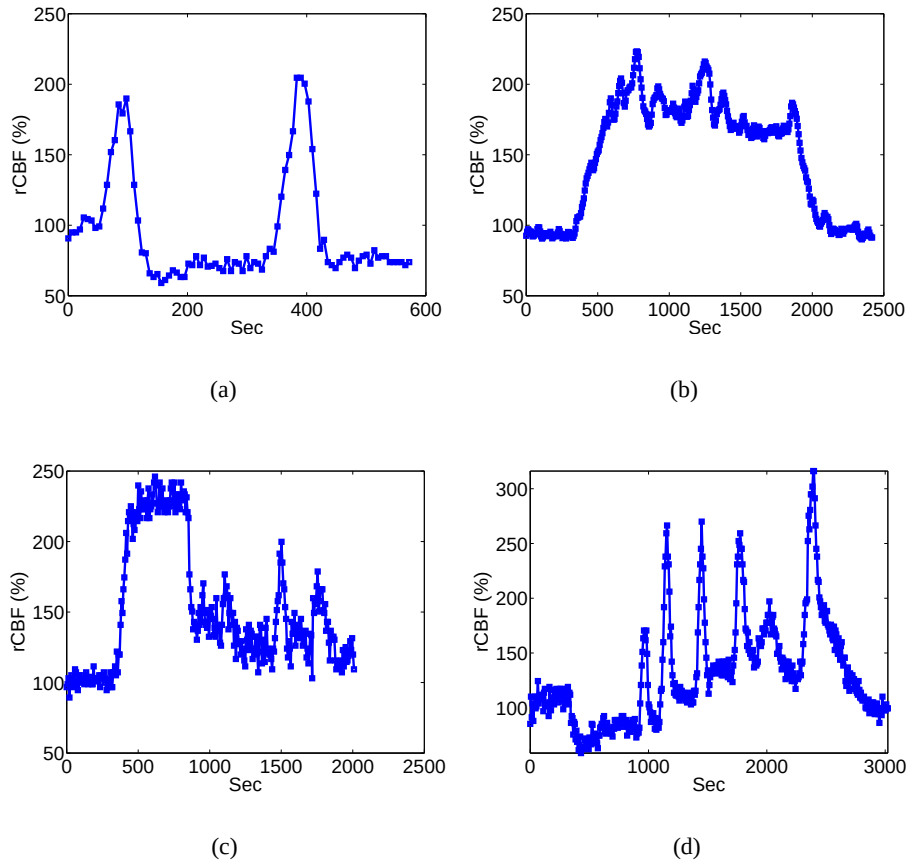

Figure 4.11: $rCBF$ for CSD under different ventilation states; (a) normoxia $[N]$, (b) hypercapnia $[H]$, (c) variant of hypercapnia $[H]$, (d) hypocapnia $[h]$.

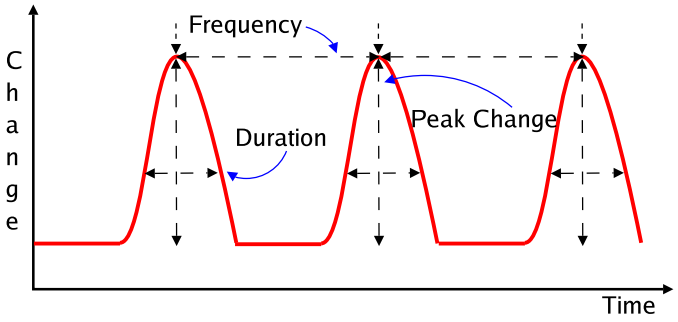

Figure 4.12: Hemodynamic response to CSD is parametrized and described by three parameters; (1) peak-duration based on the full-width at half maximum, (2) peak-amplitude as the maximal change, (3) peak-frequency as the inverse of the mean time between peaks. At least three peaks are identified for each CSD series prior to the removal of KCl and the mean values are reported.

KCl and the mean values are reported. Figure 4.12 illustrates this process. This generated twelve parameters (three parameters for each of the following; rCBF, ΔHb, ΔHbO_2, $rCMRO_2$) and we identified four representative ones for further study. Figure 4.13 shows effect of PCO_2 on rCBF. As seen in Figure 4.13(a) and Figure 4.13(c) peak-amplitude (in qualitative agreement with Wolf *et al* [394]) and peak-frequency depend inversely (R=-0.8 and R=-0.72 respectively) on the brain PCO_2. However, peak-duration is independent (R=0.1) of PCO_2 (Figure 4.13(b)). Interestingly, peak-amplitude of $rCMRO_2$ was also independent (R=-0.07) of PCO_2 level (Figure 4.14). Although, more work is necessary to ensure that the observed large deviations in peak $rCMRO_2$ is not effected by different signal-to-noise in measurements of blood flow and oxygenation.

4.2.3.6 Conclusions

We obtained first three dimensional images of $CMRO_2$ using all optical methods in rat brains by combining 3D images of rCBF and hemoglobin concentrations by use of a model. Images obtained during cortical spreading depression under different ventilation states, i.e different cerebral PCO_2 revealed significant dependence of hemodynamic parameters on PCO_2. These results may help to

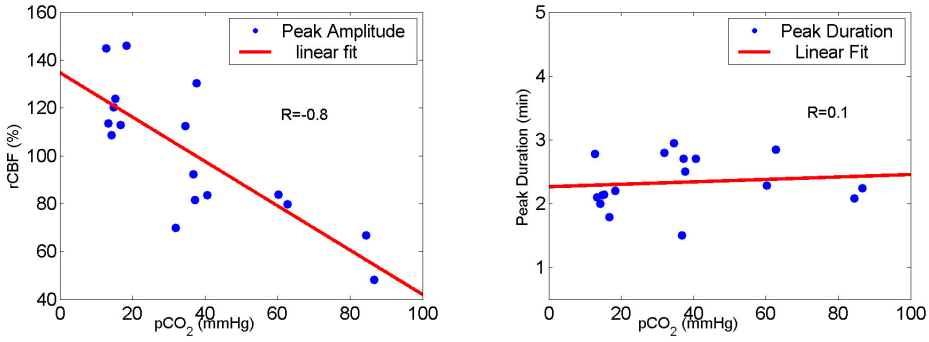

(a) (b)

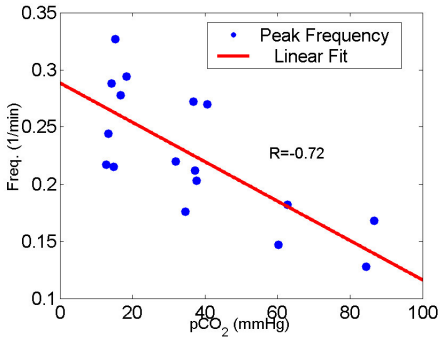

(c)

Figure 4.13: Effect of cerebral PCO_2 on (a) $rCBF$ peak amplitude, (b) $rCBF$ peak width and (c) $rCBF$ peak frequency

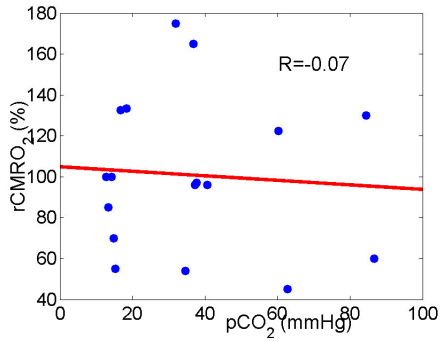

Figure 4.14: Effect of cerebral PCO_2 on $rCMRO_2$

explain important physiology about the nature of the coupling of hemodynamic parameters during cortical spreading depression which in turn has a wide-range of clinical implications. Currently, further studies are being conducted to explain these observations.

4.3 Spatio-Temporal Quantification of Cerebral Blood Flow During Functional Activation in Rat Somatosensory Cortex Using Laser Speckle Flowmetry

4.3.1 Introduction

The coupling between functional stimulation and regional changes in cerebral blood flow (CBF), often referred to as activation flow coupling (AFC), has been known for over a century, but is still poorly understood [232, 376]. Since most neuroimaging methods rely on AFC as an indicator of neuronal activity, a detailed characterization of AFC under normal conditions will improve understanding of normal as well as pathological brain physiology. Thus far numerous methods have been employed to measure blood flow changes in brain during functional activation, including positron emission tomography (PET) [141], single photon emission computed tomography (SPECT) [374], magnetic resonance imaging (MRI) [211, 219] , autoradiography [323] and laser Doppler flowmetry [4, 267], but there is still a need for relatively simple and inexpensive techniques with high spatial and temporal resolution.

Laser speckle flowmetry [52, 53] offers high spatio-temporal resolution imaging of CBF, especially for small animal models, and it is closely related to the laser Doppler technique [50]. In speckle flowmetry, scattered laser light with different paths produce a random interference pattern known as speckle, whose fluctuations contain information about the motion of particles in

the underlying medium. A variety of methods [52] use this effect for tissue studies, including deep tissue laser Doppler flowmetry [46] and diffuse correlation spectroscopy [44, 76, 91]. Laser speckle flowmetry has also been utilized to measure blood flow in *near surface* tissues such as skin [147, 320], retina [355], optic nerve [401] and recently brain [45, 112].

In this study, laser speckle flowmetry was used to characterize the near surface AFC following electrical somatosensory stimulation of forepaw and hindpaw in the rat. Statistical analyzes of the images were carried out, and "correlation coefficient images" were used to extract regions of interest (ROIs). Basic functional mapping was demonstrated by separating the activation following forepaw and hindpaw stimulation. Using high resolution temporal (5 Hz) and spatial sampling (32 μm), the affects of stimulus amplitude and duration were investigated. This information was then utilized to characterize the spatial extent of the activation, the shape of its evolution with time, and its dependence on distance from the centroid of activation. The spatio-temporal characteristics of the AFC response across the whole somatosensory area was thus determined. The discussion here closely follows our paper in press [115].

4.3.2 Materials and Methods

4.3.2.1 Surgical Preparation and Stimulus Presentation

Eight male Sprague-Dawley rats (250-300 g) were anesthetized with halothane (1%) in nitrous oxide:oxygen (70:30). They were tracheotomized, mechanically ventilated and a catheter was placed into a tail artery for monitoring blood pressure and measuring blood gases. Body temperature was maintained at 37.5 ± 0.2^o C and $PaCO_2$ levels were kept between 30-40 mmHg by periodic arterial blood gas sampling and adjustment of the respirator. A 5 mm diameter craniectomy was performed with its center over the forepaw/hindpaw somato-sensory area (2.5 mm lateral and 1 mm anterior

to the bregma) using a saline-cooled dental drill. Following surgical preparation, the halothane was discontinued and the animals were administered 60 mg/kg of α-chloralose ip., followed by hourly supplemental doses of 30 mg/kg. Electrodes for stimulation were inserted subdermally into the forepaw/hindpaw contra-lateral to the craniectomy site as described previously [103].

A rectangular constant current stimulus of 4 or 8 seconds was applied at 5 Hz and with amplitudes of 0.5 mA, 1 mA, and 2 mA. The stimulus protocol consisted of 20 seconds of data acquisition at 5 Hz, with the 4 or 8 second stimuli starting after 4 seconds. This protocol was repeated 10 times for each stimulus condition. Each condition was repeated twice and analyzed independently. Forepaw stimulation was completed in all animals (n=8), and in two animals (n=2) a single series of 4 second stimulations at 2 mA was also obtained with the electrode inserted in the hindpaw contra-lateral to the craniectomy site.

Two animals were discarded from the data analysis (n=6) because a very large vessel ran directly over the forepaw area and dominated the CBF images. For the analysis of the spatial response, the data from two animals were not used (n=4) because, it was found that the activation area extended outside our field of view precluding accurate measures of the activation area.

4.3.2.2 Laser Speckle Flowmetry Instrument

Figure 4.15(a) shows a sketch of the experimental set-up. A collimated, laser diode (Hitachi, HL 785 1G, 785nm, 50mW, Thorlabs, Newton NJ) driven by a custom made driver illuminated the exposed cortex (≈ 5 mm diameter) at about $30 - 40^o$ from vertical. The laser beam was adjusted to provide uniform illumination of the surface of the brain tissue. Images were recorded by a 12-Bit, TEC cooled CCD camera (QImaging, Retiga 1350EX, B. C., Canada) using imaging software (StreamPix, NorPix, Montreal, Canada). A 60 mm lens (AF Micro-Nikkor 60mm f/2.8D, Nikon,

NY) was used to focus the image and the aperture was adjusted so the speckle size matched the pixel dimensions (6.45x6.45 μm) [112]. The camera was externally triggered at 5 Hz using the digital output of an A/D board (DataWave Technologies, CO). The A/D board was programmed to trigger the camera continuously (for 20 seconds); after the first four seconds it also triggered the stimulator with an identical signal for the chosen duration (i.e. for 4 or 8 seconds), thereby co-registering in time the data acquisition and stimulation. There was a 5 second interval between repeated stimulations during which data was not acquired. The camera streamed output frames continuously through an IEEE 1394 port to the computer and a fast RAID array was used to store the frames. This prevented frame drops and allowed acquisition of ~ 1000 x 1000 pixel images at a rate up to 10 Hz, and for smaller regions of interest at even higher frame rates. Approximately 24 Gb of data were collected per animal.

4.3.2.3 Data Analysis

Theory of Laser Speckle Flowmetry

The theory underlying laser speckle flowmetry has been described in detail [51, 52]. Laser speckle is a random interference pattern that arises when coherent laser light is scattered from a diffuse medium such as tissue. If the scattering particles in the medium are in motion (e.g. Brownian motion or flowing blood), then the speckle pattern fluctuates randomly. These intensity variations contain information about the velocity distribution of the scatterers. In laser speckle flowmetry, blurring of the speckle pattern during the exposure time of a single image is used to extract blood flow information. Depth sensitivity depends on the optical wavelengths employed and may extend up 1 mm, albeit with decreasing information at larger depths. The spatial resolution of the method is dependent on the speckle and camera pixel size, on the tissue surface, and on tissue scattering in

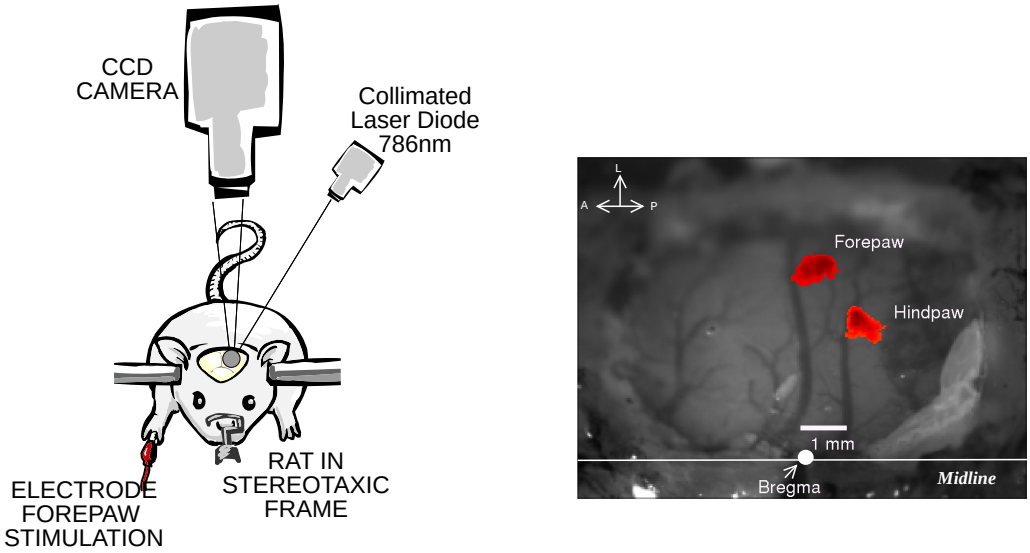

(a) (b)

Figure 4.15: (a) A sketch of the laser speckle imaging set-up. The CCD camera is positioned over the exposed area with a slightly larger field of view than the craniectomy site. A collimated beam from a 785 nm laser diode illuminates the exposed brain tissue. (b) White light image of the craniectomy at the contra-lateral side showing the location of bregma with the AFC response from the forepaw and hindpaw stimulation superimposed. The forepaw centroid is ~ 4 mm lateral to the bregma and is separated 1.8 mm from the hindpaw centroid.

the deeper tissues.

A window function of 5 pixels by 5 pixels ($32.25\ \mu\mathrm{m}$ x $32.25\ \mu\mathrm{m}$ area) was scanned across the raw data, and the ratio of the standard deviation (σ) to the mean intensity ($< I >$) was calculated in each window. This quantity is referred to hereafter as speckle contrast, $C(i,j)$, where i,j denote the pixel position. Images of $C(i,j)$ show remarkably clear maps of the vasculature. In order to reduce the data to be processed to a manageable 2 Gb per animal, the images were smoothed using a bi-cubic intrapolation method by 5 x 5, thus reducing our spatial resolution to $32.25\ \mu\mathrm{m}$.

The relative mean velocity of moving particles (i.e the relative CBF) was extracted using the relation [46, 51],

$$C(i,j) = \frac{\sigma}{< I >} = \left(\frac{\tau_c}{2T}\left(1 - e^{\frac{-2T}{\tau_c}}\right)\right)^2 \tag{4.1}$$

where $\tau_c = 1/(ak_o v)$ is the correlation time, T is the camera exposure time. Here a is an unknown factor related to the Lorentzian width of the scattered spectrum and the scattering properties of the medium, v is a mean velocity and k_o is the input light wavenumber. The mean velocity (v) was assumed to be proportional to CBF, and relative changes in flow (ΔCBF) were obtained by dividing each image by the baseline image. Twenty repeat stimulations were collapsed to one representative stimulation by aligning time points and calculating the mean/standard deviation of the images.

Correlation Coefficient Imaging

The speckle images suffer from substantial physiological and instrumental noise. A simple difference/ratio method neglects useful *a priori* information about the stimulus presentation. Therefore, we computed "correlation coefficient images" by calculating the correlation coefficient for each pixel (cc_i) with a simple step function describing the stimulus presentation ($r_i(i = 1...N)$) [20] as

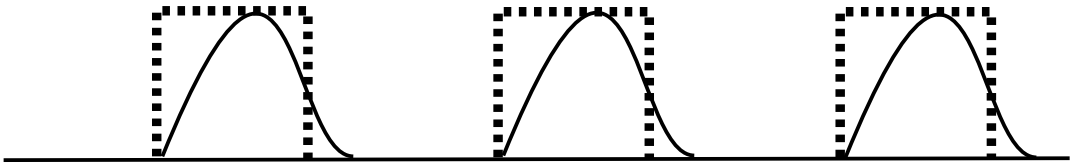

Figure 4.16: Illustration of correlation coefficient imaging where the dashed line represents the stimulus presentation and the solid line represents the variations of CBF over time for a given pixel.

illustrated in Figure 4.16. The correlation coefficient is defined as

$$cc_i = \frac{\sum_{n=1}^{N}(f_i - \mu_f)(r_i - \mu_r)}{\sqrt{\sum_{n=1}^{N}(f_i - \mu_f)^2}\sqrt{\sum_{n=1}^{N}(r_i - \mu_r)^2}} \tag{4.2}$$

where $f_i(i = 1...N)$ is the time course of ΔCBF for a given pixel, μ_f and μ_r are the mean values of f and r, and N is the number of frames. This was applied to all pixels in an averaged series, producing a single image representing the activation area. These images, re-scaled (now cc_i') by proportionally stretching the range to extend from 0 to 1, were used to calculate the centroid of the activation and to pick a region of interest (ROI) for the analysis of temporal and spatial response.

Temporal and Spatial Response

The temporal response was reduced to a curve by defining an arbitrary but consistent ROI of all pixels with $cc_i' > 0.95$, which are averaged at each time point per series per animal. A low pass filter was applied to reduce physiological noise including the cardiac rhythm at ~ 5 Hz, and an average across animals was calculated. Larger regions of interest were also examined and the qualitative shape of the response did not change with the choice of ROI.

In order to investigate the spatio-temporal response simultaneously, other ROIs were defined by either thresholding at varying ΔCBF levels, or as a function of distance from the activation centroid. The number of pixels within a given ROI at each time point was used to calculate an

"area of activation".

The area of activation was first defined by the number of pixels with ΔCBF above the half-maximum (threshold at half-height) response. In order to investigate the effect of the choice of threshold on this result, the threshold ΔCBF was varied from 2% to 20% in 3% increments. To quantify this response, the curves were averaged over 1 second around the peak ($Area_{max}$), and then normalized by the total mean over the three stimulation currents (0.5, 1 and 2 mA) ($< Area_{th} >$) plotting $\frac{Area_{max}}{<Area_{th}>}$ vs the stimulus current. This normalization brought out the salient features by keeping the same scale for different thresholds. The time to reach maximum-area was defined to be the time to reach the peak in these plots.

Statistical Analysis

Data were tested for statistical significance (when applicable) with repeated measures ANOVA. p-values were reported with $p < 0.05$ as the significance threshold.

When the linearity of the dependence on stimulus amplitude was being tested, a Pearson's correlation coefficient was further calculated and the corresponding R^2 and p-value is reported with $p < 0.05$ as the significance threshold.

4.3.3 Results

Figure 4.15(b) shows a white-light photo of the craniectomy site with the location of bregma indicated and the AFC responses from a forepaw and a hindpaw stimulation superimposed. The forepaw centroid is ~ 4 mm lateral to bregma and is separated 1.8 mm from the hindpaw centroid. A similar result was obtained in the other rat where the two centroids were separated by 1.6 mm. Thus, the functional areas corresponding to forepaw and hindpaw areas are mapped as discrete,

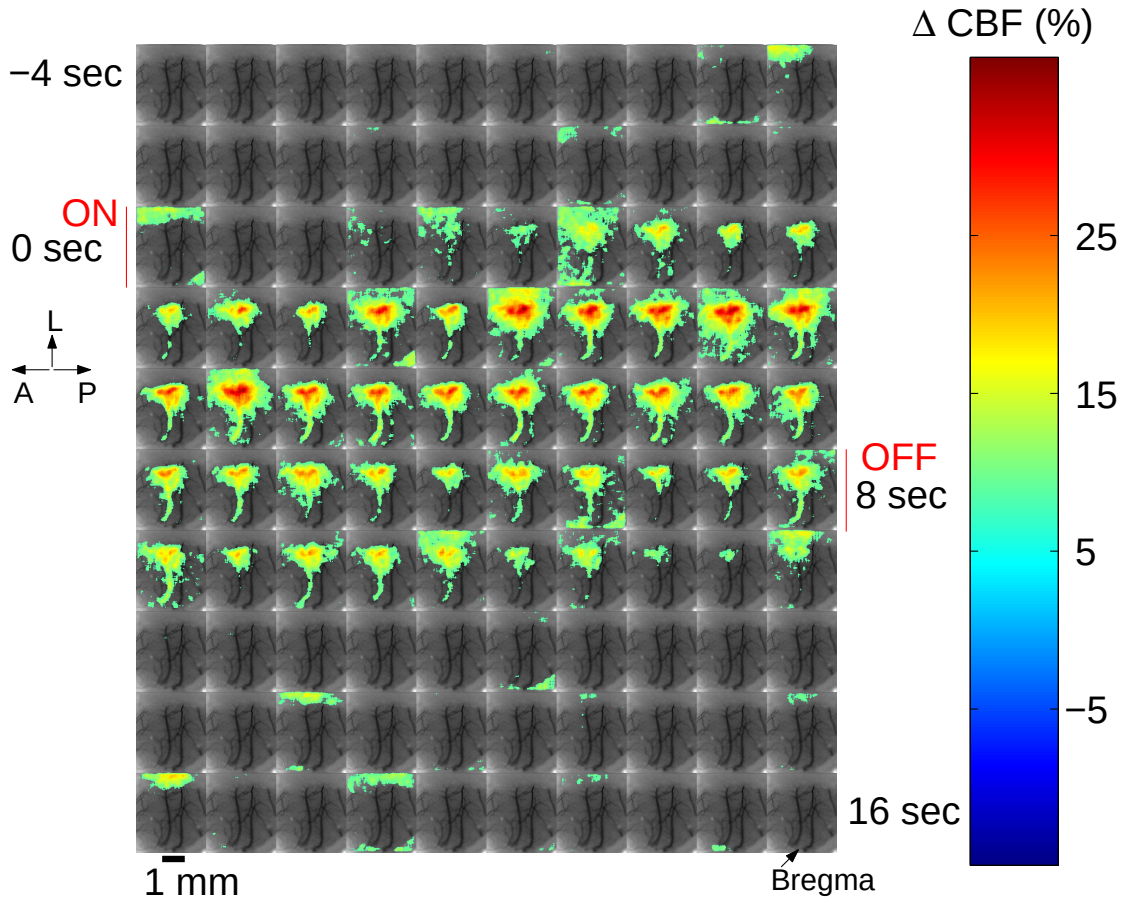

Figure 4.17: Time-series (200 ms/frame) of images showing the spatio-temporal evolution of the AFC response to 8 sec, 2 mA stimulation of the forepaw. The ROI defined by $\Delta CBF > 7\%$ is overlaid on the speckle contrast image. The stimulation is presented between 0^{th} (ON) and 8^{th} seconds (OFF). L=Lateral, A=anterior, P=posterior

anatomically separate regions.

Figure 4.17 exhibits a sequence of images (200 ms/frame) showing the spatio-temporal evolution of the AFC response to an 8 sec, 2 mA stimulation of the forepaw. The ROI, defined by $\Delta CBF > 7\%$, has been overlaid on the speckle contrast images. The stimulation was presented between the 0^{th} (ON) and 8^{th} sec (OFF). The response reached a maximum after about four seconds and was followed by a relatively rapid drop which was sustained for about one second after the stimulus was turned off.

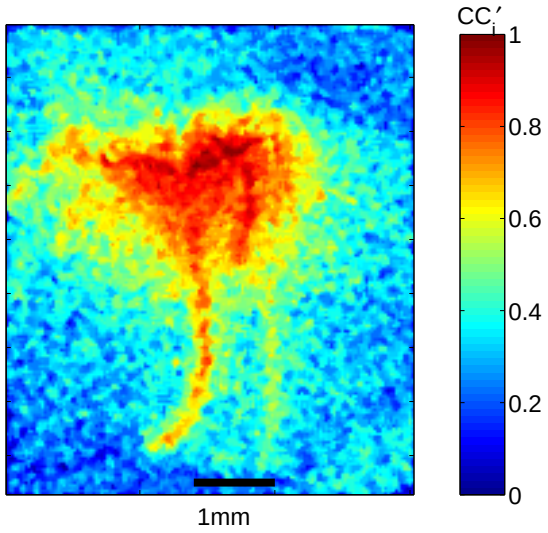

Figure 4.18: An image of cc_i' for a 2 mA, 8 seconds stimulation in one animal. The correlation coefficient (cc_i) between an input step function and the temporal evolution of the ith pixel was calculated and re-scaled to obtain cc_i'.

Figure 4.18 shows an image of cc_i' for a 2 mA, 8 seconds stimulation. Regions of interest, for which $cc_i' > 0.95$ were defined to obtain integrated temporal response curves corresponding to the blood response to activation. Examination of the amplitude of the response to stimulation revealed a nearly linear peak response as a function of stimulus amplitude for the 8 second stimulus duration (Figure 4.19(a) and Table 4.3). Similar results were obtained for the 4 second stimulus duration. Normalized responses (Figure 4.19(b)) from the two stimulus durations (4 and 8 sec) were the same for the first four seconds of the temporal trace. Blood flow decayed rapidly after reaching the peak and returned to the baseline after the end of the four second stimulus. The 8 second stimulus showed a delay of ~ 1 second decaying at a similar rate as the shorter stimulus curve until the end of the stimulus. After that point, the decay rate slowed down by a factor of four for ~ 2 seconds, which was followed by a more rapid decay over the next two seconds reaching the baseline four seconds after the end of stimulus. This was independent of the stimulus amplitude.

Table 4.3 summarizes our findings in a parameterized manner for each stimulus condition.

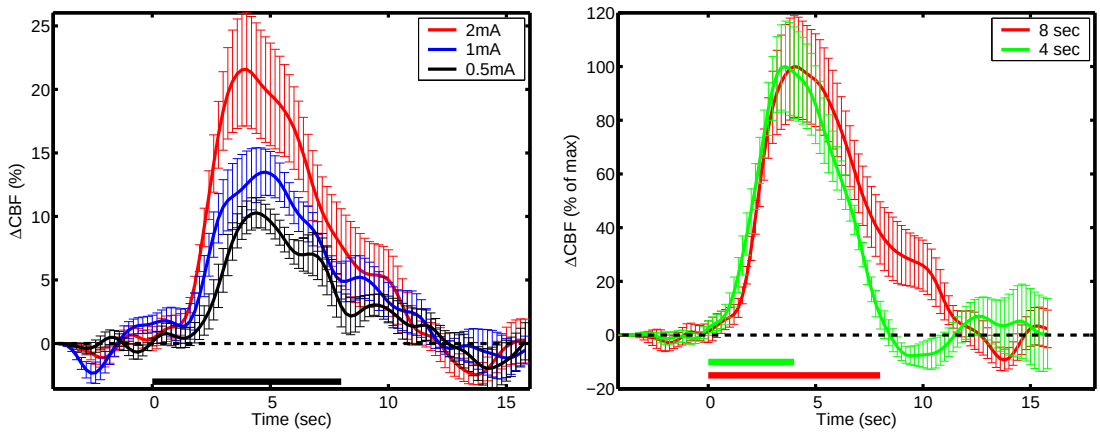

(a) (b)

Figure 4.19: (a) ΔCBF in response to 8 seconds of stimulation at three different amplitudes; 0.5 mA (black), 1 mA (blue) and 2 mA (red) averaged over pixels with > 0.95 of maximal correlation coefficient. The peak response is nearly linear with stimulus amplitude. (b) Temporal characteristics of ΔCBF in response to two different stimuli durations (4 seconds (green) and 8 seconds (red)) at 2 mA averaged over pixels with > 0.95 of maximal correlation coefficient. Color coded horizontal bars indicate the stimulus presentation. Both curves are normalized by their peak value to bring out salient features related to the stimulus duration.

Table 4.3: Time-to-peak and peak amplitude of ΔCBF as a function of stimulation duration and current.

Duration (sec)	Current (mA)	Time-to-Peak* (sec)	Peak* (%)
4	0.5	4.0±1.2	10.2±2.0
4	1	3.5±1.2	13.4± 2.5
4	2	3.2±1.5	20.0±3.0
8	0.5	4.1±1.3	10.2±1.5
8	1	4.8±1.1	13.2±2.0
8	2	4.0±1.2	21.4±4.5

* Mean ± standard deviation.

Current (mA)	Max. Area* (mm^2)	Time to Max.-Area* (sec)
0.5	6.5±3.3	4.5±1.4
1	5.4±3.8	4.6±0.9
2	4.4±3.5	4.2±0.7

* Mean ± standard deviation.

Table 4.4: Activation area and time to reach maximal-area for different stimulus levels.

Time-to-peak was independent of stimulus duration and current ($p > 0.2$). Peak flow was linearly dependent on stimulus current ($R^2 = 0.999$, $p < 0.005$ for 4 seconds, $R^2 = 0.994$, $p < 0.05$ for 8 seconds).

The area of activation was defined by the number of pixels with ΔCBF above the half-maximum (threshold at half-height) response. Data for the 0.5 mA stimulus included a good deal of noise, because the threshold was close to the noise floor of the frames, but there was no qualitative difference ($p > 0.2$) in the shape of the temporal evolution of the activation area with respect to stimulus amplitude (Figure 4.20(a)). This effect, however, was threshold dependent. Low thresholds produced a larger activation area independent of stimulus amplitude, whereas high thresholds produced a smaller activation area with a dependence on stimulus amplitude ($p < 0.05$). To quantify the response, the curves were averaged over 1 second around the peak, and then normalized by the total mean over the three stimulation currents (0.5, 1 and 2 mA). $\frac{Area_{max}}{<Area_{th}>}$ vs stimulus current for different CBF thresholds are shown in Figure 4.20(b). This normalization brought out the salient features by keeping the same scale for different thresholds. For thresholds below 8%, the thresholded area of activation is independent of stimulation current ($p = 0.5$ (2 $\%$) , $p = 0.06$ (5 $\%$)). The highest threshold (20%) measured mainly noise and was also independent of current (20 $\%$, $p > 0.1$). Table 4.4 summarizes the findings for half maximum threshold. The time to reach maximum-area was independent of stimulus current ($p > 0.2$).

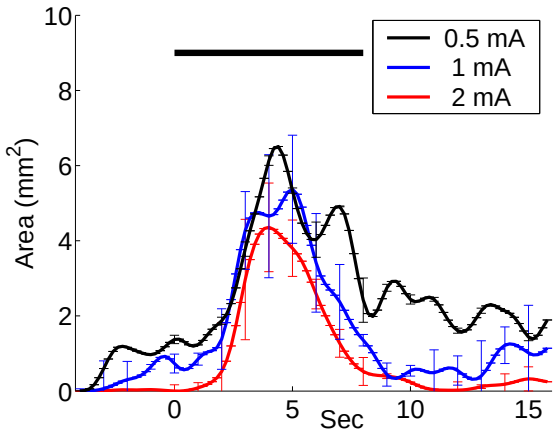

(a)

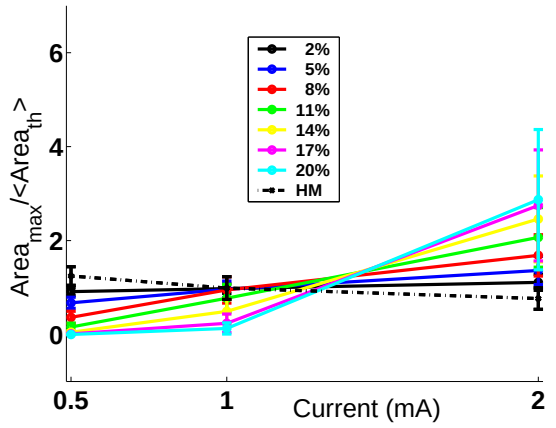

(b)

Figure 4.20: (a) Area of activation obtained from the number of pixels with ΔCBF above the half maximum response for three different stimuli amplitudes during 8 seconds stimulation. The stimulus period is shown by the black bar. There is no statistically significant difference in the activation area as a function of the stimulus amplitude. (b) Maximal area averaged over 1 second around the peak normalized by its mean over the three stimulation currents (0.5, 1 and 2 mA). The ($\frac{Area_{max}}{<Area_{th}>}$) vs current for different CBF thresholds. Half-Maximum (HM) ΔCBF is shown by the dashed line. For thresholds below 8%, the thresholded area of activation is independent of stimulation current.

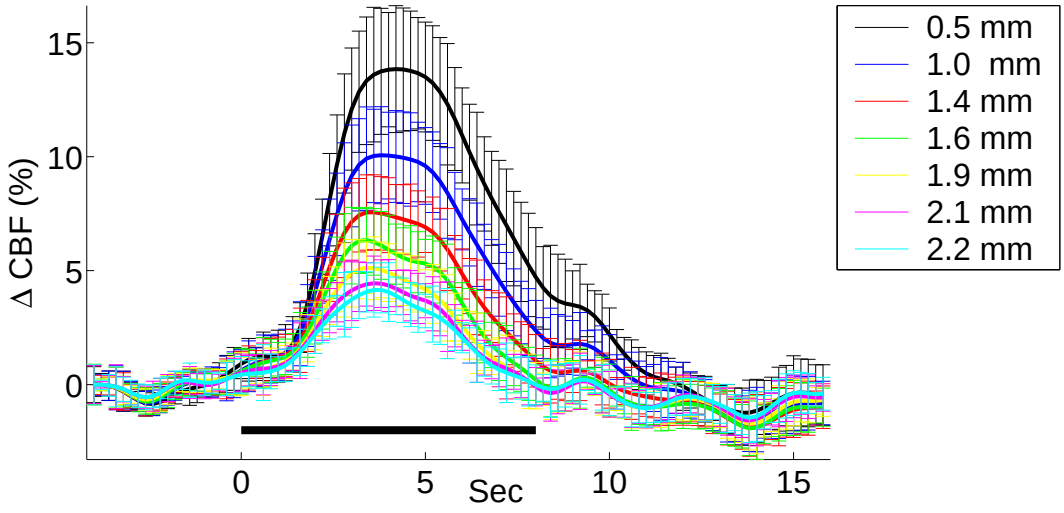

Figure 4.21: Equal area rings around the centroid of activation with radii indicated in the legend were chosen as regions of interest. The time course of $\Delta CBF(\%)$ does not depend on the distance from the center of the activation. The solid bar represents the duration of stimulation.

Images of ΔCBF indicate regional dependence of the activation. To determine whether the shape of the temporal evolution of this response is constant with distance from the activation center, ROIs were defined as non-overlapping, concentric rings of equal area around the activation centroid. The radius of the first filled ring was chosen to be ~ 0.5 mm. Twenty rings with increasing radii (maximum radius 2.29 mm) of equal area increments were used. The temporal response from every fourth ring is shown for simplicity in Figure 4.21. Qualitative changes in temporal features of ring diameters were not observed, but the peak response decreases with increasing ring diameter.

4.3.4 Discussion

The blood flow response to electrical forepaw stimulation has been extensively characterized in our laboratory with laser Doppler methods, identifying the stimulation frequency (5Hz) for maximal response [103], demonstrating a linear increase with amplitude [103], mapping the central location

of maximal response [3, 4], modeling the nonlinear effects [7], combining with changes in O_2 to estimate $CMRO_2$ [2, 6], and investigating the effect of carbon dioxide on the CBF response [5].

Even though these studies have provided a great deal of information about the AFC response to forepaw stimulation, they were limited in various aspects since laser Doppler is essentially a point measurement. The other available alternative, scanning laser Doppler imaging, offers high spatial resolution with a trade-off in temporal resolution which limits its applicability in studies of the AFC [4]. A high spatio-resolution imaging technique which is relatively simple and inexpensive to implement is clearly desirable.

These results demonstrate laser speckle flowmetry is able to effectively measure, map and characterize the CBF response to forepaw/hindpaw stimulation with high temporal and spatial resolution. The statistical methods employed including signal averaging and correlation coefficient imaging improved the method's signal-to-noise ratio. This relatively simple technique, requiring only a laser diode, a CCD camera and a computer, has provided new insights into previously relatively inaccessible aspects of the AFC.

A notable feature common to most images of relative blood flow is the presence of a large vessel above the threshold. This vessel appears to be a draining vein based on its width and proximity to the brain surface. This feature may hinder the identification of the activation area in relation to the neural representation but also delivers potentially useful physiological information. A region of interest chosen on the large vessel away from the central activation yielded a time course very similar to that in the paranchyma. It is possible to resolve vessels with diameter $\sim 32\mu m$ with the present system/analysis method. For an interesting, preliminary result using principal components analysis to separate details about the response of the vessels see Appendix 4.6.

Measurements of the temporal behavior of AFC at the center of activation yielded results that

qualitatively agree with our previous data from laser Doppler studies. However, the peak blood flow response measured with speckle contrast imaging is approximately 30% lower than that measured previously with laser Doppler flowmetry [103]. The physical and theoretical equivalence of the two techniques has been discussed at length by Briers [50, 52]. Recently Dunn and colleagues have found a high correlation between the two techniques under conditions of spreading depression and ischemia [112]. This high correlation may be attributed to the laminar homogeneity of the vascular response to both of these perturbations. Other studies, however, have shown some discrepancies between laser Doppler flowmetry and laser speckle flowmetry. Kharlamov and colleagues [207] reported an underestimation of up to 35% by laser speckle flowmetry in comparison with laser Doppler during hypercapnia. In a comparison study between the two techniques for measuring blood velocity in the optic nerve head Yaoeda *et al*. [401] also found a poor correlation.

We believe the differences seen in our forepaw activation studies may be due to factors including variations in animal preparation (open vs closed skull), and differing depth sensitivity. During functional activation, the AFC response may not extend to the topmost layers, with the maximal response occurring at layers III-IV ($\sim 600\mu$m below the cortical surface) [72, 85, 114]. Laser Doppler flowmetry, with near infrared source wavelengths, was shown to be highly sensitive to layer IV, but had lower sensitivity to shallower levels [129]. The depth sensitivity of laser speckle flowmetry begins immediately below the observed speckle and degrades rapidly from the surface. This has been modeled by Monte-Carlo methods revealing that most of the information comes from the top $\sim 300\ \mu m$ of the cortical tissue when the illuminating wavelength is 785 nm [215]. Although both techniques probe to similar depths, their partial volume effects are different. As the laser speckle flowmetry is further tested in the brain, a better understanding of these differences should emerge.

The amplitude of the response was found to monotonically increase with increasing stimulus current in a linear fashion. As expected, the longer stimulus duration (8 seconds) led to a CBF response that had behaved in a somewhat complex manner, suggestive of a peak-plateau time course [7]. The activation decayed in amplitude with distance from the centroid. By examining regions of interest surrounding the central peak, it was observed that the AFC response behaves temporally similarly in all regions activated by the forepaw stimulation. It has a spatially decaying profile across the field of view, but with the same temporal properties.

The AFC response was well localized and different functional representations of the forepaw and hindpaw were separated by $1.6 - 8$ mm in close agreement with previous results from electrophysiology wherein the areas were determined to be approximately 1.8 mm apart [72].

Another characteristic of the response that has not been possible to measure with point laser Doppler probes, is the dependence of activation area on stimulus parameters. It was found that stimulus area does not change with either the stimulus amplitude or duration. As expected, this result is threshold dependent. Half-height values provide a normalized threshold; the area of activation at this threshold level was independent of the stimulus amplitude. However, measurements above an $\sim 8\%$ threshold showed that the activation area depended on stimulus amplitude. This is a common issue in imaging modalities and extra care should be taken when comparing results from different experiments. The attempt at normalization by using the half-height of the flow response as the threshold level as well as statistical approaches can provide a way to cross-validate results between different modalities.

The AFC area at half-height evaluated by laser speckle flowmetry was between 4.4 ± 3.5 mm^2 and 6.5 ± 3.3 mm ^{2}. Assuming that our stimulus extends to several digits, this area is similar to electro-physical measurements which found that the cortical area activated was about 1.5 mm^2

per digit stimulated [72, 85]. It is also qualitatively similar to other hemodynamic measurements, such as those of diffuse optical tomography [93], fMRI [114, 189, 239] and optical intrinsic signal imaging [263].

4.3.5 Conclusion

Laser speckle flowmetry was used for the first time to characterize activation flow coupling following somatosensory stimulation. This technique provides high spatio-temporal information and is ideal for the study of basic functional mapping as well as for characterizing the AFC response. It can easily be combined with other optical techniques including optical intrinsic imaging [113], diffuse optical tomography [93, 407] and diffuse correlation tomography [91] for simultaneous measurement of tissue oxygen saturation, total hemoglobin concentration and oxygen consumption as well as for low resolution three dimensional imaging. Future studies of fundamental brain pathophysiology in animal models and in human subjects are feasible.

4.4 Hybrid Measurements of Hemodynamics of Human Brain

4.4.1 Introduction

In Section 4.2, I have described the importance of estimating oxygen consumption in the brain, and described a hybrid optical method for imaging its dynamics in the rat brain. I now describe the application of these techniques to the human brain. The discussion here follows Durduran *et al* [121].

Cerebral well-being is strongly dependent on adequate and continuous delivery of oxygen, and on clearance of the by-products of oxygen consumption, e.g. carbon dioxide. An understanding of the normal and pathologic conditions of oxygen supply and consumption is critical for clinical

applications such as traumatic brain injury (TBI), subarachnoid hemorrhage (SAH), migraine and epilepsy [412]. In intensive care units (ICUs), patients suffering from SAH or TBI are continuously monitored by multi-modality instruments following single-shot measurements by techniques such as computed tomography and MRI. Maximization of their brain physiology is critical and treatment decisions are made based on these parameters such as global cerebral blood flow, tissue pO_2 and blood pressure. Local and/or global measurements of hemodynamic parameters are critical to this end [208, 240, 413]. Optical methods are promising to fill in an important gap in this clinical application.

Despite systematic attempts at measuring CBF for many decades [413] with varying degrees of success, the optimal method is yet to be developed. There is a strong need for relatively in expensive, continuous, non-invasive measurement of CBF. This is where the methods described in this chapter offer a great deal of promise. Diffuse optical tomographic methods have been demonstrated in research and clinical settings for measurements of blood volume, blood oxygen saturation, changes in hemoglobin concentrations and through some maneuvers for the measurement of blood flow [156–158, 224, 265, 313, 330]. It has been particularly successful in infants [49, 55, 83, 84, 101, 123, 178, 184]. The development of diffuse optical correlation tomography allowed us, for the *first time*, to use all optical methods non-invasively, and to continuously measure several hemodynamic parameters which made it possible to estimate changes in oxygen metabolism. Although this is a natural extension of the methods previously described, there are many new technical complications that had to be addressed. Both as a hybrid method and on its own, diffuse correlation spectroscopy has the potential of addressing some missed issues of measurements of cerebral hemodynamics in the clinic. The feasibility of these measurements are now demonstrated in humans.

Main advantages of this technology can be outlined as follows;

1. The technique is non-invasive and involves no risk to the patient (no ionizing radiation, no gases to be inhaled or drugs to be injected).

2. The technique is able to sample in real-time or close to real time.

3. The technique is able to track changes over long periods unlike “single shot” modalities (e.g MRI, PET etc).

4. The technique is able to sample more than one point to examine regional differences in the brain simultaneously.

5. The technique is able to be at the bedside so critically ill patients do not have to be moved.

6. The technique is readily combined with other modalities so that blood flow and oxygen can be measured simultaneously.

I will, first briefly, re-introduce the instrumentation used, then describe the phantoms used for the calibration studies. After describing the the optical probe, I describe the protocol employed. The results and their implications are, then, presented. The ability to measure functional activation during global (hyperventilation) (see Appendix 4.7) and local (sensorimotor cortex activation) paradigms are demonstrated. Variations in oxygen metabolism are calculated using a basic algorithm and future applications and developments of the technique are outlined.

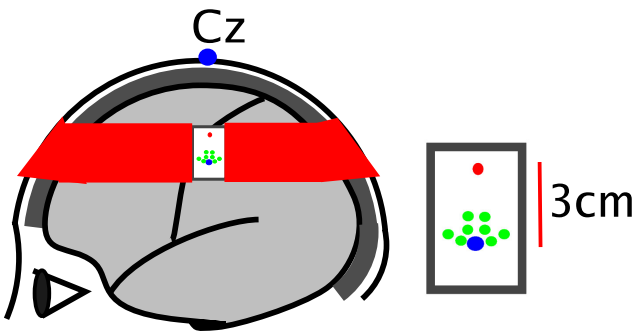

Figure 4.22: Placement of fibers; source (red) at the center of a circle (r=3cm), DOT detector (blue) placed at periphery, DCT detectors (green) at 2 cm (x2), 2.5 cm (x2) and 3 cm (x4).

4.4.2 Materials and Methods

4.4.2.1 Instrumentation

The instrumentation employed for these studies was described in details in Chapter 3, Section 3.6. Briefly, light from three amplitude modulated lasers operating at three near-infrared (NIR) wavelengths (690-830nm) (which were shown to optimize signals from brain tissue in similar experiments [43, 351]) were coupled onto the tissue surface with fiber optics. Photons transmitted into the brain were detected in reflection using fiber optics and a photomultiplier tube. These wavelength dependent data were used to determine oxy- and deoxy-hemoglobin concentrations by NIR spectroscopic analysis [110]. A high coherence length CW laser, eight photon-counting, fast avalanche-photodiodes, and an eight channel autocorrelator board facilitated measurements of blood flow; the temporal autocorrelation functions of the reflected light were used to derive flow information [91]. The time-sharing of the systems was fully automatized.

A single detector fiber at 3 cm separation for DOT was shown to provide good DOT signal [43]. DCT was more of a challenge, therefore, eight flow detectors; four at 3 cm, two at 2.5 cm and two at 1.5 cm were employed. The signal from multiple fibers at same separation were averaged to improve the signal-to-noise ratio. Furthermore, the DCT signal was averaged for three seconds at

each frame. This arrangement is illustrated in Figure 4.22.

The instrument was approved for human studies by the Radiation Safety Committee of University of Pennsylvania.

4.4.2.2 Protocol

Seven male volunteers (ages 38-73) participated in the sensorimotor cortical activation studies. Two volunteers were studied twice in intervals of two weeks in order to assess repeatability. One subject also participated in a 3 Tesla functional magnetic resonance imaging (fMRI) study [383] in which activation data based on BOLD and arterial spin labeled (ASL) perfusion using the same task were obtained sequentially before the optical study using pulsed ASL and gradient-echoplanar imaging with TR=3 sec, TE=17 msec, and T1=1 sec.

The subjects were first asked to sit while one investigator localized the hand sensorimotor cortical area contralateral to the dominant hand according to the 10-20 system [195] and the probe (Figure 4.22) was placed and secured over this region. The subject lay comfortably on a bed with his head slightly tilted so a monitor could be viewed for stimulus presentation. The subject was instructed to tap index and middle fingers against the thumb at 3 Hz, in time with an auditory cuing signal. The room was kept dark and quiet for the study duration. A one minute baseline was recorded prior to and after each stimulus, and a blocked design of fifteen such stimuli was used. One subject was asked to repeat the study using the ipsilateral hand in order to confirm the contralateral nature of the optical response, and in another subject thirty seconds of stimulus was obtained and signals were compared to those of one minute stimulus duration. In two subjects, the probe was placed slightly off the sensorimotor area and no response was obtained.

4.4.2.3 Data Analysis

Blood oxygenation data was analyzed using the differential pathlength factor (DPF) method (see Ref [110] and Section 2.1.8). Blood flow data was analyzed by fitting each source-detector pair to a semi-infinite diffusion model [44, 91]; the flow measurements yielded relative CBF, rCBF. For quantification, all of the measured data were corrected for partial volume effects as described below. Relative changes in $CMRO_2$ ($rCMRO_2$) were derived from the measured variation in blood flow, deoxy-hemoglobin concentration, and total hemoglobin concentration [43, 91]. In this model (Section 2.3), a constant arteriol-venous tissue compartmentalization is assumed, and for slow variations ($\sim$ seconds), $rCMRO_2$ is found to be proportional to the product of rCBF and relative changes in deoxy-hemoglobin and total hemoglobin concentration. The hemodynamic parameters were block averaged over repeated stimuli and further averaged over the whole group. We present mean and standard error where applicable. Further details of data analysis was described in Chapter 2.

4.4.3 Results

4.4.3.1 Partial Volume Effects

Figure 4.24(a) shows the observed changes from one volunteer. Even though, our hemoglobin concentration results are in agreement with other optical measurements [142, 257], the observed changes in hemoglobin concentration and blood flow are underestimated because of partial volume effects. In essence, the diffuse optical *spectroscopies* probe large tissue volumes without discriminating between tissue types, e.g bone and brain tissue as shown in Figure 4.23. Mehagnoul-Schipper *et al* [257] conducted a comparative study of diffuse optical tomography (DOT) and magnetic resonance imaging (MRI) and found that partial volume effects caused a significant (i.e.

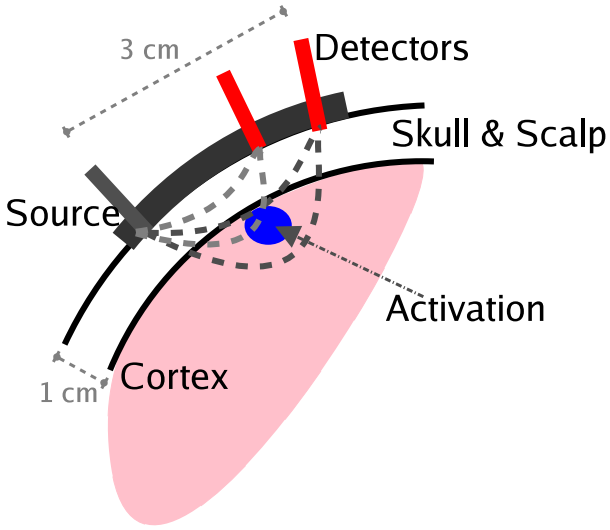

Figure 4.23: Sketch of photon paths in brain. Two source-detector separations are shown. Larger separations probe deeper into the tissue. A small activation area is shown for illustration and the partial volume effects are related to the percentage of photons passing through the activation volume

$>$ 2x) reduction in optical signal variation compared to MRI signal variation. Similarly, Boas and colleagues [40, 351] demonstrated diffuse optical spectroscopic methods are subject to errors due to tissue heterogeneity when measuring focal changes. Since these spectroscopic approaches have been used in the bulk of brain optical studies thus far, various methodologies have been suggested to account for these discrepancies [277, 346]. We have implemented the findings of Strangman *et al* [351] who empirically showed that differential pathlength analyses used in our geometry and protocol overestimate DPF by a factor of $\sim$ 20. For more details on differential pathlength formulation of photon diffusion see Chapter 2.

We also determined a correction factor for the flow data based on numerical simulation and laboratory experiments. By approximating the layered structure of the head (scalp, skull, brain) using a two-layer model [309], we simulated a series of diffuse light temporal autocorrelation curves for the *in vivo* probe geometry. The top layer (skull) thickness was set at 1 cm with a flow less than 1% of the bottom layer (brain). We varied the dynamical properties of the brain layer and

computed an estimate for the flow in the bottom layer using a semi-infinite medium model. This simulation underestimated flow by a factor of 5.0 ± 1.2 over the entire range of parameters due to partial volume effects. This underestimation was verified with *in vitro* measurements using a human skull filled with an Intralipid/ink solution that mimicked the optical and flow properties of the human brain. For more details on this measurement and two-layer approximation see Section 2.2.4.

4.4.3.2 Partial Volume Corrected Results

Figure 4.24(b) shows the corrected hemoglobin concentration and flow changes from the study shown in Figure 4.24(a). As expected there was a sustained rise in oxy-hemoglobin, a decrease in deoxy-hemoglobin and an increase in CBF. If the probe is place $\sim$ 2 cm frontal to the motor cortex, the effect of the finger tapping is clearly absent, thus demonstrating the local nature of the response (Figure 4.24(c)).

FMRI images using the same blocked finger tapping paradigm allowed us to localize the activation more precisely. Statistical maps show perfusion (Figure 4.24(d)), and BOLD (Figure 4.24(e)) activation. The CBF increase was 48$\%$ compared to the optically measured mean increase of 42$\%$. The BOLD change was 1.7$\%$ compared to the mean ΔHb decrease from optical data of 3μM. Although, BOLD signals do not directly correspond to either of the measured parameters, they can be used to estimate a range and shape for the hemoglobin concentration variation.

Figure 4.25 shows the corrected hemodynamic curves averaged across all subjects. The corrected mean flow change is $39 \pm 10\%$ which is well within the range of values determined by MRI [206, 402], $[H_2\ ^{15}O]$ PET [81], $[^{133}X_e]$ [314] and $[^{11}CH_3]$ PET [332] for similar measurement stimuli, i.e. $21\% - 60\%$. Corrected mean oxy- and deoxy-hemoglobin changes were

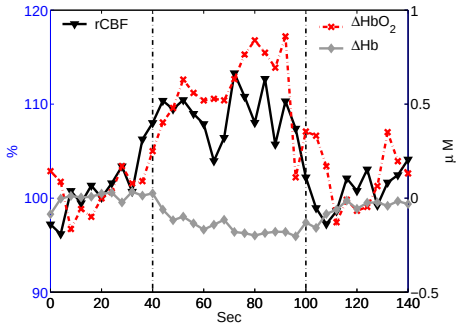

(a)

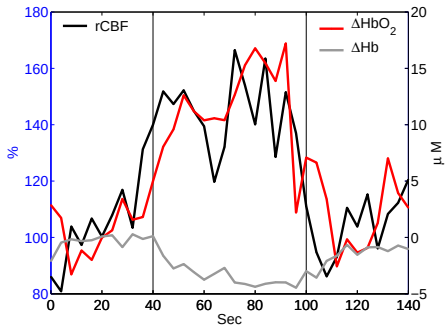

(b)

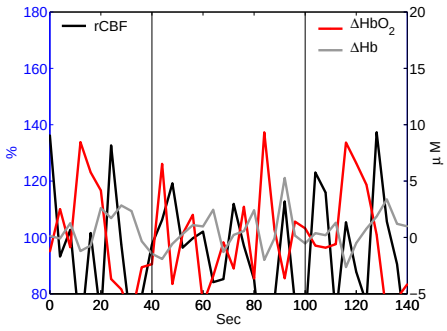

(c)

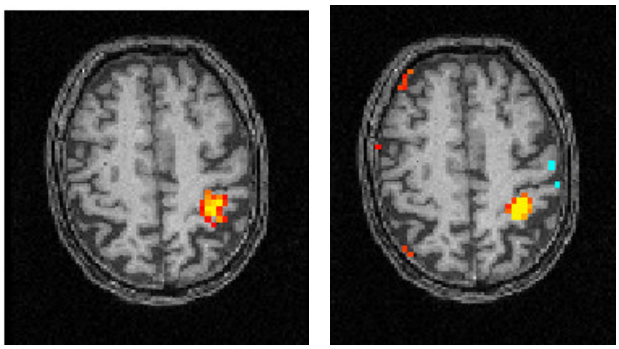

(d) (e)

Figure 4.24: (a-c) Change in oxy- and deoxy-hemoglobins (right) and rCBF (left) (a) prior to partial volume correction, (b-c) corrected data with the probe placed (b) on the motor cortex, (c) ~ 2 cm frontal. Block averaged over fifteen trials. (d-e) Representative MRI slices through motor cortex showing (d) perfusion, and (e) BOLD activation using a blocked paradigm from the same volunteer.

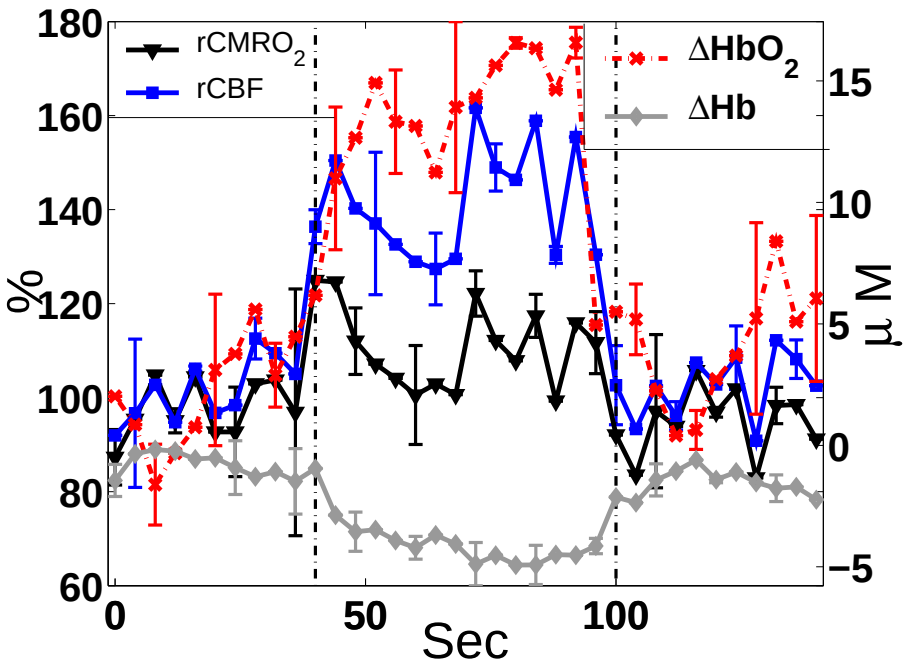

Figure 4.25: Partial volume corrected, block and group averaged results showing change in oxy- and deoxy-hemoglobins (right) and rCBF (left).

12.5 ± 2.8 μM and $-3.8 \pm 0.8\mu$M respectively, while the total hemoglobin concentration change was $8.3 \pm 2.3\mu$M. Again, these observations agree quantitatively with increases reported by BOLD of $2 - 4\%$ [206, 257].

The increase in $CMRO_2$ due to finger tapping was $10.1 \pm 4.4\%$ within the range of values (9% to 29%) from hybrid MRI measurements (Figure 4.25) [206]. The ratio of rCBF to $rCMRO_2$ is 3.8 ± 1.1, in agreement with data reported by hybrid MRI techniques [186, 206] which range from two to four. Note that our calculations of $rCMRO_2$ rely on approximations of baseline optical properties, vascular compartmentalization, as well as the partial volume correction. It is, however, a good first estimate and paves the way for future studies of oxygen metabolism by all-optical methods.

When the stimulus duration was 30 instead of 60 seconds, the measured amplitude did not

change significantly but the peak duration was halved. No response was visible on the side ipsilateral to the stimulated hand, and measurements when the probe was placed far away from the sensorimotor cortex did not exhibit any significant changes in signal. The results from all studies showed signal changes were repeatable to within 5% over a period of two weeks.

4.4.4 Conclusion

We have demonstrated a hybrid instrument which combines diffuse optical and correlation spectroscopies to measure concurrent variations of blood flow, blood oxygenation and oxygen metabolism through the intact skull of adult human brain during sensorimotor cortical activation. Our observations are consistent with other studies of the same stimuli employing different measurement techniques. Due to ease of use and portability of this instrument, we anticipate this all-optical experimental approach may become useful in the management of patients with brain disorders and for assessing functional physiology in normal subjects.

4.5 Future of Hybrid, Diffuse Optical, Cerebral Hemodynamic Measurements

A few words on the future of hybrid , optical, cerebral hemodynamic measurements are necessary to put the issues in perspective. In this Chapter, I have presented results which demonstrate the feasibility of diffuse optical methods for continuous measurement of critical hemodynamic parameters. It is possible to use these parameters to estimate one of the long desired parameters of neurophysiology, $CMRO_2$.

There is obviously a desire to improve the fidelity of these measurements. Better understanding

of the origins of the optical signal is possible with further experiments of combined methodologies. This could be combined with detailed calibration methodologies to enable absolute measures of tissue hemodynamics. The amazingly rapid developments in MRI related techniques can also be adapted for optical methods. For example, the optical signal can be calibrated in a similar manner described by Hoge *et al* [185] in which changes in the relationship between BOLD and perfusion with and without functional stimulation are used to infer oxygen metabolism. Furthermore, numerical and experimental techniques from DOT can be transferred to DCT to improve the accuracy of the measured signal. The present instrumentation is capable of acquiring basic tomographic data with a trade-off in temporal resolution. This would readily enable a better quantification in applications where this trade-off is tolerable [40].

One could immediately consider applications of the present state of this technology. Here I list a few of these applications outlining the shortcomings of existing methods and how this hybrid technology could be useful.

1. Bed-side monitoring unit in the neuro-intensive care unit (NICU) for trauma patients:

   Currently, trauma patients admitted to the NICU are monitored with a multi-probe assembly which monitors the hemodynamics parameters as well as other indicators of the physiological status of the injured brain [48, 82]. However, currently, the hemodynamic information is accessible either through single-shot measurements (MRI, Xenon-CT, PET) or probes attached directly onto the brain surface through a burr hole drilled on the skull such as Licox brain tissue O_2 monitor (Integra NeuroSciences, Plainsboro, NJ) [105, 367], intracranial pressure monitor, jugular venous oximeter, central venous or Swan-Ganz catheter, and arterial blood pressure monitor. Both options are obviously undesirable since the former does not provide adequate information and some patients can not be transfered to the instruments

and the latter is invasive and limited to one position on the brain.

Our instruments can provide important additional data as well as having the potential to replace the oximeters. This technique is unique in being able to monitor changes in cerebral blood flow through the intact skull, on many locations over the brain and through extended periods over hours and even weeks continuously. Previously optical techniques (without flow) have been applied to this patient population with some success [157, 158].

2. Pediatric Neuro-Intensive Care Monitoring of Infant Brain

   Many sick infants are admitted to the pediatric neuro-intensive care unit (PNICU) with severe cerebral hypoperfusion due to cardiac disease as well as other conditions. The management of these individuals is complicated due to their age and fragility. There are no easily accessible non-invasive methods that allow for long-term, continuous monitoring. This population is particularly accessible to our technology since the skull is thinner and even transparent. Previous studies with instrumentation of similar nature measuring cerebral oxygenation have shown that these measurements have great potential in the care of infants [28, 178]. Therefore, we expect that our technology can be readily applied to the monitoring of cerebral hemodynamics in these infants.

   Furthermore, this technique can provide the ability to do extensive research on the nature and progress of disease in comparison to the development of healthy infants.

3. Sleep studies of patients with sleep disorders

   Patients with symptoms indicating sleep disorders such as sleep apnea are regularly diagnosed through a series of doctor visits with different specialties (e.g physicians, pulmonologists, neurologists) and tests of varying complexity. The diagnosis of sleep apnea is

complicated because many factors can disturb sleep. A common test called multiple speed latency test is mostly an empirical test since it relies on the time to fall asleep. Another, more objective test is polysonmography which is a multi-function probe recording cerebral electrical activity , heart rate, respiratory function, air flow, blood oxygen levels and the muscle activity. It has the potential to not only diagnose the disorder but also to indicate its severity.

Our technique can improve the data available to the latter test. Cerebral blood flow can be monitored regionally and continuously and can be related to the brain metabolic state.

4. Monitoring of stroke patients

   A critical improvement to the treatment and management of patients who had suffered a stroke would be the ability to monitor the brain metabolism locally and continuously. Physiological problems associated with a stroke are similar to that of TBI described above [48,82]. Currently, there is no non-invasive method of this monitoring and our technique can fill in this gap.

5. Functional studies

   Functional activation studies are of great importance to neurology and neuro-science in the development of both the fundamental understanding of brain physiology and disease. It is desirable to improve upon invasive (as in bolus injections for some PET and MRI studies) and non-invasive but uncomfortable methods. One main disadvantage of other available methods for measuring regional blood flow is that it is not possible to take data in natural surroundings which impact the value of functional studies.

6. Cerebral Monitoring of Cardiac Surgery Patients

   It is widely believed that cardiac surgery patients undergoing by-pass surgery have cerebral

injury due to surgery [193, 266, 312, 358]. Currently, there are no efficient means of monitoring the cerebral well-being of these patients. A major obstacle is that invasive methods such as Licox probes described above can not be implanted since these patients are all placed on heparin (a blood thinner) at surgery which induces a high risk of a brain hemorrhage.

Our technology, could prove to be of critical use in this patient population since it does not pose any risks to the patients and the results are available real-time.

Finally, this technique can be compared to other methodologies for measuring cerebral blood flow;

1. Laser Doppler

   Laser Doppler (LD) methods are physically very similar to our techniques, and the basic principles are essentially the same [52]. However, mainly due to practical problems in detection, there is an important limitation of LD probes where point by point or scanning (Laser Doppler Scanning, LDS) is carried out with very closely spaced source-detector fibers. This limits the penetration to about ~ 0.5 mm below the surface. Therefore, the skull has to be removed to access the brain. Recently, there has been some developments which has enabled the penetration to go up to about ~ 5 mm in laboratory settings in skeletal muscles [34] but this is still prohibitive for applications on human brain where the skull thickness can exceed 10 mms.

2. Laser Speckle Flowmetry

   Laser speckle flowmetry (LSF) is another optical technique that deals with the same physics as our technique [52]. It is a camera based technique that has recently been introduced to

examine cerebral hemodynamics in rodents. It has not yet been commercialized and its application in humans is limited mostly to measurements during open-skull surgery. The penetration depth is limited to about ~ 0.5 mm and there is no apparent technique for increasing the penetration depth [112].

3. Doppler Ultrasound

   Modalities based on Doppler ultrasound use the frequency shifts in an ultrasound beam to image blood flow. However, due to technical issues, it has, so far , been able to only measure blood flow through large vessels [36, 212]. The present status of the technology limits its application to short, point measurements limiting its applicability. In contrast, the diffuse correlation methods measure an average tissue blood flow, sensitive mainly to the smaller (e.g capillaries) vessels and can be used in a regional manner and longitudinally. Furthermore, optical probes can be secured tightly on the tissue and are relatively insensitive to movements [411].

4. Arterial Spin Labeling MRI (ASL), Flow-Sensitive Alternating Inversion Recovery MRI (FAIR) and other developing MRI modalities

   ASL [22,102,104] and FAIR [211] are two modalities of magnetic resonance imaging (MRI) that are sensitive to perfusion/flow and have been used extensively in the brain. Additional MRI modalities are available for perfusion measurements but they require bolus injections making them less desirable. Although they offer a “full-head” imaging capability and can readily be co-registered with the high-resolution anatomical information of MRI and other functional MRI modalities (e.g blood oxygen level dependent, BOLD), their use in some

clinical settings is limited due the nature of the measurement. The presence of strong magnetic fields makes them difficult to use in some settings such as the intensive care unit. Therefore, they are generally single-shot measurements where the patients are transferred into the magnet and held still for $\sim 30 - 60$ minutes. Furthermore, the instruments themselves and instrument-time is expensive. Additional difficulties arise due to patient specific problems. It is sometimes difficult to hold infants still and some patients are claustrophobic.

Our techniques do not provide the rich anatomical information and "full-head" imaging capabilities of MRI modalities but instead provide long-term, non-invasive and relatively inexpensive local measurements.

5. Xenon Computer Tomography (Xenon CT)

   Xenon CT is used in the clinics for measurements of "full-head" maps of cerebral blood flow [293, 406]. It is a modality which dynamically scans the head using a CT system while the patient inhales Xenon gas. Although Xenon inhalation carries very little health risks, there is some risk due to the radiation exposure from the CT scans.

   It is gaining acceptance as a complementary modality in some intensive care units in preference over MRI and PET modalities. However, its use is still limited to several measurements at distinct time-points (i.e still essentially a "single-shot" modality). The instrument and the Xenon gas itself is quite expensive.

   Although in theory more accessible than MRI instruments (can be present at the ICU), the patients should still be transferred into the device and held still for $\sim 30 - 60$ minutes. Additional difficulties arise due to patient problems, such as infants that can not be held still without great discomfort. There is only slight issue of claustrophobic patients. Furthermore,

Xenon CT instruments are still relatively uncommon being present in only a few centers in the USA.

Our techniques do not provide the rich anatomical information and “full-head” imaging capabilities of CT modalities but instead provide long-term, non-invasive and relatively inexpensive local measurements.

6. Positron Emission Tomography (PET)

PET is a modality that offers direct measurements of a variety of physiological parameters including blood flow [141], glucose metabolism [305] and oxygen metabolism [141]. However, use of radioactive materials limits its applicability in some clinical settings such as the intensive care unit [292]. It shares similar problems as MRI and Xenon CT modalities mentioned above in terms of expense, availability, patient discomfort and inability for long-term monitoring. Furthermore, PET requires injection and/or inhalation of chemicals and uses radioactive materials.

There are a lot of issues that are yet to be resolved. A long way has already been covered for diffuse optical tomographical methods whereas diffuse correlation tomographical methods are in their infancy. I believe that the recent advances in cerebral DOT are exemplary of the potential developments in DCT. In the following years, we will see a boom in research and clinical applications.

4.6 APPENDIX: Principal Components Analysis of Speckle Flowmetry

As the analysis of the previous sections illustrates, the signal from changes in cerebral blood flow is complex. Apart from instrumental noise, there is a strong background signal possibly due to vegetative processes such as respiration and spontaneous fluctuations in blood flow. Furthermore, changes in large vessels are intermingled with signals from the smaller vessels feeding the active neurons. The speckle flowmetry technique does not distinguish depth and therefore, may be even more contaminated with signals from a mixture of vessels. There is potential in looking for methodologies that may separate response from different tissue types, extract signals from noise and identify potential signals that are different in temporal qualities.

Previous experience with optical intrinsic signals (for a recent review see [166]), which are related to the oxygenation changes showed that it is possible and useful to separate different types of responses. The data from these studies are similar to the laser speckle data sets in that they consist of a temporal series of 2D CCD images. Researchers were able to extract an approximate representation of the signal from the smaller vessels feeding the active neurons using algorithms such as the principal components analysis [62, 128, 151, 341, 342, 405], repeated measures analysis of variance [127] and independent component analysis [414]. They were able to effectively improve the spatial resolution and signal-to-noise.

In this work, I introduce an algorithm using principal components for analysis of laser speckle flowmetry data as post-script to the previous analyses described. This is a potential new path to tackle the analysis of the speckle images. Here, I simply demonstrate its feasibility and point out one additional information that became apparent at the end of this analysis. It should, however, be

noted that this method requires substantial further development and similar results were obtained on three of the animals mentioned above but not in all the series measured. This can be attributed to the nature of the principal components and that each data set should be analyzed independently of others.

For this analysis, the data set is represented as

$$d = d(\mathbf{r}, t) \tag{4.3}$$

where d is the gray level at time index t for pixel location $\mathbf{r}$ in 2D. In the "traditional difference" imaging, we would select one image as a baseline or the mean of of several images as baseline ($d_0(\mathbf{r}, t)$) and try to obtain images of the activation by subtracting this from each image either as $d(\mathbf{r}, t) - d_0(\mathbf{r}, t)$ or $(d(\mathbf{r}, t) - d_0(\mathbf{r}, t))/d_0(\mathbf{r}, t)$.

The information contained in these set of images (d) can be re-organized by the Karhunen-Loeve method or in its discrete form by a principal components expansion [341]. Following Sirovich *et al* [128, 151] I write this expansion as

$$d(\mathbf{r}, t) = \sum_n a_n(t)\psi_n(\mathbf{r}) \tag{4.4}$$

where $\psi_n(\mathbf{r})$ are images of the so-called principal components and $a_n(t)$ are vectors corresponding to temporal components. $\psi_n(\mathbf{r})$ form an orthonormal basis for the representation of the data. The principal components are the eigenvectors of the eigenvalue equation

$$\frac{1}{N}(\sum_t d(\mathbf{r}, t)d(\mathbf{r}', t))\psi_n = \sigma_n^2\psi_n(\mathbf{r}) \tag{4.5}$$

where N is the number of images (or "snapshots") and the covariance matrix (size $M\mathrm{x}M$) is

multiplied by ψ_n on the left. σ_n^2 are the eigenvalues. $a_n(t)$ are further obtained by the projection of d on the corresponding $\psi_n(\mathbf{r})$ by the inner product of the two. In our case the number of pixels, M, is larger than the number of images, N, therefore we instead solve a smaller problem

$$\frac{1}{M}\left(\sum_x d(\mathbf{r},t)d(\mathbf{r},t')\right)\psi_n = \sigma_n^2 a_n(t) \tag{4.6}$$

where the matrix (size NxN) on the left is proportional to the temporal correlation. We, now, obtain ψ_n by the projection of d on the corresponding a_n as

$$\psi_n(\mathbf{r}) = \frac{1}{\sigma_n^2}(d(\mathbf{r},t), a_n(t))_t \tag{4.7}$$

where the inner product is denoted by $(...)_t$.

Each a_n and ψ_n is uncorrelated to others and therefore, it is possible that the neuronal response map is represented by one pair of components (ψ_n and a_n). However, in general, this is not true and in trying to extract the neuronal response map a collection of components may have to be chosen. This is similar to a technique called "truncated differences" [128, 151]. A decision has to be made based the properties of the principal components and/or their visual inspection. In the simplified form, to obtain "truncated differences", one discards all the components above k^{th} components to eliminate noise.

The first eigenimage, $\psi_1(\mathbf{r})$, generally corresponds to the mean of the whole data set which corresponds to a mean "baseline" flow map which was confirmed by calculating the true mean of the images. Therefore, by excluding the first eigenimage while constructing the "truncated" images, we obtain maps of changes from the mean.

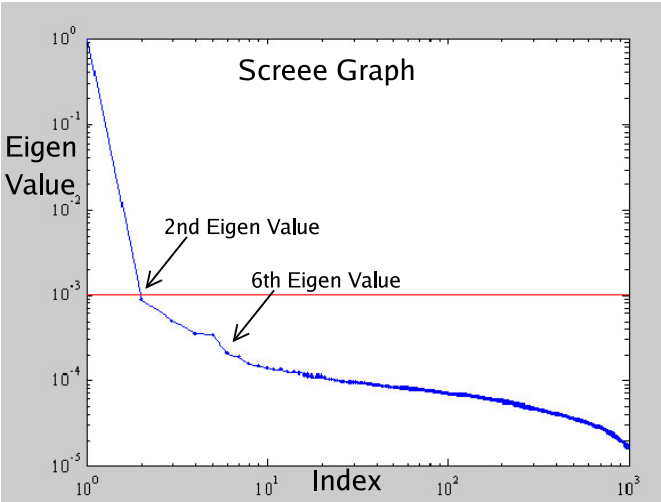

Figure 4.26: Eigenvalues vs eigenvalue index plotted as a "scree" plot. The first eigenimage has disproportionately high eigenvalue. There are discontinuities at second and sixth eigenvalues and beyond the tenth value the curve straightens out.

Generally, the eigenvalues are organized in descending order and the corresponding eigenvectors are also organized similarly. They represent the variances of each components and one could calculate the proportion of total variance (=1) described by first k components as

$$var = \frac{\sum_{i=1}^{k} \sigma_i^2}{\sum_{i=1}^{N} \sigma_i^2} \; . \tag{4.8}$$

For laser speckle data we find that the first few components contain most of the variance. Furthermore, a "scree" graph of eigenvalues vs eigenvalue index provides a visualization of the components, their contribution to each image and their relationship to each other. Figure 4.26 shows an example scree graph. We see again see that first eigenimage has disproportionately high eigenvalue. There are discontinuities at second and sixth eigenvalue and the curve flattens rapidly beyond tenth value. The discontinuities indicate a natural way of grouping the data. Any abnormalities in data such as few images with disproportionately high noise would show up as outliers in such a graph.

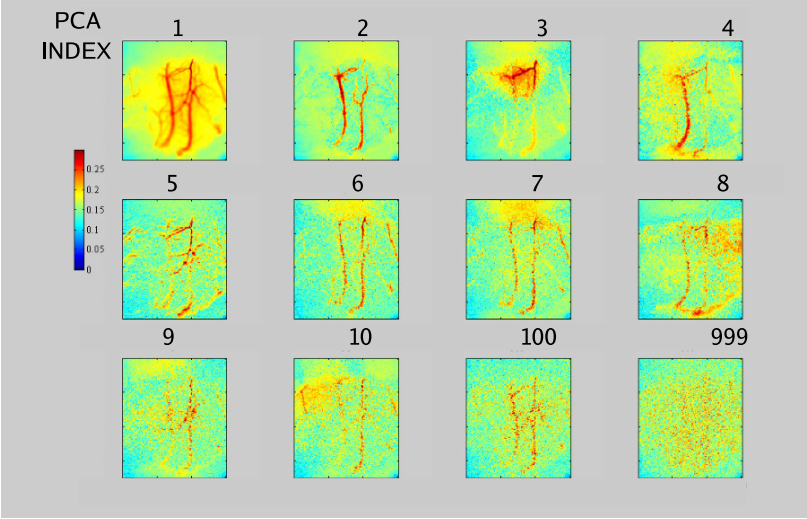

Figure 4.27: A selection of twelve eigenimages from an eight seconds, 2 mA stimulus. Eigenimages 2,4 seem to correspond to large vessels whereas eigenimage corresponds to a network of smaller vessels. Eigenimage 3 is similar to the AFC area visible from "traditional difference imaging" and presumably corresponds to response from capillaries.

Now that we have visualized the contributions due to different components, we visually inspect them to see if they contain any obvious information about the neuronal response.

First, we begin by inspecting the individual eigenimages ($\psi_n(\mathbf{r})$). Figure 4.27 shows a selection of twelve eigenimages from an eight seconds, 2mA stimulus. It is evident that the eigenimages clearly separate response from large vessels (eigenimage 2,4), localized response presumably close to the neuronal representation (eigenimage 3) and network of smaller vessels (eigenimage 5). Several other images show large vessels and the images rapidly degenerate to noise. This type of separation by single eigenimages was achieved in around sixty percent of the series investigated from three animals. In others, few (2-4) eigenimages looked alike and reconstructed images by their summation provided similar information. Most commonly the localized response was evident and was similar to the results obtained in the previous sections.

Figure 4.28 shows a selection of the temporal components ($a_n(t)$) corresponding to the shown eigenimages. For clarity, we have averaged together 10 sets of 20 second activation paradigms.

These plots correlate well with what was guessed from the eigenimages. In Fig 4.28, the third component is immediately visible as the flow time curve similar to those obtained by Laser Doppler methods and by statistical representation of "traditional difference" methods (see Figures 4.18 and 4.19). Components 2 and 4 resemble slower, flatter changes. Comparing these findings to the eigenimages, it becomes evident that this process may have separated vascular response from larger vessels and capillaries. The latter corresponding, presumably, to the capillaries that feed the active neurons and the former to larger vessels feeding those capillaries. The response of the latter is slower and does not have a peak-plateau. The mean response (component 1) has a similar temporal behavior as component 2.

This may be a complete coincidence. To further convince ourselves, we again look at the correlation of these results with the stimulus presentation. A box car is again defined as described in Section 4.3.2.3. Furthermore, we have tested two more functions, namely a box-car function that 1 second forward shifted and extended in duration relative to the stimulation and finally a gaussian curve which is visually matched to the laser Doppler curves. It was found that all three results were qualitatively identical. Figure 4.29(top) shows correlation coefficients for the first 10 components beyond which it oscillated around zero indicating that there is no correlation with the stimulation. A close look reveals that Figure 4.29(bottom) shows the highest correlation at component 3 and similar correlation for component 2 and 4. This observation supports our hypothesis that the visual inspection of the eigenimages and temporal components revealed information that is directly related to the various components of the stimulus and are not the result of a random coincidence. Other components with high positive or negative (negative coefficient is as significant as a positive due to the nature of principal components analysis) coefficients correspond to significant vascular coefficients.

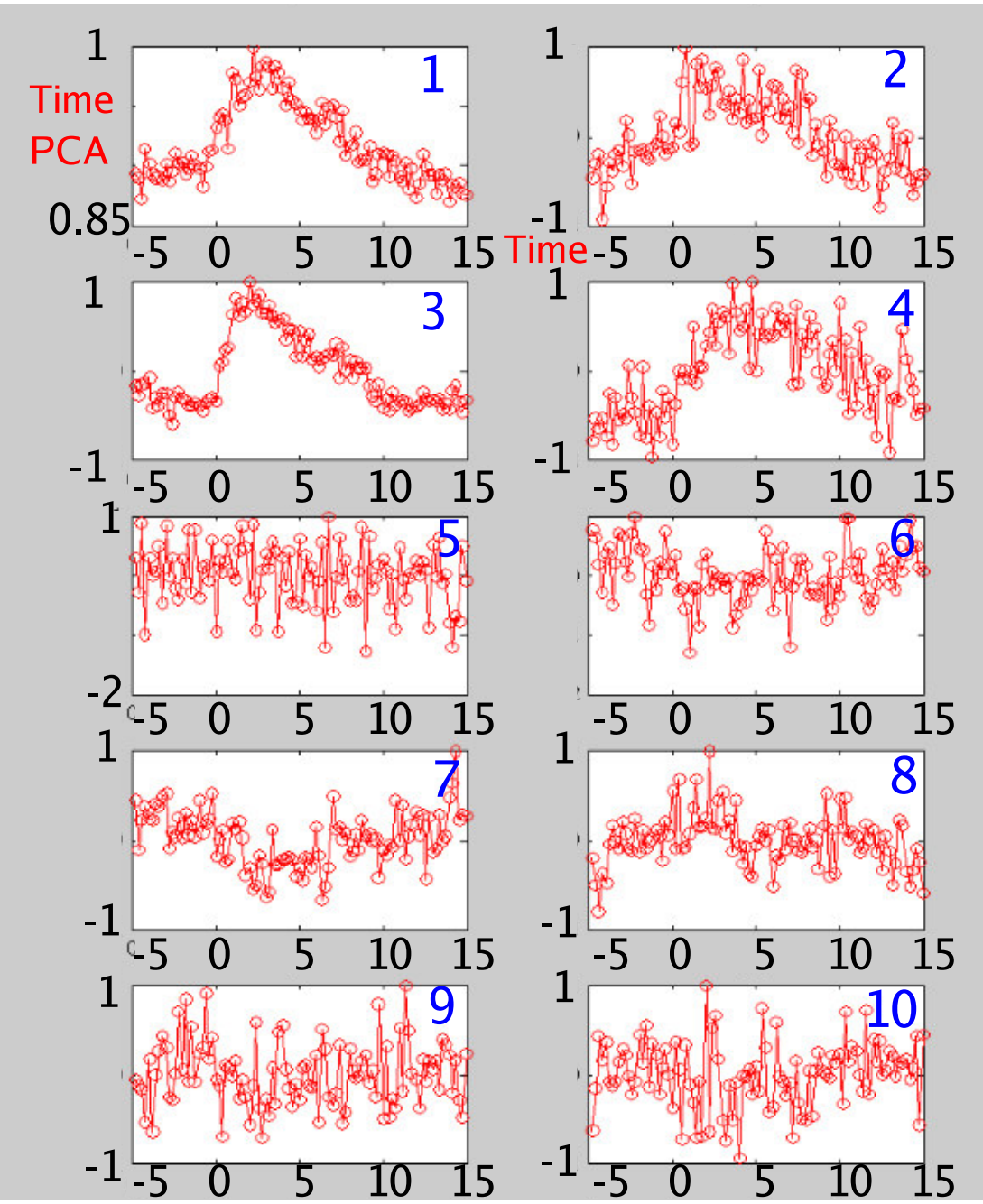

Figure 4.28: Selected temporal components from PCA corresponding to the eigenimages shown. The curves are obtained by averaging ten sets of stimuli as before.

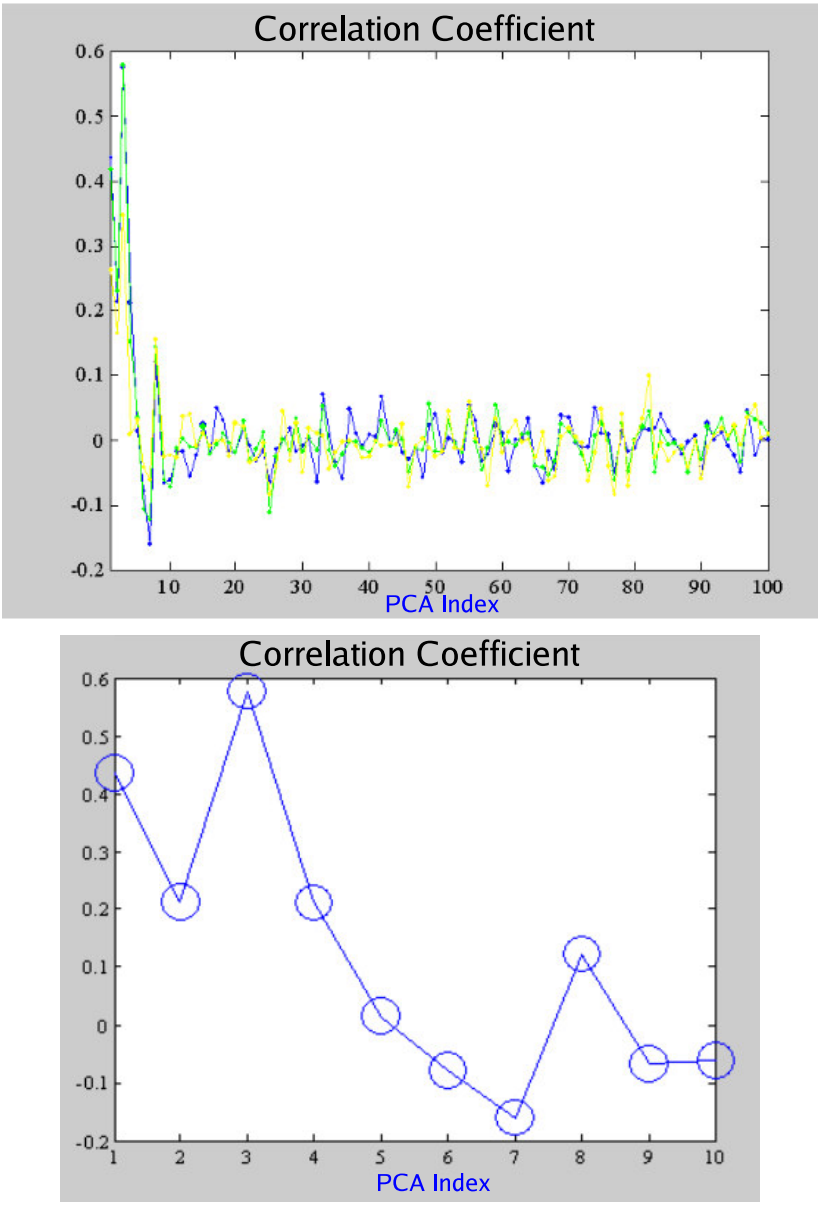

Figure 4.29: (Top) Correlation with an unshifted box-car (blue), shifted box-car (green) and gaussian (yellow) representation of the stimulus presentation. (Bottom) A closer look at only the first ten components.

The above analysis provided a basis for extracting a set of principal components for reconstructing a "truncated" image that represents the neuronal response. In some cases, this was derived from a single eigenimage, in others few eigenimages were used after inspection of the images, temporal components and the correlation coefficients with the stimulus presentation. By reconstrucing a $d_r(\mathbf{r}, t)$ using only these components in Equation 4.4, we can generate a time series images similar to Figure 4.17. This provides yet another way of separating signals from noise.

In conclusion, the principal components analysis has provided (1) a representation of the AFC response area similar and potentially more accurate than "traditional difference imaging", (2) an identification of the shape of the temporal response was without any ambiguities about the choice of thresholds, (3) a suggestion that the large vessels behaved differently than the smaller, presumably, capillaries. This is a promising new algorithm to be employed in the analyzes of speckle flowmetry images. With more experience in interpreting the PCA results, creating better input data sets and with more statistical evidence, it may prove to be a useful tool to extract information that is not easily visible (e.g the large vessel vs capillary response) from "traditional difference imaging". It should be noted here that we were *not* able to obtain similar results by choosing a ROIs that corresponded to the large vessels only and that these results are so far mainly anecdotal.

4.7 APPENDIX: Hemodynamics of Hyperventilation Measured on Human Brain

For the hyperventilation studies of global changes, four DOT and eight DCT detector positions were used with six source positions for DOT and a single source for DCT (Figure 4.30). A non-uniform range of separations were available for DOT and the inherent symmetry of the probe was

used to calibrate the source-detector coupling coefficients. Thus, we were able to obtain absolute values of the oxygenation as well as the baseline optical properties. DCT used four separations which enables us to separate signals from the skin/skull and the brain. The largest separation was 3 cm for DCT and 6 cm for DPDW. The fibers were attached to a flexible, dark, silicone pad and held in place tightly on the volunteer's head by layers of straps. One frame was acquired every two seconds.

Healthy volunteers were recruited and screened for history of previous neurological and cardio-vascular diseases. None had a reported history. A certified physician/neurosurgeon was present at all times. For the hyperventilation studies, an oxygen tank was available in case the subjects needed oxygen following the experiment. The protocol was approved by the Internal Review Board (IRB) of University of Pennsylvania.

The subject was asked to sit down comfortably and the probe was placed on the side of the forehead, right below the hairline where the skull is thinnest (Figure 4.30. It was held tightly in place with medical straps which also covered their eyes. The subjects reported a slight sense of tightness initially. They were then asked to relax for few minutes while the signal levels were tested. It was possible (in most cases) to identify problems with probe placement from the signal level and the shape of the correlation curves. If necessary, the probe was readjusted until the signals were judged to be adequate. Following a three minute baseline, the subject was asked to take very deep breaths at 2Hz. The rate was controlled by auditory signals from the experimenter. After 30 seconds of hyperventilation, the subjects stopped and relaxed for five minutes. This was repeated twice on each subject. Some subjects noted increased pulse rate and one subject had a mild sensation of dizziness. Longer baselines were obtained for subjects where abnormal shifts were observed. Ten volunteers (n=10) were recruited for the hyperventilation study. Two were

discarded because a great deal of motion was noted during the data acquisition and data analysis revealed artifacts. They were, however, used to calculate the average baseline properties. Another two were discarded because the data showed large shifts and noise, potentially a result of probe misplacement.

Different data analysis methods were described in details in Chapter 2. A multi-distance, wavelength dependent semi-infinite fit was used to extract the optical properties when using the probe shown in Figure 4.30. Absolute values of Y_t, THC and the optical properties were measured during baseline. The relative values were calculated during the stimulus presentation.

Figure 4.31 shows the typical hemodynamic response to hyperventilation. As expected, there is a distinct decrease in oxygen saturation (Figure 4.31(a) which recovers to baseline following hyperventilation. Figure 4.31(b) shows the change in cerebral blood flow normalized to the baseline from one volunteer with a characteristic decrease. In some volunteers (n=3), an initial increase was observed prior to the flow decrease during some runs (n=4) as also seen in the second run in Figure 4.31. This was unexpected and could potentially be due to increased heart rate that was reported, or perhaps due to a lag time in volunteer response, i.e shallower breaths for the early period. A small early increase in pCO_2 was reported in one prior study [300] (although the protocols are not identical) which may lead to an early increase in CBF. Better monitoring of physical parameters such as the exhaled carbon-dioxide, heart rate and blood pressure may enable us to overcome this ambiguity.

Two trials per volunteer were block averaged and the resulting curves were averaged over all volunteers (n=6). This resulted in a mean CBF decrease of $-45.5 \pm 11.5\%$. Baseline oxygen saturation was found to be $68 \pm 5.3\%$ and change was $-3.75 \pm 0.95\%$. Mean total hemoglobin concentration was 85 ± 22 μ M. However, both the absolute value and changes depended on the

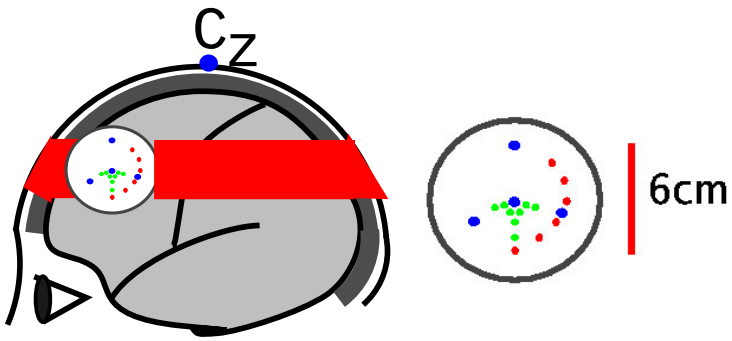

Figure 4.30: Placement of sources (red), DOT (blue) and DCT (green) detector fibers are indicated.(a) Placement of the probe for hyperventilation at the side of forehead below the hairline. Source detector separations range from 0.5 cm to 6 cm for DOT and from 0.5 cm to 3 cm for DCT. 10-20 system is indicated by the black grid.

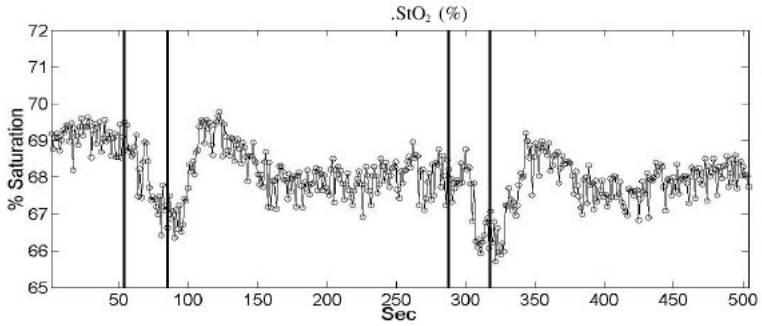

(a)

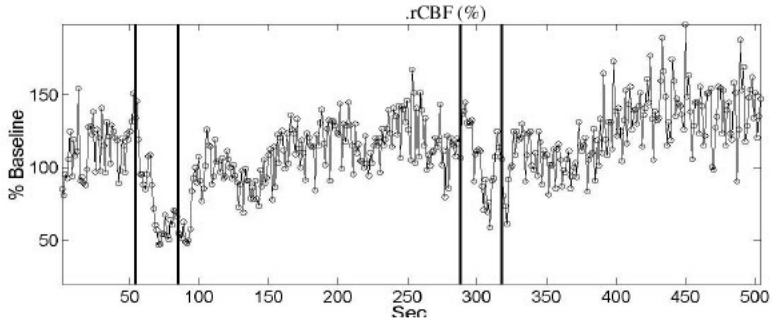

(b)

Figure 4.31: Change in (a) oxygen saturation and (b) cerebral blood flow (b) due to hyperventilation.

assumed values of the scattering ($\mu_s' = 10\ \mathrm{cm}^{-1}$) and background chromophores (water to lipid ratio of 50%). Oxygen saturation was found to be independent of this assumption. This is the result of our inability to calibrate the phase of the observed signals which could be avoided by better modeling/calibration of the source detector coupling. For the purposes of this feasibility study, this additional complication was not necessary. Observed changes in blood flow are similar to that reported in the literature ($\approx 40 - 50\%$ reduction in CBF) [340, 369]. The oxygenation and blood volume changes have the same trend observed elsewhere [137, 300].

Chapter 5

Hemodynamics of Other Physiological Conditions

5.1 Outline

In this chapter I present measurements of hemodynamics on two different physiological conditions; (1) human arm and leg muscles, (2) mice tumors undergoing photodynamic therapy. These measurements further demonstrate the utility of the hybrid method and the range of its capabilities. The measurements on muscles are examples of dynamic and large tissue volumes under extreme conditions, whereas mice tumors are relatively small, diseased tissue volumes undergoing hemodynamic changes due to treatment. Optical techniques are validated in these measurements by comparing to other modalities. In case of photodynamic therapy, a strong correlation was found between hemodynamic changes measured and treatment efficacy, indicative of great clinical potential.

5.2 Muscle oxygenation and flow during cuff occlusion of arm and leg flexor muscles and during plantar flexion exercise

5.2.1 Introduction

In this section, I describe measurements of hemodynamics in arm and leg flexor muscles of adults during exercise and cuff occlusion. After describing the clinical relevance of these measurements and presenting a case for the utility of hybrid optical techniques in this field, important instrumentation/methodology questions are answered experimentally. Specifically, diffuse correlation spectroscopy is shown to be able to penetrate through the upper layers and probe the muscle tissue with adequate signal-to-noise and without intractable problems due to motion artifacts. The hemodynamic response in healthy adults is characterized and an anecdotal study of a patient with peripheral arterial disease (PAD) is presented. These results are first of a kind where flow and oxygenation is measured simultaneously in this setting, enabling estimation of the oxygen metabolism. The results are compared to the literature as a preliminary validation. The presentation here follows our previous and upcoming papers [120, 408, 411].

5.2.1.1 Clinical Relevance

Characterization of the oxygen consumption and metabolism with optical methods in skeletal muscles has important implications in exercise medicine [269], for treatment, screening and understanding of diseases such as the peripheral vascular disease (PVD) or peripheral arterial disease (PAD) [133, 259], as well as for fundamental understanding of the workings of the muscle within the context of the cardiovascular system [64, 71].

When muscles do work, energy is consumed, which, in turn, increases the demand for oxygen. The body tries to meet the demand by supplying more oxygenated blood and by increasing the blood flow speed. Different tissues respond differently and have a varying ability to compensate for the increased demand. Skeletal muscles are particularly responsive and very large changes in hemodynamics are possible. The measurement of hemodynamics is complicated due to large changes in the physical shape of the muscle doing exercise [220]. The relationship between measurable quantities such as blood oxygen saturation (arterial, venous or tissue averaged), total hemoglobin concentrations and blood flow speed and tissue metabolism is not trivial [64]. In fact, the tissue metabolic rate of oxygen consumption ($TMRO_2$) in the skeletal muscles has been modeled in a similar manner to the cerebral metabolic rate of oxygen consumption ($CMRO_2$) (see Section 2.3) for the simplest paradigms [78, 187, 289].

In sports medicine, useful information can be obtained by monitoring the improvement of an athlete's maximum capacity [269, 283]. Diffuse optical tomography/spectroscopy [35, 71, 111, 172, 237, 322, 379, 397] has successfully been applied to measurements in a large variety of conditions from simple plantar flexions to speed skating [26, 27, 32, 68, 87, 97, 196, 237, 249, 282, 303, 319, 354, 391].

In our laboratory, we are monitoring the progress and treatment of peripheral arterial disease (PAD) which is a common circulation problem in which the arteries that carry blood to the legs or arms become narrowed or clogged. PAD affects about 1 in 20 people over the age of 50, or 10 million people in the United States. More than half the people with PAD experience leg pain, numbness or other symptoms. One of the simplest and most useful parameters to objectively assess lower extremity arterial perfusion is the Ankle Brachial Index (ABI) and Thigh Brachial Index

(TBI). The TBI and ABI help define the severity of the disease and successfully screen for hemodynamically significant disease. TBI/ABI are easily reproducible indirect measures that roughly correlate with clinical improvement. Non-invasive spectroscopic and imaging methods measuring the hemodynamic response of PAD patients would enhance the screening and monitoring of treatment by allowing simultaneous measurements of multiple parameters at multiple locations [379].

5.2.1.2 Need for Optical Techniques

Over the years, a variety of non-invasive techniques have been developed to study tissue hemodynamics of the muscle; (1) Conventional venous occlusion plethysmography has been employed for more than 50 years [318, 387], however, since venous occlusion interrupts the blood flow to the whole organ, it does not provide regional information, and can only be used in the static state or during brief exercise. (2) Ultrasound Doppler is another common clinical tool used to measure blood flow in large vessels [229, 230]. However it is not sensitive to blood flow in smaller vessels, and does not readily allow continuous measurements during exercise. (3) Laser Doppler can non-invasively monitor the flow change, but most systems measure the tissue surface only (i.e. penetration depth < 500 μm) [33, 201]. Very recently, Binzoni *et al* [34] have extended its applications to deeper tissues using a larger (1.5 cm) source-detector separation. However, they have not reported results from larger separations and the current status of the published work limits its applicability due to limitations in penetration depth (see Section 5.2.4.1). (4) MRI/NMR spectroscopy has high temporal and spatial resolution, and so has become a standard technique for noninvasive measurement of the metabolic response; however, its clinical use is limited due to high cost and poor mobility [69, 70, 144, 304, 361, 362]. (5) Finally, PET [56] has similar clinical limitations, and also has poor spatiotemporal resolution compared to MRI. NMR spectroscopy and PET can

measure metabolic response directly which is not yet possible with optical methods and hence have to rely on multi-parameter measurements (see Section 2.3).

Near-infrared spectroscopy has filled a part of this void by determining local tissue blood oxygen saturation (StO_2) and total hemoglobin concentration (THC) with high temporal and limited spatial resolution. The instruments are generally portable, relatively inexpensive and flexible. Unfortunately, it can not readily be used to measure oxygen metabolism. Some groups have estimated blood flow and oxygen consumption rate in muscle tissue from the change of THC or deoxy-hemoglobin concentration by applying a venous occlusion or an arterial occlusion to a limb [97, 218, 396]. Although successful in achieving similar results as venous occlusion plethysmography, they also suffer from the same short-comings due to the interruption of blood flow during occlusion. Therefore, it is desirable to develop methods for non-invasive, continuous measurement of dynamic blood flow in local muscles that could be combined with measurements of oxygenation. This is where, I believe the hybrid optical method combining DOT and DCT have a lot to offer for measurements of hemodynamics in muscles.

5.2.1.3 Translation of Small-Tissue Instrumentation to Human Muscles

Diffuse correlation tomography, being similar to DOT in its formalism and instrumentation should work in this realm where DOT has had great success. Our previous experience on measurements in the brain support this hypothesis. In order to translate the hybrid technique to measurement of hemodynamics in skeletal muscle and to the clinic, several issues has to be addressed:

1. Can DCT penetrate through upper layers, such as fat and skin to the muscle? (see Figure 5.1(c))

2. Are hybrid measurements sensitive to changes in oxygenation and flow in the muscle?

3. Is it feasible to design probes for exercising calf muscle that are comfortable, have adequate contact and are not affected heavily by motion?

4. What is the range of healthy response and is it separable from the diseased muscle response?

5. Can $TMRO_2$ be reliably estimated using a simple model?

This study was designed to address these issues by characterizing the response of the healthy arm and leg muscle to prolonged cuff occlusion and light exercise using the Generation IV instrument (see Chapter 3). Briefly, three wavelengths – 676 nm, 786 nm, 830 nm – modulated at 70MHz for NIRS measurements and a continuous wave laser with long coherence length at 800nm for DCS were used. The probe shown in Figure 5.1 had one source (red) fiber at the center of eight DCT detector fibers (green) and four DOT detector fibers (blue) with six source (red) fibers arranged in a 3 cm radius circle. Black, flexible silicone material was used to tightly hold the fibers in place and elastic straps were used to fix the probe around the muscle. Source detector separations ranged from 0.5 - 3 cm for DCT and 0.5 - 6 cm for DOT. The volunteers did not report any discomfort associated with the placement of the probe. A complete set of data was acquired every 2.5 seconds.

5.2.2 Experimental Protocol

5.2.2.1 Cuff Occlusion

Cuff occlusions were used to investigate the different layer responses in order to estimate the penetration depth and to validate the results in the ischemic states. The hemodynamic response to extended cuff occlusion has been fairly thoroughly measured and characterized and is, therefore, a good model to validate our results.

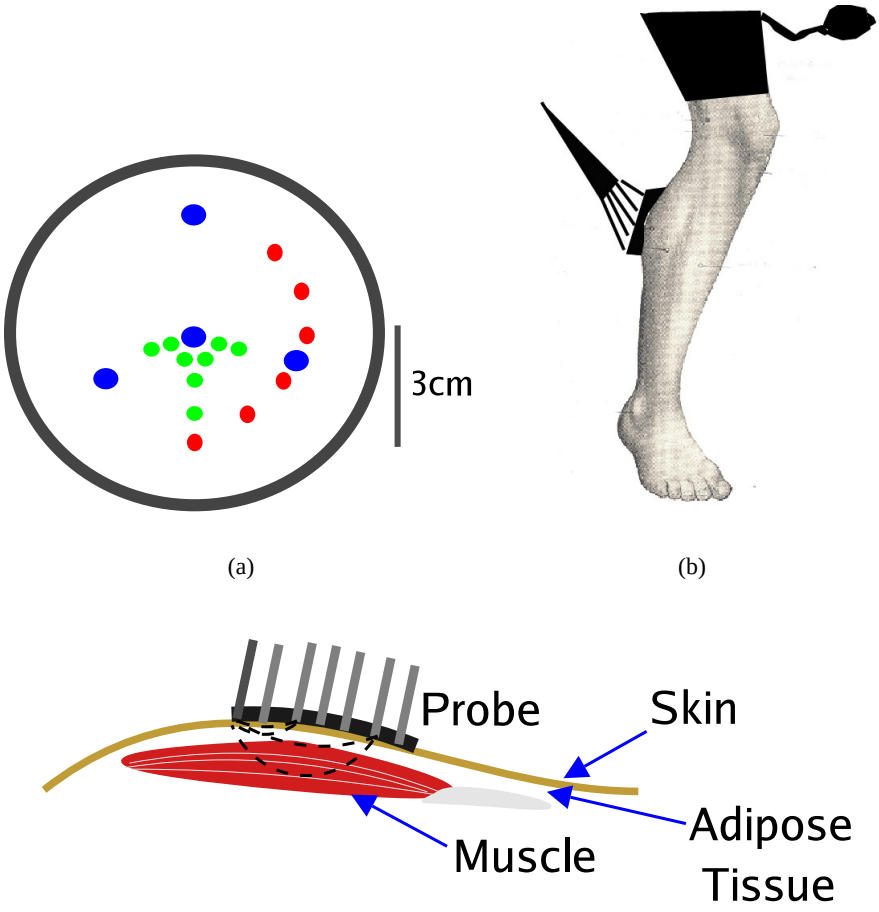

(a) (b)

(c)

Figure 5.1: (a) A circular probe made of elastic, black silicone (RTV) with four DOT detectors (blue), eight DCT detectors (green), six DOT and one DCT source fibers (red) was attached to the calf or forearm muscle with straps (see (b)). Drawing modified from ref [161]. (c) The layered structure of the muscle with overlaying adipose tissue and skin. Dashed lines indicate the photon paths for different source-detector separations.

We have particularly concentrated on the reactive hyperemia following the cuff-release. The reactive hyperemia after cuff occlusion is the transient increase in blood flow following rapid release of an inflated cuff and is related to the ability of the organ's auto-regulation [306]. It is a heterogeneous response that varies between organs. For example, skeletal muscles show moderate auto-regulation while cutaneous layers including the adipose tissue show little or none [306]. The tissue hypoxia and related build up of vasodilator metabolites during extended occlusion lead to dilation of the arterioles and a decrease of vascular resistance leading to reactive hyperemia. During this period, oxygen is replenished and metabolic stimulus for vasodilation is washed out, causing vasoconstriction and thus blood flow and oxygenation return to their normal resting levels. The amount of this accumulation depends on the metabolic rates and the lower metabolism of the adipose tissue results in lower hyperemic response than the muscle tissue. We used this observation to investigate the penetration depth of DOT and DCT at a given source detector pair by comparing the hyperemic response observed from each pair. The result was compared to expectations from modeling of light penetration (Chapter 2) and the estimates of muscle depth. A Lange Skinfold Caliper (Beta technology incorporated, Cambridge, Maryland) was used to measure mechanically the thickness of the skin and the subcutaneous fat layer (and the fascia) above muscle (see Figure 5.1(c)).

Cuff Occlusion of Arm flexors

Subjects were asked to lie supine and resting arm blood pressure in the brachial artery was measured. The optical probe was then placed over the wrist flexors (carpi ulnaris, palmaris longus, carpi radialis, digitorum superficialis) and secured with an elastic bandage. After three minutes of

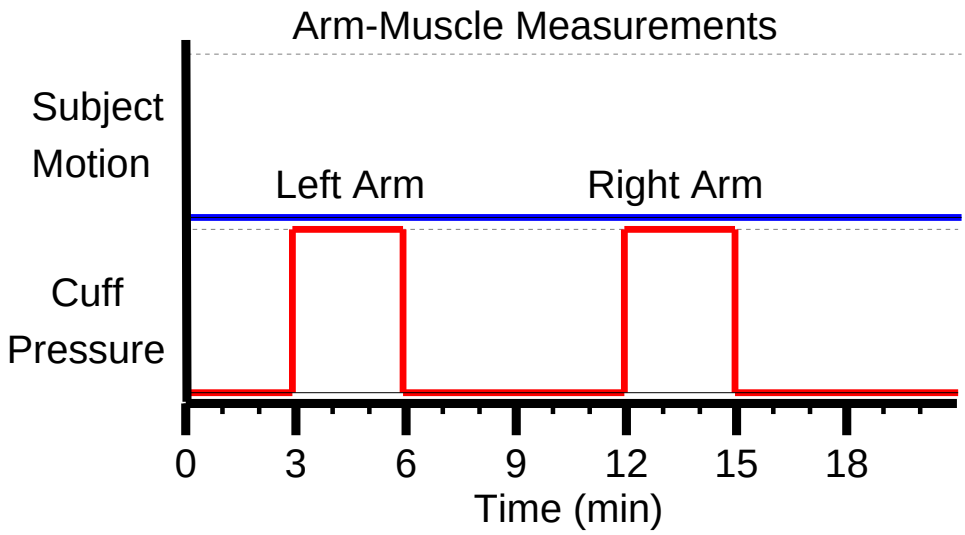

(a)

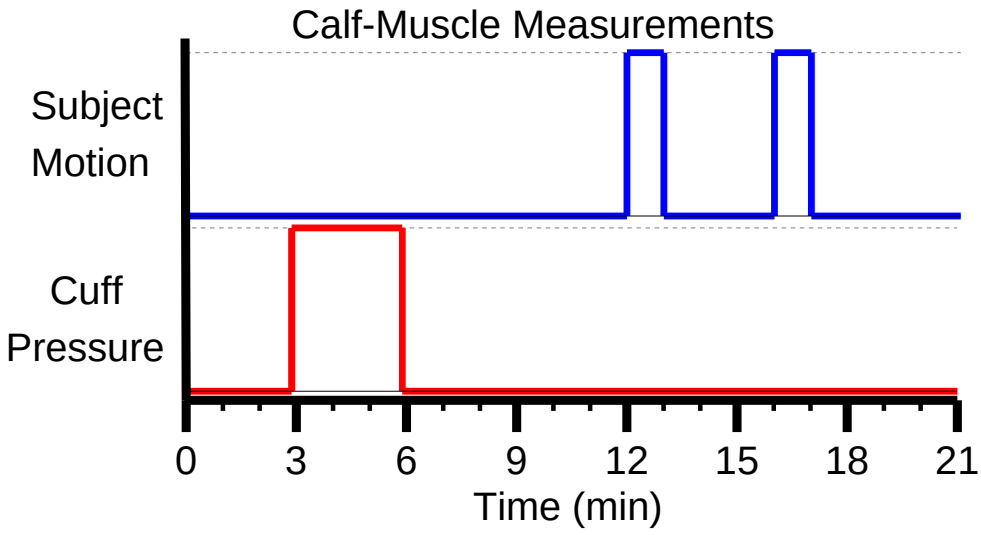

(b)

Figure 5.2: Timing diagrams for (a) arm, (b) leg. The baseline “recovery” timings are approximate. Further details are explained in the text

resting baseline measurement, the blood pressure cuff was inflated to 180 mmHg, held for 3 minutes and then released. Recovery measurements were made for 3 minutes (or longer if necessary). Figure 5.2(a) illustrates the protocol.

Cuff Occlusion of Leg flexors

Subjects were asked to lie on their side to allow for access to the popliteal artery while resting thigh blood pressure in the popliteal artery was measured. The subjects then resumed the supine position and the optical probe was placed over the calf flexor (medial gastronemius) and secured with an elastic bandage. After three minutes of resting baseline measurement, the blood pressure cuff was inflated to 200 mmHg, held for 3 minutes and then released. Recovery measurements were made for 3 minutes or longer if necessary. Figure 5.2(b) illustrates the protocol.

5.2.2.2 Plantar Flexion Exercise

Following cuff occlusion of the leg and subsequent recovery period, subjects were then asked to stand and after the 3 minute baseline, perform 30 plantar flexion exercises (toe-ups) within one minute. Figure 5.2(b) illustrates the protocol.

Plantar flexion exercise was selected because it works the gastrocnemius muscle and can be performed while stationary. This muscle is used in both stair climbing and walking and lack of sufficient blood supply to this muscle in PAD patients results in symptomatic calf pain. The gastrocnemius muscle is of adequate size and easily localized for placement of the optical probe. In an ongoing study utilizing PAD patients (unpublished study Mohler *et al*, UPENN), the exercise was sufficiently easy to be completed by all subjects. The 30/minute PF exercise intensity was rated easy to somewhat difficult, by all control subjects but PAD subjects commonly rated the exercise

as hard. Improvement in the rate of oxygen resaturation from plantar flexion exercise (half time to recovery) has been shown to correlate to improvements in TBI and ABI after revascularization in PAD patients [205].

5.2.2.3 Volunteer Population

The studies were approved by the Institutional Review Board (IRB) at University of Pennsylvania and took place at Hospital of University of Pennsylvania. Two female (n=2) and seven male subjects (n=7), ages between 24-34 (mean 28.4 ± 3.0) were recruited by verbally informing them of the ongoing study. None of the volunteers have reported any problems with their circulation or any pain in their extremities. An additional study was carried out with one PAD patient aged 65 who complained of problems in both legs but none in the arms. Volunteers were comfortable with the placing of the optical probe and the measurements procedure. The ankle brachial index (ABI) of the healthy subjects is 1.01 ± 0.02 whereas the ABI of the patient is 0.4 which is considered to be indicative of severe PAD according to the Rutherford-Becker Classification [321].

5.2.3 Data Analysis

5.2.3.1 Oxygenation and Flow

The basic analysis method follows Chapter 2. Briefly, for oxygenation, we model the tissue with the wavelength-dependent semi-infinite solution to the photon diffusion equation to fit for the changes in optical properties and estimate changes in hemoglobin concentrations. A range of source-detector separations were used simultaneously to do a multi-distance fitting. The circular symmetry of the probe was used to calibrate the source and detector fibers. A similar approach

was taken to estimate blood flow using a semi-infinite model. Our model assumes the baseline reduced scattering coefficient as $\mu_s'(\lambda) = 5$ cm^{-1} from literature [379]. This assumption could affect the estimated relative changes. We investigated this by varying the assumed value and comparing the effective change in both absolute and relative hemoglobin concentrations. A 100 $\%$ change in baseline optical properties introduces less than a 5 $\%$ error in calculated relative concentrations. The error induced into the calculated rBF was also estimated and less than 1 $\%$ change was found which is lower than the experimental noise. This assumption is a temporary limitation which could be avoided by employing more source fibers and by calibrating the coupling coefficients of the instrument more accurately. However, the hemodynamic changes to be investigated are much larger and these errors are tolerable.

5.2.3.2 Tissue metabolic rate of oxygen consumption

Tissue metabolic rate of oxygen consumption ($TMRO_2$) is modeled in the same manner $CMRO_2$ was modeled previously (Chapter 2) combining the blood flow data and oxygen saturation data. Briefly, in steady-state, $TMRO_2$ depends on the difference in oxygen concentration across the vasculature (i.e. arteriole minus venous) times the blood flow rate: $TMRO_2 = (OEF)(BF)([O_2]_a)$. Here $[O_2]_a$ is the arteriolar oxygen concentration, OEF is the oxygen extraction fraction defined as $([O_2]_a - [O_2]_v)/([O_2]_a)$, subscripts **v** and **a** denote venous and arteriole sides, x denotes multiplication, and BF is tissue blood flow. This model was applied previously to muscle by other groups [78, 187, 289]. After a series of assumptions as discussed previously in Section 2.3, the relative changes can be determined as $rTMRO_2 = (rOEF)(rBF)$ where $OEF = (SaO_2 - StO_2)/(\gamma SaO_2)$ where SaO_2, and StO_2 are arteriolar, and tissue saturations respectively, and γ indicates percentage of blood volume contained in the venous component of

the vascular system. SaO_2 is not measured by DOT but is assumed to stay constant near unity. This assumption was verified and 98% arterial saturation was assumed during the mild plantar flexion exercise [303]. As before, we also assume that γ does not change and divides out of the equation for rOEF. Although this may not be true, i.e the percentage of blood volume contained in the venous component of the vascular system can change during each plantar flexion, the influence of γ change could be decreased by the averaging effect of 2.5 sec sampling time in our study and the even controlling of mild exercise power. A detailed discussion about this assumption error is beyond the scope of this study (for its effects on measurements of rat brain hemodynamics, see Culver *et al* [91]). The changes in pH level in tissue during exercise may also influence oxygen consumption rate. Fortunately, no significant pH change during this mild plantar flexion exercise has been found [238]. We do not attempt to estimate $TMRO_2$ during cuff occlusion because this model fails in that regime. Furthermore, any potential complications due to changes in temperature and other chemicals are beyond the scope of this study. Some modeling assumptions involved are re-visited in the presentation of the results where we compare the findings to the literature.

5.2.3.3 Investigation of Response from Different Layers

As shown in Figure 5.1(c), the probed tissue volume is layered (skin, adipose tissue and muscle). From diffusion theory, the maximum penetration depth of diffuse light in tissue depends on the tissue optical properties and the source-detector separation. Therefore, signal from a given source-detector separation provides the information from different tissue layers that are being probed. In order to investigate this, data from cuff occlusion (Section 5.2.2.1) is analyzed on a single source-detector pair basis. Relative blood flow (rBF) was obtained by simply using the DCS data derived from the corresponding single source-detector pair without averaging. Similarly, the DOT data

from single source-detector pair was normalized with its baseline value to calculate the relative change of tissue blood oxygen saturation using the baseline StO_2 obtained from multi-distance DRS measurements as described before.

5.2.3.4 Data Presentation and Response Characterization

Time curves for StO_2 ($\%$), THC (μM) and relative BF ($\%$ change) with error bars are estimated by the standard deviation of 50 time points during the baseline converted to percent error are presented for both paradigms. $rTMRO_2$ curves are calculated and presented for plantar flexion. Mean and standard deviation of the mean are tabulated for maximal changes (Max Δ), time constants from manipulation onset (T_m (sec)) to maximal response, recovery half time ($T_{1/2}$ (sec)) and amount of overshoot (OS ($\Delta\%$)).

5.2.4 Results and Discussion

5.2.4.1 Do both DCT and DOT Probe Deep Muscle Tissue?

DOT is relatively well understood and has been applied and validated for measurement of skeletal muscle hemodynamics [237, 322]. The effect of the adipose tissue thickness has also been investigated [371]. However, our results are the first of their kind and and we wished to address the issue of adequate penetration experimentally. As described in Section 5.2.2.1, the hyperemia following rapid release of cuff occlusion is hypothesized to have originated from the strong auto-regulation of the muscle tissue and to a much lesser degree from other surrounding tissues. Therefore, it should be possible to estimate the depth probed by a given source detector separation by looking at the hyperemic overshoot after the cuff-release.

Figure 5.3 shows the rBF (top) and StO_2 (bottom) responses during leg cuff occlusion from

different source detector pairs measured on one healthy individual. The magnitude of reactive hyperemia derived from the source-detector separation of 2 cm is $>$2 times higher than those from other shorter separations. According to the results measured by the Lange Skinfold Caliper, the thickness of the top layers (skin and fat) of leg flexors and wrist flexor are 5.5 ± 0.4 mm and 2.8 ± 0.6 mm respectively (n=9). This is in agreement with the observed hyperemic response considering that in order to penetrate down to the muscle, the source-detector separation should be $>$1.5 cm. These observations, taken together, suggest that the strongest hyperemic signal with the separation of 2 cm is mainly derived from the muscle tissue layer, whereas the weaker responses from the shorter separations represent the signals from cutaneous tissues. It is interesting to note that the StO_2 response is weaker at 6 cm similar to that of 0.5 cm. With this large separation, we believe the diffuse light had reached the bone through the skin, fat and muscle layers and hence probed a non-reacting tissue-volume.

Reactive hyperemia from human wrist skin using Laser Doppler flowmetry [33] after 4.5-minute arterial occlusion was observed to be lower in magnitude. Hyperemic skin blood flow increased $\sim$ 2 fold which agreed with the 1-2 fold increases we observed from upper layers and was about two times lower than that from the muscle layer in this study. These findings suggest that both DRS and DCS are able to probe through the upper layers into the muscles, and it is critical to choose the source-detector separations in the appropriate range in order to separate the muscular response from the surrounding tissues.

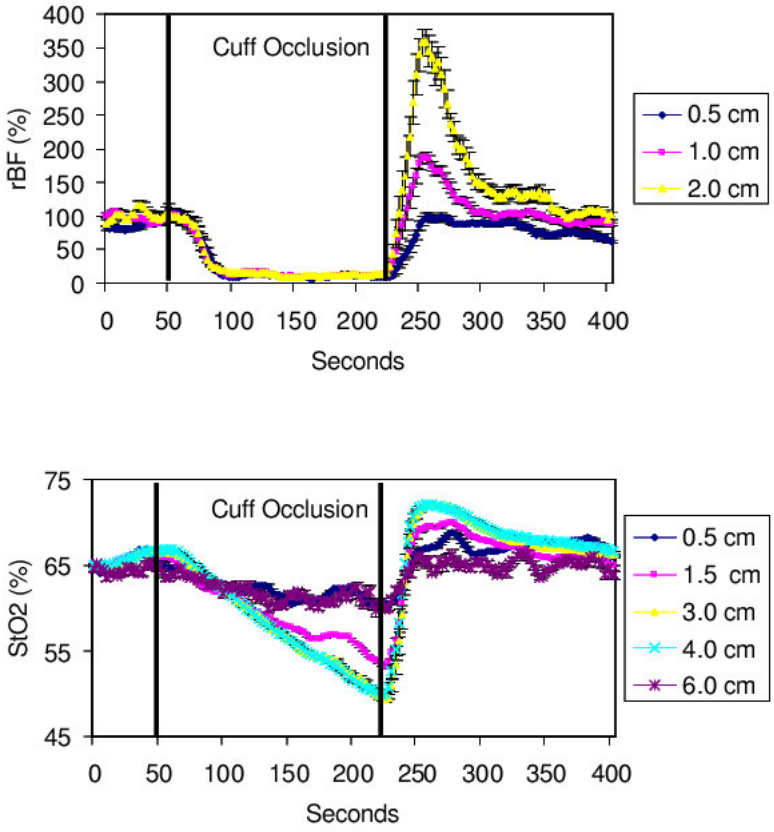

Figure 5.3: Response from different source detector pairs during cuff occlusion. (top) rBF from 0.5, 1.0 and 2.0 cm , (bottom) StO_2 from 0.5, 1.5, 3.0, 4.0, 6.0 cm source-detector separations. The hyperemic overshoot increases with increased separation until 6 cm when it becomes similar to that of 0.5 cm. It is apparent that medium source detector separations, $1.5 - 4.0$, cm probe the muscle whereas the shortest and longest separations probe upper fat, skin and/or bone.

5.2.4.2 Characterization of the Hemodynamic Response

Cuff Occlusion

Cuff occlusion of the leg flexor and wrist flexor (not shown here) produce a similarly characterizable response; a rapidly strong decrease in rBF (-90 $\pm$ 2.4%, n=9) followed by a decrease in StO_2. This lowest measurable blood flow during Cuff occlusion is the so called "biological zero" [359]. StO_2 starts to decrease rapidly but does not reach a minimum for $\sim$ 5 minutes (n=2, from separate measurements not shown here), whereas rBF reaches a minimum within the first minute. The maximum decreases of StO_2 (n=9) occurred at the end of cuff occlusion are -16.0 $\pm$ 2.8% for leg and -19.0 $\pm$ 3.4% for arm. The typical post-ischemic flow peak overshoots are much higher 126.1 $\pm$ 55.2 % for leg and 301.3 $\pm$ 114.4 % for arm, than the oxygen peak overshoots 3.5 $\pm$ 1.0 % for leg and 11.1 $\pm$ 3.4 % for arm. The THC is generally unchanged, however, there is a variation between trials (not shown here). The results are summarized in Table 5.1 and parametrization of the hemodynamic curves is shown in Figure 5.4.

The extreme responses of StO_2 are comparable with the literature if we compare the values at the 3rd minute of occlusion as in the arm [98, 262] and the leg [35, 379]. This is not surprising since similar NIRs technology and similar source-detector separations (2-5 cm) were used.

Other modalities have also been applied to study the flow changes during reactive hyperemia in similar protocols. Studies with Doppler Ultrasound imaging report a 3 to 6 fold peak hyperemic flow after 2 minutes of forearm occlusion [229, 230] which is comparable with DCT finding of ~ 4 fold reactive hyperemia. Both conventional venous occlusion plethysmography [125, 352] and MRS based plethysmography [361, 362] observed $\sim$ 7.5 fold (range 5-12 fold) increases during 3 to 5 minute forearm or calf arterial occlusion which is about 2 times higher than DCT findings in

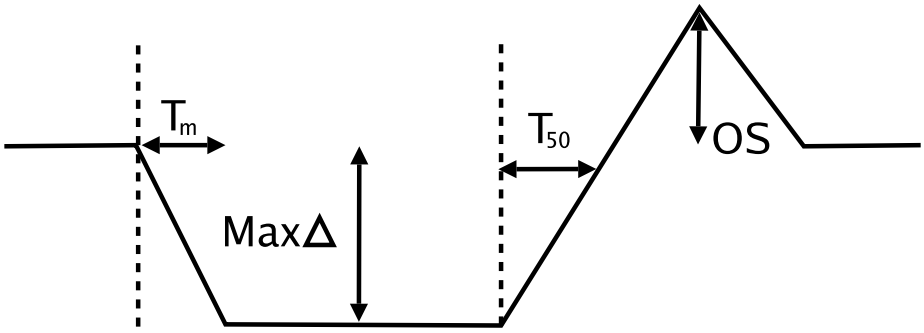

Figure 5.4: Illustration of the parametrization of the hemodynamic curves during cuff-occlusion

agreement with findings of earlier optical studies with NIRS [99, 371, 372]. Arterial spin labeling (ASL) MRI was found to be in good agreement with other established standards, such as PET and radioactive microsphere measurements [304], however, large variations in reperfusion peaks after 5-minute calf occlusion were found [304, 361, 362] which may be due to the inability of MRI to measure baseline flow accurately which necessitates the use of other modalities to approximate the baseline flow [304]. Therefore, we rely on comparison of MRI to plethysmography where a 3.8 fold larger increase was observed [361, 362]. Since DCT flow is 2 times lower than plethysmographic flow which is 3.8 times lower than ASL flow, we roughly estimate the difference between DCS flow and ASL flow by multiplying these two factors: 2x3.8 = 7.6, that is, the DCT flow is $\sim$7.6 times lower than MRI flow. All these inconsistencies between different modalities can be explained in terms of methodological differences which result in differences in the probed vasculature, tissue volume and regions of interest that are being monitored. However, overall, our results are promising and are in relatively good agreement with the literature. More direct comparisons between modalities are being designed in our laboratory.

Parameter	Subject	T_m (sec)	Max (%)	$T_{1/2}$ (sec)	OS (%)
		Leg occlusion			
StO_2	Healthy (n=9)	180	-16.0 $\pm$ 3.3	35.2 $\pm$ 9.0	3.5 $\pm$ 1.7
(%)	PAD (n=1)	180	-15	98	1.5
THC	Healthy (n=9)	N/A	2.6 $\pm$ 5.3	N/A	N/A
(μM)	PAD (n=1)	N/A	-8	N/A	N/A
rBF	Healthy (n=9)	52.2 $\pm$ 11.5	-90.0$\pm$2.4	27.3$\pm$ 4.7	326.1 $\pm$ 55.2
(%)	PAD (n=1)	60	-93	67	165
		Arm occlusion			
StO_2	Healthy (n=9)	180	-24.4 $\pm$ 4.2	20.3 $\pm$ 5.3	11.1 $\pm$ 3.4
(%)	PAD (n=1)	180	-23	23	10
THC	Healthy (n=9)	N/A	2.0 $\pm$ 6.2	N/A	N/A
(μM)	PAD (n=1)	N/A	-5	N/A	N/A
rBF	Healthy (n=9)	27.7 $\pm$ 9.1	-90.4$\pm$2.8	11.9$\pm$ 2	401.3 $\pm$ 114.4
(%)	PAD (n=1)	21	-92	12	310

Table 5.1: Tabulation of the hemodynamic response to cuff-occlusion. Time to reach maximal change (T_m), maximal change (Max Δ), recovery half time ($T_{1/2}$) and relative, hyperemic overshoot (OS) are shown for StO_2, THC and rBF. Average and standard deviation of the mean are reported for nine healthy subjects. Anecdotal results from one PAD patient are also shown.

Plantar Flexion Exercise

Figure 5.5 shows typical time curves for StO_2 (%), THC (μM), rBF (%) and $rTMRO_2$ during plantar flexion exercise from one healthy individual. rBF is calculated by averaging signals from four 2 cm source-detector separations in slightly different locations (results from 3 cm are similar but more noisy). In studies not shown here, we have tested repeatability of the measurements on the same individual (2 trials, n=2) and the variation falls with the error bars shown here. A similar variation is observed between left/right arm/leg of healthy individuals. The general trends are repeatable in all the subjects studied, however, the variation is well above the error bars (see Table 5.2). We characterize the physiological response by the mean maximal change (Max Δ), time constant from manipulation onset to peak maximal response (T_m(sec)) , recovery half time ($T_{1/2}$ (sec)) and amount of peak overshoot (OS). Table 5.2 summarizes this characterization with the mean $\pm$ standard deviation from nine volunteers and one PAD patient are shown.

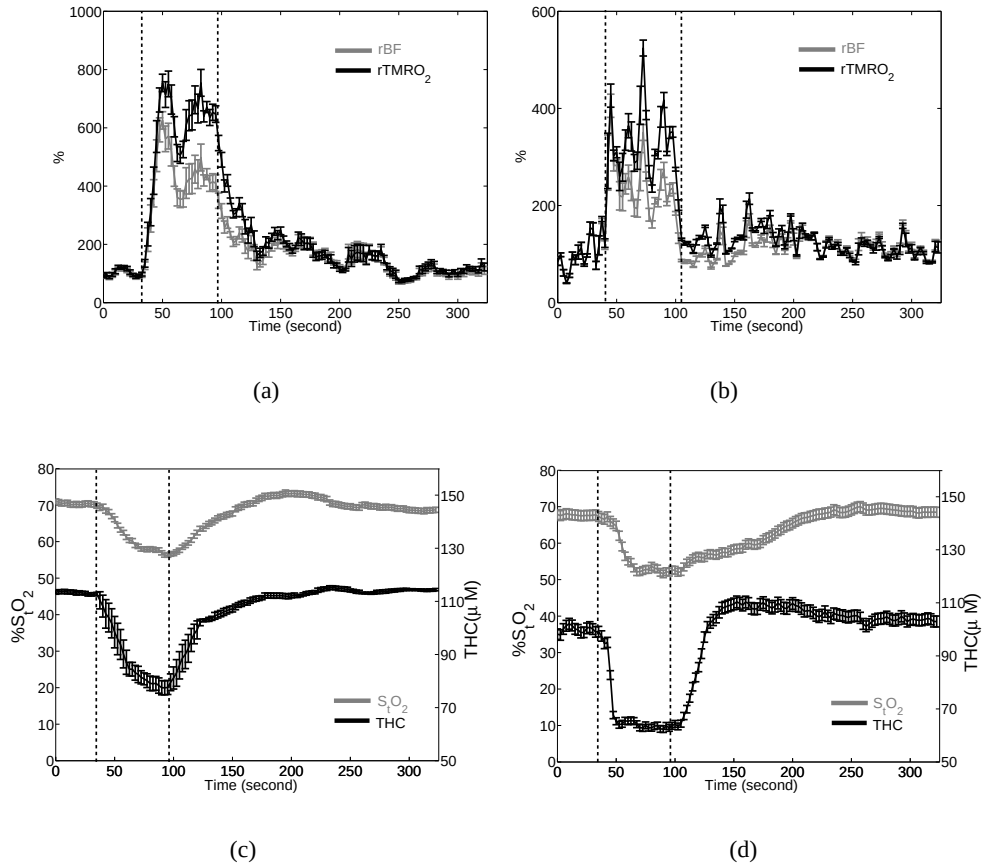

Figure 5.5: Hemodynamic responses during one-minute plantar flexion exercise from a healthy individual (left) and a PAD patient (right). The time curves of rBF and $rTMRO_2$ (top) and StO_2 and THC (bottom) are shown. The error bars are estimated by the standard deviation of 50 time points during the baseline converted to percent error. Vertical lines indicate the beginning and end of the exercise.

Parameter	Subject	T_m (sec)	Max (%)	$T_{1/2}$ (sec)	OS (%)
StO_2 (%)	Healthy (n=9)	29.5 ± 6.0	-19.0 ± 3.4	36.6 ± 7.5	5.3 ± 2.3
	PAD (n=1)	22	-17	80	3
THC (μM)	Healthy (n=9)	16.5 ± 5.0	-20.2 ± 7.6	23.5 ± 4.5	3.6 ± 2.6
	PAD (n=1)	12	-18	25.5	10
rBF (%)	Healthy (n=9)	16.0 ± 5.0	458.8 ± 78.3	12.5 ± 4.0	-10.5 ± 6.7
	PAD (n=1)	12	240	9.5	-10
$rTMRO_2$ (%)	Healthy (n=9)	17.5 ± 7.0	710.1 ± 135.4	12.5 ± 3.5	-8.3 ± 5.5
	PAD (n=1)	12	376	9.5	0

Table 5.2: Tabulation of the hemodynamic response to plantar flexion exercise. Time to reach maximal change (T_m), maximal change (Max Δ), recovery half time ($T_{1/2}$) and relative, hyperemic overshoot (OS) are shown for StO_2, THC, rBF and $rTMRO_2$. Average and standard deviation of the mean are reported for nine healthy subjects. Anecdotal results from one PAD patient are also shown.

The healthy muscle responses (n=9) show a fair amount of variation. At the beginning of the exercise, the oxygen consumption rate in muscle increased greatly (from 100 % to 710.1 $\pm$ 135.4 %). To meet the large increase of oxygen demand, rBF increased rapidly and reached a maximum (458.8 $\pm$ 78.3 %) in a short time (16 $\pm$ 5.0 sec). THC decreased and reached a minimum ($\Delta = -20.2 \pm 7.6 \mu M$) as fast as rBF due to the contraction of working muscle. The largest difference between rBF and rTMRO$_2$ was reached in 17.5 $\pm$ 7.0 sec, which demonstrated the maximum mismatch between oxygen delivery and oxygen demand. Note here, a good understanding of the temporal resolution of the measurements is crucial to evaluate this mismatch. StO$_2$ started to decrease slowly when this maximal mismatch occurred, and reached a minimum (Δ= -19.0 $\pm$ 3.4 %) in 29.5 $\pm$ 6.0 sec. After reaching to the maxima or minima those variables fluctuated around their extrema. Once exercise was stopped, rBF and rTMRO$_2$ recovered to their baselines rapidly, whereas THC and StO$_2$ slowly increased toward their baselines. The time delay between onset of blood flow change and oxygenation response was very clear. rBF responded up to $\sim$50 % faster than StO$_2$. This confirms blood flow as a major driving mechanism for muscle hemodynamics and stresses the importance of measuring blood flow and oxygenation simultaneously to better

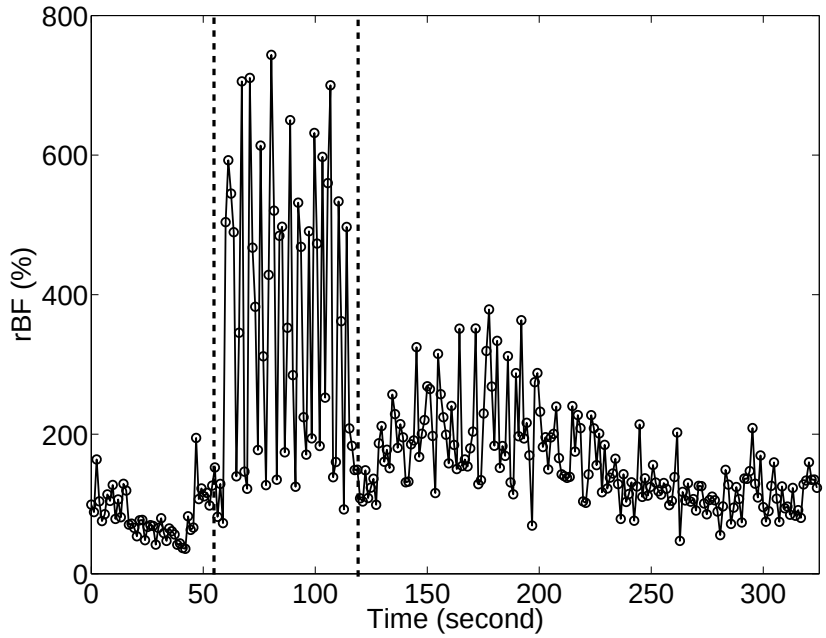

Figure 5.6: Faster (3Hz) measurements reveal flow changes that reveal two different phases during rhythmical exercise: flow decrease during muscle contraction and increase during muscle relaxation.

characterize the working muscle.

The rBF shown in Figure 5.5 has larger error bars than oxygenation and shows a greater variation which is probably due to high sensitivity of the flow measurement. In a separate trial with higher temporal resolution (3 Hz) achieved by changing the measurement duration for DCS (in expense of lower signal-to-noise ratio), we saw flow oscillations that correlated well with individual "toe-ups" during plantar flexions (Figure 5.6). These reveal two different phases during rhythmical exercise that correspond to flow decrease during muscle contraction and increase during relaxation.

Quaresima *et al* [303] used DOT with a similar protocol (40∼80 Plantar Flexion/min) and reported that StO_2 of medial gastrocnemius begun about 15 sec after the onset of the exercise to decrease significantly from baseline value of 69 $\%$ reaching a minimal value (approximately 30$\%$) in about 15 sec, and it recovered to the baseline value within 32 $\sim$ 45 sec after the end of the exercise. The trend and time responses (T_m and $T_{1/2}$) of StO_2 are in good agreement with our

observations shown in Figure 5.5 and Table 5.2. An ultrasound Doppler device was also used to measure the femoral artery blood flow at several time-points, such as, before and at the end of exercise. Two to three fold rBF increase was found at the end of exercise. The maximal changes (Max Δ) of StO_2(-40 $\%$) and rBF (2$\sim$3 fold) during exercise that were reported in their studies are different from those we observed. Their results are approximately two times larger in StO_2 and equally underestimated for rBF. The poor temporal resolution of Ultrasound Doppler could produce a significant difference in the flow measurement and those discrepancies in both StO_2 and rBF may also due to the different power of the exercise.

$TMRO_2$ during Exercise

As previously described in Section 5.2.3.2, the accuracy of the calculated $rTMRO_2$ depends not only on the accuracy of StO_2 and rBF measurement, but also on the various assumptions that were made in its derivation. The comparison of hyperemic perfusion results to other modalities has shown that DCT flow is underestimated compared to MRI and plethysmography. Unfortunately, there are very few other reported studies using the same protocol which makes the comparison complicated since apart from methodological differences, it is possible that the results are affected by the differences of the exercise power (supramaximal vs. moderate),the exercise duration (30 sec vs. 60 sec), the level of tissue metabolisms in different groups, such as age, weight and sex of the subjects, insufficient metabolic substrates (e.g., glucose, protein, ion), as well as the retained waste metabolites (e.g. CO_2, H+, and lactate). Bae *et al* [19] quantified muscle oxygen consumption response during 30 sec supramaximal sitting plantar flexion exercise using 31 P-MRS and reported that the oxygen consumption rate increased progressively after onset of exercise about 52 fold which is much higher than the increase of $rTMRO_2$ calculated in this study ($\sim$ 7 fold). However,

after multiplying the rBF by a factor of 7.6 (the amount of underestimation during hyperemia as discussed above) and recalculating the $rTMRO_2$, we observe a 53 fold increase, which is similar to the observed MRI value (52 fold). However, this study also differs in protocol and exercise power, therefore more quantitative comparisons are not yet possible.

5.2.4.3 Diseased Tissue Response

One PAD patient was also characterized in this study. Table 5.2 shows the summary of the response during exercise shown in Figure 5.5. As observed by many previous studies, a substantially longer half recovery time of StO_2 ($T_{1/2}$= 80 sec) is observed in the diseased leg. A similar observation was made during the cuff occlusion of the leg and for the arm it was within the normal range (Table 5.1). This is in agreement with lack of symptoms from the patient's arm. While the longer recovery time is not surprising, the mean maximum increases of rBF and $rTMRO_2$ during exercise in this patient are only half of those in healthy volunteers, which may have important implications for estimating the oxygen delivery ability and muscle metabolism. Using DOT and PET, others [56, 289, 396] have independently reported that there is no significant difference in blood flow and oxygen consumption at rest between PAD patients and healthy subjects. Although, our study has no statistical power for the patients at the moment, tbis is potentially indicative of the need for measurement of the dynamic responses during exercise. We also note that there was no significant difference in the maximum change of StO_2 during exercise between this patient and healthy volunteers, which was expected from the other studies. It is possible that the auto-regulation of the patient was able to compensate the mismatch between oxygen delivery and demand by lowering the tissue metabolism, thus, kept moderate oxygen saturations in the muscle. This matter requires further exploration by increased statistics.

5.2.4.4 Myoglobin or Hemoglobin?

In case of muscle tissue, the optical signals are expected to be contaminated by myoglobin related signals since myoglobins and hemoglobins have very similar optical spectra. Therefore, they can not readily be separated by optical measurements. The importance of this contamination has been a topic of debate where some studies argued that most of the near-infrared signals originated from hemoglobins ($> 90\%$) [68, 237, 333, 384] whereas others argued that the myoglobin contribution was higher than that of hemoglobin [260, 363].

I believe that most of the signals in our study originate from the hemoglobins since; (1) Decreases in total hemoglobin concentration were observed during exercise (see Figure 5.5(c)) which indicate larger signal contribution from vascular chromophores (hemoglobins) than those that reside statically in tissue (myoglobins), (2) During one minute exercise protocol and three minute cuff occlusion which are both relatively mild physiological perturbations, we expect that myoglobins would remain mostly oxygenated due to their higher affinity for oxygen than hemoglobins [237].

Our study is not designed to resolve this issue. Therefore, the hemodynamic changes in hemoglobin concentrations presented here would be more accurately viewed as a combination of hemoglobin and myoglobin deoxygenation with a relatively low contribution from the myoglobins. The effect of this contribution on the calculation of the changes in muscle oxygen metabolism where we have used a vascular model for oxygen extraction fraction can be the subject of future studies where measures of myoglobin and metabolism through magnetic resonance spectroscopic methods will be compared to optical results.

5.2.5 Conclusions

DCT was shown to be capable of penetrating through the upper layers to the muscle and relaying information about the muscle hemodynamics. The hybrid method is sensitive to changes in all parameters during different physiological manipulations dynamically. The volunteers did not report any discomfort with the probe and the signal-to-noise level was demonstrated to be adequately high such that the error bars are lower than the inter-volunteer variations.

We have measured blood oxygen saturation, total hemoglobin concentration and blood flow simultaneously during cuff occlusion of arm and leg flexors and plantar flexion exercise. Measurements on healthy volunteers (n=9) allowed us to quantify the healthy tissue response. Muscle responses have a large variation and are reported to be heterogeneous in different locations [396]. Studies done on a single PAD patient indicated that despite this variation, we are able to distinguish features between normal and diseased response. Multi-parameter dynamic measurements in same local region is essential for the diagnostics of disease and for evaluating of healthy muscle oxidative metabolism. Further studies are being conducted to increase the statistics and to improve the probe and the instrument. An imaging system for muscle metabolism is being built, which maybe helpful for the diagnostics of disease [396]. PAD patients are now being recruited to characterize the disease tissue response.

5.3 Monitoring of Tissue Hemodynamic Response to Photodynamic Therapy for the Prediction of Treatment Efficacy

5.3.1 Introduction

Photodynamic therapy (PDT) is a relatively new experimental cancer therapy that has been used with some success for the treatment of solid tumors and surface malignancies [106–109, 134, 233]. The method requires administration of a molecular photosensitizer that localizes in tumor tissue and is subsequently activated by exposure to optical radiation. The excited photosensitizer initiates a cascade of chemical reactions, often involving highly reactive oxygen intermediates that can produce selective tumor regression and destruction. The efficacy of PDT depends on sufficient concentrations of photons, photosensitizer and oxygen in the tumor tissue. Necrosis is brought about by a variety of mechanisms [57, 132, 138–140, 261, 343, 389, 390]; for example, the action of irradiation-induced singlet oxygen on critical cellular components is believed to cause vascular collapse leading further to the regional breakdown of O_2 and nutrient delivery.

Unfortunately, both tumor cells and normal cells are susceptible to damage by reactive intermediates. The efficacy of clinical treatment relies on several critical parameters including; (1) the type of photosensitizer used, its optical properties such as its quantum efficiency, its quenching and internal conversion rates, as well as its time-dependent microscopic and macroscopic concentration distribution within target and normal tissues, (2) the light dose used, which in turn depends on the excitation wavelength, the excitation geometry, and the time-dependent optical properties of target and normal tissues, (3) the spatio-temporal distribution of ground-state oxygen concentration in target and normal tissues. A range of experimental techniques have been developed and utilized to study variations in each of these critical parameters during PDT [138, 364, 390]. However, only

light dose has been measured routinely during clinical treatment which does not explicitly account for tissue optical property variations. The optical property variations; (1) are indicative of the variations in local oxygenation status of the tissue, (2) are a measure of the local drug concentration. It has, therefore, been suggested by many researchers that time-dependent measurements of these variables in tissues before, during, and after PDT treatment may provide valuable information to clinicians that can be used to optimize treatment [291, 296, 343, 364]. The treatment can be optimized by adjusting the light dose heterogeneously both in space and time, as well as by adjusting the drug delivery.

The research described in this chapter is part of a much larger project at PENN. For the overall aims of this unit, several instruments are employed either simultaneously or in series providing a large variety of information. DOT is used to determine the optical properties of macroscopic tissue volumes, fluorescence spectroscopy to characterize photosensitizer distributions in macroscopic tissue volumes, and DCT to estimate tissue blood perfusion. Light dose is also measured using a conventional dosimetry system. All these are combined to investigate whether macroscopic or tissue-averaged *in situ* measurements of this type can provide critical feedback to the clinician needed to improve PDT treatment.

Monitoring of the *in vivo* hemodynamic changes within tumors during PDT may reveal the extent of cellular and vascular damage. Studies designed to quantify the photochemical oxygen consumption and blood flow during and after PDT may improve our understanding of PDT mechanisms and lead to improved therapeutic strategies. There are a number of techniques for measuring the oxygenation of tumors. Polarographic needle electrodes (pO_2 Histograph) enable macroscopic, invasive measurements of tissue pO_2 [343]. These O_2 microelectrodes can sample tissue volumes that are much smaller than the distance between capillaries and hence can provide information on

how PDT treatment affects oxygen transport at the microregional level [296, 343, 364]. However, the invasive nature and poor spatial resolution of both of these techniques limits their application in humans. DOT on the other hand can provide non-invasive, continuous measurements over both small and large tissue volumes and has been applied for PDT monitoring [291].

Laser Doppler flowmetry can monitor non-invasively the flow change only in tissue surface (penetration depth $< 500\mu m$). Pogue *et al* invasively monitored flow changes during PDT with laser Doppler using fiber probes inserted into the tumor [296]. Their results indicated that the irradiation light saturates the Doppler probe so that the only useful data are between light fractions. Power Doppler ultrasound can also non-invasively follow changes in tumor perfusion after PDT through determination of the color-weighted fractional average (CWFA) in acquired images. However, it can not readily be used during PDT. Optical coherence tomography (OCT) in its Doppler implementation could also be used to measure the blood flow changes at several time points during PDT [73, 74] providing very high spatial and temporal resolution and can monitor the vascular changes directly. However, at the current state of development OCT can only measure small volume of tissue which is similar to the laser Doppler technique. It is, however, more difficult to develop reliable techniques for *in vivo* detection of hemodynamic changes containing independent information about hemoglobin concentration, oxygenation and flow. Pogue *et al* have attempted this by employing laser Doppler (flow) and O_2 microelectrodes (pO_2) to invasively study the heterogeneity of pO_2 dynamics during PDT with Verteporfin [296]. All these techniques are limited in their applicability to clinical situations.

The flow component of the hybrid instrumentation is used in this research with initial aims; (1) to establish DCT as a feasible methodology to monitor blood flow continuously on small animal

models, (2) to investigate the value of the extra information provided by the blood flow measurement, (3) to combine the oxygenation and flow information in derivation of predictive parameters and (4) to investigate different (implicit and explicit) dosimetry models.

The utility of this system is demonstrated by monitoring hemodynamic changes during and after PDT on mice bearing radiation-induced fibrosarcoma tumors (RIF tumors) . The flow measurements obtained by DCT are compared to another modality for validation and are shown to have the same trends as those measured by Power Doppler ultrasound on a separate set of animals under same treatment conditions. The time traces of blood flow before, during and after PDT are investigated and common characteristics are used to develop indices that can predict the tumor regrowth time. The tumor regrowth time is used as an indicator of the PDT efficacy based on the assumption that the better the PDT response is, the slower the tumors would regrow to a given volume. This is true because the drug/light dose is kept at a low level such that all the tumors regrow. Furthermore, to quantify the optical properties of the tumors, a broadband absorption spectrometer was employed to simultaneously measure the wavelength-dependent reflectance of tissue at many source-detector separations before and after PDT. This instrument was chosen over the DOT component of the hybrid instrument to avoid potential problems in the quantification of hemoglobin concentrations due to the small tissue volumes probed with a more limited number of wavelengths. This additional information was also shown in a separate study [381, 382] to have predictive capability of PDT efficacy. Finally, the relative tissue metabolic rate of oxygen consumption ($TMRO_2$) was computed by combining the blood flow data by DCT with blood oxygen saturation data by broadband absorption spectrometer. The discussion here closely follows Yu *et al* [409, 410].

5.3.2 Materials and Methods

5.3.2.1 Tumor Model and PDT Dose

Radiation-induced fibrosarcoma (RIF) tumors were grown on the shoulders of C3H mice (Taconic, Germantown, NY) by the intradermal injection of 3 x 10^5 cells. Animals were treated $\sim$1 week later when tumors were about 6 mm in diameter. The photosensitizer Photofrin (Axcan Pharma Inc., Mont-Saint-Hilaire, Quebec) was administered via a tail vein at 5 mg/kg at $\sim$24 h before illumination. The laser system consisted of a KTP YAG pumped dye module (Laserscope, San Jose, CA) tuned to produce 630 nm light. Light was delivered to a 1 cm diameter treatment field through microlens-tipped fibers (CardioFocus, Norton MA) and the power density was measured with a power meter (Coherent, Auburn, CA). Treatment was to a total fluence of 135 J/cm^2, delivered at 75 mW/cm^2. Mice were divided into two groups; (1) treated group = tumor + drug + light, and (2) control group = tumor + light. During PDT and for any consequent optical measurements the mice were anesthetized with isoflurane and kept warm on a regulated heating pad. The treatment efficacy was estimated by measuring number of days passed for the tumor volume to increase to 400 mm^3.

5.3.2.2 Non-contact DCT System

The DCT component of the Generation II hybrid system was used with a non-contact probe with 13 source and four detector fibers. This avoided potential alterations in hemodynamics due to compression and allowed the ability to compare long term ($>$ 6 hours) changes to the baseline. The fibers were held by a camera back whose lens was 15 cm away from the tumor, which allowed the treatment light illuminate from the sides of camera (see Figure 5.7). The optical fibers for the sources and detectors, were bounded and arranged in a two-dimensional pattern shown in Figure

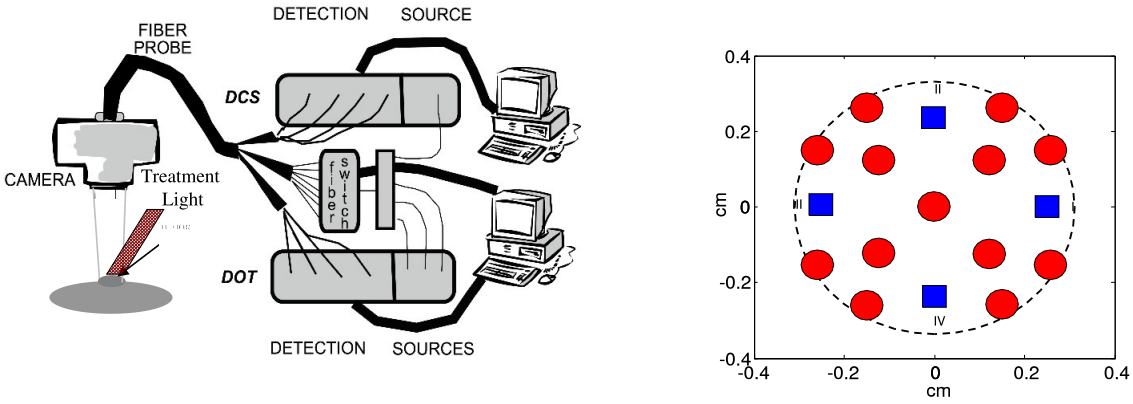

Figure 5.7: Sketch of instrument, probe and tumor for PDT studies. Red circles represent the source positions and blue squares are the detector fiber positions for both DOT and DCT.

5.7 covering a 6×6 mm^2 area. One optical filter mounted in front of the camera lens attenuates light below 650nm, which allows monitoring blood flow while the treatment laser is being shone. The sampling time for one frame is $\sim$ 18 seconds.

The DCT instrument monitored the blood flow changes continuously during PDT (from 15 minutes pre-PDT to 15 minutes after PDT). Additional measurements were performed for ten minutes at three time-points after PDT (3 hours, 6.5 hours and 24 hours after PDT). The normalized percent changes from pre-PDT values were calculated. Fifteen (n=15) treated and six (n=6) control mice were measured.

5.3.2.3 Broadband absorption spectrometer

A broadband absorption spectrometer was used to measure the wavelength-dependent reflectance of tissue at many source-detector separations at a wide range of wavelengths simultaneously. This instrument was chosen over the DOT component of the hybrid instrument to avoid potential problems in the quantification of hemoglobin concentrations due to the small tissue volumes probed

with a more limited number of wavelengths. The system shown in Figure 5.8 consists of four major parts: the light source, the fiber-optics probe head, the CCD camera, and the dispersion system (monochromator). Light from a 250 W quartz tungsten halogen lamp is coupled to the tissue surface through a source fiber and detected in the reflectance mode from the tissue surface by 10 detection fibers. These fibers are arranged in a line with source-detector separations of ρ= 0.6, 1.2, 1.8, 2.4, 3, 4, 5, 6, 8, and 10 mm. The collection fibers are then coupled back to the monochromator entrance slit where the ends of the detector fibers are arranged in a vertical line with equal spacing and well positioned relative to the monochromator such that the image of the fiber tips is projected and focused on the liquid nitrogen cooled CCD camera sensor. The grating disperses this light so that the image plane of monochromator output contains ten vertically spaced bright lines corresponding to the spectra, $R_{tissue}(\rho, \lambda)$ of the detection fibers. The reflectance spectra $R_{tissue}(\rho, \lambda)$ can be used to recover tissue optical properties. A physical model to quantify these values is described in detail elsewhere [382]. Measurements were made at several time points: 15 minutes before PDT, 15 minutes, 3 hours, 6.5 hours and 24 hours after PDT. The normalized percent changes from pre-PDT values were calculated. Fifteen (n=15) treated and six (n=6) control mice were measured.

5.3.2.4 Power Doppler Ultrasound

Doppler ultrasound has been used extensively to assess vascularity in a range of animal and human tumors. In particular, power mode Doppler ultrasound appears to be a more sensitive and specific method for measuring tumor blood flow than traditional Doppler ultrasound [153]. Ultrasound imaging was performed on mice anesthetized i.e. with ketamine/ xylazine (150/10 mg/kg) and

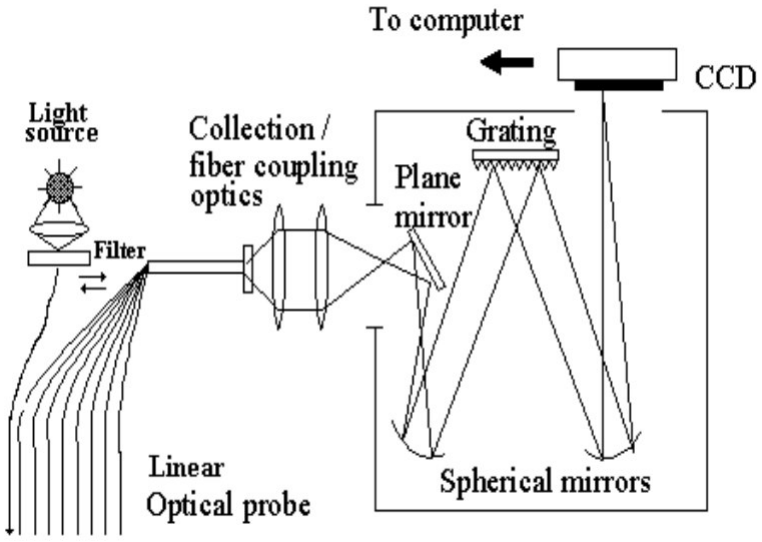

Figure 5.8: Sketch of broadband Spectrometer.

kept warm on a heating pad. Approximately 10 images were acquired of each tumor at each time-point studied at 15 minutes, 3 hours and 6.5 hours after PDT. From each image the Color Weighted Fractional Area (CWFA) was determined as a measure of perfusion, and values were averaged for each mouse at each time-point. Five (n=5) treated and five (n=5) control mice were measured forming a distinct set from those measured optically.

5.3.2.5 Statistical Analysis

Statistical analyses were carried out using R v.1.70 (www.r-project.org) [1]. All tests were two-sided and used a Type I error rate of 0.05. We used mixed effects models to compare blood flow patterns in DCT and Power Doppler and to compare patterns of %StO2 and $rTMRO_2$ over time in PDT versus Control animals [295]. This approach accounts for correlations between repeated

[1] Special thanks for Dr Mary Putt of Department of Biostatistics Epidemiology, U. Penn for this analysis

measurements on the same animal. For the comparison of DCT and Power Doppler, the model had time, modality (Power Doppler versus DCT) and treatment (Control versus PDT) as main effects and included interaction terms between time and treatment to allow the effect of PDT to differ over time. Based on the Akaike Information Criteria, separate random effects were used to model the inter-animal variance for animals measured with Power Doppler and DCT, with a common random error term to model the intra-animal variance The statistical significance of incorporating separate random effects for the two modalities versus a single random effect was assessed using a likelihood ratio test. [175]. Statistical significance of main effects in the mixed effects models was also assessed using likelihood ratio tests. For the comparison of DCT and Power Doppler we report results from a model where not all terms were statistically significant (see Results). In this experiment we were interested in determining whether the results for the two modalities were equivalent, and even in the absence of statistically significant differences, wanted to report estimates of the magnitude of the differences between the modalities.

For the experiments reporting $\%StO_2$ and $rTMRO_2$, results from the model that best fit the data, and incorporated the effects of time, PDT and time by PDT interactions are reported. Note that for rBF and $rTMRO_2$, where the outcome for each animal was normalized to baseline, time effects in the mixed effects models did not include the baseline measurements since by definition it did not vary from 100% across animals. Estimates and 95% confidence intervals (CI) were constructed for each time point for control and PDT-treated animals. For each of the measured variables (rBF, StO_2, and $rTMRO_2$), individual time-points for the PDT-treated animals were compared to their baseline levels using Wald tests derived from the parameters estimates in the mixed effects models.

Lastly, associations between flow or oxygen parameters and time to tumor regrowth were assessed using linear regression.

Where relevant, $p<0.05$ was considered to be significant.

5.3.3 Results

5.3.3.1 Comparison of Power Doppler Ultrasound and DCT Flow

The flow changes measured by DCT were compared with the Power Doppler ultrasound at 15 minutes, 3 hours and 6.5 hours after PDT as shown in Figure 5.9 and Table 5.3. Values at each time point are shown as percent change relative to the baseline value (15 minutes before PDT) and the error bars indicate the standard error from all mice in the group. We estimated a separate inter-animal standard deviation (s.d.) for each modality, i.e. a measure of the variability in the measurements between animals at the same time. In addition, an intra-animal s.d, i.e. a measure of the precision of repeated measurements of the same animal was estimated. The inter-animal s.d in the Power Doppler measurements of blood flow was substantially larger than for DCT ($p=0.003$). For Power Doppler the estimated inter-animal s.d. was 40.3%; for DCT the estimated inter-animal s.d. was 0.1%. The estimated intra-animal s.d. common to both modalities was 36.3%. These differences in precision was reflected in the confidence intervals around the individual time-points. For the control animals, where sample sizes were similar for DCT and Doppler, these intervals were substantially wider for Doppler. The model-based estimate of the mean difference between relative blood flow measured using DCT and Power Doppler was 9.4% (95% CI, -22.6-41.4%), a difference which was not statistically significant ($p<0.545$) and which suggested overall good agreement between the two modalities. Differences between mean relative blood flow over time for DCT and Power Doppler were also not statistically significant ($p<0.659$).

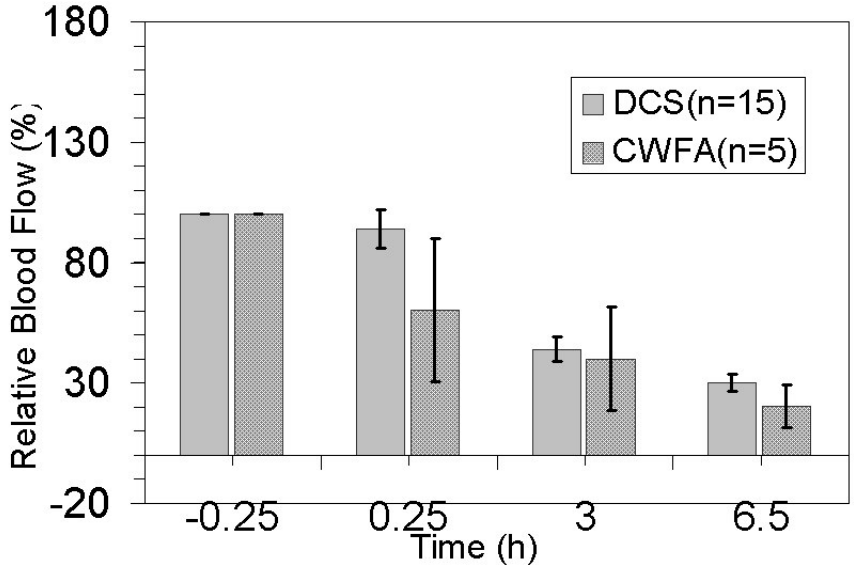

(a)

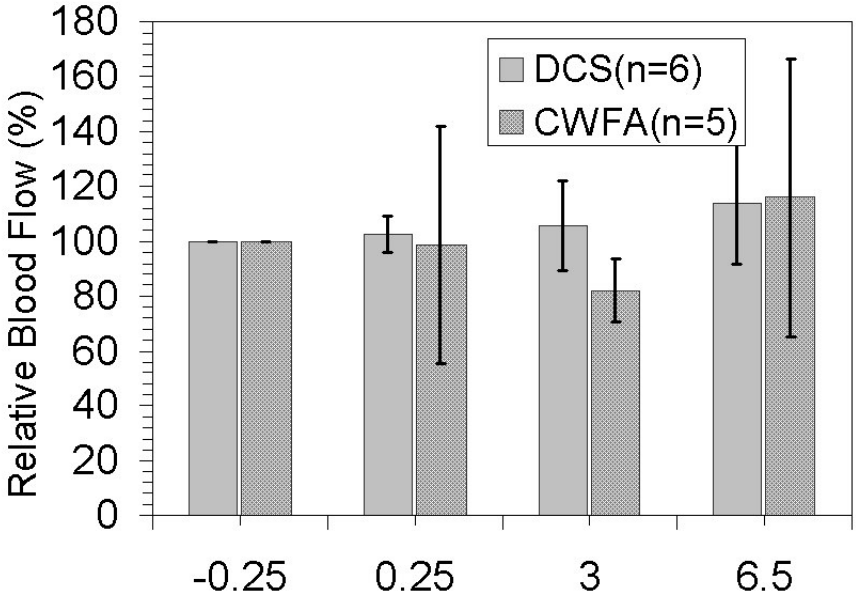

(b)

Figure 5.9: Comparison of flow changes measured by Doppler Ultrasound and DCT in (a) treated and (b) control animals shows good agreement between two methods.

Time	Control (DCT, n=6)	Control (Ultraso., n=5)	PDT (DCT, n=15)	PDT (Ultraso., n=5)
0	100	100	100	100
15 min	102.7 (71,134)	93.3 (44,142)	88.4 (70,107)	79.0 (33,125)
3 h	98.6 (66,131)	89.2 (31,147)	47.6 (29,66)	38.2 (0,84)
6.5 h	117.6 (86,149)	108.2 (59,157)	31.1 (13,49)	21.6 (0,68)

Table 5.3: Tumor blood flow following light exposure in control and PDT-treated animals comparing DCT and Doppler Ultrasound results. Means with 95% confidence intervals based on the full mixed effects model.

5.3.3.2 Effect of PDT treatment on Relative Blood Flow, Oxygenation and Oxygen Consumption

The flow changes observed during PDT by DCT are monitored for two groups (in 15 treated mice and 6 control mice). A typical curve during and after PDT in a treated mouse is shown in Figure 5.10(a). The flow value at each time point is given in percent change relative to the baseline value (before PDT) and the error bar presents the standard deviation of the mean value from many source-detector pairs in the probe. The characteristic shape of this curve is observed in all animals and is further investigated in the following section. Figure 5.10(b) shows the same curve from a control mouse and the trends in Figure 5.10(a) are not visible as expected. Therefore, those trends are expected to be due to the treatment effects.

Figure 5.11 shows the tissue oxygen saturation (Y_t), relative blood flow (rBF) and relative tissue metabolic rate of oxygen consumption (rTMRO$_2$) after PDT in 15 treated mice (Figure 5.11(a)) and 6 control mice (Figure 5.11(b)). The rBF and rTMRO$_2$ at each time point are given in percent change relative to the baseline value (15 minutes before PDT) and Y_t is absolute value measured by the broadband absorption spectroscopy. The error bar shows the standard error.

Blood flow changes estimated on the full mixed effects model with mean and 95% confidence intervals are shown in Table 5.3. Relative tumor blood flow was reasonably stable for the control

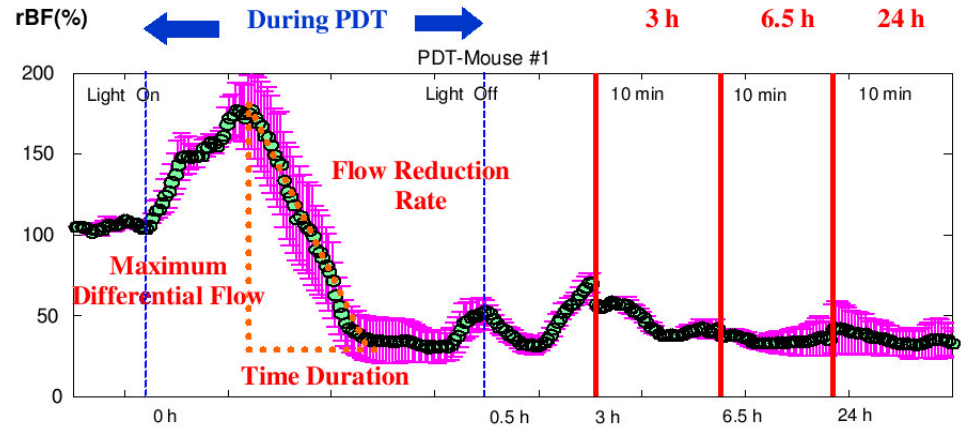

(a)

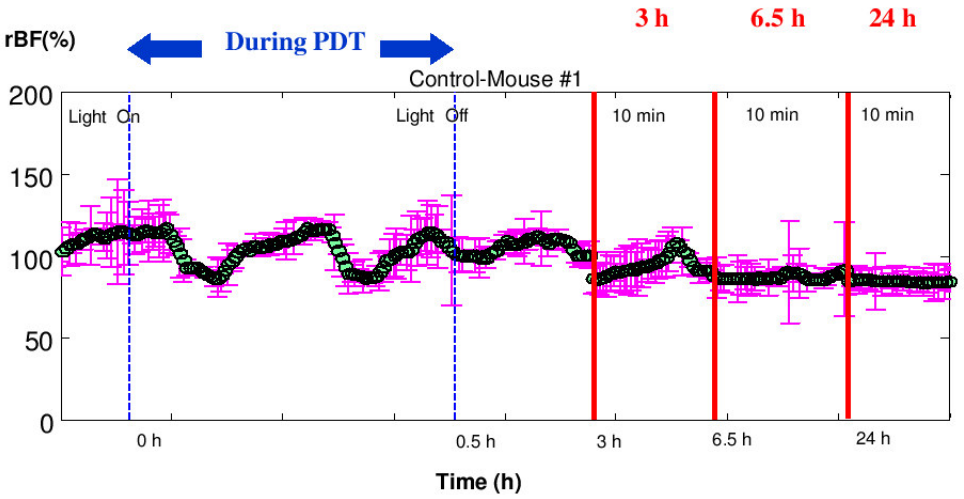

(b)

Figure 5.10: Flow response before, during and after treatment for (a) PDT-treated and (b) control group. Significant repeatable changes are observed during treatment with this curve characterized with flow reduction rate – as indicated in figure legends – as a treatment efficacy predictor. 15 min, 3 hour and 6.5 hour after time-points are also shown. There are no significant changes due to treatment in the control group.

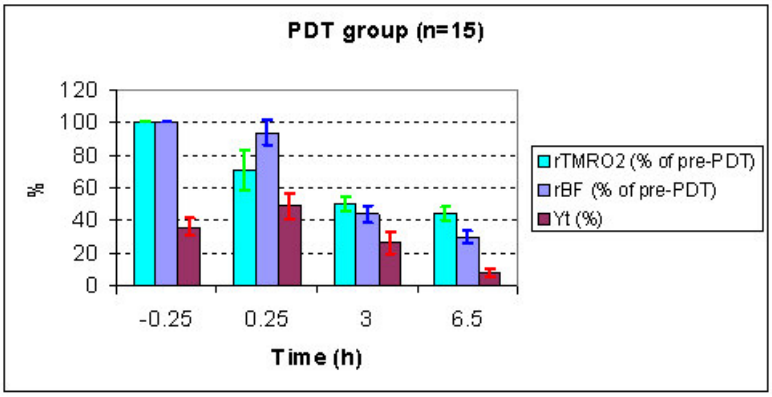

(a)

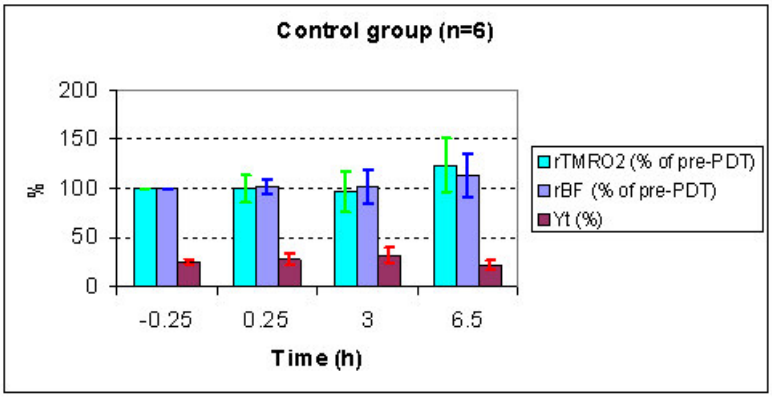

(b)

Figure 5.11: Mean hemodynamic response to treatment in (a) PDT-treated and (b) control groups. Changes from baseline for $rTMRO_2$, StO_2 and rBF are shown.

Time	StO_2(%)		$rTMRO_2$ (%)	
	Control (n=5)	PDT (n=15)	Control (n=5)	PDT (n=15)
0	24.3 (4,44)	35.7 (25,46)	100*	100*
15 min	28.9 (9,49)	47.2 (36,58)	96.7 (58,135)	68.7 (48,90)
3 h	27.9 (8,48)	19.7 (9,31)	102.4 (64,141)	60.1 (39,81)
6.5 h	21.9 (2,42)	8.4 (0,21)	120.0 (82,158)	48.4 (25,72)

Table 5.4: StO_2 and $rTMRO_2$ following treatment in control and PDT-treated animals. Means with 95% confidence intervals based on the mixed effects model with time and a treatment effect that varied over time.

animals but progressively decreased with time after PDT. These differences between control and PDT-treated groups over time were statistically significant (p=0.002). Although not statistically different from baseline (p=0.196), mean rBF at 15 minutes for both DCT and Power Doppler was less than 90% of baseline. By 3 hours, mean rBF was less than 50% of baseline ($p<0.0001$) and at 6.5 hours, it declined to 33% ($p<0.0001$).

Changes in other tumor physiological parameters may be expected to accompany decreases in blood flow after PDT. Measured StO_2 and $rTMRO_2$ followed changes in blood flow closely.

Table 5.4 shows the estimated mean and confidence intervals for StO_2 and $rTMRO_2$ for control and PDT-treated groups. For StO_2, an overall effect of PDT-treatment ($p<0.0001$) as well as changes over time, again related to treatment (P=0.004) were observed. In the control animals, the estimated mean values following treatment were similar to the mean at time zero. In contrast, for the PDT-treated animals, it was somewhat elevated at 15 minutes (p=0.54), then fell close to 50% of the baseline mean after 3 hours (p=0.011), and close to 25% of the baseline at 6.5 hours (p=0.002).

Similar results were observed for $rTMRO_2$. An overall effect (p=0.002) as well as changes over time (p=0.002) were again observed. The estimated mean $rTMRO_2$ level for the individual time-points ranged from 97 to 120% of baseline for controls compared to 48 to 69% for PDT treated

animals. Each of the individual PDT timepoints were significantly lower than baseline (p=0.007, p=0.001 and p=0.002 for 15 minutes, 3 hours and 6.5 hours respectively).

5.3.3.3 Prediction of long-term Tumor Response to Treatment

The decreases in relative blood flow, relative oxygen consumption rate, and oxygen saturation at 3 and 6.5 hours after PDT are all consistent with the progressive development of PDT-induced vascular damage, leading to tumor cell death. The overall efficacy of PDT is reflected in tumor time-to-recurrence or the tumor regrowth delay. Thus, we determined if tumor physiology, characterized by rBF and %StO2, were predictive of the time required for tumor regrowth to a volume of 400 mm^3. A highly significant negative correlation (p=5.63e-6) was detected between rBF at 3 hour after PDT and time-to-regrowth as shown in Figure 5.12(a). This was modeled and was found that doubling of rBF leads to a 7.00$\pm$0.95 day decrease in tumor time-to-regrowth. rBF at 6.5 hour after PDT was also highly correlated (p = 3.00e-5) with tumor response (data not shown). A model of the effect at 6.5 h indicates that a doubling of the rBF leads to a 5.86$\pm$0.94 day decrease in time-to-regrowth which is very similar to that found at 3 hour time-point.

StO_2 at 3 hour time point was also predictive (p=0.015) of tumor response. The more the StO_2 decreased, the longer it took for regrowth. A similar model was applied indicating that for every 1% increase in StO_2, the tumor time-to-regrowth was reduced by 0.17 days. The 6.5 hour time point was not modeled since the oxygenation data is not reliable at the point and included, potentially false, 0% values.

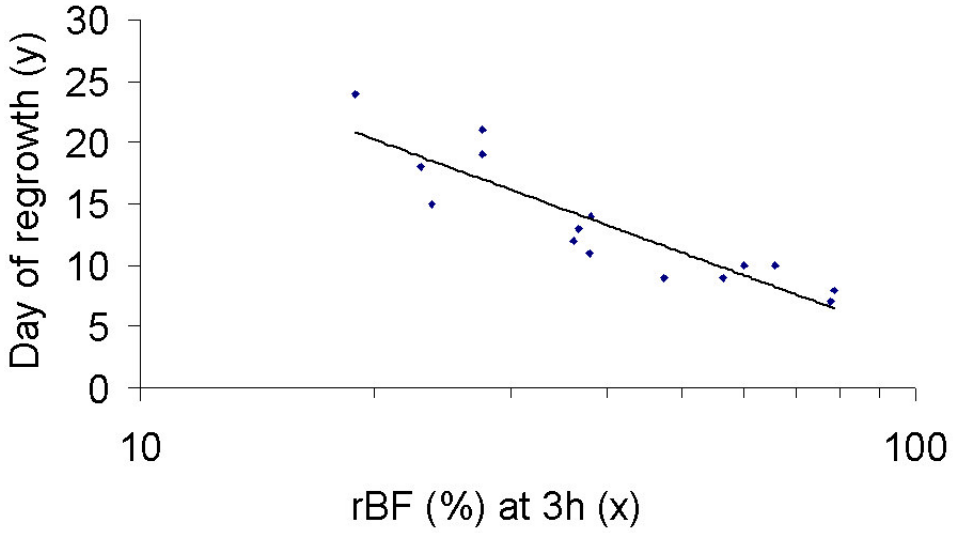

(a)

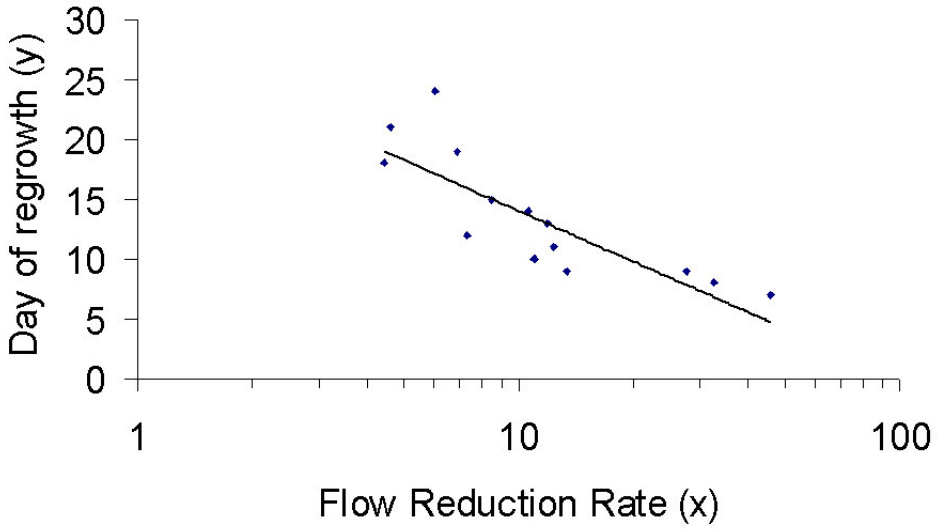

(b)

Figure 5.12: Correlation between tumor time-to-regrowth and (a) rBF at 3 hour, (b) flow reduction rate during PDT. Significant correlation is observed in both cases. Details in the text.

5.3.3.4 Prediction of PDT efficacy from Flow Dynamics *During* Treatment

Another characteristic of the flow traces is their behavior during the treatment as seen in Figure 5.10. After 15 minutes of pre-PDT measurements, the laser was turned on without interrupting the measurement. Blood flow increased rapidly to its maximum value (168.1$\pm$39.5%), and then decreased slowly below the baseline (59.2$\pm$29.1%). The initial rapid increase was consistent over all animals and happened within the first 10 minutes. The time for maximal decrease varied greatly between 4.0 to 24.2 minutes. After this increase, blood flow increased slowly toward the baseline which continued after the treatment laser was turned off. A similar trend was observed in all 15 treated tumors during PDT although the maxima, minima, and time to reach the extrema varied. In animals where a rapid decrease was observed, secondary (even tertiary) similar oscillations occurred. In contrast, in the control mice the blood flow fluctuated around the baseline, and no significant flow change was found during and after PDT as was discussed above.

The data from previous section demonstrate that rBF after PDT is a potential predictor of long term tumor response. This may be because PDT-induced flow changes are related to the degree of PDT-induced vascular damage. This, in turn, implies that the observed flow dynamics during PDT may also reveal previously unavailable predictors for tumor response. We have characterized these curves based on a variety of parameters and identified that the maximum differential blood flow (rBF_{max} - rBF_{min}) divided by the time between extrema (T_{min}-T_{max}), i.e. the slope of flow reduction ("Flow Reduction Rate"), is the strongest predictor of tumor response. This data is presented in Figure 5.12(b). Statistical analysis indicated that flow reduction rate during PDT is highly correlated with treatment efficacy (p=2.02e-4). A doubling of the flow reduction rate predicted a mean time-to-regrowth decrease of 4.24$\pm$0.83 days.

This effect may be understood by dynamic changes in tumor vasculature during treatment. The

decrease to below baseline following the rapid initial increase in flow is indicative of temporary vessel constriction or occlusion during PDT. This observation is further strengthened since the recovery in flow began before the treatment concluded. After, the vascular shutdown occurred, the blood oxygen levels dropped to levels such that the treatment was no longer effective since PDT treatment requires adequate oxygen supply to initiate the cascade of chemical reactions that lead to cell-death. This, in turn, leads to the recovery of some of the vessels, and hence, to increased blood flow. However, if the treatment light is turned off before the cells were treated for an adequate time, a large percentage of tumor vasculature may remain intact. If, on the other hand, this process occurs fast enough, the treatment effect can increase once more leading to a cyclic behavior. Some of the mice showed 2-3 such oscillations in blood flow. Furthermore, in some mice the recovery led to an overshoot of flow after PDT beyond the baseline. In contrast, the flow reduction that was observed at the three hour time point was unrecoverable, suggesting that permanent vessel damage had occurred. Similar initial temporary vessel occlusion during PDT followed by permanent vessel occlusion was also observed by OCT [2].

It is worthwhile to note that the tumor regrowth time had a broad range from 7∼24 days, despite that fact that the same PDT dose was applied to all treated mice (n=15). This indicates that PDT treatment efficacy can not be predicted or estimated by pre-calculating the PDT dose, and it has to be evaluated by real-time monitoring of the PDT dose or the hemodynamic responses.

5.3.4 Conclusion

DCT can be used to continuously and non-invasively measure dynamic blood flow in deeper tumor tissue during and after PDT. Blood flow measurements by DCT agree well with tumor perfusion

[2] Personal communication with B. Wilson

measured by Doppler ultrasound. For the first time to our knowledge, using DCT we continuously monitored blood flow changes during PDT. During PDT, photosensitized mice exhibited significant changes in blood flow compared to controls. Mice with rapid decreases in blood flow led to shorter tumor regrowth times, identified as poorer PDT treatment efficacy. After PDT, significant differences in blood flow, tissue oxygen saturation, and $TMRO_2$ were found between control and PDT-treated mice. Mice with larger flow reductions following PDT showed better PDT efficacy. The blood flow responses to PDT (Flow Reduction, Flow Reduction Rate, and Time Duration) can be used to predict/evaluate treatment efficacy. This observation is promising since the measurement of hemodynamic responses during PDT is more feasible than monitoring many hours/days after the treatment since many tumors are not accessible without a surgery in clinical applications. The real-time monitoring is promising for controlling the treatment immediately. To get good treatment efficacy, potentially a clinician may control Flow Reduction Rate and Time Duration by changing the PDT light dose (light intensity and/or duration). PDT light dose can be set in advance or adjusted in real time according to the flow responses. The combination of hemodynamic responses to PDT during and after PDT (if it is feasible) may provide clinicians more accurate evaluation to predict the treatment efficacy and determine whether the tumor needs to be re-treated. This is yet an optimistic look for the future and the hybrid instrumentation is now being transferred to measurements in the clinic.

Chapter 6

Summary

In this work, I have described an extensive set of measurements of hemodynamics using diffuse optical methods. Variety of instrumentation was developed combining diffuse optical tomography (for oxygenation) and diffuse correlation tomography (for blood flow) in novel hybrid systems (Chapter 3). These hybrid systems, using all optical methods, for the first time, allowed estimates of metabolic rate of oxygen through thick tissues by employing a steady state model of tissue hemodynamics (Chapter 2). Longitudinal spectroscopic and dynamic three dimensional imaging applications were demonstrated under various physiological states.

A bulk of the studies described in this work were from measurements of cerebral hemodynamics in rats. The hybrid method is verified by measurements of global hemodynamics in rat brain by comparing to other physiological information such as independent laser doppler measurements, blood gases and the literature (Section 4.2.1). First three dimensional images of tissue oxygen saturation, total hemoglobin concentration, relative cerebral blood flow and relative metabolic rate of oxygen ($CMRO_2$) were obtained during middle cerebral artery occlusion induced focal ischemia (Section 4.2.2). Again, the results showed excellent agreement with other modalities. In another

study, hemodynamics of cortical spreading depression were imaged under different states of brain oxygenation and ventilation (Section 4.2.3). Three dimensional imaging of cortical spreading depression under these conditions revealed interesting physiological information with potential implications in understanding of migraine headaches and cerebral events following a stroke.

In yet another set of studies on rat brains, a laser speckle flowmetry instrument was constructed and used to image the spatio-temporal properties of the activation flow coupling response to somatosensory cortex stimulation (Section 4.3). Different stimulus durations and amplitudes of electrical forepaw stimulation were investigated. First, the results were shown to be in agreement by point measurements such as Laser doppler. Then the spatial response was investigated and previously unavailable physiological information was obtained.

Finally, the sensitivity of the instrumentation was improved and the hemodynamic response to motor cortex stimulus by controlled finger tapping was measured using all optical methods (Section 4.4). Changes in oxy- and deoxy-hemoglobin concentrations and cerebral blood flow were measured near simultaneously *through* the scalp and skull. $CMRO_2$ was measured using all optical methods in human brain for the first time. The signals were robust and are in good agreement with other modalities.

Collectively, these studies demonstrated; (1) that hybrid methodology is capable of penetrating through intact skull in rats, (2) three dimensional imaging of cerebral hemodynamics over many (~ 8) hours is possible, (3) measurements of $CMRO_2$ provides supplementary information that is critical in characterization of the physiological state of brain and is not possible with only the knowledge of oxygenation and/or blood flow state, and (4) the diffuse correlation measurements are transferrable to humans being able to penetrate ~ 1 cm into brain *through* the skull. This has for the first time enabled combination of diffuse optical tomography measurements of oxygenation

and diffuse correlation tomography measurements of blood flow to estimate changes in $CMRO_2$ in humans.

Hemodynamics of arm and leg flexor muscles in response to cuff-occlusion and plantar flexion exercise were measured (Section 5.2). Both diffuse optical tomography and diffuse correlation tomography are shown to be able to penetrate through the upper layers deep into the muscle. The results are in good agreement with other modalities. The optical method is shown to have a significant advantage in allowing *continous* measurements non-invasively and unobstructively during both modulations. A similar model to $CMRO_2$ is employed to estimate changes in muscle oxygen metabolism. The difference between normal and disease response is anecdotally investigated by comparing a patient with peripheral arterial disease. Hybrid optical method is promising for monitoring of treatment and progress of vascular diseases in extremeties and also for exercise medicine.

Finally, the response to photodynamic therapy (PDT) was measured in RIF tumors implanted on mice (Section 5.3). Good agreement was obtained in comparing blood flow measured by diffuse correlation spectroscopy and power Doppler ultrasound. Significant changes were observed in blood flow, oxygenation and tissue metabolism following PDT treatment which was absent in control animals. For the first time to our knowledge, using DCS we continuously monitored blood flow changes *during* PDT showing that photosensitized mice exhibited significant changes in blood flow compared to controls. Mice with rapid decreases in blood flow led to shorter tumor regrowth times, identified as poorer PDT treatment efficacy. After PDT, significant differences in blood flow, tissue oxygen saturation, and $TMRO_2$ were found between control and PDT-treated mice. Mice with larger flow reductions following PDT showed better PDT efficacy. A combination of these measures may be used in the clinical setting to predict treatment efficacy and even control the treatment parameters to obtain optimal treatment. This tumor studies also demonstrated that

the hybrid method is capable of monitoring changes spanning even twenty four hours.

A major contribution of this manuscript was the introduction of diffuse correlation tomography as a viable technique for non-invasive, relatively inexpensive measurements of blood flow in thick tissues. The technique was applied to a wide range of physiological settings and validated extensively. Interesting new physiological information was revealed. This technique on its own and hybridized with diffuse optical tomographical methods has promising applications in laboratory and clinical studies.

Glossary

—— SYMBOLS ——

λ	Wavelength of Light usually in nano-meters (nm).
λ_r	Regularization Parameter.
μ_a	Absorption Coefficient.
μ_s'	Reduced Scattering Coefficient, $\mu_s' = \mu_s(1-g)$.
Φ	Photon-Fluence Rate at position $\mathbf{r}$ and time t.
ω	Laser/Source Modulation Frequency.

—— A ——

AFC	Activation Flow Coupling.

—— B ——

BF	Blood Flow.

—— C ——

c_{Hb} De-oxy hemoglobin concentration.

c_{HbO_2} Oxy hemoglobin concentration.

c_i Concentration of the ith chromophore.

CMRO$_2$ Cerebral Metabolic Rate of Oxygen.

CSD Cortical-Spreading Depression.

CW Continous Wave.

—— D ——

D Photon Diffusion Coefficient.

DCT Diffuse Correlation Tomography.

DOT Diffuse Optical Tomography.

DPF Differential Pathlength Factor.

—— F ——

FD Frequency Domain.

—— H ——

HbO$_2$ Oxy Hemoglobin Concentration.

Hbr De-oxy Hemoglobin Concentration.

—— I ——

I/Q In-phase/Quadrature Demodulator.

—— L ——

LDF Laser Doppler Flowmetry.

LSF Laser Speckle Flowmetry.

—— M ——

MCAO Middle Cerebral Artery Occlusion.

MRO$_2$ Metabolic Rate of Oxygen.

MRI Magnetic Resonance Imaging.

—— N ——

NICU Neuro-Intensive Care Unit.

NIRS Near Infrared Spectroscopy.

—— P ——

$PaCO_2$ Partial pressure of carbon dioxie (CO_2).

PAD Peripheral Arterial Disease.

pCO_2 Partial pressure of carbon dioxie (CO_2).

PET Positron Emission Tomography.

PM Photon Migration.

PPF Partial Pathlength Factor.

PVD Peripheral Vascular Disease.

—— R ——

r Position in 3D.

—— S ——

S_{DC} DC component of the source term.

S_o Amplitude of AC component of the source term.

SPECT Single Photon Emission Computed Tomography.

S_ϕ Amplitude of AC component of the source term.

StO$_2$ Tissue Oxygen Saturation.

—— T ——

THC Total Hemoglobin Concentration.

TMRO$_2$ Tissue Metabolic Rate of Oxygen.

TRS Time Domain Spectroscopy.

—— Y ——

Y$_t$ Tissue Oxygen Saturation.

Bibliography

[1] N. J. Alkayed, I. Harukuni, A. S. Kimes, E. D. London, R. J. Traystman, and P. D. Hurn. Gender-linked brain injury in experimental stroke. *Stroke* **29**, 159–165 (1998).

[2] B. M. Ances, D. G. Buerk, J. H. Greenberg, and J. A. Detre. Temporal dynamics of the partial pressure of brain tissue oxygen during functional forepaw stimulation in rats. *Neurosci Lett* **306**(1-2), 106–10. (2001).

[3] B. M. Ances, J. A. Detre, K. Takahashi, and J. H. Greenberg. Transcranial laser doppler mapping of activation flow coupling of the rat somatosensory cortex. *Neurosci. Lett.* **257**, 25–28 (1998).

[4] B. M. Ances, J. H. Greenberg, and J. A. Detre. Laser doppler imaging of activation-flow coupling in the rat somatosensory cortex. *NeuroImage* **10**, 716–23 (1999).

[5] B. M. Ances, J. H. Greenberg, and J. A. Detre. The effects of graded hypercapnia on the activation flow coupling response due to forepaw stimulation in α-chloralose anesthetized rats. *Brain Res.* **911**, 82–88 (2001).

[6] B. M. Ances, D. F. Wilson, J. H. Greenberg, and J. A. Detre. Dynamic changes in cerebral blood flow, O-2 tension, and calculated cerebral metabolic rate of O-2 during functional

activation using oxygen phosphorescence quenching. *J. Cereb. Blood Flow Metab.* **21**, 511–516 (2001).

[7] B. M. Ances, E. Zarahn, J. H. Greenberg, and J. A. Detre. Coupling of neural activation to blood flow in the somatosensory cortex of rats is time-intensity separable, but not linear. *J. Cereb. Blood Flow Metab.* **20**, 921–30 (2000).

[8] R. Aronson. Boundary conditions for diffusion of light. *J.Opt.Soc.of Am.A* **12**, 2532–2539 (1995).

[9] R. Aronson and N. Corngold. Photon diffusion coefficient in an absorbing medium. *J. Opt. Soc. Am. A* **16**, 1066–1071 (1999).

[10] S. R. Arridge. Optical tomography in medical imaging. *Inverse Problems* **15**, R41–R93 (1999).

[11] S. R. Arridge, M. Cope, and D. T. Delpy. The theoretical basis for the determination of optical pathlengths in tissue: temporal and frequency analysis. *Phys Med Biol* **37**(7), 1531–60 (1992).

[12] S. R. Arridge and J. C. Hebden. Optical imaging in medicine: II. modelling and reconstruction. *Phys. Med. Biol.* **42**(5), 841–854 (1997).

[13] S. R. Arridge and W. R. B. Lionheart. Nonuniqueness in diffusion-based optical tomography. *Opt Lett* **23**, 882–884 (1998).

[14] S. R. Arridge and M. Schweiger. Inverse methods for optical tomography. In *Information Processing in Medical Imaging (IPMI'93 Proceedings), Lecture Notes in Computer Science* volume 687 pages 259–277. Springer-Verlag (1993).

[15] S. R. Arridge and M. Schweiger. Photon-measurement density-functions .2. finite-element-method calculations. *Appl Opt* **34**(34), 8026–8037 (1995).

[16] S. R. Arridge and M. Schweiger. Image reconstruction in optical tomography. *Philosophical Transactions of the Royal Society of London Series B-Biological Sciences* **352**(1354), 717–726 (1997).

[17] S. R. Arridge and M. Schweiger. A gradient-based optimisation scheme for optical tomography. *Optics Express* **2**(6), 213–226 (1998).

[18] S. Arridge. Photo-measurement density functions. part 1: Analytical forms. *Appl Opt* **34**(31), 7395–7409 (1995).

[19] S. Y. Bae, S. Haga, T. Hamaoka, and R. Kime. Quantitative contribution of oxidative metabolism in the human calf during supramaximal plantar flexion exercise. *Adv Exp Med* , 7–16 (1999).

[20] P. A. Bandettini, A. Jesmanowicz, E. C. Wong, and J. S. Hyde. Processing strategies for time-course data sets in functional MRI of the human brain. *Mag. Res. Med.* **30**, 161–73 (1993).

[21] A. J. Banos. *Dipole Radiation in the Presence of a Conducting Half-Space*. Pergamon Press New York (1966).

[22] E. L. Barbier, A. C. Silva, S. G. Kim, and A. P. Koretsky. Perfusion imaging using dynamic arterial spin labeling (DASL). *Mag Res Med* **45**, 1021–9 (2001).

[23] C. Barfod, N. Akgoren, M. Fabricius, U. Dirnagl, and M. Lauritzen. Laser-Doppler measurements of concentration and velocity of moving blood cells in rat cerebral circulation. *Acta Physiologica Scandinavica* **160**, 123–32 (1997).

[24] R. J. Bartrum and H. C. Crow. Transillumination lightscanning to diagnose breast cancer: A feasibility study. *AJR* **142**, 409414 (1984).

[25] M. Bassani, F. Martelli, G. Zaccanti, and D. Contini. Independence of the diffusion coefficient from absorption: experimental and numerical evidence. *Opt Lett* **22**, 853–855 (1997).

[26] R. Belardinelli, T. J. Barstow, J. Porszasz, and K. Wasserman. Changes in skeletal muscle oxygenation during incremental exercise measured with near infra-red spectroscopy. *Med & Sci in Sports & Exer* **27**, 487–92 (1995).

[27] R. Belardinelli, T. J. Barstow, J. Porszasz, and K. Wasserman. Skeletal muscle oxygenation during constant work rate exercise. *Med & Sci in Sports & Exer* **27**, 512–19 (1995).

[28] D. A. Benaron, S. R. Hintz, A. Villringer, D. Boas, A. Kleinschmidt, J. Frahm, C. Hirth, H. Obrig, J. C. van Houten, E. L. Kermit, W. F. Cheong, and D. K. Stevenson. Noninvasive functional imaging of human brain using light. *J Cereb Blood Flow Metab* **20**(3), 469–477 (2000).

[29] D. A. Benaron and D. K. Stevenson. Optical time-of-flight and absorbance imaging of biologic media. *Science* **259**(5100), 1463–6. (1993).

[30] B. J. Berne and R. Pecora. *Dynamic Light Scattering with Applications to Chemistry, Biology, and Physics*. Krieger Malabar, FL (1990).

[31] M. Bertolotti, B. Crosignani, P. Di Porto, and D. Sette. Light scattering by particles suspended in a turbulent fluid. *J. Phys. A* **2**, 126–128 (1969).

[32] Y. Bhambhani, S. Buckley, and T. Susaki. Detection of ventilatory threshold using near-infrared spectroscopy in men and women. *Med & Sci in Sports & Exer* **29**, 402–9 (1997).

[33] C. Binggeli, L. E. Spieker, R. Corti, I. Sudano, V. Stojanovic, D. Hayoz, T. F. Luscher, and G. Noll. Statins enhance postischemic hyperemia in the skin circulation of hypercholesterolemic patients: a monitoring test of endothelial dysfunction for clinical practice? *J Am Coll Cardiol* , 71–77 (2003).

[34] T. Binzoni, T. S. Leung, D. Boggett, and D. T. Delpy. Non-invasive laser Doppler perfusion measurements of large tissue volumes and human skeletal muscle blood RMS velocity. *Phys Med Biol* **48**, 2527–49 (2003).

[35] T. Binzoni, R. Springett, J. C. P. Dalton, and D. T. Delpy. A new combined deep body temperature/nir spectroscopy probe for non-invasive metabolic measurements on human skeletal muscle. *Adv. Exp. Biol.* **471**, 623–29 (1999).

[36] C. C. Bishop, S. Powell, D. Rutt, and N. L. Browse. Transcranial doppler measurement of middle cerebral artery blood flow velocity: a validation study. *Stroke* **17**, 913–5 (1986).

[37] D. A. Boas. *Diffuse Photon Probes of Structural and Dynamical Properties of Turbid Media: Theory and Biomedical Applications*. Ph.d. dissertation University of Pennsylvania (1996).

[38] D. A. Boas, D. H. Brooks, E. L. Miller, C. A. DiMarzio, M. Kilmer, R. J. Gaudette, and Q. Zhang. Imaging the body with diffuse optical tomography. *IEEE Signal Processing Magazine* **18**, 57–75 (2001).

[39] D. A. Boas, L. E. Campbell, and A. G. Yodh. Scattering and imaging with diffusing temporal field correlations. *Phys Rev Lett* **75**(9), 1855–1858 (1995).

[40] D. A. Boas, T. Gaudette, G. Strangman, X. Cheng, J. J. A. Marota, and J. B. Mandeville. The accuracy of near infrared spectroscopy and imaging during focal changes in cerebral hemodynamics. *NeuroImage* **13**, 76–90 (2001).

[41] D. A. Boas, I. V. Meglinsky, L. Zemany, L. E. Campbell, B. Chance, and A. G. Yodh. Diffusion of temporal field correlation with selected applications. *Biophys J* **70**(2), Wp306–Wp306 (1996).

[42] D. A. Boas, M. A. O'Leary, B. Chance, and A. G. Yodh. Scattering and wavelength transduction of diffuse photon density waves. *Phys Rev E* **47**(5), R2999–R3002 (1993).

[43] D. A. Boas, G. Strangman, J. P. Culver, R. D. Hoge, G. Jasdzewski, R. A. Poldrack, B. R. Rosen, and J. B. Mandeville. Can the cerebral metabolic rate of oxygen be estimated with near-infrared spectroscopy? *Phys Med Biol* **48**, 2405–18 (2003).

[44] D. A. Boas and A. G. Yodh. Spatially varying dynamical properties of turbid media probed with diffusing temporal light correlation. *J. Opt. Soc. Am. A* **14**(1), 192–215 (1997).

[45] H. Bolay, U. Reuter, A. K. Dunn, Z. Huang, D. A. Boas, and M. A. Moskowitz. Intrinsic brain activity triggers trigeminal meningeal afferents in a migraine model. *Nat. Med.* **8**, 136–42 (2002).

[46] R. F. Bonner and R. Nossal. *Laser-Doppler blood flowmetry* volume 107 chapter Principles of laser-Doppler flowmetry, pages 17–45. Kluwer Academic Publishers Boston (1990).

[47] P. J. Bourke, J. Butterworth, L. E. Drain, P. A. Egelstaff, E. Jakeman, and E. R. Pike. A study of the spatial structure of turbulent flow by intensity-fluctuation spectroscopy. *J.Phys.A* **3**, 216–228 (1970).

[48] H. M. Bramlett and W. D. Dietrich. Pathophysiology of cerebral ischemia and brain trauma: Similarities and differences. *J Cereb Blood Flow Metab* **24**, 133–50 (2004).

[49] J. E. Brazy, D. V. Lewis, M. H. Mitnick, and F. F. Jobsis. Noninvasive monitoring of cerebral oxygenation in preterm infants: preliminary observations. *Pediatrics* **75**, 217–225 (1985).

[50] J. D. Briers. Laser doppler and time-varying speckle: A reconciliation. *J. Opt. Soc. of Am. A* **13**, 345–350 (1996).

[51] J. D. Briers. Time-varying speckle for measuring motion and flow. In *Saratov Fall Meeting 2000 Report* (2000).

[52] J. D. Briers. Laser doppler, speckle and related techniques for blood perfusion mapping and imaging. *Physiol. Meas.* **22**, R35–66 (2001).

[53] J. D. Briers and S. Webster. Laser speckle contrast analysis (LASCA): A nonscanning, full-field technique for monitoring capillary blood flow. *J Biomed Opt* **1**, 174–179 (1996).

[54] W. Brown. *Dynamic Light Scattering: The Method and Some Applications*. Clarendon New York (1993).

[55] H. U. Bucher, A. D. Edwards, A. E. Lipp, and G. Duc. Comparison between near infrared spectroscopy and 133xenon clearance for estimation of cerebral blood flow in critically ill preterm infants. *Pediatric Research* **33**, 56–59 (1993).

[56] W. Burchert, S. Schellong, J. van den Hoff, G. J. Meyer, K. A. K. Alexander, and H. Hundeshagen. Oxygen-15-water PET assessment of muscular blood flow in peripheral vascular disease. *J Nucl Med* , 93–98 (1997).

[57] T. M. Busch, E. P. Wileyto, M. J. Emanuele, F. D. Piero, L. Marconato, E. Gladstein, and C. J. Koch. Photodynamic therapy creates fluence rate-dependent gradients in the intratumoral spatial distribution of oxygen. *Cancer Res* **62**, 7273–79 (2002).

[58] R. B. Buxton and L. R. Frank. 'a model for the coupling between cerebral blood flow and oxygen metabolism during neural stimulation. *J. Cereb. Blood Flow Metab.* **17**, 64–72 (1997).

[59] R. B. Buxton, E. C. Wong, and L. R. Frank. Dynamics of blood flow and oxygenation changes during brain activation: the balloon model. *Magn Reson Med* **39**(6), 855–64 (1998).

[60] W. Cai, M. Xu, and R. R. Alfano. Three-dimensional radiative transfer tomography for turbid media. *IEEE J Sel. Top. Q. Elec.* **9**, 189–98 (2003).

[61] W. Cai, M. Xu, M. Lax, and R. R. Alfano. Diffusion coefficient depends on time, not on absorption. *Opt Lett* **27**, 731–33 (2002).

[62] A. F. Cannestra, A. J. Blood, K. L. Black, and A. W. Toga. The evolution of optical signals in human and rodent cortex. *NeuroImage* **3**, 202–8 (1996).

[63] E. N. Carlsen. Transillumination light scanning. *Diagn. Imaging* **4**, 28–34 (1982).

[64] P. Cerretelli and T. Binzoni. The contribution of NMR, NIRS and their combination to the functional assessment of human muscle. *Int J Sports Med* **18**, S270–9 (1997).

[65] A. E. Cerussi, A. J. Berger, F. Bevilacqua, N. Shah, D. Jakubowski, J. Butler, R. F. Holcombe, and B. J. Tromberg. Sources of absorption and scattering contrast for near-infrared optical mammography. *Acad Radiol* **8**(3), 211–8. (2001).

[66] B. Chance and R. Alfano. Proceedings of optical tomography, photon migration, and spectroscopy of tissue and model media: Theory, human studies, and instrumentation. page 2389. SPIE (1995).

[67] B. Chance, M. Cope, E. Gratton, N. Ramanujam, and B. Tromberg. Phase measurement of light absorption and scattering in human tissues. *Rev. Sci. Instru.* **689**, 3457–3481 (1998).

[68] B. Chance, M. T. Dait, C. Zhang, T. Hamaoka, and F. Hagerman. Recovery from excercise-induced desaturation in the quadriceps muscles of elite competitive rowers. *Am. J. Physiol.* **262**, C766–C775 (1992).

[69] B. Chance, S. Eleff, W. Bank, J. S. Leigh, and R. Warnell. 31 P NMR studies of control of mitochondrial function in phosphofructokinase deficient human skeletal muscle. *Proc Natl Acad Sci USA* **79**, 7714–18 (1982).

[70] B. Chance, S. Eleff, J. S. Leigh, D. Sokolow, and A. Sapega. Mitochondrial regulation of phosphocreatine/inorganic phosphate ratios in exercising human muscle: a gated 31 P NMR study. *Proc Natl Acad Sci USA* **78**, 6714–18 (1981).

[71] B. Chance, S. Nioka, J. Kent, K. McCully, M. Fountain, R. Greenfeld, and G. Holtom. Time-resolved spectroscopy of hemoglobin and myoglobin in resting ischemic muscle. *Anal. Biochem.* **174**, 698–707 (1988).

[72] J. K. Chapin and C. S. Lin. Mapping the body representation in the SI cortex of anesthetized and awake rats. *J. Comp. Neurol.* **229**, 199–213 (1984).

[73] Z. Chen, T. E. Milner, S. Srinivas, X. Wang, A. Malekafzali, M. J. C. van Gemert, and S. J. Nelson. Noninvasive imaging in vivo blood flow velocity using optical doppler tomography. *Opt Lett* **22**(14), 1119–1121 (1997).

[74] Z. Chen, T. E. Milner, X. Wang, S. Srinivas, and J. S. Nelson. Optical doppler tomography: imaging in vivo blood flow dynamics following pharmacological intervention and photodynamic therapy. *Photochem. Photobiol.* **67**, 56–60 (1998).

[75] X. Cheng and D. A. Boas. Diffuse optical reflectance tomography with continuous-wave illumination. *Opt Express* **3**, 118–123 (1998).

[76] C. Cheung, J. P. Culver, K. Takahashi, J. H. Greenberg, and A. G. Yodh. In vivo cerebrovascular measurement combining diffuse near-infrared absorption and correlation spectroscopies. *Phys. Med. and Biol.* **46**(8), 2053–2065 (2001).

[77] R. Choe, A. Corlu, J. P. Culver, T. Durduran, B. Chance, and A. G. Yodh. 3-Dimensional diffuse optical tomography of *in vivo* human breasts in parallel plates geometry. *SPIE Photonics West* (2003).

[78] M. Cicoira, L. Zanolla, L. Franceschini, A. Rossi, G. Golia, M. Zamboni, P. Tosoni, and P. Zardini. Skeletal muscle mass independently predicts peak oxygen consumption and ventilatory response during exercise in noncachectic patients with chronic heart failure. *J Am Coll Cardiol* **37**, 2080–85 (2001).

[79] N. A. Clark, J. H. Lunacek, and G. B. Benedek. A study of brownian motion using light scattering. *Am J Phys* **38**, 575–585 (1970).

[80] S. B. Colak, D. G. Papaioannou, G. W. 't Hooft, M. B. van der Mark, H. Schomberg, J. C. J. Paasschens, J. M. Melissen, and N. A. A. J. van Asten. Tomographic image reconstruction from optical projections in light-diffusing media. *Appl Opt* **36**(1), 180–213 (1997).

[81] J. G. Colebatch, M. P. Deiber, R. E. Passingham, K. J. Friston, and R. S. Frackowiak. Regional cerebral blood flow during voluntary arm and hand movements in human subjects. *J Neurophysiol.* **65**, 1392–401 (1991).

[82] J. P. Coles, T. D. Fryer, P. Smielewski, D. A. Chatfield, L. A. Steiner, A. J. Johnston, S. P. M. J. Downey, G. B. Williams, F. Aigbirhio, P. J. Hutchinson, K. Rice, T. A. Carpenter, J. C. Clark, J. D. Pickard, and D. K. Menon. Incidence and mechanisms of cerebral ischemia in early clinical head injury. *J Cereb Blood Flow Metab* **24**, 202–11 (2004).

[83] M. Cope. *The Development of a Near-Infrared Spectroscopy System and Its Application for Noninvasive Monitoring of Cerebral Blood and Tissue Oxygenation in the Newborn Infant*. University College London London (1991).

[84] M. Cope and D. T. Delpy. System for long-term measurement of cerebral blood flow and tissue oxygenation on newborn infants by infra-red transillumination. *Med Biol Eng Comput* **26**, 289–294 (1988).

[85] J. O. Coq and C. Xerri. Environmental enrichment alters organizational features of the forepaw representation in the primary somatosensory cortex of adult rats. *Exp. Brain Res.* **121**, 191–204 (1998).

[86] A. Corlu, T. Durduran, R. Choe, M. Schweiger, E. M. C. Hillman, S. R. Arridge, and A. G. Yodh. Uniqueness and wavelength optimization in continous-wave multispectral diffuse optical tomography. *Opt. Lett* **28**, 2339–2341 (2003).

[87] F. Costes, B. Jean-Claude, L. Feasson, T. Busso, A. Geyssant, and C. Denis. Comparison of muscle near-infrared spectroscopy and femoral blood gases during steady-state exercise in humans. *J Appl Physiol* **80**, 1345–50 (1996).

[88] R. Cubeddu, C. D'Andrea, A. Pifferi, P. Taroni, A. Torricelli, and G. Valentini. Effects of the menstrual cycle on the red and near-infrared optical properties of the human breast. *Photochem and Photobiol* **72**, 383–391 (2000).

[89] J. P. Culver, R. Choe, M. J. Holboke, L. Zubkov, T. Durduran, A. Slemp, V. Ntziachristos, D. N. Pattanayak, B. Chance, and A. G. Yodh. 3D diffuse optical tomography in the plane parallel transmission geometry: Evaluation of a hybrid frequency domain/continuous wave clinical system for breast imaging. *Med Phys* **30**, 235–247 (2003).

[90] J. P. Culver, T. Durduran, D. Furuya, C. Cheung, J. H. Greenberg, and A. G. Yodh. Diffuse optical measurement of hemoglobin and cerebral blood flow in rat brain during hypercapnia, hypoxia and cardiac arrest. In D. Wilson, S. Evans, J. Biaglow, and A. Pastuszko, editors, *Adv. Exp. Biol.* volume XXIII pages 293–298. Plenum Press (2002).

[91] J. P. Culver, T. Durduran, D. Furuya, C. Cheung, J. H. Greenberg, and A. G. Yodh. Diffuse optical tomography of cerebral blood flow, oxygenation and metabolism in rat during focal ischemia. *J. Cereb. Blood Flow Metab.* **23**, 911–24 (2003).

[92] J. P. Culver, V. Ntziachristos, M. J. Holboke, and A. G. Yodh. Optimization of optode arrangements for diffuse optical tomography: A singular-value analysis. *Opt Lett* **26**(10), 701–703 (2001).

[93] J. P. Culver, A. Siegel, J. J. Stott, and D. A. Boas. Volumetric diffuse optical tomography of brain activity. *Opt. Lett.* **28**, 2061–63 (2003).

[94] H. Z. Cummings and E. R. Pike. *Photon Correlation and Light-Bearing Spectroscopy*. Vol. 3 of NATO Advanced Study Institute Series B: Physics. Plenum New York (1974).

[95] H. Z. Cummings and H. L. Swinney. Light beating spectroscopy. *Prog. Opt.* **8**, 133–200 (1970).

[96] M. Cutler. Transillumination of the breast. *Surg Gynecol Obstet* **48**, 721–727 (1929).

[97] R. A. De Blasi, M. Cope, C. Elwell, F. Safoue, and M. Ferrari. Noninvasive measurement of human forearm oxygen consumption by near infrared spectroscopy. *Eur J Appl Physiol Occup Physiol* **67**, 20–25 (1993).

[98] R. A. De Blasi, S. Fantini, M. A. Franceschini, M. Ferrari, and E. Gratton. Cerebral and muscle oxygen saturation measurement by frequency-domain near-infrared spectrometer. *Med Biol Eng Comput* **33**, 228–30 (1995).

[99] R. A. De Blasi, M. Ferrari, A. Natali, G. Conti, A. Mega, and A. Gasparetto. Noninvasive measurement of forearm blood flow and oxygen consumption by near-infrared spectroscopy. *J Appl Physiol* **76**, 1388–93 (1994).

[100] D. T. Delpy, M. Cope, P. van der Zee, S. Arridge, S. Wray, and J. Wyatt. Estimation of optical pathlength through tissue from direct time of flight measurement. *Phys Med Biol* **33**, 1433–1442 (1988).

[101] D. T. Delpy, M. C. Cope, E. B. Cady, J. S. Wyatt, P. A. Hamilton, P. L. Hope, S. Wray, and E. O. Reynolds. Cerebral monitoring in newborn infants by magentic resonance and near infrared spectroscopy. *Scand. J. Clin. Lab. Invest. Suppl.* **188**, 9–17 (1987).

[102] J. A. Detre and D. C. Alsop. Perfusion magnetic resonance imaging with continuous arterial spin labeling: methods and clinical applications in the central nervous system. *Euro J Rad* **30**(2), 115–124 (1999).

[103] J. A. Detre, B. M. Ances, K. Takahashi, and J. H. Greenberg. Signal averaged laser doppler measurements of activation-flow coupling in the rat forepaw somatosensory cortex. *Brain Res.* **796**, 91–98 (1998).

[104] J. A. Detre, W. Zhang, D. A. Roberts, A. C. Silva, D. S. Williams, D. J. Grandis, A. P. Koretsky, and J. S. Leigh. Tissue specific perfusion imaging using arterial spin labeling. *NMR in Biomedicine* **7**, 75–82 (1994).

[105] J. Dings, J. Meixensberger, A. Jager, and K. Roosen. clinical experience with 118 brain tissue oxygen partial pressure catheter probes. *Neurosurgery* **43**, 1082–95 (1998).

[106] T. J. Dougherty, K. J. E, A. Goldfarb, K. R. Weishaupt, D. Boyle, and A. Mittleman. Photodynamic therapy for the treatment of malignant tumors. *Can. Res.* **38**, 2628–35 (1978).

[107] T. J. Dougherty, C. J. Gomer, B. W. Henderson, G. Jori, D. Kessel, M. Korbelik, J. Moan, , and Q. Peng. Photodynamic therapy. *J. Nat. Cancer Inst.* **90**, 889–905 (1998).

[108] T. J. Dougherty, G. B. Grindley, R. Fiel, K. R. Weishaupt, and B. D. Photoradiation therapy. ii. cure of animal tumors with hematoporphyrin and light. *J. Natl. Cancer Inst.* **55**, 115–21 (1975).

[109] T. J. Dougherty and A. Katzir. Optical methods for tumor treatment and detection: mechanisms and techniques in photodynamic therapy. *SPIE, Photonics West* **1645**(7), 103–114 (1992).

[110] A. Duncan, J. H. Meek, M. Clemence, C. E. Elwell, L. Tyszczuk, M. Cope, and D. T. Delpy. Optical pathlength measurements on adult head, calf and forearm and the head of the newborn infant using phase resolved optical spectroscopy. *Phys Med Biol* **40**(2), 295–304. (1995).

[111] A. Duncan, T. L. Wheatlock, M. Cope, and D. T. Delpy. Measurements of changes in optical pathlength through human muscle during cuff occlusion on the arm. *Optic and Laser Tech* **27**, 269–74 (1995).

[112] A. K. Dunn, T. Bolay, M. A. Moskowitz, and D. A. Boas. Dynamic imaging of cerebral blood flow using laser speckle. *J. Cereb. Blood Flow Metab.* **21**(3), 195–201 (2001).

[113] A. K. Dunn, A. Devor, H. Bolay, M. L. Andermann, M. A. Moskowitz, A. M. Dale, and D. A. Boas. Simultaneous imaging of total cerebral hemoglobin concentration, oxygenation, and blood flow during functional activation. *Opt. Lett.* **28**, 28–30 (2003).

[114] T. Q. Duong, A. C. Silva, S. P. Lee, and S. Kim. Functional MRI of calcium-dependent synaptic activity: Cross correlation with CBF and BOLD measurements. *Mag. Res. Med.* **43** (2000).

[115] T. Durduran, M. G. Burnett, G. Yu, C. Zhou, D. Furuya, A. G. Yodh, J. A. Detre, and J. H. Grenberg. Spatio-temporal quantification of cerebral blood flow during functional activation in rat somatosensory cortex using laser speckle flowmetry. *J. Cereb. Blood Flow Metab.* **accepted, in press** (2003).

[116] T. Durduran, B. Chance, A. G. Yodh, and D. A. Boas. Does the photon diffusion coefficient depend on absorption? *J. Opt. Soc. Am. A* **14**, 3358–3365 (1997).

[117] T. Durduran, R. Choe, J. P. Culver, L. Zubkov, M. J. Holboke, J. Giammarco, B. Chance, and A. G. Yodh. Bulk optical properties of healthy female breast tissue. *Phys Med Biol* **47**, 2847–2861 (2002).

[118] T. Durduran, J. P. Culver, M. J. Holboke, X. D. Li, L. Zubkov, B. Chance, D. N. Pattanayak, and A. G. Yodh. Algorithms for 3d localization and imaging using near-field diffraction tomography with diffuse light. *Optics Express* **4**(8), 247–262 (1999).

[119] T. Durduran, J. Giammarco, J. P. Culver, R. Choe, L. Zubkov, M. J. Holboke, B. Chance, and A. G. Yodh. Explicit inclusion of chromophore absorption and scattering spectra for diffuse optical imaging and spectroscopy. *Photonics West, SPIE* **4250-85** (2001).

[120] T. Durduran, G. Yu, G. Lech, C. Zhou, B. Chance, and A. G. Yodh. Noninvasive simultaneous measurements of tissue oxygenation and blood flow during exercise and cuff-ischemia in human calf muscle. In *Proc. SPIE, Photonics West* (2003).

[121] T. Durduran, G. Yu, C. Zhou, J. A. Detre, J. H. Greenberg, M. G. Burnett, and A. G. Yodh. Diffuse optical measurements of blood flow, blood oxygenation and metabolism in human brain during sensorimotor cortex activation. *Opt Lett* **submitted** (2004).

[122] D. J. Durian. The diffusion coefficient depends on absorption. *Opt Lett* **23**, 1502–1504 (1998).

[123] B. J. E and L. D. V. Changes in cerebral blood volume and cytochrome AA3 during hypertensive peaks in preterm infants. *J Pediatr* **108**, 983–987 (1986).

[124] R. Elaloufi, R. Carminati, and J. J. Greffet. Definition of the diffusion coefficient in scattering in absorbing media. *J. Opt. Soc. Am. A* **20**, 678–85 (2003).

[125] K. A. Engelke, J. R. Halliwill, D. N. Proctor, N. M. Dietz, and M. J. Joyner. Contribution of nitric oxide and prostaglandins to reactive hyperemia. *J Appl Physiol* **81**, 1807–14 (1996).

[126] M. J. Eppstein, D. E. Dougherty, T. L. Troy, and E. M. Sevick-Muraca. Biomedical optical tomography using dynamic parameterization and bayesian conditioning on photon migration measurements. *Appl Opt* **38**, 2138–2150 (1999).

[127] J. P. Erinjeri and T. A. Woolsey. Spatial integration of vascular changes with neural activity in mouse cortex. *J Cereb Blood Flow Metab* **22**, 353–60 (2002).

[128] R. Everson, B. W. Knight, and L. Sirovich. Separating spatially distributed response to stimulation from background. i. optical imaging. *Biol Cybernetics* **77**, 407–17 (1997).

[129] M. Fabricius, N. Akgoren, U. Dirnagl, and M. Lauritzen. Laminar analysis of cerebral blood flow in cortex of rats by laser-doppler flowmetry: A pilot study. *J. Cereb. Blood Flow Metab.* **17**, 1326 (1997).

[130] M. Fabricius and M. Lauritzen. Examination of the role of nitric-oxide for the hypercapnic rise of cerebral blood-flow in rats. *Am J Physiol* **266**, H1457–64 (1994).

[131] M. Fabricius, I. Rubin, M. Bundgaard, and M. Lauritzen. NOS activity in brain and endothelium: Relation to hypercapnic rise of cerebral blood flow in rats. *Am J Physiol-Heart and Circulatory Physiology* **40**, H2035–44 (1996).

[132] T. J. Farrell, R. P. Hawkes, M. S. Patterson, and B. C. Wilson. Modeling of photosensitizer fluorescence emission and photobleaching for photodynamic therapy dosimetry. *Appl Opt* **37**(31), 7168–7183 (1998).

[133] M. Ferrari, Q. Wei, L. Carraresi, R. De Blasi, and G. Zaccanti. Time-resolved spectroscopy of the human forearm. *J. Photochem. Photobiol.* **16**, 141–153 (1992).

[134] A. M. R. Fisher, A. L. Murphere, and C. J. Gomer. Clinical and preclinical photodynamic therapy. *Las. Surg. Med.* **17**, 2–31 (1995).

[135] J. B. Fishkin and E. Gratton. Propagation of photon density waves in strongly scattering media containing an absorbing 'semi-infinite' plane bounded by a straight edge. *J. Opt. Soc. Am. A* **10**, 127–140 (1993).

[136] M. L. Forbes. Assessment of cerebral blood flow and CO_2 reactivity after controlled cortical impact by perfusion magnetic resonance imaging using arterial spin-labelling in rats. *J Cereb Blood Flow and Metab* **17**, 1263 (1997).

[137] J. B. Fortune, P. J. Feustel, L. Carlo, L. Graca, J. Hasselbarth, and A. M. Kupinski. Cerebral blood flow and blood volume in response to osub 2 and cosub 2 changes in normal humans. *J Trauma* **39**, 463–72 (1995).

[138] T. H. Foster and L. Gao. Dosimetry in photodynamic therapy: Oxygen and the critical importance of capillary density. *Radiation Res* **130** (1992).

[139] T. H. Foster, D. F. Hartley, M. G. Nichols, and R. Hilf. Fluence rate effects in photodynamic therapy of multicell tumor spheroids. *Cancer Res* **53**, 1249–1254 (1993).

[140] T. H. Foster, R. S. Murant, R. G. Byrant, R. S. Knox, S. L. Gibson, and R. Hilf. Oxygen consumption and diffusion effects in photodynamic therapy. *Radiation Res* **126**, 296–303 (1991).

[141] R. S. Frackowiak, G. L. Lenzi, T. Jones, and J. D. Heather. Quantitative measurement of regional cerebral blood flow and oxygen metabolism in man using 150 and positron emission tomography: theory, procedure, and normal values. *J. Comput. Assit. Tomogr.* **4**, 727–36 (1980).

[142] M. A. Franceschini, S. Fantini, J. H. Thompson, J. P. Culver, and D. A. Boas. Hemodynamic evoked response of the sensorimotor cortex measured noninvasively with near-infrared optical imaging. *Psychophysiol.* **40**, 548–60 (2003).

[143] M. A. Franceschini, V. Toronov, M. E. Filiaci, E. Gratton, and S. Fantini. On-line optical imaging of the human brain with 160-ms temporal resolution. *Optics Express* **6**(3), 49–57 (2000).

[144] L. R. Frank, E. C. Wong, L. J. Haseler, and R. B. Buxton. Dynamic imaging of perfusion in human skeletal muscle during exercise with arterial spin labeling. *Magn Reson Med* **42** (1999).

[145] K. J. Friston, A. Mechelli, R. Turner, and C. J. Price. Nonlinear responses in fMRI: the balloon model, volterra kernels, and other hemodynamics. *NeuroImage* **12**(4), 466–77. (2000).

[146] R. D. Frostig, E. E. Lieke, D. Y. Tso, and A. Grinvald. Cortical functional architecture and local coupling between neuronal activity and the microcirculation revealed by in vivo high-resolution optical imaging of intrinsic signals. *Proc Natl Acad Sci USA* **87**(16), 6082–6 (1990).

[147] H. Fujii, T. Asakura, K. Nohira, Y. Shintomi, and T. Ohura. Blood flow observed by time-varying laser speckle. *Opt. Lett.* **10**, 104–6 (1985).

[148] G. G. Fuller, J. M. Rallison, R. L. Schmidt, and L. G. Leal. The measurement of velocity gradients in laminar flow by homodyne light-scattering spectroscopy. *J.Fluid Mech.* **100**, 555–575 (1980).

[149] K. Furutsu. On the diffusion equation derived from the space-time transport equation. *J. Opt. Soc. Am. A* **70**, 360 (1980).

[150] K. Furutsu and Y. Yamada. Diffusion approximation for a dissipative random medium and the applications. *Phys. Rev. E* **50**, 3634 (1994).

[151] M. Gabbay, C. Brennan, E. Kaplan, and L. Sirovich. A principal components-based method for the detection of neuronal activity maps: application to optical imaging. *NeuroImage* **11**, 313–25 (2000).

[152] R. Gaudette. Constrained reconstruction techniques for diffuse optical tomography. Master's thesis Harvard University (2000).

[153] M. S. Gee, H. M. Saunders, J. C. Lee, J. F. Sanzo, W. T. Jenkins, S. M. Evans, G. Trinchieri, C. M. Seghal, M. D. Feldman, and W. M. F. Lee. Doppler ultrasound imaging detects

changes in tumor perfusion during antivascular therapy associated with vascular anatomic alterations. *Cancer Res* **61**, 2974–82 (2001).

[154] J. J. Gisvold, L. R. Brown, R. G. Swee, D. J. Raygor, N. Dickerson, and M. K. Ranfranz. Comparison of mammography and transillumination light scanning in the detection of breast lesions. *AJR* **147**, 191–194 (1986).

[155] A. Gjedde. *Cerebrovascular disease* chapter on The relation between brain function and cerebral blood flow and metabolism, pages 23–40. Lippincott-Raven Philadelphia (1997).

[156] C. D. Gomersall, G. M. Joynt, T. Gin, R. Freebairn, and I. E. Stewart. Failure of the INVOS3100 cerebral oximeter to detect complete absence of cerebral blood flow. *Crit. Care. Med.* **25**, 1252–4 (1997).

[157] S. P. Gopinath, C. S. Robertson, C. F. Contant, R. K. Narayan, R. G. Grossman, and B. Chance. Early detection of delayed traumatic intracranial hematomas using near-infrared spectroscopy. *J Neurosurg.* **83**, 438–44 (1995).

[158] S. P. Gopinath, C. S. Robertson, R. G. Grossman, and B. Chance. Near-infrared spectroscopic localization of intracranial hematomas. *J Neurosurg.* **79**, 43–7 (1993).

[159] A. Gorji. Spreading depression: a review of the clinical relevance. *Brain Res Rev* **38**, 33–60 (2001).

[160] E. Gratton, W. Mantulin, M. J. Ven, M. van de Ven, J. Fishkin, M. Maris, and B. Chance, editors. *Proceedings of The Third International Conference: Peace through Mind/Brain Science.* Hamamatsu, Japan (1990).

[161] H. Gray. *Anatomy of the Human Body*. Bartleby.com http://www.bartleby.com/107/ 20 edition (1918).

[162] A. Grinvald, L. Anglister, J. A. Freeman, R. Hildesheim, and A. Manker. Real-time optical imaging of naturally evoked electrical activity in intact frog brain. *Nature* **308**, 848–850 (1984).

[163] A. Grinvald, R. D. Frostig, E. Lieke, and R. Hildesheim. Optical imaging of neuronal activity. *Physiol Rev* **68**, 1285–1366 (1988).

[164] A. Grinvald, R. D. Frostig, R. M. Siegel, and E. Bartfeld. High-resolution optical imaging of functional brain architecture in the awake monkey. *Proc. natl. Acad. Sci. USA* **88**, 11559–11563 (1991).

[165] A. Grinvald, E. Lieke, R. D. Frostig, C. D. Gilbert, and T. N. Wiesel. Functional architecture of cortex revealed by optical imaging of intrinsic signals. *Nature* **324**, 361–364 (1986).

[166] A. Grinvald, D. Shoham, A. Shmuel, D. E. Glaser, I. Vanzetta, E. Shtoyerman, H. slovin, C. Winjbergen, R. Hildesheim, A. Sterkin, and A. Arieli. *Modern Techniques in Neuroscience Research* chapter *In vivo* optical imaging of cortical architecture and dynamics. Methods and New Frontiers in Neuroscience. Springer-Verlag (1999).

[167] R. A. J. Groenhuis, H. A. Ferwerda, and T. J. J. Bosch. Scattering and absorption of turbid materials determined from reflection measurements, I. theory. *Appl Opt* **22**, 2456–2462 (1983).

[168] R. L. J. Grubb, M. Raichle, J. O. Eichling, and M. M. Ter-Pogossian. The effects of changes in paco2 on cerebral blood volume, blood flow, and vascular mean transit time. *Stroke* **5**(5), 630–9 (1974).

[169] Y. A. Gryazin, M. V. Klibanov, and T. R. Lucas. Imaging the diffusion coefficient in a parabolic inverse problem in optical tomography. *Inverse Problems* **1**, 373–397 (1999).

[170] M. Hackmeier, S. E. Skipetrov, G. Maret, and R. Maynard. Imaging of dynamic heterogeneities in mulitiple-scattering media. *J Opt Soc Am A* **14**, 185–191 (1997).

[171] N. Hadjihani, M. S. del Rio, O. Wu, D. Schwarz, D. Bakker, B. Fischl, K. K. Kwong, F. M. Cutrer, R. B. H. Tootell, A. G. Sorensen, and M. A. Moskowitz. Mechanisms of migraine aura revealed by functional MRI in human visual cortex. *Proc Natl Acad Sci* **98**, 4687–92 (2001).

[172] N. B. Hampson and C. A. Piantadosi. Near infrared monitoring of human skeletal muscle oxygenation during forearm ischemia. *J. Appl. Physiol.* **64**, 2449–57 (1988).

[173] P. Hansen. Analysis of discrete ill-power problems by means of the L-curve. *SIAM Rev.* **34**, 561–80 (1992).

[174] P. Hanson and D. O'Leary. The use of the L-curve in the regularization of discrete ill-posed problems. *SIAM J. Sci. Comput.* **14**, 1487–1503 (1993).

[175] F. Harrell. *Regression Modeling Strategies*. Springer New York (2001).

[176] R. C. Haskell, L. O. Svaasand, T. Tsay, T. Feng, M. S. McAdams, and B. J. Tromberg. Boundary conditions for the diffusion equation in radiative transfer. *J Opt Soc Am A* **11**, 2727–2741 (1994).

[177] D. J. Hawrysz and E. M. Sevick-Muraca. Developments toward diagnostic breast cancer imaging using near-infrared optical measurements and fluorescent contrast agents. *Neoplasia* **2**(5), 388–417. (2000).

[178] J. C. Hebden. Advances in optical imaging of the newborn infant brain. *Psychophysiol.* **40**, 501–10 (2003).

[179] J. C. Hebden, S. R. Arridge, and D. T. Delpy. Optical imaging in medicine: I. experimental techniques. *Phys Med Biol* **42**, 825–840 (1997).

[180] J. C. Hebden and D. T. Delpy. Diagnostic imaging with light. *Br J Radiol* **70 Spec No**, S206–14. (1997).

[181] W. D. Heiss, R. Graf, J. Lottgen, K. Ohta, T. Fujita, R. Wagner, M. Grond, and K. Weinhard. Repeat positron emission tomographic studies in transient middle cerebral artery occlusion in cats: Residual perfusion and efficacy of postischemic reperfusion. *J Cereb Blood Flow Metab* **17**, 388–400 (1997).

[182] W. D. Heiss, R. Graf, K. Wienhard, J. Lottgen, R. Saito, T. Fujita, G. Rosner, and R. Wagner. Dynamic penumbra demonstrated by sequential multitracer PET after middle cerebral-artery occlusion in cats. *J Cereb Blood Flow Metab* **14**, 892–902 (1994).

[183] S. Hellem, L. S. Jacobsson, G. E. Nilsson, and D. H. Lewis. Measurements of microvascular blood flow in cancellous bone using laser doppler flowmetry and 133Xe-clearance. *Int. J. Oral Surg.* **12**, 165–177 (1983).

[184] S. R. Hintz, D. A. Benaron, A. M. Siegel, D. K. Stevenson, and D. A. Boas. Bedside functional imaging of the premature infant brain during passive motor activation. *Journal of Investigative Medicine* **47**(2), 60a–60a (1999).

[185] R. D. Hoge, J. Atkinson, B. Gill, G. R. Crelier, S. Marrett, and G. B. Pike. Investigation of BOLD signal dependence on cerebral blood flow and oxygen consumption: the deoxyhemoglobin dilution model. *Magn Reson Med* **42**(5), 849–63 (1999).

[186] R. D. Hoge, J. Atkinson, B. Gill, G. R. Crelier, S. Marrett, and G. B. Pike. Linear coupling between cerebral blood flow and oxygen consumption in activated human cortex. *Proc Natl Acad Sci U S A* **96**(16), 9403–8 (1999).

[187] S. Homma, H. Eda, S. Ogasawara, and A. Kagaya. Near-infrared estimation of O2 supply and consumption in forearm muscles working at varying intensity. *J Appl Physiol* **80**, 1279–1284 (1996).

[188] D. M. Hueber, M. A. Franceschini, H. Y. Ma, Q. Zhang, J. R. Ballesteros, S. Fantini, D. Wallace, V. Ntziachristos, and B. Chance. Non-invasive and quantitative near-infrared haemoglobin spectrometry in the piglet brain during hypoxic stress, using a frequency-domain multidistance instrument. *Phys Med Biol* **46**(1), 41–62. (2001).

[189] F. Hyder, K. L. Behar, M. A. Martin, A. M. Blamire, and R. G. Shulman. Dynamic magnetic resonance imaging of the rat brain during forepaw stimulation. *J. Cereb. Blood Flow Metab.* **14**, 649–655 (1994).

[190] F. Hyder, R. G. Shulman, and D. L. Rothman. A model for the regulation of cerebral oxygen delivery. *J Appl Physiol* **85**(2), 554–64. (1998).

[191] N. Iftimia and H. B. Jiang. Quantitative optical image reconstruction of turbid media by use of direct-current measurements. *Appl Opt* **39**(28), 5256–5261 (2000).

[192] A. Ishimaru. *Wave Propagation and Scattering in Random Media*. Academic Press, Inc. San Diego (1978).

[193] A. J and S. M. Brain injury after adult cardiac surgery. *Acta Anaesthesiol Scan* **48**, 4–19 (2004).

[194] S. L. Jacques. Time resolved propagation of ultrashort laser pulses within turbid tissues. *Appl Opt* **28**, 2223–2229 (1989).

[195] H. Jasper. Report of the committe on methods of clinical examination in electroencephalography. *Clin. Neurophysiol.* **10**, 370–5 (1958).

[196] M. Jensen-Urstad, I. Hallback, and K. Sahlin. Effect of hypoxia on muscle oxygenation and metabolism during arm exercise in humans. *Clin Physiol* **15**, 27–37 (1995).

[197] H. Jiang, K. D. Paulsen, U. L. Oesterberg, and M. S. Patterson. Frequency-domain optical image reconstruction in turbid media: an experimental study of single-target detectability. *Appl Opt* **36**(1), 52–63 (1997).

[198] H. Jiang, K. D. Paulsen, and U. L. Osterberg. Optical image reconstruction using dc data: simulations and experiments. *Phys. Med. Biol.* **41**, 1483–1498 (1996).

[199] H. Jiang, K. D. Paulsen, U. L. Osterberg, and M. S. Patterson. Improved continuous light diffusion imaging in single- and multi-target tissue-like phantoms. *Phys Med Biol* **43**(3), 675–93. (1998).

[200] H. Jiang, Y. Xu, N. Iftimia, J. Eggert, K. Klove, L. Baron, and L. Fajardo. Three-dimensional optical tomographic imaging of breast in a human subject. *IEEE Transactions on Medical Imaging* **20**(12), 1334–1340 (2001).

[201] R. Joannides, W. E. Haefeli, L. Linder, V. Richard, E. H. Bakkali, C. Thuillez, and T. F. Luscher. Nitric oxide is responsible for flow-dependent dilatation of human peripheral conduit arteries in vivo. *Circulation* **91**, 1314–19 (1995).

[202] F. F. Jobsis. Noninvasive infrared monitoring of cerebral and myocardial sufficiency and circulatory parameters. *Science* **198**, 1264–1267 (1977).

[203] C. C. Johnson. Optical diffusion in blood. *IEEE Transactions on Biomedical Engineering* **BME17**, 129–133 (1970).

[204] A. C. Kak and M. Slaney. *Principles of Computerized Tomographic Imaging*. IEEE Press New York (1988).

[205] J. R. Kappa, H. D. Berkowitz, R. Seestedt, and B. Chance. *Medical intelligence unit: vascular surgery 2000* chapter Evaluation of calf muscle oxygen content. Using NIRS in patients with peripheral vascular disease, pages 10–16. (1991).

[206] A. Kastrup, G. Kruger, T. Neumann-Haefelin, G. H. Glover, and M. E. Moseley. Changes of cerebral blood flow, oxygenation, and oxidative metabolism during graded motor activation. *NeuroImage* , 74–82 (2002).

[207] A. Kharlamov, B. R. Brown, K. A. Easley, and S. C. Jones. Heterogeneous changes in cerebral blood flow during hypotension demonstrated by laser speckle technique. *J. Cereb. Blood Flow Metab., Suppl* **23**(S1), 84 (2003).

[208] K. C. Kidd and L. Criddle. Using jugular venous catheters in patients with traumatic brain injury. *Critical Care Nurse* **21**(6), 16–22 (2001).

[209] J. W. Kiel, G. L. Riedel, G. R. DiResta, and A. P. Shepherd. Gastric mucosal blood flow measured by laser-doppler velocimetry. *Am. J. Physiol.* **249**, G539–545 (1985).

[210] M. E. Kilmer, E. L. Miller, A. Barbaro, and D. A. Boas. Three-dimensional shape-based imaging of absorption perturbation for diffuse optical tomography. *Appl. Opt.* **42**, 3129–44 (2003).

[211] S. G. Kim. Quantification of relative cerebral blood flow change by flow-sensitive alternating inversion recovery (FAIR) technique: application to functional mapping. *Mag. Res. Med.* **34**, 293–301 (1995).

[212] F. J. Kirkham, T. S. Padayachee, S. Parsons, L. S. Seargeant, F. R. House, and R. G. Gosling. Transcranial measurement of blood velocities in the basal cerebral arteries using pulsed doppler ultrasound: velocity as an index of flow. *Ultrasound Med Biol* **12**, 15–21 (1986).

[213] M. V. Klibanov, T. R. Lucas, and R. M. Frank. A fast and accurate imaging algorithm in optical /diffusion tomography. *Inverse Problems* **13**, 1341–1361 (1997).

[214] M. Kohl, U. Lindauer, U. Dirnagl, and A. Villringer. Separation of changes in light scattering and chromophore concentrations during cortical spreading depression in rats. *Opt. Lett.* **23**, 555–57 (1998).

[215] M. Kohl, U. Lindauer, G. Royl, M. Kuhl, L. Gold, A. Villringer, and U. Dirnagl. Physical model for the spectroscopic analysis of cortical intrinsic optical signals. *Phys. Med. Biol.* **45**, 3749–3764 (2000).

[216] H. Koizumi, A. Naki, and T. Yamamoto. Optical tomography: Practical problems and novel applications. In *OSA Biomedical Topical Meetings, OSA Technical Digest* pages 294–6 Miami, FL (2002). Optical Society of America.

[217] J. Koizumi, T. Nakazawa, and Y. Yoshida. Reperfusable brain infarction model in the rat. In *Proceedings of the 10th Meeting of the Japanese Stroke Society* page 159 Kyoto, Japan (1985).

[218] H. M. Kooijman, M. T. Hopman, W. N. Colier, J. A. van der Vliet, and B. Oeseburg. Near infrared spectroscopy for noninvasive assessment of claudication. *J Surg Res* **72**, 1–7 (1997).

[219] K. K. Kwong, J. W. Belliveau, D. A. Chesler, I. E. Goldberg, R. M. Weisskoff, B. P. Poncelet, D. N. Kennedy, B. E. Hoppel, M. S. Cohen, R. Turner, H. Cheng, T. J. Brady, and B. R. Rosen. Dynamic magnetic resonance imaging of human brain activity during primary sensory stimulation. *Proc. Natl. Acad. Sci. USA* **89**(12), 5675–9 (1992).

[220] M. H. Laughlin. Skeletal muscle blood flow capacity: role of muscle pump in exercise hyperemina. *Am. J. Physiol.* **253**, H993–1004 (1987).

[221] M. Lauritzen. Long-lasting reduction of cortical blood flow of the rat brain after spreading depression with preserved autoregulation and impaired co_2 response. *J Cereb Blood Flow and Metab* **4**, 546–54 (1984).

[222] M. Lauritzen and N. H. Diemer. Uncoupling of cerebral blood flow and metabolism after single episode of cortical spreading depression in the rat brain. *Brain Res* **370**, 405–8 (1986).

[223] A. A. P. Leao. Spreading depression of activity in cerebral cortex. *J. Neurophys.* **7**, 359–90 (1944).

[224] S. B. Lewis, J. A. Myburgh, E. L. Thornton, and P. L. Reilly. Cerebral oxygenation monitoring by near-infrared spectroscopy is not clinically useful in patients with severe closed-head injury: A comparison with jugular venous bulb oximetry. *Crit. Care. Med.* **24**, 1334–8 (1996).

[225] A. Li, E. L. Miller, M. E. Kilmer, T. J. Brukilacchio, T. Chaves, J. Stott, Q. Zhang, T. Wu, M. Chorlton, R. H. Moore, D. B. Kopans, and D. A. Boas. Tomographic optical breast imaging guided by three-dimensional mammography. *Appl. Opt.* **42**, 5181–90 (2003).

[226] X. D. Li. *Fluorescence and diffusive wave diffraction tomographic probes in turbid media*. Ph.d University of Pennsylvania (1998).

[227] X. D. Li, T. Durduran, B. Chance, A. G. Yodh, and D. N. Pattanayak. Diffraction tomography for biochemical imaging with diffuse-photon density waves. *Opt Lett* **22**(8), 573–575 (1997).

[228] X. D. Li, D. N. Pattanayak, T. Durduran, J. P. Culver, B. Chance, and A. G. Yodh. Near-field diffraction tomography with diffuse photon density waves. *Phys Rev E* **61**(4), 4295–4309 (2000).

[229] J. R. Libonati, M. Cox, N. Incanno, S. K. Melville, F. C. Musante, and H. L. Glassberg. Brief periods of occlusion and reperfusion increase skeletal muscle force output in humans. *Cardiologia* **43**, 1355–60 (1998).

[230] J. R. Libonati, A. K. Howell, N. M. Incanno, K. K. Pettee, and H. L. Glassberg. Brief muscle hypoperfusion/hyperemia: an ergogenic aid? *J Strength Cond Res* **15**, 362–66 (2001).

[231] E. Z. Longa, P. R. Weinstein, S. Carlson, and R. Cummins. Reversible middle cerebral artery occlusion without craniectomy in rats. *Stroke* **20**, 84–91 (1989).

[232] H. C. Lou, L. Edvinsson, and E. T. Mackenzie. The concept of coupling blood-flow to brain-function - revision required. *An. of Neurol.* **22**(3), 289–297 (1987).

[233] Z. Luksiene. Photodynamic therapy: mechanism of action and ways to improve the efficiency of treatment. *Medicina (Kaunas)* **39**, 1137–50 (2003).

[234] F. C. MacKintosh and S. John. Diffusing-wave spectroscopy and multiple scattering of light in correlated random media. *Phys.Rev.B* **40**, 2382–2406 (1989).

[235] D. Magatti and F. Ferri. Fast multi-tau real-time software correlator for dynamic light scattering. *Appl. Opt.* **40**, 4011–21 (2001).

[236] D. Magatti and F. Ferri. 25 ns software correlator for photon and fluorescence correlation spectroscopy. *Rev. Sci. Inst.* **74**, 1135–44 (2003).

[237] D. M. Mancini, L. Bolinger, H. Li, K. Kendrick, B. Chance, and J. R. Wilson. Validation of near-infrared spectroscopy in humans. *J Appl Physiol* **77**, 2740–47 (1994).

[238] D. M. Mancini, N. Ferraro, M. Tuchler, B. Chance, and J. R. Wilson. Detection of abnormal calf muscle metabolism in patients with heart failure using phosphorus-31 nuclear magnetic resonance. *Am J Cardiol* **62**, 1234–40 (1988).

[239] J. B. Mandeville, J. J. A. Marota, B. E. Kosofsky, J. R. Keltner, R. Weissleder, B. R. Rosen, and R. M. Weisskoff. Dynamic functional imaging of relative cerebral blood volume during rat forepaw stimulation. *Mag. Res. Med.* **39**, 615–624 (1998).

[240] H. Mao and G. S. Berns. MRI in the study of brain functions: clinical perspectives. *Medicamundi* **46**, 28–38 (2002).

[241] G. Maret and P. E. Wolf. Multiple light scattering from disordered media. the effect of brownian motion of scatterers. *Z. Phys. B.* **65**, 409–413 (1987).

[242] V. A. Markel, V. Mital, and J. C. Schotland. Inverse problem in optical diffusion tomography. III. inversion formulas and singular-value decomposition. *J. Opt. Soc. Am. A* **20**, 890–902 (2003).

[243] V. A. Markel, J. A. O'Sullivan, and J. C. Schotland. Inverse problem in optical diffusion tomography. iv. nonlinear inversion formulas. *J. Opt. Soc. Am. A* **20**, 903–12 (2003).

[244] V. A. Markel and J. C. Schotland. Inverse problem in optical diffusion tomography: I. Fourier-Laplace inversion formulas. *J. Opt. Soc. Am. A* **18**, 1336–47 (2001).

[245] V. A. Markel and J. C. Schotland. Inverse problem in optical diffusion tomography. II. role of boundary conditions. *J. Opt. Soc. Am. A* **19**, 558–66 (2002).

[246] V. Marshall, D. C. Williams, and K. D. Smith. Diaphanography as a means of detecting breast cancer. *Radiology* **150**, 339–343 (1984).

[247] C. L. Matson. A diffraction tomographic model of the forward problem using diffuse photon density waves. *Optics Express* **1**, 6–11 (1997).

[248] C. L. Matson, N. Clark, L. McMackin, and J. S. Fender. Three-dimensional tumor localization in thick tissue with the use of diffuse photon-density waves. *Appl Opt* **36**(1), 214–220 (1997).

[249] S. Matsui, N. Tamura, T. Hirakawa, S. Kobayashi, N. Takekoshi, and E. Murakami. Assessment of working skeletal muscle oxygenation in patients with chronic heart failure. *Am Heart J* **129**, 690–5 (1995).

[250] A. Mayevsky and B. Chance. Repetitive patterns of metabolic changes during cortical spreading depression of the awake rat. *Brain Res.* **65**, 529–33 (1974).

[251] A. Mayevsky, A. Doron, T. Manor, S. Meilin, N. Zarchin, and G. E. Ouaknine. Cortical spreading depression recorded from the human brain using a multiparametric monitoring system. *Brain Res* **740**, 268–74 (1996).

[252] A. Mayevsky and H. R. Weiss. Cerebral blood flow and oxygen consumption in cortical spreading depression. *J. Cereb. Blood Flow Metab.* **11**, 829–36 (1991).

[253] J. Mayhew, D. Johnston, J. Berwick, M. Jones, P. Coffey, and Y. Zheng. Spectroscopic analysis of neural activity in brain: Increased oxygen consumption following activation of barrel cortex. *NeuroImage* **12**(6), 664–675 (2000).

[254] J. Mayhew, D. Johnston, J. Martindale, M. Jones, J. Berwick, and Y. Zheng. Increased oxygen consumption following activation of brain: Theoretical footnotes using spectroscopic data from barrel cortex. *NeuroImage* **13**(6), 975–987 (2001).

[255] T. O. McBride, B. W. Pogue, S. D. Jiang, and U. L. Osterberg. A parallel-detection frequency-domain near-infrared tomography system for hemoglobin imaging of the breast in vivo. *Rev. Sci. Instrum.* **72**, 1817–24 (2001).

[256] T. O. McBride, B. W. Pogue, S. Poplack, S. Soho, W. A. Wells, K. S. Osterman, U. L. Osterberg, and K. D. Paulsen. Multispectral near-infrared tomography: a case study in compensating for water and lipid content in hemoglobin imaging of the breast. *Journal of Biomedical Optics* **7**, 72–79 (2002).

[257] D. J. Mehagnoul-Schipper, B. F. W. van der Kallen, W. N. J. M. Colier, M. C. van der Sluijs, L. J. T. O. van Erning, H. O. M. Thijssen, B. Oeseburg, W. H. L. Hoefnagels, and R. W. M. M. Jansen. Simultaneous measurements of cerebral oxygenation changes during brain activation by near-infrared spectroscopy and functional magnetic resonance imaging in healthy young and elderly subjects. *Human Brain Mapping* **16**, 14–23 (2002).

[258] C. Menon, G. M. Polin, I. Prabakaran, A. Hs, C. Cheung, J. P. Culver, J. . Pingpank, C. S. Sehgal, A. G. Yodh, D. G. Buerk, and D. L. Fraker. An integrated approach to measuring tumor oxygen status using human melanoma xenografts as a model. *Cancer Res* **in press** (2003).

[259] E. R. Mohler. Peripheral arterial disease: identification and implications. *Arch Intern Med* **163**, 2306–14 (2003).

[260] P. A. Mole, Y. Chung, T. K. Tran, N. Sailasuta, R. Hurd, and T. Jue. Myoglobin desaturation with exercise intensity in human gastrochemius muscle. *Am J Physiol* **277**, R173–80 (1999).

[261] J. V. Moore, C. M. West, and C. Whitehurst. The biology of photodynamic therapy. *Physics in Medicine & Biology* **42**, 913–935 (1997).

[262] T. Muellner, A. Nikolic, W. Schramm, and V. Vecsei. New instrument that uses near-infrared spectroscopy for the monitoring of human muscle oxygenation. *J Trauma* **46**, 1082–4 (1999).

[263] S. M. Narayan, E. M. Santori, A. J. Blood, J. S. Burton, and A. W. Toga. Imaging optical reflectance in rodent barrel and forelimb sensory cortex. *NeuroImage* **1**(3), 181–90 (1994).

[264] U. Narayanan, O. Z. Chi, X. Liu, and H. R. Weiss. Effect of AMPA on cerebral cortical oxygen balance of ischemic rat brain. *Neurochemical Research* **25**, 405–411 (2000).

[265] E. M. Nemoto, H. Yonas, and A. Kassam. Clinical experience with cerebral oximetry in stroke and cardiac arrest. *Crit. Care. Med.* **28**(4), 1052–4 (2000).

[266] M. F. Newman, J. L. Kirchner, B. Phillips-Bute, V. Gaver, H. Grocott, R. H. Jones, D. B. Mark, J. G. Reves, and J. A. Blumenthal. Longitudinal assessment of neurocognitive function after coronary-artery bypass surgery. *N Engl J Med* **344**, 395–402 (2001).

[267] A. N. Nielsen, M. Fabricius, and M. Lauritzen. Scanning laser-doppler flowmetry of rat cerebral circulation during cortical spreading depression. *J. Vasc. Res.* **37**(6), 513–522 (2000).

[268] A. M. Nilsson, K. C. Sturesson, D. L. Liu, and A. S. Changes in spectral shape of tissue optical properties in conjuction with laser-induced thermotherapy. *Appl Opt* **37**, 1256–67 (1998).

[269] S. Nioka, D. Moser, G. Lech, M. Evengelisti, T. Verde, B. Chance, and S. Kuno. Muscle deoxygenation in aerobic and anaerobic exercise. *Adv Exp Med Biol* **454**, 63–70 (1998).

[270] J. R. Nourant, F. T, B. J, J. T. M, and I. J. Bigio. Predictions and measurement of scattering and absorption over broad wavelenth ranges in tissue phantoms. *Appl Opt* **36**, 949–57 (1997).

[271] V. Ntziachristos and B. Chance. Probing physiology and molecular function using optical imaging: applications to breast cancer. *Breast Cancer Res* **3**(1), 41–6 (2001).

[272] V. Ntziachristos, B. Chance, and A. G. Yodh. Differential diffuse optical tomography. *Optics Express* **5**(10), 230–242 (1999).

[273] V. Ntziachristos, X. H. Ma, and B. Chance. Time-correlated single photon counting imager for simultaneous magnetic resonance and near-infrared mammography. *Rev. Sci. Instru.* **69**, 4221–4233 (1998).

[274] V. Ntziachristos, A. G. Yodh, M. Schnall, and B. Chance. Concurrent mri and diffuse optical tomography of breast after indocyanine green enhancement. *Proc Natl Acad USA* **97**(6), 2767–2772 (2000).

[275] V. Ntziachristos, A. Yodh, M. Schnall, and B. Chance. Mri-guided diffuse optical spectroscopy of malignant and benign breast lesions. *Neoplasia* **4**, 347–354 (2002).

[276] P. A. Oberg, G. E. Nilsson, T. Tenland, A. Holmstrom, and D. H. Lewis. Use of a new laser doppler flowmeter for measurements of capillary blood flow in skeletal muscle after bullet wounding. *Acta Chir Scand Suppl.* **489**, 145–150 (1979).

[277] E. Okada and D. T. Delpy. Near-infrared light propagation in an adult head model. II. effect of superficial tissue thickness on the sensitivity of the near-infrared spectroscopy signal. *Appl. Opt.* **42**, 2915–21 (2003).

[278] M. A. O'Leary. *Imaging with diffuse photon density waves*. Ph.D. Dissertation Unversity of Pennsylvania (1996).

[279] M. A. O'Leary, D. A. Boas, B. Chance, and A. G. Yodh. Refraction of diffuse photon density waves. *Phy Rev Lett* **69**(18), 2658–2661 (1992).

[280] M. A. O'Leary, D. A. Boas, B. Chance, and A. G. Yodh. Refraction of diffuse photon density waves. *Biophysical Journal* **64**(2), A357–A357 (1993).

[281] M. A. O'Leary, D. A. Boas, B. Chance, and A. G. Yodh. Experimental images of heterogeneous turbid media by frequency-domain diffusing-photon tomography. *Opt Lett* **20**(5), 426–428 (1995).

[282] H. Otaga, T. Yumoki, and T. Yano. Effect of arm cranking on the NIRS determined blood volume and oxygenation of human inactive and exercising vastus lateralis muscle. *J Appl Physiol* **86**, 191–5 (2002).

[283] F. Ozyener. Evaluation of intra-muscular oxgenation during exercise in humans. *Journal of Sports Science and Medicine* **1**, 15–19 (2002).

[284] D. N. Pattanayak. Resolution of optical images formed by diffusion waves in highly scattering media. *GE Tech Info Series* **91CRD241** (1991).

[285] M. S. Patterson, B. Chance, and B. C. Wilson. Time resolved reflectance and transmittance for the non-invasive measurement of tissue optical properties. *Appl Opt* **28**, 2331–2336 (1989).

[286] M. S. Patterson, J. D. Moulton, B. C. Wilson, K. W. Berndt, and J. R. Lakowicz. Frequency-Domain reflectance for the determination of the scattering and absorption properties of tissue. *Appl Opt* **30**(31), 4474–4476 (1991).

[287] K. D. Paulsen and H. Jiang. Spatially varying optical property reconstruction using a finite element diffusion equation approximation. *Am. Assoc. Med. Phys.* **22**(6), 691–701. (1995).

[288] K. D. Paulsen and H. Jiang. Enhanced frequency-domain optical image reconstruction in tissues through total variation minimization. *Appl Opt* **35**, 3447–3458 (1996).

[289] L. A. Paunescu. *Tissue blood flow and oxygen consumption measured with near-infrared frequency-domain spectroscopy*. Dissertation U Illinois at Urbana-Champaign (2001).

[290] Y. Pei, H. L. Graber, and R. L. Barbour. Influence of systematic error in reference states on image quality and on stability of derived information for DC optical imaging. *Appl Opt* **40**, 5755–69 (2001).

[291] T. H. Pham, R. Hornung, M. W. Berns, Y. Tadir, and B. J. Tromberg. Monitoring tumor response during photodynamic therapy using near-infrared photon-migration spectroscopy. *Photochem. Photobiol.* **73**, 669–77 (2001).

[292] M. E. Phelps, J. C. Mazziotta, H. R. Schelbert, R. A. Hawkins, and J. Engel. Clinical PET - what are the issues. *J Nucl Med* **26**(12), 1353–1358 (1985).

[293] R. R. Pindzola and H. Yonas. The xenon-enhanced computed tomography cerebral blood flow method. *Neurosurgery* **43**, 1488–92 (1998).

[294] D. J. Pine, D. A. Weitz, P. M. Chaikin, and Herbolzheimer. Diffusing-wave spectroscopy. *Phys. Rev. Lett.* **60**, 1134–1137 (1988).

[295] J. C. Pinheiro and D. M. Bates. *Mixed-effects models in S and S-Plus*. Springer New York (2000).

[296] B. W. Pogue, R. D. Braun, J. L. Lanzen, C. Erickson, and M. W. Dewhirst. Analysis of the heterogeneity of pO2 dynamics during photodynamic therapy with verteporfin. *Photochem. Photobiol.* **74**, 700–6 (2001).

[297] B. W. Pogue, T. O. McBride, J. Prewitt, U. L. Osterberg, and K. D. Paulsen. Spatially variant regularization improves diffuse optical tomography. *Appl Opt* **38**(13), 2950–2961 (1999).

[298] B. W. Pogue and K. D. Paulsen. High-resolution near-infrared tomographic imaging simulations of the rat cranium by use of apriori magnetic resonance imaging structural information. *Opt Lett* **23**(21), 1716–1718 (1998).

[299] B. W. Pogue, S. P. Poplack, T. O. McBride, W. A. Wells, K. S. Osterman, U. L. Osterberg, and K. D. Paulsen. Quantitative hemoglobin tomography with diffuse near-infrared spectroscopy: Pilot results in the breast. *Radiology* **218**(1), 261–266 (2001).

[300] S. Posse, U. Olthoff, M. Weckesser, L. Jancke, H. W. Muller-Gartner, and S. R. Dager. Regional dynamic signal changes during controlled hyperventilation assessed with blood oxygen level-dependent functional mr imaging. *Am. J. Neurorad.* **18**, 1763–70 (1997).

[301] A. E. Profio and G. A. Navarro. Scientific basis of breast diaphanography. *Med. Phys.* **16**, 60–65 (1989).

[302] P. N. Pusey and J. M. Vaughan. *Dielectric and Related Molecular Processes X - Ed. M. D. Specialist Periodical Report* volume 2 chapter Light Scattering and Intensity Fluctuation Spectroscopy. The Chemical Society London (1975).

[303] V. Quaresima, S. Homma, K. Azuma, S. Shimizu, F. Chiarotti, M. Ferrari, and A. Kagaya. Calf and shin muscle oxygenation patterns and femoral artery blood flow during dynamic plantar flexion exercise in humans. *Eur J Appl Physiol* (2001).

[304] J. S. Raynaud, S. Duteil, J. T. Vaughan, F. Hennel, C. Wary, A. Leroy-Willig, and P. G. Carlier. Determination of skeletal muscle perfusion using arterial spin labeling NMRI: validation by comparison with venous occlusion plethysmography. *Magn Reson Med* **46**, 305–11 (2001).

[305] M. Reivich, D. Kuhl, A. Wolf, J. H. Greenberg, M. Phelps, T. Ido, V. Casella, J. Fowler, E. Hoffman, A. Alavi, P. Som, and L. Sokoloff. The [18F] fluorodeoxyglucose method for the measurement of local cerebral glucose utilization in man. *Circ Res* **44**, 127–37 (1979).

[306] E. K. Richard. Cardiovascular physiology concepts. Online: `http://www.cvphysiology.com` accessed at 3/2004 (1999-2004).

[307] J. Ripoll. *Ligth Diffusion in Turbid Media With Biomedical Applications*. Ph.D. Dissertation Universidad Autonoma de Madrid (2000).

[308] J. Ripoll and M. Nieto-Vesperinas. Reflectance and transmission coefficients for diffuse photon density waves. *Opt Lett* **24**, 796–798 (1999).

[309] J. Ripoll, V. Ntziachristos, J. P. Culver, D. N. Pattanayak, A. G. Yodh, and M. Nieto-Vesperinas. Recovery of optical parameters in multiple-layered diffusive media: theory and experiments. *J. Opt. Soc. A* **18**(4), 821–830 (2001).

[310] J. Ripoll, R. B. Schulz, and V. Ntziachristos. Free-space propagation of diffuse light: Theory and experiments. *Phys Rev Lett* **91**, 1039011–1039014 (2003).

[311] C. E. Riva, B. Ross, and G. B. Benedek. Laser doppler measurements of blood flow in capillary tubes and retinal arteries. *Invest. Ophthalmol.* **11**, 936–944 (1972).

[312] G. W. Roach, M. Kanchuger, C. M. Mangano, M. Newman, N. Nussmeier, R. Wolman, A. Aggarwal, K. Marschall, S. H. Graham, and L. C. Adverse cerebral outcomes after coronary bypass surgery. multicenter study of perioperative ischemia research group and the ischemia research and education foundation investigators. *N Engl J Med* **335**, 1857–63 (1996).

[313] C. S. Robertson, S. P. Gopinath, and B. Chance. A new application for near-infrared spectroscopy: Detection of delayed intracranial hematomas after head injury. *Journal of Neurotrauma* **12**, 591–600 (1995).

[314] P. E. Roland, B. Larsen, N. A. Lassen, and E. Skinhoj. Supplementarymclaughlinfinger motor area and other cortical areas in organization of voluntary movements in man. *J. Neurophysiol.* **43**, 118–36 (1980).

[315] R. Roy and E. M. Sevick-Muraca. Truncated newton's optimization scheme for absorption and fluorescence optical tomography: Part i theory and formulation. *Opt Express* **4**, 353–71 (1999).

[316] R. Roy and E. M. Sevick-Muraca. Truncated newton's optimization scheme for absorption and fluorescence optical tomography: Part ii reconstruction from synthetic measurements. *Opt Express* **4**, 372–82 (1999).

[317] R. Roy and E. M. Sevick-Muraca. Active constrained truncated newton method for simple-bound optical tomography. *J. Opt. Soc. Am. A* **17**, 1627–41 (2000).

[318] P. A. Rueckert and P. Hanson. Comparison of arterial occlusion and ischaemic exercise for the study of vasodilatation in the human calf. *Clin Sci (Lond)* **88**, 643–9 (1995).

[319] K. W. Rundell, S. Niola, and B. Chance. Haemoglobin/myoglobin desaturation during speed skating. *Med & Sci in Sports & Exer* **29**, 248–58 (1997).

[320] B. Ruth. Measuring the steady-state value and the dynamics of the skin blood flow using the non-contact laser speckle method. *Med. Eng. Phys.* **16**, 105–11 (1994).

[321] R. B. Rutherford, J. D. Baker, C. Ernst, K. W. Johnston, J. M. Porter, S. Ahn, and D. N. Jones. Recommended standards for reports dealing with lower extremity ischemia: revised version. *J Vasc Surg* **26**, 517–38 (1997).

[322] T. Sako, T. Hamaoka, H. Higuchi, Y. Kurosawa, and T. Katsumura. Validity of NIR spectroscopy for quantitatively measuring muscle oxidative metabolic rate in exercise. *J Appl Physiol* **90**, 338–344 (2001).

[323] O. Sakurada, C. Kennedy, J. Jehle, J. D. Brown, G. L. Carbin, and L. Sokoloff. Measurement of local cerebral blood flow with iodo [14c] antipyrine. *Am. J. Physiol.* **234**(1), H59–66 (1978).

[324] F. E. W. Schmit, M. E. Fry, E. M. C. Hillman, J. C. Hebden, and D. T. Delpy. A 32-channel time-resolved instrument for medical optical tomography. *Rev. Sci. Instrum.* **69**, 4221–33 (1998).

[325] J. M. Schmitt, A. Knuttel, and J. R. Knutson. Interference of diffusive light waves. *J. Opt. Soc. Am. A* **9**, 1832 (1992).

[326] C. H. Schmitz, M. Locker, J. Mlasker, A. H. Hielscher, and R. L. Barbour. Instrumentation for fast functional optical tomography. *Rev. Sci. Instrum.* **73**, 1–11 (2002).

[327] J. C. Schotland. Continous-wave diffusion imaging. *J. Opt. Soc. Am. A* **14**(1), 275–279 (1997).

[328] J. C. Schotland, J. C. Haselgrove, and J. S. Leigh. Photon hitting density. *Appl Opt* **32**, 448–453 (1993).

[329] R. B. Schulz, J. Ripoll, and V. Ntziachristos. Noncontact optical tomography of turbid media. *Opt Lett* **28**, 1701–3 (2003).

[330] G. Schwarz, G. Litscher, R. Kleinert, and R. Jobstmann. Cerebral oximetry in dead subjects. *J Neurosurg. Anesthesiol.* **8**, 189–93 (1996).

[331] M. Schweiger and S. R. Arridge. Optical tomographic reconstruction in a complex head model using a priori region boundary information. *Phy Med Biol* **44**(11), 2703–2721 (1999).

[332] R. J. Seitz and P. E. Roland. Learning of sequential finger movements in man: a combined kinematic and positron emission tomography (pet) study. *Eur. J. Neurosci.* **4**, 154–65 (1992).

[333] A. Seiyama, O. Hazeki, and M. Tamura. Noninvasive quantitative analysis of blood oxygenation in rat skeletal muscle. *J Biochem (Tokyo)* **103**, 419–24 (1988).

[334] E. M. Sevick, J. R. Lakowicz, H. Szmacinski, K. Nowaczyk, and M. L. Johnson. Frequency domain imaging of absorbers obscured by scattering. *J.Photochem.Photobiol.B: Biol.* **16**, 169–185 (1992).

[335] N. Shah, A. Cerussi, C. Eker, J. Espinoza, J. Butler, J. Fishkin, R. Hornung, and B. Tromberg. Noninvasive functional optical spectroscopy of human breast tissue. *Proc Natl Acad Sci U S A* **98**(8), 4420–5. (2001).

[336] A. P. Shepherd and G. L. Riedel. Continuous measurements of intestinal mucosal blood flow by laser-doppler velocimetry. *Am. J. Physiol.* **242**, G668–G672 (1982).

[337] E. A. Sickles. Breast cancer detection with transillumination and mammography. *Am. J. Roentgenology* **142**, 841–844 (1984).

[338] E. A. Sickles. Periodic mammographic follow-up of probably benign lesions: results in 3,184 consecutive cases. *Radiology* **179**(2), 463–8. (1991).

[339] A. M. Siegel, J. A. Marota, and D. A. Boas. Design and evaluation of a continuous-wave diffuse optical tomography system. *Optics Express* **4**, 287–298 (1999).

[340] B. K. Siesjo. *Brain Energy Metabolism* chapter Carbon Dioxide in Brain Energy Metabolism, pages 131–50. Wiley New York (1978).

[341] L. Sirovich and R. Everson. Management and analysis of large scientific datasets. *The international journal of supercomputer applications* **6**(1), 50–68 (1992).

[342] L. Sirovich and E. Kaplan. *In vivo optical imaging of brain function* chapter Analysis methods for optical imaging. Methods and New Frontiers in Neuroscience. CRC Press (2002).

[343] T. M. Sitnik, J. A. Hampton, and B. W. Henderson. Reduction of tumor oxygenation during and after photodynamic therapy in vivo: effects of fluence rate. *Cancer Res* **77**, 1386–94 (1998).

[344] G. G. Somjen. Mechanisms of spreading depression and hypoxic spreading depression-like depolarization. *Physiological Rev* **81**, 1065–96 (2001).

[345] J. Sonn and A. Mayevsky. Effects of brain oxygenation on metabolic, hemodynamic, ionic and electrical responses to spreading depression in the rat. *Brain Res.* **882**, 212–6 (2000).

[346] J. Steinbrink, H. Wabnitz, H. Obrig, A. Villringer, and H. Rinneberg. Determining changes in NIR absorption using a layered model of the human head. *Phys Med Biol* **46**(3), 879–96. (2001).

[347] M. J. Stephen. Temporal fluctuations in wave propagation in random media. *Phys. Rev. B* **37**, 1–5 (1988).

[348] M. D. Stern. In vivo evaluation of microcirculation by coherent light scattering. *Nature* **254**, 56–58 (1975).

[349] M. D. Stern, P. D. Bowen, R. Parma, R. W. Osgood, R. L. Bowman, and J. H. Stein. Measurements of renal cortical and medullary blood flow by laser-doppler spectroscopy in the rat. *Am. J. Physiol.* **236**, F80–F87 (1979).

[350] M. D. Stern, D. L. Lappe, P. D. Bowen, and J. E. Chimosky. Continuous measurements of tissue blood flow by laser-doppler spectroscopy. *Am. J. Physiol.* **232**, H441–H448 (1977).

[351] G. Strangman, M. A. Franceschini, and D. A. Boas. Factors affecting the accuracy of near-infrared spectroscopy concentration calculations for focal changes in oxygenation parameters. *NeuroImage* **18**, 865–79 (2003).

[352] T. Tagawa, T. Imaizumi, T. Endo, M. Shiramoto, Y. Harasawa, and A. Takeshita. Role of nitric oxide in reactive hyperemia in human forearm vessels. *Circulation* **90**, 2285–90 (1994).

[353] K. Takahashi, J. H. Greenberg, P. Jackson, K. Maclin, and J. Zhang. Neuroprotective effects of inhibiting poly(ADP-ribose) synthetase on focal cerebral ischemia in rats. *Journal of Cerebral Blood Flow & Metabolism* **17**, 1137–1142 (1997).

[354] T. Tamaki, S. Uchiyama, T. Tamura, and S. Nokana. Changes in muscle oxygenation during weight lifting exercise. *Eur J of Appl Physiol* **68**, 465–9 (1994).

[355] Y. Tamaki, M. Araie, E. Kawamoto, S. Eguchi, and H. Fujii. Non-contact two-dimensional measurement of retinal microcirculation using laser speckle phenomenon. *Inv. Opth.. and Vis. Sci.* **35**, 3825–34 (1994).

[356] T. Tanaka and G. B. Benedek. Measurement of the velocity of blood flow (in vivo) using a fiber optic catheter and optical mixing spectroscopy. *Appl Opt* **14**, 189–196 (1975).

[357] T. Tanaka, C. Riva, and I. Ben-Sira. Blood velocity measurements in human retinal vessels. *Science* **186**, 830–831 (1974).

[358] K. M. Taylor. Central nervous system effects of cardiopulmonary bypass. *Ann Thorac Surg* **66**, S20–24 (1998).

[359] T. Tenland, E. G. Salerud, G. E. Nilsson, and P. A. Oberg. Spatial and temporal variations in human skin blood flow. *Int J Microcirc Clin Exp* **2**, 81–90 (1983).

[360] P. Tong, W. I. Goldburg, C. K. Chan, and A. Sirivat. Turbulent transition by photon-correlation spectroscopy. *Phys. Rev. A* **37**, 2125–2133 (1988).

[361] J. F. Toussaint, K. K. Kwong, F. O. M'Kparu, R. M. Weisskoff, P. J. LaRaia, and H. L. Kantor. Interrelationship of oxidative metabolism and local perfusion demonstrated by NMR in human skeletal muscle. *J Appl Physiol* **81**, 2221–8 (1996).

[362] J. F. Toussaint, K. K. Kwong, F. O. M'Kparu, R. M. Weisskoff, P. J. LaRaia, and H. L. Kantor. Perfusion changes in human skeletal muscle during reactive hyperemia measured by echo-planar imaging. *Magn Reson Med* **35**, 62–69 (1996).

[363] T. K. Tran, N. Sailasuta, U. Kreutzer, R. Hurd, Y. chung, P. Mole, S. Kuno, and T. Jue. Comparative analysis of NMR and NIRS measurements of intracellular PO_2 in human skeletal muscle. *Am J Physiol* **276**, R1682–90 (1999).

[364] B. J. Tromberg, A. Orenstein, S. J. Barker, J. Hyatt, J. S. Nelson, and M. W. Berns. In vivo tumor oxygen tension measurements for the evaluation of the efficiency of photodynamic therapy. *Photochem. Photobiol.* **52**, 375–85 (1990).

[365] B. J. Tromberg, N. Shah, R. Lanning, A. Cerussi, J. Espinoza, T. Pham, L. Svaasand, and J. Butler. Non-invasive in vivo characterization of breast tumors using photon migration spectroscopy. *Neoplasia* **2**(1-2), 26–40. (2000).

[366] B. J. Tromberg, L. O. Svaasand, T. Tsay, and R. C. Haskell. Properties of photon density waves in multiple-scattering media. *Appl Opt* **32**, 607–616 (1993).

[367] H. vab Santbrink, A. I. Maas, and C. J. Avezaat. Continous monitoring of partial pressure of brain tissue oxygen in patients with severe head injury. *Neurosurgery* **38**, 21–31 (1996).

[368] R. Valabregue, A. Aubert, J. Burger, J. Bittoun, and R. Costalat. Relation between cerebral blood flow and metabolism explained by a model of oxygen exchange. *J. Cereb. Blood Flow and Metab.* **23**, 536–45 (2003).

[369] J. M. Valdueza, J. O. Balzer, A. Villringer, T. J. Vogl, R. Kutter, and K. M. Einhaupl. Changes in blood flow velocity and diameter of the middle cerebral artery during hyper-vnetilation: assessment with mr and transcranial doppler sonography. *Am. J. Neurorad.* , 1929–34 (1997).

[370] A. Y. Valkov and V. P. Romanov. Characteristics of propagation and scattering of light in nematic liquid crystals. *Sov. Phys. JETP* **63**, 737–743 (1986).

[371] M. C. Van Beekvelt, M. S. Borghuis, B. G. Van Engelen, R. A. Wevers, and W. N. Colier. Adipose tissue thieckness affects in vivo quantitative near-IR spectroscopy in human skeletal muscle. *Clin Sci (Lond)* **101**, 21–28 (2001).

[372] M. C. Van Beekvelt, W. N. Colier, R. A. Wevers, and B. G. Van Engelen. Performance of near-infrared spectroscopy in measuring local O(2) consumption and blood flow in skeletal muscle. *J Appl Physiol* **90**, 511–19 (2001).

[373] P. van der Zee, M. Cope, S. R. Arridge, M. Essenpreis, L. A. Potter, A. D. Edwards, J. S. Wyatt, D. C. McCormick, S. C. Toth, E. O. R. Reynolds, and D. T. Delpy. Experimentally measured optical pathlengths for the adult's head, calf and forearm and the head of the

newborn infant asa function of interoptode spacing. *Adv. Exp. Med. Biol.* **316**, 143–153 (1992).

[374] R. L. Van Heertum and R. S. Tikofsky. *Functional Cerebral SPECT in PET imaging*. Lippincott Williams and Wilkins (2000).

[375] A. Villringer and B. Chance. Non-invasive optical spectroscopy and imaging of human brain function. *Trends Neurosci* **20**, 435–442 (1997).

[376] A. Villringer and U. Dirnagl. Coupling of brain activity and cerebral blood flow: basis of functional neuroimaging. *Cereb. Brain. Metab. Rev.* **7**, 240–76 (1995).

[377] A. Villringer, A. Them, U. Lindauer, K. Einhaupl, and U. Dirnagl. Capillary perfusion of the rat brain cortex - an in vivo confocal microscopy study. *Circ. Res.* **75**, 55–62 (1994).

[378] S. A. Walker, S. Fantini, and E. Gratton. Image reconstruction by backprojection from frequency-domain optical measurements in highly scattering media. *Appl Opt* **36**(1), 170–179 (1997).

[379] D. J. Wallace, B. Michener, D. Choudhury, M. Levi, P. Fennelly, D. M. Huber, and B. Barbieri. Summary of the results of a 95 subject human clinical trial for the diagnosis if peripheral vascular disease using a near infrared frequency domain hemoglobin spectrometer. In *Proc. SPIE* pages 300–16 (1999).

[380] H. Wallberg, A. Alveryd, U. Bergvall, K. Nasiell, P. Sundelin, and S. Troel. Diaphanography in breast carcinoma. *Acta Radiologica Diagnosis* **26**, 33–44 (1985).

[381] H. Wang, M. E. Putt, M. J. Emanuele, D. B. Shin, V. Madrak, A. G. Yodh, and T. M. Busch. Tumor oxygenation measured by noninvasive spectroscopy predicts photodynamic therapy outcome. *Cancer Res* **submitted** (2004).

[382] H. Wang, T. C. Zhu, M. Solonenko, S. M. Hahn, J. M. Metz, A. Dimofte, J. Mile, and A. G. Yodh. In vivo measurements of penetration depth, oxygenation, and drug concentration using broadband absorption in human tissues before and after photodynamic therapy. *Photonics West, SPIE* **PDT**, na (2003).

[383] J. Wang, G. K. Aguirre, D. Y. Kimberg, A. C. Roc, L. Li, and J. A. Detre. Arterial spin labeling perfusion fMRI with very low task frequency. *Magn Reson Med* **49**, 796–802 (2003).

[384] Z. Y. Wang, E. A. Noyszewski, and J. S. Leigh. In vivo MRS measurement of deoymyoglobin in human forearms. *Magn Reson Med* **14**, 562–7 (1990).

[385] D. J. Watmough. Transillumination of breast tissues: factors governing optimal imaging of lesions. *Radiology* **147**, 89–92 (1983).

[386] H. R. Weiss, A. K. Sinha, and X. W. Lu. Effect of up-regulation of NMDA receptors on cerebral O-2 consumption and blood flow in rat. *Brain Res* **730**, 193–198 (1996).

[387] R. J. Whitney. The measurement of volume changes in human limbs. *J Physiol* **121**, 1–27 (1953).

[388] P. C. Williams, M. D. Stern, P. D. Bowen, R. A. Brooks, M. K. Hammock, R. L. Bowman, and G. Chiro. Mapping of cerebral cortical strokes in rhesus monkeys by laser doppler spectroscopy. *Med. Res. Eng.* **13**, 3–5 (1980).

[389] B. C. Wilson, , and M. S. Patterson. The physics of photodynamic therapy. *Phys. Med. Biol.* **31**, 327 (1986).

[390] B. C. Wilson, M. S. Patterson, and L. Lilge. Implicit and explicit dosimetry in photodynamic therapy: a new paradigm. *Las. Med. Sci.* **12**, 182–92 (1997).

[391] J. R. Wilson, D. M. Mancini, K. McKully, N. Ferraro, V. Lanoce, and B. Chance. Noninvasive detection of skeletal muscle underperfusion with near infra-red spectroscopy in patients with heart failure. *Circulation* **80**, 1668–74 (1989).

[392] M. Wolf, U. Wolf, J. H. Choi, L. P. Safonova, R. Gupta, V. Toronov, A. Michalos, L. A. Paunescu, and E. Gratton. Functional fast neuronal signals in the visual and motor cortex detected by frequency-domain near-infrared spectroscopy. In *OSA Biomedical Topical Meetings, OSA Technical Digest* pages 205–7 Miami, FL (2002). Optical Society of America.

[393] T. Wolf, U. Lindauer, U. Reuter, T. Back, A. Villringer, K. Einhäupl, and U. Dirnagl. Noninvasive near infrared spectroscopy monitoring of regional cerebral blood oxygenation changes during peri-infarct depolarizations in focal cerebral ischemia in the rat. *J Cereb Blood Flow and Metab* **17**, 950–54 (1997).

[394] T. Wolf, U. Lindauer, A. Villringer, and U. Dirnagl. Excessive oxygen or glucose supply does not alter the blood flow response to somatosensory stimulation or spreading depression in rats. *Brain Res.* **761**, 290–99 (1997).

[395] T. Wolf, H. Obrig, J. Dreier, T. Back, A. Villringer, and U. Dirnagl. Systemic nitric oxide synthase inhibition does not affect brain oxygenation during cortical spreading depression in

rats: A noninvasive near-infrared spectroscopy and laser-doppler flowmetry study. *J. Cereb. Blood Flow and Metab.* **16**, 1100–07 (1996).

[396] U. Wolf, M. Wolf, J. H. Choi, M. Levi, D. Choudhury, S. Hull, D. Coussirat, L. A. Paunescu, L. P. Safonova, A. Michalos, W. W. Mantulin, and E. Gratton. Localized irregularities in hemoglobin flow and oxygenation incalf muscle in patients with peripheral vascular disease detected with near-infrared spectrophotometry. *J Vasc Surg* **37**, 1017–26 (2003).

[397] U. Wolf, M. Wolf, J. H. Choi, L. A. Paunescu, L. P. Safonova, A. Michalos, and E. Gratton. Mapping of hemodynamics on the human calf with near infrared spectroscopy and the influence of the adipose tissue thickness. *Adv Exp Med Biol* **510**, 225–30 (2003).

[398] M. Xu, W. Cai, M. Lax, and R. R. Alfano. Photon-transport forward model for imaging in turbid media. *Opt. Lett.* **26**, 1066–68 (2001).

[399] Y. Yang, H. L. Liu, X. D. Li, and B. Chance. Low cost frequency-domain photon migration instrument for tissue spectroscopy, oximetry, and imaging. *Opt. Eng.* **36950**, 1562–69 (1997).

[400] Y. Yao, Y. Wang, Y. Pei, W. Zhu, and R. L. Barbour. Frequency-domain optical imaging of absorption and scattering distributions using a born iterative method. *J. Opt. Soc. Am. A* **14**, 325–342 (1997).

[401] K. Yaoeda, M. Shirakashi, S. Funaki, H. Funaki, T. Nakatsue, and H. Abe. Measurement of microcirculation in the optic nerve head by laser speckle flowgraphy and scanning laser doppler flowmetry. *Am. J. Opthalmol.* **129**, 734–39 (2000).

[402] F. Q. Ye, A. M. Smith, Y. Yang, J. Duyn, V. S. Mattay, U. E. Ruttimann, J. A. Frank, D. R. Weinberger, and A. C. McLaughlin. Quantitation of regional cerebral blood flow increases during motor activation: A steady-state arterial spin tagging study. *Mag Res Med* **42**, 404–7 (1999).

[403] A. Yodh and B. Chance. Spectroscopy and imaging with diffusing light. *Physics Today* **48**(3), 34–40 (1995).

[404] A. G. Yodh and D. A. Boas. *Biomedical Photonics* chapter Functional Imaging with Diffusing Light, pages 21/1–45. CRC Press (2003).

[405] T. Yokoo, B. W. Knight, and L. Sirovich. An optimization approach to signal extraction from noisy multivariate data. *NeuroImage* **14**, 1309–26 (2001).

[406] R. P. Yonas, H andPindzola and D. W. Johnson. Xenon/computed tomography cerebral blood flow and its use in clinical management. *Neurosurg Clin N Am* **7**, 605–16 (1996).

[407] G. Yu, T. Durduran, D. Furuya, J. H. Greenberg, and A. G. Yodh. Frequency-domain multiplexing system for in vivo diffuse light measurements of rapid cerebral hemodynamics. *Appl. Opt.* **42**, 2931–39 (2003).

[408] G. Yu, T. Durduran, D. Furuya, G. Lech, C. Zhou, B. Chance, J. H. Greenberg, and A. G. Yodh. Hemodynamic measurements in rat brain and human muscle combining diffuse near-infrared absorption and correlation spectroscopies. In *Proc. SPIE, Photonics West* (2003).

[409] G. Yu, T. Durduran, H. W. Wang, C. Zhou, H. M. Saunders, C. M. Sehgal, T. M. Busch, and A. G. Yodh. Non-invasive monitoring hemodynamic responses in rif tumors during and after pdt. In *Proc. SPIE, Photonics West* (2003).

[410] G. Yu, T. Durduran, C. Zhou, D. Shin, H. M. Saunders, C. M. Sehgal, M. Putt, A. G. Yodh, and T. M. Busch. Monitoring of tissue hemodynamic response to photodynamic therapy for the prediction of treatment efficacy. *J Appl Physiol* **in prep.** (2004).

[411] G. Yu, D. T, G. Lech, C. Zhou, B. Chance, and A. G. Yodh. Noninvasive,simultaneous measurements of tissue oxgenation and blood flow to estimate oxygen metabolism during exercise and cuff ischemia in human calf muscle. *J Appl Physiol* **in preparation** (2004).

[412] A. Zauner, W. P. Daugherty, M. R. Bullock, and D. S. Warner. Brain oxygenation and energy metabolism: Part i - biological function and pathophysiology. *Neurosurgery* **51**(2), 289–302 (2002).

[413] A. Zauner and J. P. Muizelaar. *Head Injury* chapter 11. Measuring Cerebral Blood Flow and Metabolism, pages 217–27. Chapman and Hall (1997).

[414] Y. Zheng, D. Johnston, J. Berwick, and J. Mayhew. Signal source separation in the analysis of neural activity in brain. *NeuroImage* **13**, 447–58 (2001).

[415] Y. Zheng, J. Martindale, D. Johnston, M. Jones, J. Berwick, and J. Mayhew. A model of the hemodynamic response and oxygen delivery to brain. *NeuroImage* **16**, 617–637 (2002).

[416] C. Zhou, T. Durduran, G. Yu, and A. G. Yodh. Optimizing image reconstruction of tissue blood flow by diffuse correlation tomography. *Photonics West, SPIE* **4955-43** (2003).

[417] Q. Zhu, T. Durduran, V. Ntziachristos, M. Holboke, and A. G. Yodh. Imager that combines near-infrared diffusive light and ultrasound. *Opt Lett* **24**(15), 1050–1052 (1999).